

**DESIGN AND SYNTHESIS OF COLLOIDAL QUANTUM DOTS AND
THEIR OPTOELECTRONIC PROPERTIES**

Par
Hui Zhang

Thèse présentée pour l'obtention du grade de
Philosophiae Doctor (Ph.D.)
en sciences de l'énergie et des matériaux

Jury d'évaluation

| | |
|---|---|
| Président du jury et examineur interne | Prof. Kulbir Kaur Ghuman INRS-EMT |
| Examineur externe | Prof. Dilip Kumar Sarkar Université du Québec à Chicoutimi |
| Examineur externe | Prof. Karthik Shankar University of Alberta |
| Directeur de recherche | Prof. Federico Rosei INRS-EMT |
| Codirecteur de recherche | Prof. Shuhui Sun INRS-EMT |

ACKNOWLEDGEMENTS

First and foremost, I would like to thank my supervisors, Prof. Federico Rosei and Prof. Shuhui Sun, for their continuous guidance and assistance throughout every stage of my Ph.D. study. Their enthusiasm and effort make my research work rich and colorful, allowing me to step in and grow in a fascinating scientific field. Their invaluable inspirations and professional advices make me find the right direction both in my academic research and daily life. The experience under their supervision is one of the most important achievements in my life. Their professional attitude has also greatly motivated me to explore my future academic career.

I also would like to extend my gratitude to my group leaders, Prof. Haiguang Zhao and Dr. Gurpreet Singh Selopal, for their kind help in motivating me. They provide me lots of invaluable suggestions, which helped me reach my research goals. They always make meaningful discussion with me to help me solve problems both in experimental and theoretical parts.

I extend my gratitude to all the group members from Nano-FemtoLAB and other collaborators for their support and help throughout my Ph.D. work. I feel lucky to be part of such a hardworking, supportive and inspiring group with graduate students and postdoctoral fellows, including Dr. Daniele Benetti, Dr. Louis Vervoort, Dr. Fabiola Navarro-Pardo, Dr. Lucas V. Besteiro, Dr. Emek G. Durmusoglu, Dr. Lei Jin, Dr. Kaustubh Basu, Chao Wang, Jiabin Liu, Dr. Rusoma Akilimali, Dr. Mahyar Mohammadnezhad, Omar Abdelkarim, Imran Deem, Faying Li, Xin Liu, *et al.* I also want to thank Dr. Yue Huang for his encouragement when I feel down and his helps in my study and daily life.

I would like to thank all the staff and technicians in INRS-EMT center, especially Mrs. H  l  ne Sabourin, Mrs. Michelle Marcotte, Mrs. Tatiana Brahmi and Mrs. H  l  ne Tanguay for their professionalism and their kindness. Also thanks Mr. Christophe Chabanier for helping me address

problems when I worked on X-ray diffraction, X-ray photoelectron spectroscopy, and scanning electron microscopy.

I am grateful to my beloved parents for their unconditional love, support, and encouragement, which are important parts of my study life abroad. I wish to thank my other family members and friends for their continuous love and heartfelt support.

Finally, I wish to acknowledge the doctoral excellence scholarships from the UNESCO Chair Materials and Technologies for Energy Conversion, Saving and Storage (MATECSS) and the Fonds de recherche du Québec Nature et technologies (FRQNT) for supporting my Ph.D. study.

ABSTRACT

Colloidal quantum dots (QDs) are semiconductor nanocrystals (several to tens nm), whose size is smaller than the exciton Bohr radius of the bulk material. QDs exhibit discrete energy levels resulting from quantum confinement effect in all three spatial dimensions, rendering them unique size/composition/shape-dependent optoelectronic properties. Compared to bulk materials, QDs have unique properties such as tunable band gaps, broad absorption spectra, multiple exciton generation and high extinction coefficients. The controlled synthesis of colloidal semiconductor QDs has defined a new way to use them as potential building blocks in multiple emerging technologies such as biomedical labels, thermal sensors, light-emitting diodes, QDs sensitized solar cells (QDSCs), solar-driven photoelectrochemical (PEC) cells for hydrogen (H_2) generation and photodetectors. In this thesis, colloidal bare, doped and core/shell QDs are designed and synthesized with tunable size and narrow size distribution. Subsequently, their structural and optoelectronic properties are investigated systematically.

A facile approach was designed for the synthesis of colloidal PbS QDs using thiourea and lead acetate as precursors for sulfur and lead, respectively. The sizes of the PbS QDs could be systematically controlled by simply adjusting the reaction parameters. Then, a Cd post-treatment on the bare PbS QDs via a cation exchange method was performed for increasing the stability of QDs, which is favorable for the fabrication of device under ambient environment. As a proof of concept, as-synthesized PbS QDs were employed as light harvesters for both (i) solar-driven PEC cells for H_2 generation and (ii) QDSCs. A saturated photocurrent density of $\sim 2 \text{ mA/cm}^2$ under one sun illumination (AM 1.5G, 100 mW/cm^2) is observed for PEC device based on PbS QDs synthesized using thiourea, which is comparable with that of PEC device based on PbS QDs synthesized using air-sensitive and unstable bis(trimethylsilyl) sulfide $[(TMS)_2S]$. For QDSCs, the devices fabricated with QDs synthesized from thiourea reveal a better power conversion efficiency (2.00%) compared to devices fabricated with QDs synthesized from traditional $(TMS)_2S$ (1.40%)

under one sun illumination (AM 1.5G, 100 mW/cm²). This work demonstrates that the developed synthetic method is a promising alternative to existing methodologies of PbS QDs and holds great potential for future solar technologies.

Instead of adjusting the size of bare QDs to tune their optoelectronic properties, doping of transition metal ions (such as Mn, Co, Cu, Ag, *etc.*) in semiconductor QDs is another promising approach for introducing unique properties. Although manganese (Mn) ions doped wide band gap (larger than the energy for Mn ⁴T₁-⁶A₁ transition of 2.12 eV, such as ZnSe) QDs have been widely studied, the optical properties and emission mechanisms of Mn-doped narrow band gap (smaller than 2.12 eV, such as PbS) QDs are not well understood. The oil-soluble Mn-doped PbS QDs of identical size were designed and synthesized with different Mn contents. Compared with pure PbS QDs, the photoluminescence (PL) peak positions of Mn-doped PbS QDs are observed significantly red shifts, resulting in an enlarged Stokes shift. The large Stokes shift of Mn-doped QDs is attributed to a new emission mechanism (named as “Mn-PbS” emission), in which the photogenerated electron is transferred to the electronic states of Mn ions (⁴T₁) and then recombined with holes in the valence band (VB) of QDs host. The Mn-doped PbS QDs is also found to exhibit a faster temperature-dependent PL response compared to pure PbS QDs, demonstrating that the Mn-doped PbS QDs are promising alternatives for use in thermal sensing. Colloidal bare QDs suffer from high density of surface traps that acts as recombination center, resulting in undesirable charge recombination and limiting the efficiency and long-term stability for their application in optoelectronic device. The core/shell architecture is regarded as a promising approach to resolve these issues. The optoelectronic properties and band alignment in colloidal heterostructured CdS/CdSe core/shell QDs are engineered by tuning the shell thickness. The changes in structural and optical properties were investigated as a function of CdSe shell thickness (0.6-1.9 nm) overgrowth on a CdS core QD with a size of 3.0 nm in diameter. Results demonstrate that the optimization of the shell thickness can significantly broaden the light

absorption range towards longer wavelengths and enhance the rate of photoelectron separation and transport in QDs/TiO₂ photoanode. Complementing by theoretical modeling, it is found that the band alignment in this heterostructured system could be engineered from a quasi type-II (electrons are localized over the whole QDs region but holes are delocalized mostly in the shell) to an inverted type-I (both electrons and holes are mostly delocalized in the shell) localization regime by changing the shell thickness. Optimizing the optoelectronic properties and band alignment in this colloidal core/shell QD system with a shell thickness of 1.6 nm together with carbon nanotubes (CNTs)-TiO₂ hybrid photoanode has enabled the demonstration of a PEC cell with a high photocurrent density of up to ~16.0 mA/cm² (at 0.9 V vs. reversible hydrogen electrode, RHE), which represents the highest value ever reported for PEC cells based on CdS/CdSe QDs. The PEC cells also reveal excellent long-term stability, remaining 83% of its initial value after 4 h under one continuous sun illumination (AM 1.5G, 100 mW/cm²). These results indicate that the design and optimization of the optoelectronics and band alignment of heterostructured core/shell QDs is a facile and efficient approach to fabricate highly efficient and stable QD-based PEC cells for H₂ generation and other optoelectronic devices.

Keywords: *Quantum dots, thiourea, manganese doped, photoluminescence mechanism, lead sulfide, temperature-dependent optical properties, engineered optoelectronic properties; Heterostructured core/shell quantum dots; band alignment tunable; theoretical calculation; quantum dots sensitized solar cells; photoelectrochemical cells.*

TABLE OF CONTENTS

| | |
|---|-------------|
| ACKNOWLEDGEMENTS | I |
| ABSTRACT | III |
| TABLE OF CONTENTS | VI |
| LIST OF FIGURES | IX |
| LIST OF TABLES | XVII |
| CHAPTER 1. INTRODUCTION AND BACKGROUND | 1 |
| 1.1 NANOMATERIAL AND ITS CLASSIFICATION..... | 1 |
| 1.2 WHAT ARE COLLOIDAL QDS?..... | 4 |
| 1.3 PROPERTIES OF COLLOIDAL BARE QDS | 5 |
| 1.4 DOPED QDS..... | 10 |
| 1.5 CORE/SHELL STRUCTURED QDS..... | 12 |
| 1.6 METHODOLOGIES FOR QDS SYNTHESIS..... | 15 |
| 1.7 SYNTHESIS OF COLLOIDAL CORE/SHELL QDS..... | 17 |
| 1.8 APPLICATION OF QDS | 18 |
| 1.8.1 <i>Application in QDSCs</i> | 21 |
| 1.8.2 <i>Application in PEC cells for H₂ generation</i> | 23 |
| 1.9 RESEARCH OBJECTIVES..... | 26 |
| 1.10 THESIS ORGANIZATION | 29 |
| CHAPTER 2. MATERIALS AND CHARACTERIZATION | 32 |
| 2.1 MATERIALS | 32 |
| 2.2 CHARACTERIZATION | 33 |
| 2.2.1 <i>X-ray diffraction (XRD)</i> | 33 |
| 2.2.2 <i>Transmission electron microscopy (TEM)</i> | 34 |
| 2.2.3 <i>Scanning electron microscopy (SEM)</i> | 35 |
| 2.2.4 <i>Energy dispersive X-ray spectroscopy (EDS)</i> | 36 |
| 2.2.5 <i>X-ray photoelectron spectroscopy (XPS)</i> | 37 |
| 2.2.6 <i>Inductively coupled plasma optical emission spectrometry (ICP-OES)</i> | 38 |
| 2.2.7 <i>Electron paramagnetic resonance (EPR)</i> | 38 |
| 2.2.8 <i>Optical properties</i> | 39 |
| 2.2.9 <i>Quantum yield (QY) measurement</i> | 39 |
| 2.3 DEVICE FABRICATION AND CHARACTERIZATION | 41 |
| 2.3.1 <i>Preparation of TiO₂ film</i> | 41 |
| 2.3.2 <i>Sensitization of TiO₂ mesoporous film with QDs</i> | 42 |
| 2.3.3 <i>QDSCs fabrication and characterization</i> | 44 |
| 2.3.4 <i>PEC devices fabrication and characterization</i> | 46 |

| | |
|---|-----------|
| CHAPTER 3. CONTROLLED SYNTHESIS OF NEAR-INFRARED QUANTUM DOTS FOR OPTOELECTRONIC DEVICES..... | 49 |
| 3.1 EXPERIMENTAL SECTION..... | 49 |
| 3.1.1 <i>Synthesis of PbS QDs and further post-treated by Cd(oleate)₂</i> | 49 |
| 3.1.2 <i>Fabrication of QDSCs and PEC Cells</i> | 51 |
| 3.1.3 <i>Characterization</i> | 53 |
| 3.2 RESULTS AND DISCUSSION | 54 |
| 3.2.1 <i>Morphological, structural and optical properties</i> | 54 |
| 3.2.2 <i>Quality of photoanode</i> | 57 |
| 3.2.3 <i>Properties of PEC cells</i> | 59 |
| 3.2.4 <i>Properties of QDSCs</i> | 61 |
| 3.3 CONCLUSIONS | 67 |
| CHAPTER 4. NEAR-INFRARED COLLOIDAL MANGANESE DOPED QUANTUM DOTS: PHOTOLUMINESCENCE MECHANISM AND TEMPERATURE RESPONSE..... | 69 |
| 4.1 EXPERIMENT SECTION..... | 70 |
| 4.1.1 <i>Synthesis of pure PbS QDs and Mn-doped PbS QDs</i> | 70 |
| 4.1.2 <i>QDs film preparation</i> | 71 |
| 4.1.3 <i>Characterization</i> | 71 |
| 4.2 RESULTS AND DISCUSSIONS | 71 |
| 4.2.1 <i>Morphological and structural properties</i> | 71 |
| 4.2.2 <i>Optical properties</i> | 77 |
| 4.2.3 <i>Emission mechanism</i> | 81 |
| 4.2.4 <i>Temperature response</i> | 83 |
| 4.3 CONCLUSIONS | 87 |
| CHAPTER 5. EFFICIENT AND STABLE PHOTOELECTROCHEMICAL HYDROGEN GENERATION USING OPTIMIZED COLLOIDAL HETEROSTRUCTURED QUANTUM DOTS | 89 |
| 5.1 EXPERIMENTAL SECTION..... | 90 |
| 5.1.1 <i>Synthesis of CdS QDs</i> | 90 |
| 5.1.2 <i>Synthesis of CdS/CdSe core/shell QDs</i> | 91 |
| 5.1.3 <i>Synthesis of CdSe QDs</i> | 92 |
| 5.1.4 <i>Fabrication of PEC cells</i> | 92 |
| 5.1.5 <i>Characterization</i> | 93 |
| 5.1.6 <i>Theoretical methods</i> | 95 |
| 5.2 RESULTS AND DISCUSSIONS | 95 |
| 5.2.1 <i>Synthesis and structural characterization</i> | 95 |
| 5.2.2 <i>Optical properties</i> | 100 |
| 5.2.3 <i>Theoretical simulation</i> | 104 |
| 5.2.4 <i>PEC measurements</i> | 107 |

| | |
|--|------------|
| 5.2.5 Carrier dynamics..... | 121 |
| 5.3 CONCLUSIONS | 124 |
| CHAPTER 6. CONCLUSIONS AND PERSPECTIVES | 126 |
| 6.1 CONCLUSIONS | 126 |
| 6.2 PERSPECTIVES | 128 |
| BIBLIOGRAPHY | 130 |
| APPENDIX A ABBREVIATIONS | 140 |
| APPENDIX B RÉSUMÉ..... | 143 |
| CONCEPTION ET SYNTHÈSE DE POINTS QUANTIQUES COLLOÏDAUX ET LEURS PROPRIÉTÉS | |
| OPTOÉLECTRONIQUES | 143 |
| <i>Introduction et contexte</i> | 143 |
| <i>Objectifs de recherche</i> | 145 |
| <i>Résultats et discussions</i> | 147 |

LIST OF FIGURES

Figure 1.1 Schematic illustration of DOS as a function of energy for different classification of nanomaterials of (a) a bulk 3D semiconductor, (b) a 2D quantum well, (c) a 1D quantum wire or nanotube, and (d) a 0D QD. For this illustration, only the conduction band (CB) is shown here. DOS represents the density of states for electrons.

Figure 1.2 (a) Schematic illustration of a 5 nm diameter PbS QDs passivated with oleate and hydroxyl ligands. (b) A typical High-resolution TEM (HR-TEM) image of the synthesized PbS QDs. Figures adapted from literature.

Figure 1.3 Schematic representation of the quantum confinement effects in QDs, indicating the size-dependent bandgap of semiconductor QDs and the formation of discrete states near the band-edges. The bandgap of the QDs increases with decreasing size, while discrete energy levels arise at the band-edges.

Figure 1.4 (a) Size-tunable emission spectra of CdSe QDs with the emission peaks increased from 443 to 655 nm from left to right (blue to red) and (b) differently distinguishable emission color photographs of ZnS-capped CdSe QDs under UV exposure, adapted from literature. (c) Composition-dependent PL spectra of CsPbX₃ QDs and (d) seven representative color photos of QDs in solution under UV lamp, including violet, blue, cyan, green, yellow, orange and red from left to right, adapted from literature.

Figure 1.5 Schematic representation for the emission range from variously representative QDs, adapted from literature.

Figure 1.6 (a) Schematic illustration of the electronic transitions involved in modulating PL from Mn-doped ZnSe QDs. Initially, electrons are pumped from the VB to the CB of the ZnSe host, and are subsequently transferred to the ⁴T₁ level of the Mn²⁺ dopant. Here, the electrons can relax radiatively to the ⁶A₁ level, adapted from literature. (b) The typical absorption and PL spectra of colloidal Mn-doped ZnSe or Mn-doped ZnSe/ZnS QDs in toluene, adapted from literature.

Figure 1.7 Schematic representation of different classes of carrier localization regimes in core/shell heterostructured QD systems depending on the energy-level alignment and electron (red color) and hole (green color) wave functions in different rectangles correspond to the position of CB and VB of the core (center) and shell materials (outer), respectively: a) type-I; b) inverted type-I; c) type-II; d) quasi type-II.

Figure 1.8 (a) Schematic representation of an air-free reaction setup for synthesizing colloidal QDs by the hot injection method. (b) Synthesis of core/shell QDs by cation exchange method. First, the core QDs can be synthesized via the hot-injection method, then core/shell structured QDs synthesized by the growth of shell over the as-synthesized core QDs via cation exchange approach. Figures adapted from literature.

Figure 1.9 Schematic illustration of the process of synthesis of core/shell QDs by syringe pump injection method (top of the Figure). First, the core QDs can be synthesized via the hot injection method, then core/shell structured QDs are synthesized by the adsorption and reaction of gradually injected cation and anion precursors over the as-synthesized core QDs. Figure adapted from literature.

Figure 1.10 Schematic illustration of carrier dynamics (generation, separation/transport and recombination) in the QDs-sensitized TiO₂ photoanode in contact with electrolyte. Black solid arrows show three processes that is favorable for the QDSCs or PEC devices based on the described photoanode: (1) photoexcitation; (2) electron injection; (3) hole extraction. Red dash arrows show four major undesirable recombination paths, showing the main electronic processes at the TiO₂/QDs/electrolyte interface: (a) recombination inside the absorber (semiconductor QDs); (b) recombination of injected electrons with holes in the VB of TiO₂; (c) recombination of injected electrons with electrolyte and (d) recombination of electrons in the CB of QDs with electrolyte.

Figure 1.11 Schematic illustration of the structure and working principle of QDSCs, adapted from reference.

Figure 1.12 Multiple exciton generation in QDs, referred and adapted from literature.

Figure 1.13 Honda–Fujishima configuration of water splitting system using a TiO₂ photoanode, referred and adapted from literature.

Figure 1.14 Spectrum of solar radiation at the top of the atmosphere and at sea level from 230 nm to 2.6 μm wavelengths, adapted from literature.

Figure 1.15 Schematic illustration of different classifications of colloidal QDs: (a) bare QDs, (b) doped QDs and (c) core/shell QDs.

Figure 2.1 Principle of XRD.

Figure 2.2 The most important interactions between the incident electron beam and specimen in a TEM.

Figure 2.3 Signals generated from the interactions between the incident electron beam and specimen in an SEM.

Figure 2.4 The illustration schematic of principle for XPS.

Figure 2.5 Linear plots for sample and reference. The gradient for each one is proportional to that its QY. Conversion into an absolute QY is achieved through the equation given below.

Figure 2.6 Schematic illustration of a flowchart for the doctor-blade method.

Figure 2.7 Schematic illustration of the sensitization of TiO₂ mesoporous film with QDs prepared through *in-situ* or *ex-situ* approach. For the *in-situ* approach, the QDs are grown directly on the surface of the scaffold in TiO₂ mesoporous film, forming a QDs/TiO₂ photoanode during synthesis. In comparison with CBD, SILAR method requires the repetitive immersing operation of a TiO₂ film in precursor solutions containing cation and anion ions. For the *ex-situ* approach, after synthesis of the colloidal QDs, EPD and drop-casting approaches are employed to prepare QDs/TiO₂ photoanode.

Figure 2.8 Schematic representation of *J-V* curve of a solar cell. The red point represents the maximum power density output.

Figure 3.1 TEM images for different sizes of the as-synthesized QDs by controlling injection temperature and reaction time with size ranging from 3.0 to 5.1 nm: (a) 95 °C and 2 min, (b) 100 °C and 5 min, (c) 105 °C and 5 min, (d) 110 °C and 1 min and (e) 115 °C and 1 min. (f) The corresponding absorption spectra of PbS QDs.

Figure 3.2 Representative TEM images of Cd-PbS QDs from (a) (TMS)₂S and (b) thiourea. Inset of (a) and (b) is HR-TEM images of two different kinds of QDs. The size distribution of colloidal Cd-PbS QDs from (c) (TMS)₂S and (d) thiourea. Red lines show the fitting results. Sizes are measured from more than 200 QDs in the TEM images respectively. The absorbance spectra of prepared pure PbS and Cd-PbS QDs from (e) (TMS)₂S (f) thiourea.

Figure 3.3 (a) Representative SEM cross-sectional image of TiO₂/QDs photoanode capped with ZnS, (b-i) EDS 2D mapping: the elements distribution of Ti (b), O(c), Si(d), Sn(e), Cd(f), Zn(g), Pb(h) and S(i); (j) EDS spectra; (k) EDS line mapping.

Figure 3.4 Schematic illustration of PEC cells with the prepared QDs as light harvesters. Energy levels (at pH=12.5) of TiO₂, prepared QDs (3 nm in diameter), related characteristic redox potentials. The arrows indicate the electrons and holes transfer process.

Figure 3.5 (a) A typical photograph of the configuration for PEC measurement, (b) Photocurrent density versus the applied voltage (vs. RHE) curves of PEC devices assembled using bare TiO₂ under one simulated sunlight illumination (AM 1.5G, 100 mW·cm⁻²) in the dark (black line) and constant one sunlight illumination (red line).

Figure 3.6 Photocurrent density versus the applied voltage (vs. RHE) curves of PEC devices assembled using the as-prepared QDs from (a) (TMS)₂S and (b) thiourea respectively under one simulated sunlight illumination (AM 1.5G, 100 mW·cm⁻²) in the dark (blue line) under chopped (black line) and constant one sunlight illumination (red line), (c) Measured current density as a function of time for the devices of PbS QDs from (TMS)₂S and thiourea at 0.4 V versus RHE under 100 mW·cm⁻² illumination with AM 1.5G filter.

Figure 3.7 Schematic illustration of QDSCs with the prepared QDs as sensitizer for photoanode and Cu₂S as the counter electrode.

Figure 3.8 *J-V* curves of devices with only TiO₂ as photo-harvester under one simulated sunlight.

Figure 3.9 (a) *J-V* curves of QDSCs sensitized by the as-prepared QDs from sulfur precursors of thiourea and (TMS)₂S respectively, under one simulated sunlight, (b) Transient photovoltage decay measurements of corresponding QDSCs, (c) Extracted electron lifetime as a function of *V*_{oc}.

Figure 3.10 *J-V* curves of QDSCs which sensitized by prepared QDs with similar overall size of 3.2 nm and shell thickness of 0.2 nm from different sulfur precursors under one simulated sunlight.

Figure 3.11 *J-V* curves of QDSCs which sensitized by prepared oil-soluble and water-soluble QDs from sulfur precursor of thiourea under one simulated sunlight.

Figure 3.12 EIS of representative samples of devices sensitized with QDs from thiourea and (TMS)₂S. (a) Recombination resistance, (b) chemical capacitance.

Figure 4.1 Representative TEM images of (a) pure PbS QDs, (b) Mn_{0.007}PbS, (c) Mn_{0.0115}PbS and (d) Mn_{0.0166}PbS. The inset images are the HR-TEM images of each QDs.

Figure 4.2 Size distributions of (a) PbS QDs, (b) Mn_{0.007}PbS sample, (c) Mn_{0.0115}PbS sample and (d) Mn_{0.0166}PbS sample.

Figure 4.3 Different sizes of PbS and Mn-doped PbS QDs as a function of band gaps.

Figure 4.4 EDS spectra of (a) PbS, (b) Mn_{0.007}PbS, (c) Mn_{0.0115}PbS and (d) Mn_{0.0166}PbS QDs.

Figure 4.5 (a) XRD spectra of the as-synthesized pure and Mn-doped PbS QDs. The right pattern shows the XRD spectra from 24° to 32° . The JCPDS card data for PbS (No. 05-0592, black line) is shown for identification. EPR spectra of the as-synthesized (b) $\text{Mn}_{0.007}\text{PbS}$ sample, (c) $\text{Mn}_{0.0115}\text{PbS}$ sample and (d) $\text{Mn}_{0.0166}\text{PbS}$ sample at 298 K and 114 K, respectively.

Figure 4.6 EPR spectra of the as-synthesized pure PbS sample at 298 K and 114 K, respectively.

Figure 4.7 Optical properties of PbS QDs and Mn-doped PbS QDs in toluene: (a) absorption and PL spectra. The excitation wavelength is $\lambda_{\text{ex}} = 450$ nm; (b) PL decay curves. The excitation wavelength is $\lambda_{\text{ex}} = 444$ nm.

Figure 4.8 Summarized Stokes shift as a function of the absorption peak of PbS and Mn-doped PbS QDs.

Figure 4.9 (a) Band energy levels of PbS QDs and Mn d-state (left). Radiative processes are indicated as straight lines and non-radiative processes as wavy lines. (b) Schematic illustration of the change in emitting excited state of PbS QDs (left) and with the incorporation of Mn in PbS QDs (right).

Figure 4.10 Temperature-related PL quenching. Normalized PL spectra of PbS QDs and Mn-doped PbS QDs (from left to right, corresponding to samples of PbS, $\text{Mn}_{0.007}\text{PbS}$, $\text{Mn}_{0.0115}\text{PbS}$ and $\text{Mn}_{0.0166}\text{PbS}$, respectively) recorded at different temperatures. From top to bottom: 96, 106, 116, 126, 136, 146, 156, 166, 176, 186, 196, 206, 216, 226, 236, 246, 256, 266, 276, 286 and 296 K. The excitation wavelength is $\lambda_{\text{ex}} = 450$ nm for the three samples of QDs.

Figure 4.11 (a) Normalized integrated area of PL peak as a function of $1000/T$ for pure and Mn-doped PbS QDs, where T is temperature. (b) PL peak position as a function of temperature for pure and Mn-doped PbS QDs. (c) Temperature dependence of FWHM of PbS, $\text{Mn}_{0.007}\text{PbS}$, $\text{Mn}_{0.0115}\text{PbS}$ and $\text{Mn}_{0.0166}\text{PbS}$ QDs.

Figure 5.1 Approximate energy levels (correspond to $\text{pH}=12.5$) of TiO_2 and QDs, together with related characteristic redox potentials. The arrows indicate the electron and hole transfer process.

Figure 5.2 TEM image of the as-synthesized CdS QDs.

Figure 5.3 Representative TEM images of (a) CdS/CdSe (0.6 nm) QDs, (b) CdS/CdSe (1.1 nm) QDs, (c) CdS/CdSe (1.6 nm) QDs and (d) CdS/CdSe (1.9 nm) QDs. (e) A representative HR-TEM image and (f) SAED pattern of CdS/CdSe (1.6 nm) QDs. (g) EDS spectra of CdS (dark color), CdS/CdSe (0.6 nm) (red color), CdS/CdSe (1.1 nm) (blue color), CdS/CdSe (1.6 nm) (orange color) and CdS/CdSe (1.9 nm) QDs (green color), respectively. (h) Schematic illustration of band

alignment of the as-synthesized QDs by tuning the shell thickness. The electron and hole distribution probability with varying shell thickness is shown as green and blue areas, respectively.

(i) XRD patterns of CdS and CdS/CdSe core/shell QDs. The JCPDS for ZB crystal structure of CdS (No. 00-001-0647, dark vertical line) and WZ crystal structure of CdSe (No. 00-002-0330, orange vertical line) are shown for identification.

Figure 5.4 Size distributions of (a) CdS, (b) CdS/CdSe (0.6 nm), (c) CdS/CdSe (1.1 nm), (d) CdS/CdSe (1.6 nm) and (e) CdS/CdSe (1.9 nm) QDs, respectively.

Figure 5.5 SAED patterns of (a) CdS, (b) CdS/CdSe (0.6 nm), (c) CdS/CdSe (1.1 nm), and (d) CdS/CdSe (1.9 nm) QDs, respectively.

Figure 5.6 High-resolution XPS spectra of (a) Cd 3d, (b) S 2p, Se 3p and (c) Se 3d for CdS/CdSe (1.6 nm) QDs.

Figure 5.7 Optical properties of CdS and CdS/CdSe QDs in toluene. (a) Absorption spectra, (b) PL spectra. The PL of the CdS QDs shows a noticeable secondary emission peak at the range of 500-650 nm, arising from recombination at the surface trap states. The excitation wavelength is $\lambda_{ex}= 400$ nm. (c) Experimental TRPL measurements of CdS (cyan color), CdS/CdSe (0.6 nm) (dark color), CdS/CdSe (1.1 nm) (blue color) and CdS/CdSe (1.6 nm) (green color), and CdS/CdSe (1.9 nm) (purple) QDs in toluene. Fitted curves are shown in black, red, blue, green and brown color lines, respectively. The excitation wavelengths are $\lambda_{ex}= 380$ nm for CdS QDs and $\lambda_{ex}= 444$ nm for CdS/CdSe QDs samples.

Figure 5.8 Theoretical modelling of the CdS/CdSe core/shell QDs. (a) Geometrical model of the spherical CdS/CdSe core/shell QDs, alongside the key geometrical parameters, radius core and thickness shell (top panel). R_{total} represents the radius of the core/shell QDs. The QDs are assumed to have a standard spherical shape. Band alignment diagram of bulk CdS and CdSe showing the positions of CB and VB (bottom panel). (b, c) Radial probability distribution, $dP/dr = 4\pi r^2 |\Psi|^2$, (b) electrons and (c) holes in the model system, showing how the low-energy carriers are more likely to populate the volume of the shell when it becomes thicker. (d) Evolution of the HOMO and LUMO, each taken as the lowest eigenstate of the corresponding quantum potential well for electrons and holes. The evolution of the theoretical bandgap, calculated as the difference between these states, is compared with the experimental bandgaps, estimated from the absorption wavelengths listed in Table 6.1. (e) The inverse electron and hole overlap (solid black line), normalized over its value for the CdS QDs, and $\tau_{rad}/\tau_{rad\ core}$ (red dash line) values as a function of shell thickness.

Figure 5.9 Schematic illustration of the structural variations in photoanodes sensitized with CdS/CdSe QDs made via different preparation processes of (a) *in-situ* CBD/SILAR method and (b) *ex-situ* colloidal synthesized CdS/CdSe QDs method. The scenarios of electron transfer in these two cases exhibit fundamental differences, as indicated by the blue arrows. This difference is caused by a significant structural discrepancy in photoanodes fabricated via these two different approaches.

Figure 5.10 (a) Representative cross-sectional SEM image of CdS/CdSe (1.6 nm) QDs-sensitized photoanode. (b-g) EDS 2D mapping (in the selected area surrounded by the white line): the elemental distributions of (b) O, (c) Ti, (d) Se, (e) S and (f) Cd. (g) EDS line mapping of all the elements as the direction of the arrow in image (a). (h) Absorption spectra of the QDs sensitized TiO₂ films (only transparent layer).

Figure 5.11 (a) Schematic of the working mechanism of a PEC device based on TiO₂ nanoparticle mesoporous anode sensitized colloidal heterostructured CdS/CdSe core/shell QDs. (b) Photocurrent density versus the applied voltage (vs. RHE) curves of PEC cells fabricated using the as-synthesized QDs of CdS, CdS/CdSe (0.6 nm), CdS/CdSe (1.1 nm), CdS/CdSe (1.6 nm), and CdS/CdSe (1.9 nm) in dark (solid line) and under continuous one sun illumination (dash line). (c) CdS/CdSe (1.6 nm) with CNTs-TiO₂ photoanode in dark (black line), under constant one sunlight illumination (magenta line) and under chopped one simulated sunlight illumination (blue line). (d) Measured photocurrent density versus time for PEC devices at 0.6 V vs. RHE under continuous 100 mW·cm⁻² illumination.

Figure 5.12 The high-resolution XPS spectra of Cd 3d and Zn 2p for photoanodes based on CdS/CdSe (1.6 nm) QDs treated with ZnS passivation layer (a and b) before and (c and d) after 2 h of PEC stability test.

Figure 5.13 H₂ evolution of PEC cells based on CdS/CdSe (1.6 nm) QDs sensitized CNTs-TiO₂ photoanode as a function of time. The measurement was conducted at 0.6 V vs. RHE under continuous one sun illumination (100 mW/cm², AM 1.5G). The theoretical (calculated from the measured photocurrent) and experimental (measured from GC) evolution of H₂ are shown as black square and red circle, respectively. The FE value (blue star) of the corresponding PEC device is shown in the right vertical axis.

Figure 5.14 IPCE spectra of PEC devices based on CdS/CdSe QDs with different CdSe shell thickness (0, 0.6, 1.1, 1.6 and 1.9 nm), measured at 0.9 V vs. RHE.

Figure 5.15 (a) Absorption spectra and (b) PL spectra of a series of CdSe QDs in toluene with different size synthesized by adjusting the reaction time: 1 min (violet color), 3 min (cyan color), 30 min (green color), 1 h (yellow color), 2.5 h (orange color) and 4 h (red color), respectively. The excitation wavelength is $\lambda_{ex} = 405$ nm.

Figure 5.16 Photocurrent density versus the applied voltage (vs. RHE) curves of PEC devices assembled using the as-prepared QDs from CdSe, with sizes of (a) 2.9, (b) 3.5 and (c) 5.1 nm in dark (black line), under constant one sun illumination (AM 1.5G, $100 \text{ mW} \cdot \text{cm}^{-2}$, red line) and under chopped one simulated sunlight illumination (blue line).

Figure 5.17 (a) Photocurrent density versus potential (vs. RHE) curves of PEC cells fabricated using CdS/CdSe (1.6 nm) QDs in dark (black curve), under 650 nm long-pass filter (blue curve) and under continuous one sun illumination (red curve). (b) The ratio of photocurrent density with or without 650 nm long-pass filter (J_{650nm}/J) as a function of shell thickness. (c) TRPL dynamic study of CdS/CdSe (1.6 nm) core/shell QDs deposited on TiO_2 and ZrO_2 mesoporous film. The excitation wavelength is $\lambda_{ex} = 444$ nm.

Figure 5.18 Photocurrent density versus potential (RHE) curves of PEC devices assembled using as-synthesized (a) CdS, (b) CdS/CdSe (0.6 nm), (c) CdS/CdSe (1.1 nm) and (d) CdS/CdSe (1.9 nm) QDs sensitized TiO_2 photoanode in the dark (black curve), under 650 nm long-pass filter (blue curve) and continuous one sun illumination (red curve), respectively.

Figure 5.19 TRPL dynamic study of (a) CdS, (b) CdS/CdSe (0.6 nm), (c) CdS/CdSe (1.1 nm) and (d) CdS/CdSe (1.9 nm) QDs deposited on TiO_2 and ZrO_2 mesoporous film, respectively.

LIST OF TABLES

Table 1.1 Classification of nanomaterials.

Table 3.1 Functional parameters of QDSCs sensitized with QDs from different sulfur precursors.

Table 3.2 Functional performances of QDSCs sensitized with QDs of ~3.2 nm size from different sulfur precursors.

Table 3.3 Functional performances of QDSCs sensitized with oil-soluble and water-soluble QDs from sulfur precursor of thiourea.

Table 4.1 Size, absorption peak, PL peak and Stokes shift, Mn molar concentration and lifetime of as-prepared PbS QDs and Mn-doped PbS QDs in toluene.

Table 4.2 QY, K_{et} and K_{net} of as-prepared PbS and Mn-doped PbS QDs in toluene.

Table 5.1 Optical and size parameters of the as-synthesized bare CdS and CdS/CdSe core/shell QDs with tunable shell thickness in toluene. (^aR is the CdS core radius and ^bH is the CdSe shell thickness)

Table 5.2 Calculated radiative lifetime, non-radiative lifetime, radiative decay rate and non-radiative decay rate of the as-synthesized bare and core/shell QDs.

Table 5.3 Comparison of saturated photocurrent density of PEC devices based on various types of QDs sensitized TiO₂ of this work and reported in the literature. The configuration of the PEC cell is identical in all devices.

Table 5.4 Comparison of photocurrent densities of PEC devices based on bare CdSe QDs, and that based on the similar size of CdS/CdSe core/shell QDs.

Table 5.5 PL lifetimes of QDs with different substrates and calculated electron transfer rate.

Chapter 1. INTRODUCTION AND BACKGROUND

1.1 Nanomaterial and its classification

Nanomaterials, commonly defined as materials with an average size (in at least one dimension) less than 100 nanometers, attract more and more attention by researchers over the past several decades due to their high surface-to-volume ratio and unique physical/chemical properties compared to their related bulk materials. The precisely engineered nanomaterials are considered as building blocks in modern high-technology applications such as bio-imaging ¹, biosensing ², solar cells ³, luminescent solar concentrators ^{4, 5}, fuel cells ⁶, lithium-ion batteries ⁷ and supercapacitors ⁸. The classification of nanomaterials is based on the numbers of dimensions of materials confined to the nanoscale range (between 1 and 100 nm) (as shown in Table 1.1), including 0-dimensional (0D) nanomaterials [e.g., quantum dots (QDs)], 1-dimensional (1D) nanomaterials (e.g., nanowires, nanotubes), 2-dimensional (2D) nanomaterials (e.g., nanoplates), and 3-dimensional (3D) nanomaterials (e.g., bulk semiconductor).

Table 1.1 Classification of nanomaterials.

| Classification | Nanomaterials | Numbers of dimensions in quantum confinement | Numbers of free dimensions |
|------------------|-------------------------|--|----------------------------|
| 0D nanomaterials | QDs | 3 | 0 |
| 1D nanomaterials | Nanotubes/Quantum wire | 2 | 1 |
| 2D nanomaterials | Nanoplates/Quantum well | 1 | 2 |
| 3D nanomaterials | Bulk semiconductors | 0 | 3 |

Quantum confinement is an important effect in semiconductor materials that enables the tuning of their optoelectronic properties. To better explain this effect, the understanding of exciton Bohr radius is required.

Niels Bohr introduced the Bohr hydrogen atomic model in 1913, which is used to describe the structure of hydrogen energy levels. This model describes a hydrogen atom consisting of a small and dense positively charged nucleus surrounded by orbiting negatively charged electrons, similar to the structure of the Solar System, yet with attraction provided by electrostatic forces rather than gravity. The Bohr radius is a physical constant, approximately equal to the most probable distance between the nucleus and the electron in a hydrogen atom in its ground state. Its value is 5.29×10^{-11} m.

In general, when a bulk semiconductor is illuminated by an incident photon with higher energy than its bandgap, the electron will be excited to the CB, leaving a hole in the valence band (VB). This photogenerated electron-hole pair is called an exciton, which occupied a certain physical space. This space (the distance between these two charge carriers) is called the exciton Bohr radius, which depends on the effective masses of the electron and hole of the specific materials as expressed by the following equation: ⁹

$$r_B = \frac{\epsilon h^2}{\pi e^2} \left(\frac{1}{m_e^*} + \frac{1}{m_h^*} \right) \quad (1)$$

where r_B is the exciton Bohr radius, ϵ is the dielectric constant of the materials, h is Planck's constant, e is the electronic charge. m_e^* and m_h^* are the effective masses of electron and hole, respectively.

Excitons are often treated in the two limiting cases of small dielectric constant versus large dielectric constant, corresponding to Frenkel exciton and Wannier–Mott exciton, respectively. Frenkel excitons are usually found in materials with a relatively small dielectric constant. In this case, the Coulomb interaction between an electron and a hole may be strong and therefore the excitons tend to be small (as the same order as the size of the unit cell). Wannier–Mott excitons are usually found in semiconductors, which have a large dielectric constant. A Wannier–Mott

exciton has a radius larger than the lattice spacing. The generally small effective mass of electrons in semiconductors also favors large exciton radius.

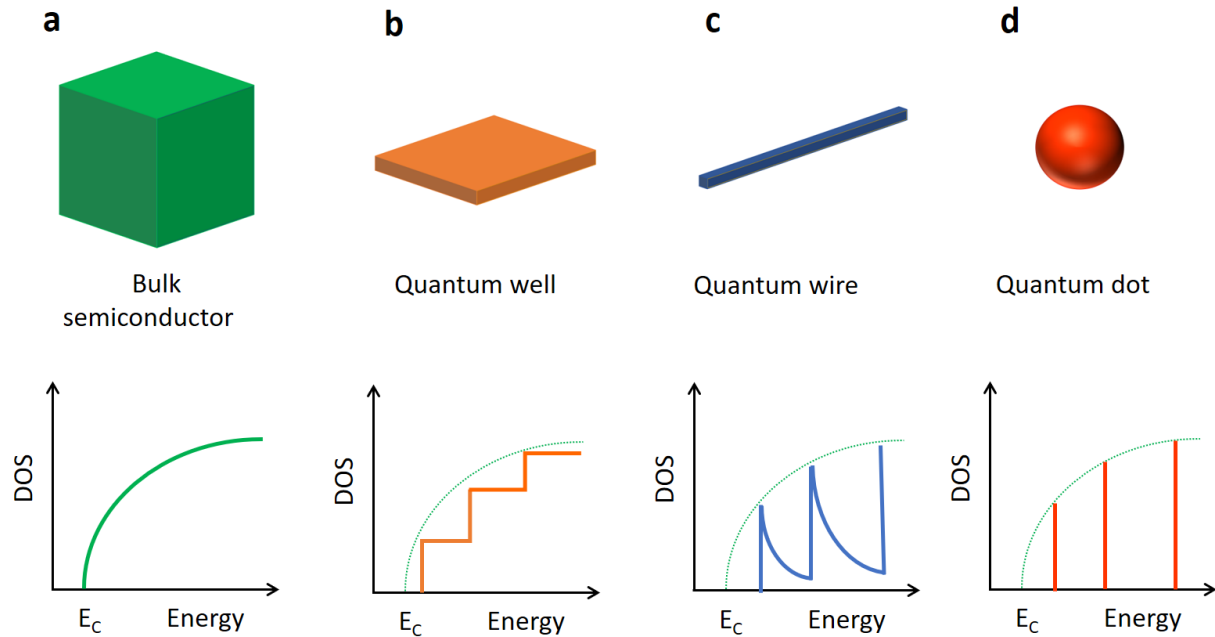


Figure 1.1 Schematic illustration of DOS as a function of energy for different classification of nanomaterials of (a) a bulk 3D semiconductor, (b) a 2D quantum well, (c) a 1D quantum wire or nanotube, and (d) a 0D QD. For this illustration, only the conduction band (CB) is shown here. DOS represents the density of states for electrons.¹⁰

Quantum confinement may be different in different directions of the nanomaterials. For example, the exciton is spatially confined in all three directions in a QD, while in the quantum wire or quantum well, it is confined only in two dimensions (cross-sectional directions) or one dimension (thickness direction), respectively. Therefore, the properties of nanomaterials are also strongly shape-dependent, which makes them promising to be used as building blocks in emerging technologies.

As shown in Figure 1.1, nanomaterials with different dimensionalities show significantly different optical and electronic properties, which arise from their peculiar density of states (DOS).¹¹ The DOS shows the number of allowed electron (or hole) states per volume at a given energy. Depending on the dimensionality of the materials, the DOS may or may not be a continuous

function of the electron energy as shown in Figure 1.1. For QDs, all available states exist only at discrete energies since the electron is confined in all three spatial dimensions. This makes the mobility of electrons and holes confined in specific energy levels, which can affect the electrical, optical and magnetic properties of the materials.

1.2 What are colloidal QDs?

Colloidal QDs are very small-sized semiconductor nanocrystals (several to tens nm), which have unique size-dependent properties due to the quantum confinement effect in all three spatial dimensions. "Colloidal" means that these dots are still able to remain evenly dispersed throughout the solution and exist in the form of a steady suspension (do not precipitate on the bottom of the container). A QD is composed of hundreds to thousands of atoms and surrounded by organic, inorganic or organic/inorganic hybrid ligands, which can make it stable in organic/inorganic solution. For instance, Figure 1.2a displays a typical schematic illustration of PbS QDs with a 5 nm diameter passivated with oleate and hydroxyl ligands and representative transmission electron microscopy (TEM) image of corresponding PbS QDs is shown in Figure 1.2b.¹²

In the last three decades, colloidal QDs were produced in the form of stable nanocrystals in solution, allowing controllable sizes and shapes during the synthetic process and enabling solution processability for further applications. The field of colloidal QDs started to gain attention in the 1980s. At the same time, the discovery and development of the TEM (reaching the required resolution until around the 1980s) allowed researchers to be able to directly observe and accurately determine the shape and size of QDs in the range of 1-10 nm. In 1985, the first "image" of QDs with size of ~2.5 nm was reported for spherical semiconductor PbS QDs.^{13, 14} A subsequent breakthrough was reported in 1993, when Bawendi's group reported a synthetic procedure that was able to produce nearly monodispersed colloidal CdSe QDs.¹⁵ Over the following decades, the synthesis has been expanded to different materials such as CdS, CuInS₂, InP and ZnSe, *etc.* Synthetic approaches were widely developed, allowing precisely engineering

the sizes and shapes of these QDs. Details of different synthetic methodologies are reported in Section 1.6 and 1.7 of this chapter.

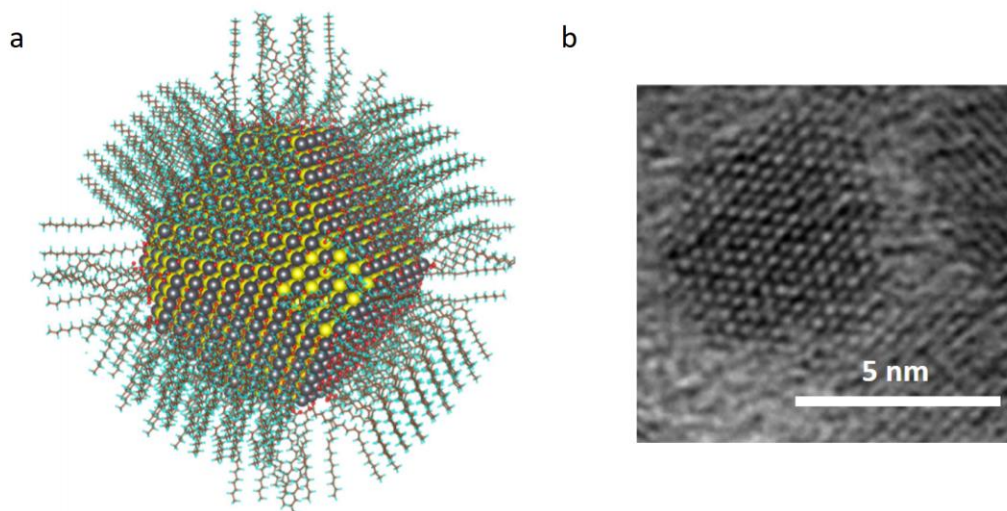


Figure 1.2 (a) Schematic illustration of a 5 nm diameter PbS QDs passivated with oleate and hydroxyl ligands. (b) A typical High-resolution TEM (HR-TEM) image of the synthesized PbS QDs. Figures adapted from literature ¹².

1.3 Properties of colloidal bare QDs

The extremely small size of QDs renders their optical and electronic properties different from those of bulk materials. QDs have the properties of high quantum yield (QY), high photostability, high extinction coefficients and tunable absorption/photoluminescence (PL) spectra.

QDs have properties intermediate between bulk semiconductors and discrete atoms or molecules. As depicted in Figure 1.3, a small molecule (a few atoms) has discrete energy states. Considering a small QD (few hundred to thousand atoms) as a very large molecule, which still remains discrete energy states with higher density of energy levels than that in a small molecule. If the size of QDs is less than its exciton Bohr radius, then the carrier resides in the strong confinement regime, the continuum band of energies becomes discrete. In a bulk semiconductor solid, all states within a band merge into a continuum, and the energy difference between the CB

and VB is the bandgap energy of this specific material. In QDs, the bandgap increases with decreasing size. The widening of the bandgap in QDs is attributed to the quantum confinement effect, which indicates that the carriers in semiconductor nanocrystals with dimensions smaller than the exciton Bohr radius are confined. Accordingly, the optical spectra including absorption and PL of semiconductor QDs can be tuned by simply changing their size without engineering the composition of their constituents.

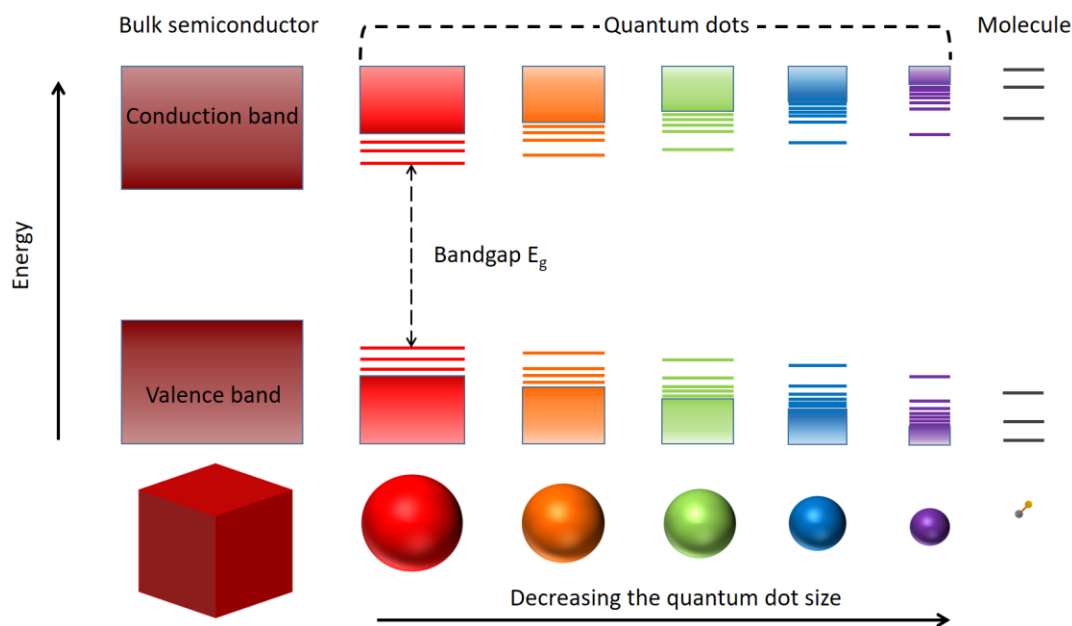


Figure 1.3 Schematic representation of the quantum confinement effects in QDs, indicating the size-dependent bandgap of semiconductor QDs and the formation of discrete states near the band-edges. The bandgap of the QDs increases with decreasing size, while discrete energy levels arise at the band-edges.

Based on the numbers of involving elements in QDs (excluding the elements of ligands), there are mainly four kinds of QDs including unary [e.g., carbon QDs (C-dots), silicon QDs (Si QDs)]^{16, 17}, binary (e.g., PbS QDs, CdTe QDs)^{18, 19}, ternary (e.g., CuInS₂ QDs)²⁰, quaternary QDs (e.g., CuInSe_xS_{2-x} QDs)²¹. The exciton Bohr radius is strongly depending on the nature of material, which means it is characteristic of each bulk semiconductor materials. As such, different kind of QDs experience quantum confinement at different QD sizes, depending on their exciton Bohr

radius. For example, PbS and CdS have an exciton Bohr radius of 18²² and 5.8 nm²³, respectively. As a result, the bandgap of different semiconductor QDs is tunable over different spectral windows. For example, the emission peak of PbS QDs can be tuned from 800 to 1800 nm for diameters ranging from 2.6 to 8.0 nm,¹⁸ while that of CdS QDs can be tuned from 350 to 450 nm for diameters ranging from 2.0 to 5.3 nm.²⁴ The optoelectronic properties of semiconductor QDs can thus be tailored by choosing their composition and controlling their size.

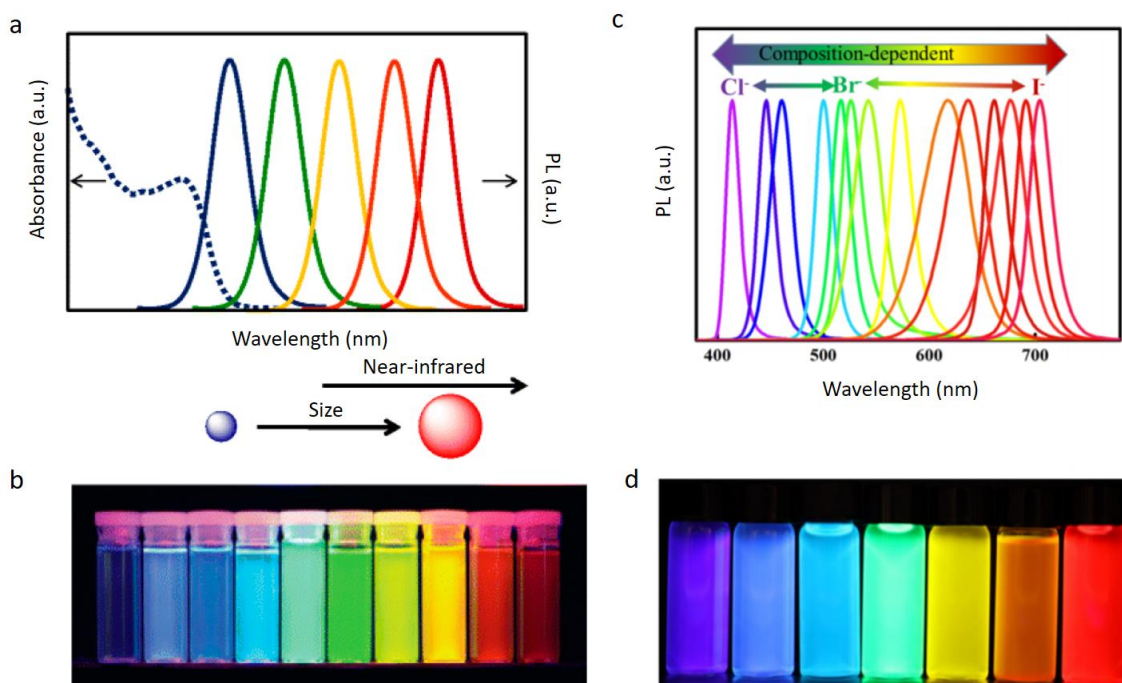


Figure 1.4 (a) Size-tunable emission spectra of CdSe QDs with the emission peaks increased from 443 to 655 nm from left to right (blue to red) and (b) differently distinguishable emission color photographs of ZnS-capped CdSe QDs under UV exposure, adapted from literature². (c) Composition-dependent PL spectra of CsPbX₃ QDs and (d) seven representative color photos of QDs in solution under UV lamp, including violet, blue, cyan, green, yellow, orange and red from left to right, adapted from literature²⁵.

Colloidal QDs possess excellent optical properties including broad and consecutive excitation bands, high absorptivity, narrow and symmetric emission and tunable emission wavelength^{26,27}. For example, Figures 1.4a-b show the tunable emission peaks and the corresponding emission

colors by only tailoring the sizes of CdSe QDs in the entire visible region, respectively ². Figure 1.4c and d present the tunable emission peaks from ~400 to 700 nm and corresponding emission colors by changing the compositions of CsPbX₃ perovskite QDs, respectively ²⁵.

Owing to the quantum confinement effect in QDs, the absorption and PL spectra of QDs can be tailored in all entire ultraviolet (UV)-visible-near infrared (NIR) regions by simply changing the size, composition and structure (e.g., involving core/shell structure) of QDs, shown in Figure 1.5

²⁸.

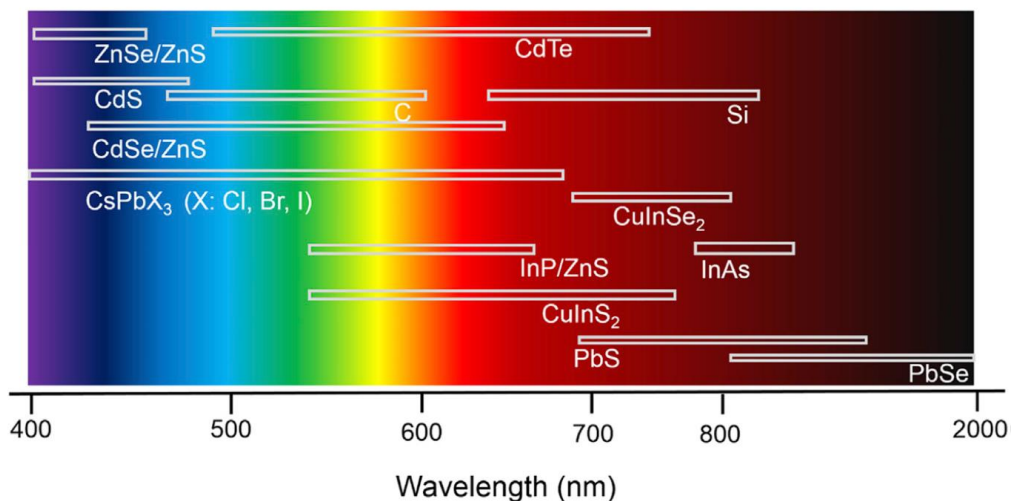


Figure 1.5 Schematic representation for the emission range from variously representative QDs, adapted from literature ²⁸.

The absorbance of QDs sample as a function of the molar concentration of the QDs are commonly described by the Beer-Lambert's law:²⁹

$$A = \epsilon CL \quad (2)$$

where A is the absorbance at the peak position of the first-excitonic absorption peak, ϵ is the extinction coefficient ($M^{-1} \text{ cm}^{-1}$, $L \text{ mol}^{-1} \text{ cm}^{-1}$). C is the molar concentration of QDs (M , mol L^{-1}), and L is the light path length (cm), respectively. In this thesis, A is measured by UV-visible-NIR spectroscopy. L is the path length of light in the cuvette (1 cm). As a consequence, if ϵ of the QDs

can be determined, the concentration of QDs can be easily determined using the Beer-Lambert's law. For PbS QDs, ε value can be determined by an empirical equation:³⁰

$$\varepsilon = 19600 (r)^{2.32} \quad (3)$$

where r is the radius of QDs expressed in nm. The size of QDs can be measured by TEM with good precision by counting more than 200 QDs for each sample and analyzing with a Gaussian distribution.

For other commonly reported QDs such as CdSe, CdTe and CdS QDs, their extinction coefficients can be estimated by the following empirical equations:¹⁹

$$\text{CdSe: } \varepsilon = 5857 (D)^{2.65} \quad (4)$$

$$\text{CdTe: } \varepsilon = 10043 (D)^{2.12} \quad (5)$$

$$\text{CdS: } \varepsilon = 21536 (D)^{2.3} \quad (6)$$

where D is the diameter of QDs expressed in nm.

The quality of QDs is evaluated and characterized by QY, which gives the efficiency of the PL process. It is defined as the ratio of the number of photons emitted to the number of photons absorbed. It can be expressed as:

$$\text{QY} = \frac{\text{Number of photons emitted}}{\text{Number of photons absorbed}} \quad (7)$$

In QDs, the red shift of an emission peak with respect to the corresponding absorption peak is known as the Stokes shift. It has been reported that the origins of Stokes shifts are attributed to two different mechanisms, namely, the dark exciton and the Franck–Condon relaxation.³¹ The dark exciton arises from the exciton fine structure. In the dark exciton, absorption occurs from a valence state that lies lower than the band edge states to form an exciton, while the emission process takes place through band-edge transitions with the assistance of phonons, giving rise to

a red shift of photons.³¹ Franck–Condon relaxation describes the vibrational relaxations upon photoexcitation. Upon excitation, atoms in the QDs experience excited-state forces and undergo consequent structural relaxations, leading to a shift of the total energy in the system.³¹

1.4 Doped QDs

Among various types of QDs (bare QDs, doped QDs, core/shell QDs, *etc.*), doped QDs exhibit unique features as they allow the introduction of magnetic, optical, and electronic properties originating from the confined interaction between the charge carriers of the semiconductor host and the dopant ions.³² Doping with transition metal ions such as manganese (Mn) and copper (Cu) allows the modification of the electronic, magnetic and photophysical properties of QDs.³²⁻⁴⁰ For instance, Mn doping significantly changes the electronic and magnetic properties of $\text{Cu}_2\text{ZnSnS}_4$ and perovskite (CsPbX_3 , CsGeX_3) nanocrystals.^{32, 41-45} The optoelectronic devices using doped QDs as light harvesters reported an improved performance compared to pure QDs, such as QDs sensitized solar cells (QDSCs) using Mn-doped CdS/CdSe QDs³³ and QD-based luminescent solar concentrators using Mn-doped ZnSe QDs⁴⁶. In addition, doped QDs have also been used for nanoscale optical thermometry. For example, Vlaskin *et al.* reported a dual-emission temperature sensor based on Mn-doped $\text{Zn}_{1-x}\text{Mn}_x\text{Se}/\text{ZnCdSe}$ QDs.⁴⁷ Besides the quasi-0D QDs, Mn doping in 1D nanowires and 2D nanoplatelets attracted considerable research interest in recent years.^{44, 48-50}

Dopants in semiconductor QDs can create electronic states that allow the alteration of the exciton recombination dynamics.^{33, 36} In general, most reported exciton dynamic mechanisms belong to either band edge emission (also named exciton emission) or dopant emission (d-emission). An electron-hole pair is generated when the intrinsic QD is excited by a photon of energy higher than the semiconductor band gap. The band edge emission occurs by the direct recombination of the electron-hole pair, which is “quantum confined”.⁵¹ The d-emission occurs in particular cases of the transition metal ion doped QDs, which is fundamentally different from band edge emission.

For instance, the dopant could create electronic states in the intragap region of the QDs, thus altering the exciton recombination dynamics. Specifically, the photoexcited electrons are transferred to the electronic levels of the transition metal ions and subsequently recombination in the transition metal ion center results in a characteristic d-emission from this metal ion.⁵² Generally, the above-mentioned d-emission only occurs when the energy levels of doped transition metal ions are located between the CB and VB of the wide bandgap (larger than the energy for Mn 4T_1 - 6A_1 transition of 2.12 eV, such as ZnSe) host semiconductor QDs.

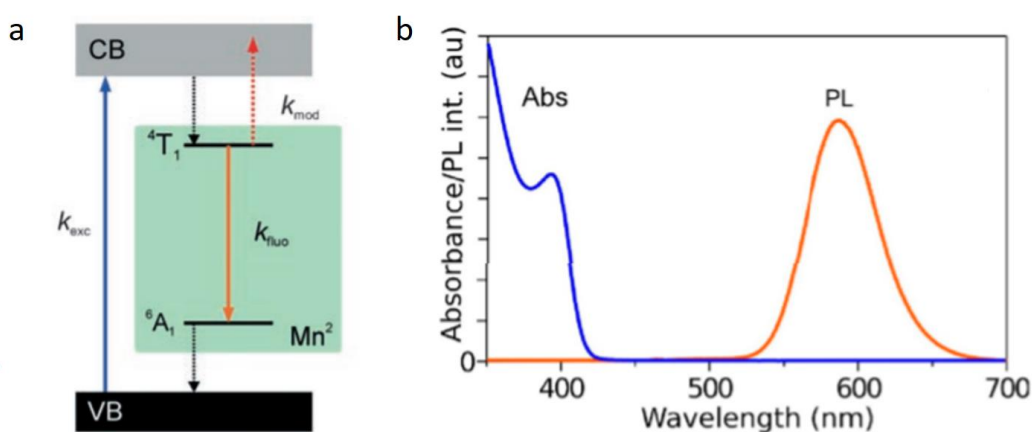


Figure 1.6 (a) Schematic illustration of the electronic transitions involved in modulating PL from Mn-doped ZnSe QDs. Initially, electrons are pumped from the VB to the CB of the ZnSe host, and are subsequently transferred to the 4T_1 level of the Mn²⁺ dopant. Here, the electrons can relax radiatively to the 6A_1 level, adapted from literature⁵³. (b) The typical absorption and PL spectra of colloidal Mn-doped ZnSe or Mn-doped ZnSe/ZnS QDs in toluene, adapted from literature^{46, 47, 54}.

The above-mentioned emissions all belong to radiative recombination. As a widely reported non-radiative recombination, Auger recombination is a process involving three carriers. Direct Auger recombination occurs when an electron and hole recombine, but instead of producing a photon, either an electron is moved to higher levels in the CB or a hole is moved to lower levels in the VB.⁵⁵ That means, the energy is given to a third carrier, which is excited to a higher energy level without moving to another energy band. After the interaction, the third carrier normally loses its

excess energy to thermal vibrations.⁵⁵ In another case, when an electron and hole recombine, giving up their energy to another two carriers which are excited to a higher energy level at the same time, this process is referred to Auger bi-exciton recombination.^{55, 56} Auger recombination has been a long-standing obstacle to many prospective applications of colloidal QDs ranging from lasing, light-emitting diodes to bio-labeling.^{56, 57}

To date, Mn-doped semiconductors were investigated for their PL properties. As QDs has a tunable bandgap (tunable CB and VB position) and Mn has been reported to have fixed d-states³⁵⁻³⁷, the relative position of the Mn d-states could be tuned with respect to CB and VB of QDs by changing the size of the QDs. As such, Mn ions exhibit exchange interactions with band edge carriers in several semiconductor QDs, such as CdS,⁵⁸ CdSe,³⁶ ZnS⁵⁹ and ZnSe^{46, 51, 53, 60} QDs. For example, as shown in Figure 1.6, Irvine *et al.*⁵³ reported that in Mn-doped ZnSe QDs electrons are photoexcited from VB to CB of ZnSe QDs, and subsequently, the excited electrons are transferred to the 4T_1 upper fluorescent state of Mn ions within a short time (picosecond time-scale) and decay radiatively to the 6A_1 state within a microsecond time-scale. These studies focused on Mn-doped wide band gap semiconductor hosts, in which the excitation energy is transferred to a Mn d-state, resulting in short-range d-emission. In these cases, both electrons and holes generated by the excitation of the QD host migrate to its d-states (6A_1 and 4T_1) and recombine. More details will be discussed in Chapter 4.

1.5 Core/shell structured QDs

Colloidal bare QDs (such as PbS, CdS, CdSe and InP, *etc.*) suffer from the high density of surface defects/trap states due to their small size (large surface-to-volume ratio), which act as fast non-radiative centers for photogenerated carrier recombination, resulting in reducing long-term photostability. A core/shell QD architecture allows the possibility to improve stability, thanks to the improved surface passivation achieved by protecting the core from surface defect states and trap sites with the growth of the shell layer. In addition, the core/shell approach offers the ability to

tune the electron/hole distribution by optimization of the electronic band alignment between core and shell.⁶¹

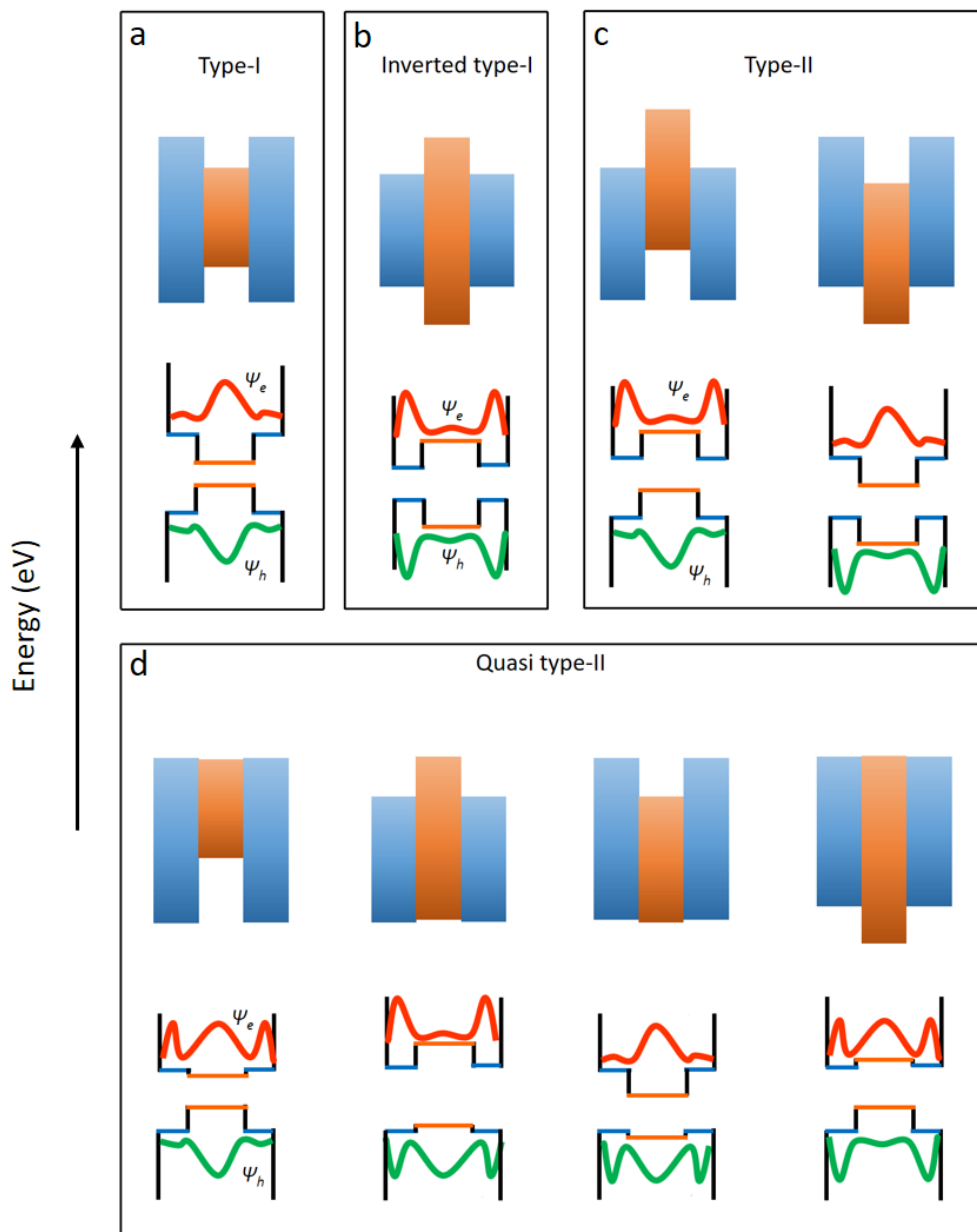


Figure 1.7 Schematic representation of different classes of carrier localization regimes in core/shell heterostructured QD systems depending on the energy-level alignment and electron (red color) and hole (green color) wave functions in different rectangles correspond to the position of CB and VB of the core (center) and shell materials (outer), respectively: (a) type-I; (b) inverted type-I; (c) type-II; (d) quasi type-II.

In general, the heterostructured core/shell QDs are typically classified into four different types depending on the spatial localization of the photogenerated charge carriers related to the relative energy alignment of CB and VB edges of the core and shell materials, as denominated as type-I, inverted type-I (or reverse type-I), type-II, and quasi type-II structured core/shell QDs.^{28, 62, 63}

Figure 1.7 illustrates the wave functions of the electrons and holes (describing the spatial distributions of CB electrons and VB holes) in different core/shell QD systems, indicating the probability of electrons and holes occurring in different positions of core/shell QDs. For type-I core/shell QDs (for example, CdSe/ZnS and InP/ZnS, Figure 1.7a), both CB and VB of core material located within the band gap of shell material, making electrons and holes all confined in the core region. In the inverted type-I core/shell QDs (Figure 1.7b), where a material with a narrower band gap is grown over the core QD material with a higher band gap, both electrons and holes are delocalized largely in the shell region. Type-II core/shell QDs present a staggered band alignment with the CB and VB of the core much lower (or higher) than that of the shell (for instance, CdSe/CdTe and CdSe/ZnTe, Figure 1.7c). As such, two different charge carriers are localized in different parts of the heterostructure. One of them is confined in the core region, and another one is localized in the shell region. This means two different charge carriers are spatially separated. For quasi type-II core/shell QDs (e.g., ZnSe/CdSe and CdSe/CdS, Figure 1.7d), one charge carrier delocalizes over the entire QD region, while the other one is localized in one part.

These different classifications in core/shell QDs allow the electron-hole spatial overlap to be tailored by controlling the size, shape, and composition of each segment of the heterostructured core/shell QDs, which has a dramatic impact on several properties (e.g., QY, stability, PL wavelength and radiative lifetime, *etc.*). More details will be discussed in Chapter 5.

1.6 Methodologies for QDs synthesis

There are mainly two different routes reported for synthesizing QDs by wet chemistry method, namely, *in-situ* and *ex-situ* method.^{28, 64} The *in-situ* synthesis of QDs are commonly reported via a room-temperature successive ionic layer adsorption and reaction (SILAR) or chemical bath deposition (CBD).⁶⁴⁻⁶⁶ These methods allow direct nucleation and growth of the QDs at the surface of the scaffold of substrates, resulting in the QDs directly grown onto the mesoporous metal oxide (for example, TiO₂, ZnO and SnO₂). Typically, QDs synthesized via *in-situ* methods suffer from a much broad size distribution and they usually present an increased density of surface traps due to lack of control over nucleation and growth of the QDs, making it difficult to finely tune the optoelectronic properties.⁶⁴ For the *ex-situ* method, the QDs are pre-synthesized following usually a wet-chemistry approach at high temperature that forms colloidal QDs, which are surrounded with ligands. Compared to the *in-situ* synthesized QDs, the *ex-situ* method takes the advantage of fine control of the QD size, very narrow size distribution and good crystallization. Consequently, colloidal QDs reveal well-controlled optical and electronic properties in terms of the band gap, absorption, PL and lifetime. In this thesis, colloidal QDs were synthesized by the *ex-situ* approach.

For applications in emerging technologies, it is highly desirable to use high-quality QDs presenting monodispersity, narrow size distribution, high QY and good photo- and colloidal stability, which could be obtained by simple, well-controlled, inexpensive and large-scale colloidal synthetic approaches. The previous synthesis of colloidal QDs with high QY are mostly reported by a high-temperature organometallic route using the hot injection method⁶⁷, forming oil-soluble QDs with organic ligands surrounding the surface of QDs. This approach is a well-established and most commonly used methodology for colloidal QDs synthesis. For instance, Bawendi's group¹⁵ reported a simple route for the synthesis of high-quality binary CdX (X = S, Se, Te) semiconductor QDs by the hot injection approach, which permits precisely controllable growth of QDs with narrow size distributions and tunable optical properties. Scholes' group¹⁸ reported the synthesis of

colloidal PbS QDs with size-tunable NIR emission between 800 and 1800 nm by the hot injection method.

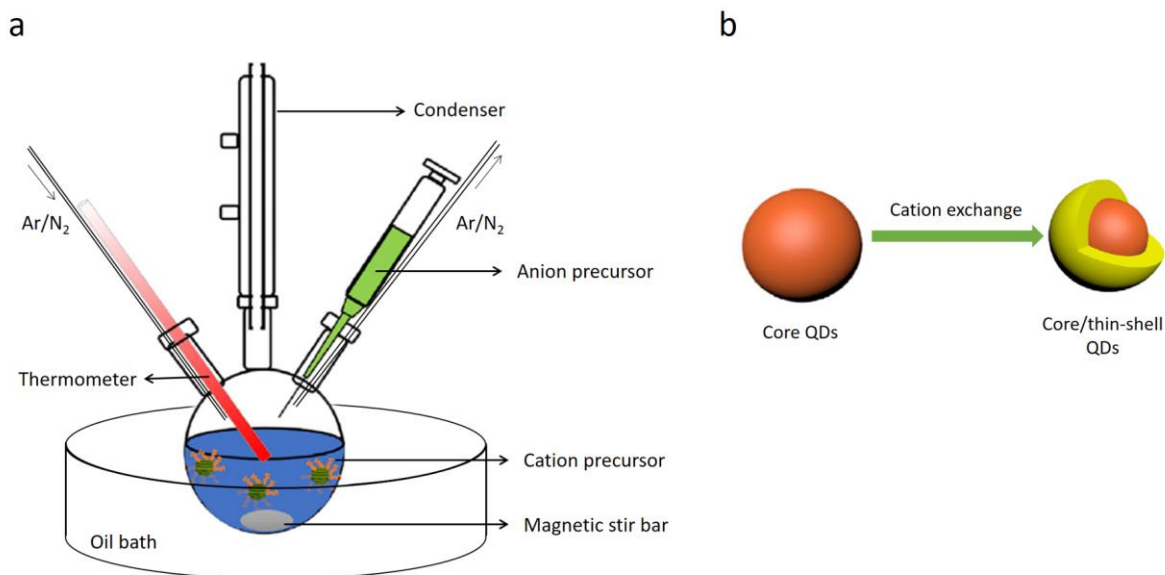


Figure 1.8 (a) Schematic representation of an air-free reaction setup for synthesizing colloidal QDs by the hot injection method. (b) Synthesis of core/shell QDs by cation exchange method. First, the core QDs can be synthesized via the hot injection method, then core/shell structured QDs synthesized by the growth of shell over the as-synthesized core QDs via cation exchange approach. Figures adapted from literature.²⁸

The reaction set-up of the hot injection method for synthesizing colloidal QDs is shown in Figure 1.8a.²⁸ In a typical procedure, the mixture of cation precursors and solvent is heated up to a relatively high temperature, obtaining a clear solution. The pre-prepared anion precursors are subsequent injected into the obtained clear solution, followed by the nucleation and growth of QDs.²⁴ The size and optical properties of QDs are able to be tuned by controlling the reaction parameters including reaction temperature, reaction time and the choice of precursors during synthesis in this reaction system.³⁰

1.7 Synthesis of colloidal core/shell QDs

Usually, colloidal core/shell QDs are mostly synthesized by a two-step procedure. First, nearly monodispersed core QDs are synthesized using the hot injection method, followed by a purification step. An intermediate purification step is conducted to eliminate unreacted precursors or side products before the shell growth. The purification process of core QDs is performed by precipitation and redispersion cycles, and finally dissolved in the solvent for the further shell growth process. Subsequently, the shell growth reaction is performed based on the as-prepared core QDs, forming the final core/shell QDs.

The strategies for the second step of colloidal core/shell QDs synthesis from a core QDs were reported by cation exchange or syringe pump injection method at high temperature, as illustrated in Figure 1.8b and Figure 1.9.

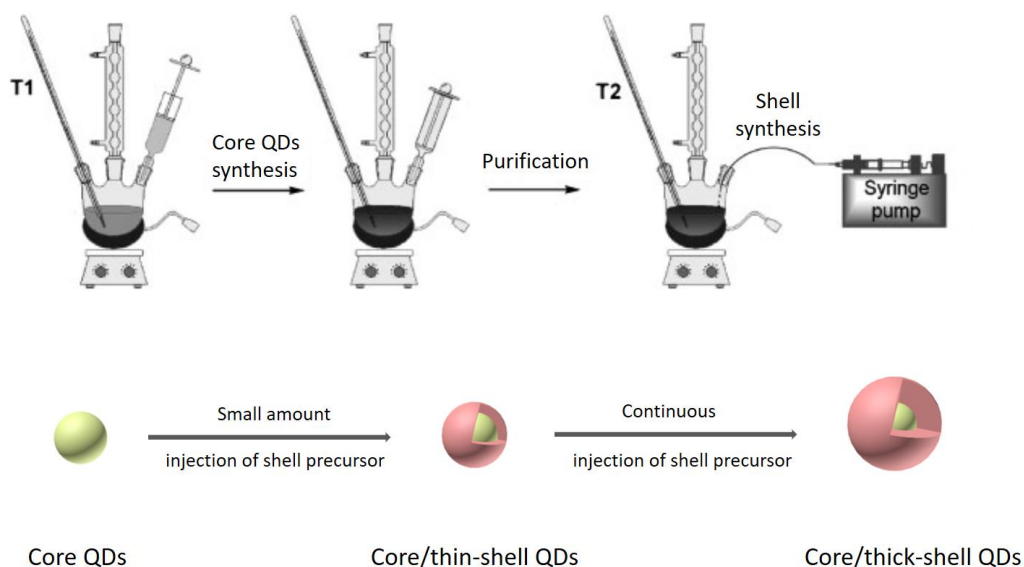


Figure 1.9 Schematic illustration of the process of synthesis of core/shell QDs by syringe pump injection method (top of the Figure). First, the core QDs can be synthesized via the hot injection method, then core/shell structured QDs are synthesized by the adsorption and reaction of gradually injected cation and anion precursors over the as-synthesized core QDs. Figure adapted from literature ²⁹.

Figure 1.8b shows the illustration of the cation exchange process. The metal ions in the prepared QDs, especially those near the surface, would be easier to exchange with other metal ions from the solution. This method does not result in any size difference of QDs before and after shell growth.

As shown in Figure 1.9, for the syringe pump injection method, the shell materials are deposited on the cores by slow and continuous injection of the shell precursors by a syringe pump at a shell growth temperature. This approach allows the adsorption of the cation and anion precursors on the surface of the core during the addition of them, followed by a reaction. During the reaction process, the size of QDs gradually increases with the continuous injection of cation and anion precursors. In this work, this syringe pump injection approach was used toward the growth of colloidal core/shell CdS/CdSe QDs in solution.

1.8 Application of QDs

Colloidal QDs have been widely used as ideal building blocks for applications in numerous emerging technologies, thanks to their unique optoelectronic properties including tunable bandgaps, broad absorption spectra, high absorption coefficients and the possibility of multiple exciton generation (MEG). Considering the urgency of the energy challenge, solar energy conversion devices such as QDSCs and solar-driven photoelectrochemical (PEC) cells for hydrogen (H_2) generation are considered very promising, due to their ability for converting renewable and abundant solar energy to other forms of energy (electricity or H_2).⁶⁸⁻⁸⁸ In addition, PEC cells for H_2 generation and QDSCs take advantages of cost-effective and easy fabrication as candidates for renewable and clean energy conversion devices.^{28, 89, 90} Nonetheless, there are several challenges for improving the performance of PEC cells and QDSCs such as the limited light-harvesting range of semiconductor photoanode and charge separation/transport efficiency, which are largely influenced by the material's band structure.⁹¹⁻⁹⁴

This thesis focuses on the design and synthesis of QDs and their application in QDSCs and PEC cells. Generally, the photoanodes for these devices are fabricated by depositing the colloidal QDs onto mesoporous wide-bandgap semiconductor films [e.g., titanium dioxide (TiO_2)]. The performance of QDSCs and PEC cells strongly depends on the separation/transport efficiency and recombination rate of photogenerated carriers inside the photoanode and photoanode/electrolyte interface. As such, it is essential to investigate thoroughly the carrier dynamics (generation, separation/transport and recombination of photogenerated carriers) between the QDs-sensitized TiO_2 photoanode and electrolyte in these devices.

Figure 1.10 shows the carrier dynamics of a QDs-sensitized TiO_2 photoanode. Under light illumination, QDs absorb photons and subsequently the electrons in the VB of QDs are excited to the CB of QDs, showing the photoexcitation process (black solid arrow indicated in process 1). After photoexcitation, shown in process 2 of Figure 1.10, the photoexcited electrons are injected from the CB of QDs into the CB of TiO_2 due to the favorable energy alignment of CB between QDs and TiO_2 . Simultaneously, photogenerated holes that remained in VB of QDs are reduced by a redox couple in the electrolyte (process 3). This process avoids the accumulation of holes inside QDs, protecting QDs from oxidation and the device performance from degradation. These three transfer processes are favorable for an efficient device, allowing high photon-to-current (or fuel) conversion efficiency.

In addition to the above-mentioned carrier generation and separation/transport processes, however, several undesirable carrier recombination paths undermine these favorable processes and reduce the overall performance of the device. Carrier recombination mainly occurred within QDs and at the interfaces of TiO_2 /QDs/electrolyte, including four major recombination paths shown in Figure 1.10 (red dash arrows) as the following: a) carrier recombination inside the QDs, namely, photoexcited electrons in the CB of QDs can recombine with holes in the VB of QDs, b) injected electrons in the CB of TiO_2 back transfer and recombine with photoexcited holes in the

VB of QDs at the TiO_2 /QD interface, c) recombination of the injected electrons in the CB of TiO_2 with the oxidized species of the redox couple electrolyte at the TiO_2 /electrolyte interface, and d) recombination of the excited electron in the CB of QDs with the oxidized species of the redox couple electrolyte at the QDs/electrolyte interface.

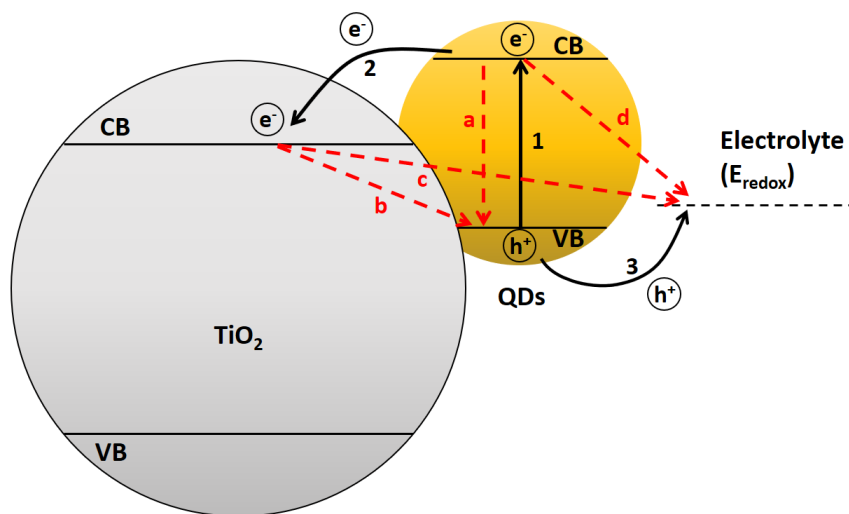


Figure 1.10 Schematic illustration of carrier dynamics (generation, separation/transport and recombination) in the QDs-sensitized TiO_2 photoanode in contact with electrolyte. Black solid arrows show three processes that are favorable for the QDSCs or PEC devices based on the described photoanode: (1) photoexcitation; (2) electron injection; (3) hole extraction. Red dash arrows show four major undesirable recombination paths, showing the main electronic processes at the TiO_2 /QDs/electrolyte interface: (a) recombination inside the absorber (semiconductor QDs); (b) recombination of injected electrons with holes in the VB of TiO_2 ; (c) recombination of injected electrons with electrolyte and (d) recombination of electrons in the CB of QDs with electrolyte.

The major recombination processes (red dash arrows a-d in Figure 1.10) occur in PEC cells and QDSCs are directly dependent on the optoelectronic properties of the QDs such as the ability of exciton generation upon the photon absorption, carrier (electron/hole) separation and transport at QDs/carrier scavengers (QDs/ TiO_2 , QDs/electrolyte) interfaces.⁷¹ These carrier recombination paths in QD-based devices (PEC cells or QDSCs) are also attributed to the surface trap states within QDs. The presence of intra-band traps state in the QDs originating from the surface defects,

which act as recombination centers during device operation and reduces the overall device performance.⁹⁵ As such, understanding the correlation between the tailoring of the carrier dynamics and the structure of QDs is crucial to minimize undesirable recombination and fabricate highly efficient and stable QDSCs and QD-based PEC cells.

In this thesis, QDs were employed as light harvesters for application for both QDSCs and PEC cells. The architectures for both of these two devices contain a similar QDs/TiO₂ photoanode as an important building block such as illustrated in Figure 1.11.

1.8.1 Application in QDSCs

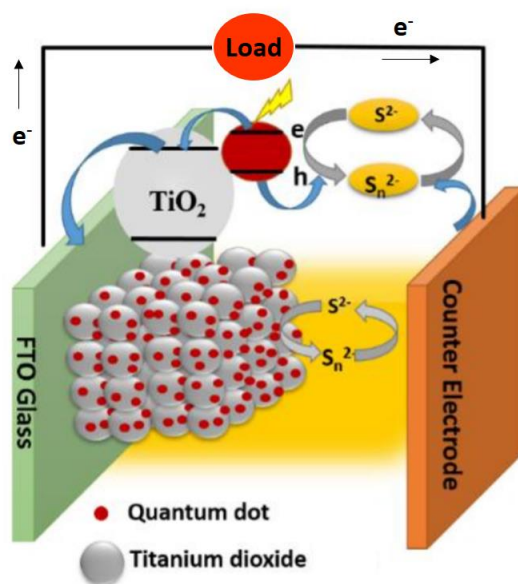


Figure 1.11 Schematic illustration of the structure and working principle of QDSCs, adapted from reference⁹⁶.

Typically, QDSCs consist of a photoanode, a counter electrode and redox couple electrolyte.⁹⁷

Figure 1.11 shows the schematic illustration of the structure and working principle of QDSCs.

Briefly, under illumination, QDs absorb photons and electrons in the VB get excited to the CB in the QDs. The excited electrons from the CB of QDs are then injected to that of TiO₂ due to favorable band offset potential between the CB of QDs and CB of TiO₂, followed by transportation

to the transparent FTO and then to the external circuit. The holes in the VB of QDs are absorbed by a redox couple in the electrolyte, while the oxidized electrolyte is regenerated by gaining electrons from the external circuit at the electrolyte/counter electrode interface and complete the one-cycle of QDSC.⁷¹

As mentioned above, the possibility of MEG and hot electron extraction in the QDs, could boost the theoretical power conversion efficiency (PCE) limit of QDSCs beyond the Shockley-Queisser limit of 32.7%.^{71, 98} As shown in Figure 1.12, MEG is a process that can occur in semiconductor QDs, whereby absorption of a photon of at least twice the bandgap energy produces two or more electron-hole pairs.⁹⁸ It was already reported MEG being occurred in lead selenide (PbSe) QD-based solar cells, as evidenced by an external quantum efficiency (the spectrally resolved ratio of collected charge carriers to incident photons) that peaked at 114 % in the best device measured.⁹⁹ To date, the record PCE value of more than 13% reported for QDSCs¹⁰⁰, which is still significantly lower than that of the commercial silicon solar cells (typically in the range of 20-40%) due to above-mentioned undesirable carrier recombination.^{101, 102}

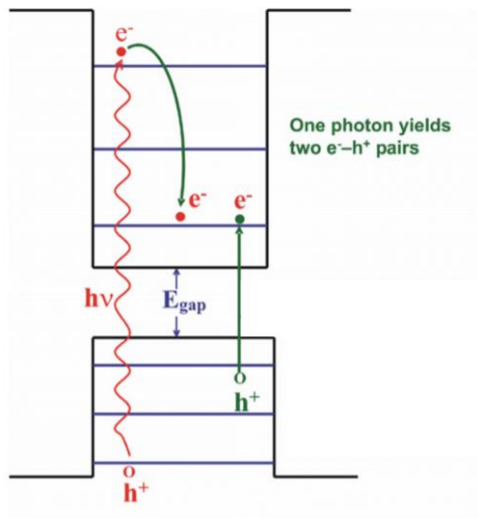


Figure 1.12 Multiple exciton generation in QDs, referred and adapted from literature^{103, 104}.

1.8.2 Application in PEC cells for H₂ generation

Aside from solar energy converted to electric power by QDSCs, solar energy could also be converted into chemical energy in the form of fuels such as H₂. H₂ is a clean fuel, which combines the advantages of high energy storage densities, cost-effectiveness, ease of transportation, and generating water as the only byproduct of H₂ use. PEC cells, which realize the conversion of solar energy into H₂ by splitting water under solar irradiation, provide a simple and environmentally friendly methodology for H₂ generation with the potential to enable the widespread deployment of H₂ as a clean fuel.^{69, 94}

In 1972, Fujishima and Honda firstly reported using an n-type wide bandgap TiO₂ semiconductor as a photoanode for water splitting,¹⁰⁵ thanks to its appropriate band energy position. Figure 1.13 shows the Honda–Fujishima configuration of the water splitting system using a TiO₂ photoanode. Photons of energy exceeding that of the band gap of TiO₂ generate electron-hole pairs. The negative charge carriers (electrons) in the CB of TiO₂ move through the bulk of the semiconductor and the external circuit to the platinum (Pt) counter electrode. Water is reduced by electrons in the surface of Pt, generating H₂.

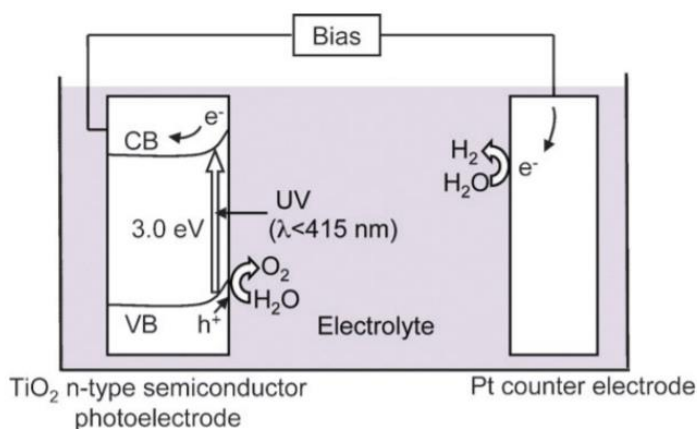


Figure 1.13 Honda–Fujishima configuration of water splitting system using a TiO₂ photoanode, referred and adapted from literature.^{105, 106}

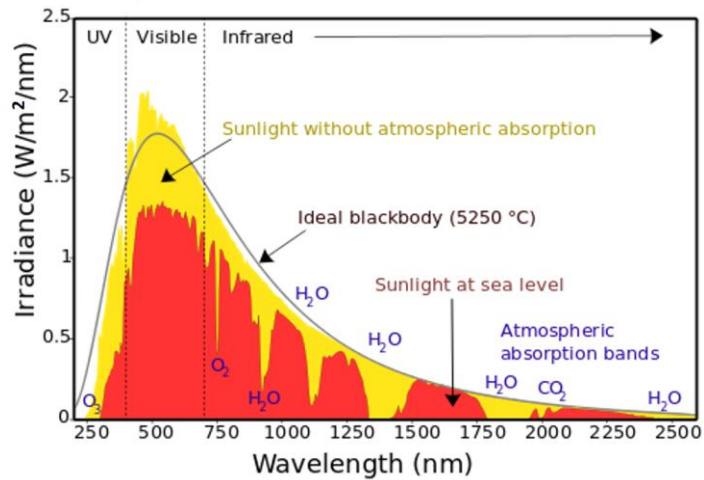


Figure 1.14 Spectrum of solar radiation at the top of the atmosphere and at sea level from 230 nm to 2.6 μm wavelengths, adapted from literature ¹⁰⁷.

Afterward, semiconductor TiO_2 , ZnO and SnO_2 have been the favoured materials for water splitting and attracts extensive attention.¹⁰⁸⁻¹¹⁰ However, the conversion efficiency from sunlight energy to fuels (H_2) is low, because these wide bandgap (larger than 3 eV) semiconductors absorb only the UV photons of the solar spectrum (representing about 5% of the solar spectrum as shown in Figure 1.14). As such, shifting the spectral response of photoanode into the visible and NIR regions is regarded as an important way to increase the conversion efficiency of solar energy into clean chemical fuel. In general, two main strategies have been reported for enhancing absorption of photoanode, including doping metal or non-metal elements, and sensitizing with narrow bandgap materials.^{88, 109, 110} For example, N-doped ZnO film enables a significant red shift of light absorption wavelength towards the visible region, thus enhancing the photo-to-fuel conversion efficiency.¹⁰⁹ PbS/CdS QDs are involved to sensitize TiO_2 for significantly efficient and durable PEC cells for H_2 generation.⁸⁸ Among all, sensitization of wide band gap semiconductors (for example, TiO_2 and ZnO) with QDs are considered as an effective way, forming an absorption enhanced QDs/ TiO_2 photoanode, thanks to their broad absorption profile that overlaps significantly with the solar spectrum. Thus, it is possible to capture more photons under sunlight

illumination, enhancing the photon-to-fuel conversion efficiency for H₂ generation in PEC cells.^{108,}

¹¹¹ As such, numerous types of bare QDs, such as PbS,⁸⁸ CdS,⁶⁶ CdSe,⁹⁴ and CuInSe_xS_{1-x},^{112, 113} have been used to fabricate QDs sensitized TiO₂ based PEC cells. Among these QDs, it was found that, generally, heavy-metal-based QDs exhibit better PEC performance for H₂ generation with respect to the non-toxic heavy-metal-free QDs. Although the absorption limit of these photoanodes has been extended to the visible or even NIR regions, the photon-to-current (or fuel) conversion efficiency is still limited due to the low carrier separation/transport efficiency and undesirable carrier recombination. Due to their small size (large surface-to-volume ratio), these bare QDs suffer from the high density of surface-defects/trap states, which act as fast non-radiative centers for photogenerated carrier recombination, resulting in reducing long-term photostability and decrease of QY. For instance, PEC devices based on bare CdSe QDs yield low photocurrent density of 6 mA/cm² due to high density of surface-trap states, poor stability under illumination, short carrier lifetime and undesirable non-radiative recombination of bare QDs.⁹⁴

To solve these issues, core/shell structured QDs are considered as the promising architecture, thanks to the ability to optimize the electronic band alignment between core and shell as well as interfacial carrier dynamics.⁶¹ For example, electrons and holes are partially separated between core and shell in a quasi type-II band structure of CdSe/CdS core/shell QDs, in which the holes are confined in the CdSe core and electrons are delocalized over the entire QD region.⁶³ This spatial separation of electrons and holes reduces the possibility of carrier recombination, making the core/shell systems suitable to be used as light harvesters in QDSCs¹⁰¹ and PEC cells⁹⁴. As such, a high photocurrent density of 10 mA/cm² has been reported in colloidal “giant” CdSe/CdS core/shell QD-based PEC devices.⁹⁴ In contrast, PEC devices based on bare CdS and CdSe QDs yield low values of photocurrent density (5 and 6 mA/cm² for CdS and CdSe, respectively) due to the limited absorption range for CdS and low electron injection efficiency for CdSe based devices.^{64, 66, 94} Therefore, heterostructured core/shell QDs are among the most attractive material

to use in solar technologies since their optoelectronic properties can be tailored through the core or/and shell components and sizes.

1.9 Research objectives

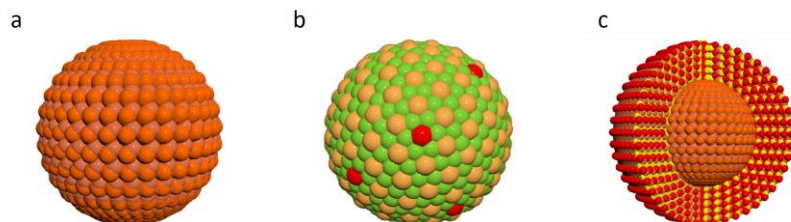


Figure 1.15 Schematic illustration of different classifications of colloidal QDs: (a) bare QDs, (b) doped QDs and (c) core/shell QDs.

My research project will focus on research of controlled synthesis of different types of colloidal semiconductor QDs such as bare QDs, doped QDs and core/shell QDs (as shown in Figure 1.15) and exploring their size/composition/structure-dependent optoelectronic properties based on the quantum confinement effect.

Colloidal PbS QDs are becoming increasingly attractive due to their spectrally size-dependent broad absorption in the UV-visible-NIR region ranging from 300 to 2000 nm, rendering them useful as absorbers in solar technologies. Typically, high-quality PbS QDs can be synthesized via a hot injection organometallic approach.¹¹⁴ However, the most widely used sulfur precursors for the synthesis of PbS QDs include bis(trimethylsilyl) sulfide [(TMS)₂S] and sulfur (S). (TMS)₂S is very reactive, expensive, toxic, unstable and must be handled in an inert atmosphere.¹¹⁵ The use of S can enable a different synthesis route, to obtain high-quality PbS QDs. However, the low reaction activity of S leads to limitations in the size control of QDs with first absorption excitonic peak larger than 1000 nm). These drawbacks largely affect their use in solar technologies. Therefore, it is very desirable to synthesize PbS QDs without using a glove box by optimizing reaction conditions, such as the solvent and lead/sulfur precursors.

Doping transition metal ions in semiconductor QDs is a promising approach for introducing unique properties compared to pure QDs. Mn ions doped wide bandgap (larger than the energy for Mn $^4T_1-^6A_1$ transition of 2.12 eV, such as ZnS and ZnSe) QDs have been widely studied. These reports demonstrate that the PL of Mn-doped QDs was found to change significantly due to the presence of Mn d-emission that arises due to $^4T_1-^6A_1$ radiative transition. To date, few reports have described Mn-doped narrow bandgap (smaller than 2.12 eV) materials. For example, Turyanska *et al.* reported the synthesis of Mn-doped PbS QDs with a large particle size of 5 nm in an aqueous solution and demonstrated their application in medical imaging and toxicology.¹¹⁶ ¹¹⁷ However, the emission mechanism and temperature-dependent optical properties of Mn-doped PbS QDs are still not well understood, in particular concerning small-sized and oil-soluble Mn-doped PbS QDs.

Solar-driven PEC H₂ generation is widely considered a promising approach to transform solar energy into clean chemical fuels. PEC cells based on colloidal QDs are of great interest due to the QD's size-dependent optoelectronic properties and the ability to control exciton generation and carrier transport. However, low solar energy to fuel conversion efficiency and limited long-term stability of QD-based PEC cells are still major unresolved challenges, which are mainly attributed to (i) inadequate light absorption, (ii) slow charge injection/transfer rate from QDs to carrier scavengers, and (iii) undesirable carrier recombination within QDs due to presence of surface traps and defects at QDs surface (for bare QDs). Recently, QDs in the core/shell architecture have been developed as promising light-harvesting materials in solar energy conversion devices, thanks to their enhanced stability, prolonged PL lifetime, improved QY and the possibility to engineer the carrier generation/transport. Over the last few years, research in core/shell QDs has been rapidly growing. The electron-hole wave functions of core/shell QD systems can be tailored through a suitable modulation of the size/thickness/composition of core and shell materials. Several recent studies demonstrated the size-dependent optical properties

for the quasi-type-II band alignment of CdSe/CdS core/shell QDs, providing fundamental knowledge and insights for their application in PEC cells. However, the band alignment of the inverted heterostructure of colloidal CdS/CdSe core/shell QDs is still not well understood. In particular, there is as yet no report on how the electronic band alignment of CdS/CdSe QDs evolves by tuning the shell thickness, limiting the ability to optimize the band alignment and carrier dynamics for this system. It is therefore crucial to understand the band alignment of colloidal CdS/CdSe core/shell QDs, as it will pave the way for their application in optoelectronic devices.

To address all the above-mentioned issues, my research projects will follow the subsequent objectives:

- (i) Exploring a facile and optimized approach based on thiourea precursors to replace 'traditional' air-sensitive and unstable $(\text{TMS})_2\text{S}$ precursor for synthesizing NIR PbS QDs via the hot injection method. The aim is to develop a simple, glove box-free and greener approach for the controlled synthesis of PbS QDs with good reproducibility and easy manipulation. The as-prepared QDs are then employed as light harvesters, to evaluate their performance for application in both solar-driven PEC H_2 generation and QDSCs.
- (ii) Synthesizing Mn-doped narrow band gap PbS QDs with small sizes and hence introducing unique properties with respect to pure PbS QDs. The optical properties of Mn-doped PbS QDs are subsequently investigated thoroughly. The emission mechanism of Mn-doped PbS QDs and temperature-dependent optical properties is well understood and reported.
- (iii) Designing and synthesizing colloidal heterostructured CdS/CdSe core/shell QDs and optimizing the shell thickness of QDs to tailor their optical properties and electronic band alignment. The as-prepared QDs are then employed as light harvesters, to evaluate their performance for application in QD-based solar-driven PEC cells for H_2

generation. Deep insights about how tunable shell thickness of CdS/CdSe core/shell QDs affects the performance of optoelectronic devices are investigated based on both theoretical and experimental aspects such as carrier dynamics, light absorption and electron transfer rate.

1.10 Thesis organization

This thesis is divided into seven parts, organized as follows:

Chapter 1 generally introduces the basics and background of my PhD research work and also presents the motivation and main goals of my projects.

Chapter 2 describes experimental method details, and the main characterizations for QDs and devices are also described in this chapter.

Chapter 3 reports a facile, greener and glove box-free approach for the synthesis of PbS QDs using thiourea as a sulfur source. The sizes of the PbS QDs could be systematically controlled by simply adjusting the reaction parameters. Employing colloidal PbS QDs synthesized using air-stable thiourea as light harvesters to fabricate optoelectronic devices (solar-driven PEC H₂ generation and QDSCs), a comparable or even better performance compared to devices fabricated with QDs synthesized from traditionally used air-sensitive and unstable (TMS)₂S. These results demonstrate the developed approach is a promising alternative to existing synthetic methodologies of PbS QDs and holds great potential for future solar technologies application. The publication related to this chapter is:¹¹⁸

H. Zhang, G. S. Selopal, Y. Zhou, X. Tong, D. Benetti, L. Jin, F. Navarro-Pardo, Z. Wang, S. Sun, H. Zhao and F. Rosei. Controlled Synthesis of Near-infrared Quantum Dots for Optoelectronic Devices. Nanoscale, 2017, 9, 16843–16851.

Chapter 4 presents the synthesis of oil-soluble Mn-doped PbS QDs of identical size with different Mn contents. A novel photoluminescence mechanism is proposed in Mn-doped PbS QDs. The

midgap states created by Mn doping cause photoexcited electrons to be transferred from the CB of the PbS host to the Mn 4T_1 state and then recombination with holes in the VB, which leads to a “Mn–PbS” emission. Mn-doped PbS QDs exhibit a faster temperature-dependent PL response compared to pure PbS QDs, demonstrating that the Mn-doped PbS QDs are promising alternatives for use as thermal sensors. The publication related to this chapter is:¹¹⁹

H. Zhang, J. Liu, C. Wang, G. S. Selopal, D. Barba, Z. M. Wang, S. Sun, H. Zhao and F. Rosei. *Near-infrared Colloidal Manganese Doped Quantum Dots: Photoluminescence mechanism and Temperature Response. ACS Photonics, 2019, 6, 2421–2431; Cover Article.*

Chapter 5 reports the engineer the optoelectronic properties and band alignment in colloidal heterostructured CdS/CdSe core/shell QDs by tuning the shell thickness (0.6-1.9 nm). Employing QDs (with an optimal shell thickness of 1.60 nm) sensitized TiO₂ as photoanode, a record photocurrent density of ~16.0 mA/cm² was obtained for PEC cells based on CdS/CdSe QDs and also observed excellent long-term stability (maintaining 83% of its initial value after four hours) under one sun illumination. The excellent performance was investigated and explained from both the theoretical and experimental aspects. The publication related to this chapter is:¹²⁰

H. Zhang, L. V. Besteiro, J. Liu, C. Wang, G. S. Selopal, Z. Chen, D. Barba, Z. M. Wang, H. Zhao, G. P. Lopinski, S. Sun, and F. Rosei. *Efficient and stable photoelectrochemical hydrogen generation using optimized colloidal heterostructured quantum dots. Nano Energy, 2021, 79, 105416.*

Chapter 6 finally summarizes the most significant contributions of my PhD research work and discusses future challenges and perspectives in this field.

Most of the work in this thesis was done by myself, Hui Zhang, however, some parts were carried out through collaboration. More specifically, theoretical calculations of electron/hole wavefunctions were performed by Dr. Lucas V. Besteiro, at the time working in our group at the

INRS-EMT center. In the theoretical calculation part, Hui Zhang I only participated in developing the model and discussing the results. I did not conduct the simulations. Dr. Gurpreet S. Selopal helped on the J-V curves analysis. Steady and transit PL measurements in this thesis were conducted by Dr. Haiguang Zhao and Mr. Jiabin Liu in our group, who also assisted with the temperature-dependent PL measurements.

Following the main body of this thesis is an appendix containing a summary of this thesis in French according to INRS policy.

Chapter 2. Materials and characterization

2.1 Materials

Aniline, 3,5-bis(trifluoromethyl)phenyl isothiocyanate, toluene, chloroform, lead (II) acetate trihydrate [$\text{Pb}(\text{CH}_3\text{CO}_2)_2 \cdot 3\text{H}_2\text{O}$], oleic acid (OAc), hexadecane, diphenyl ether, acetone, ethanol, methanol, cadmium oxide (CdO) (99.99 %), 1-octadecene (ODE), $(\text{TMS})_2\text{S}$, trioctylphosphine (TOP) (97%), poly(methylmethacrylate) (PMMA), cadmium nitrate tetrahydrate [$\text{Cd}(\text{NO}_3)_2 \cdot 4\text{H}_2\text{O}$], manganese acetate trihydrate [$\text{Mn}(\text{CH}_3\text{CO}_2)_2 \cdot 4\text{H}_2\text{O}$], cadmium acetate dihydrate [$\text{Cd}(\text{CH}_3\text{COO})_2 \cdot 2\text{H}_2\text{O}$], thioglycolic acid (TGA), sodium hydroxide (NaOH), phenyl isothiocyanate, sulfur (100%), selenium powder, oleylamine (OLA) (technical grade, 70%), rhodamine 6G, indocyanine green (ICG), Manganese Standard for ICP (1000 mg/L Mn in 2% nitric acid), Lead Standard for ICP (1000 mg/L Pb in 2% nitric acid), Cadmium Standard for ICP (1000 mg/L Cd in 2% nitric acid) trioctylphosphine oxide (TOPO, 99%), tetraethyl orthosilicate, zinc acetate dihydrate [$\text{Zn}(\text{CH}_3\text{COO})_2 \cdot 2\text{H}_2\text{O}$], hydrochloric acid (HCl) (37 %), sodium sulfide (Na_2S), sodium sulfite (Na_2SO_3), zirconium(IV) oxide (ZrO_2) nanopowder (particle size < 100 nm), carbon nanotubes (multi-walled with an average length of 10 μm and an average diameter of 12 nm) (CNTs), cetyl-trimethyl ammonium bromide (CTAB). All the above-mentioned chemicals were purchased from Sigma-Aldrich Inc. and used as purchased without any further purification. Brass was purchased from McMaster-Carr Company. Ti-Nanoxide BL/SC was bought from Solaronix. Titania paste containing active anatase nanoparticles ~20 nm in diameter (18 NR-T) and a blend of active anatase particles (~20 nm) and larger anatase scattering particles (up to 450 nm in diameter) paste (18 NR-AO) were supplied by Dyesol/GreatCell Solar (Queanbeyan, Australia). Transparent fluorine-doped tin oxide (FTO) coated conducting glass substrates with sheet resistance of 8 Ω /square were purchased from Pilkington glasses.

2.2 Characterization

This part deals with various physical techniques employed for morphological, structural, compositional and optical characterization of the as-synthesized QDs and photoanode prepared in this work.

2.2.1 X-ray diffraction (XRD)

Crystals are composed of regular arrays of atoms and they are arranged in a way that a series of parallel planes separated from one another by a distance “d” so-called the interplanar distance. XRD gives information about the crystalline phase, composition, orientation, and lattice parameters of crystalline solid samples. It is a powerful tool to study the crystal structure of QDs. As shown in Figure 2.1, XRD is based on constructive interference of monochromatic X-rays and a crystalline sample. If an x-ray beam strikes the sample with an incident angle, then the incident X-ray is scattered by the crystalline sample according to Bragg’s law:

$$n\lambda = 2d\sin\theta \quad (8)$$

where n is an integer, λ is the wavelength of the X-ray beam, d is the spacing distance between diffracting crystal planes, and θ is the incident angle of the beam.

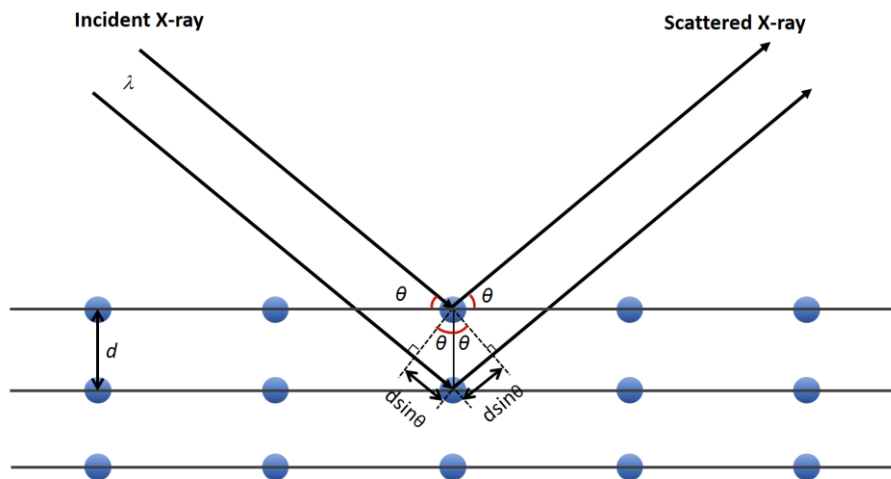


Figure 2.1 Principle of XRD.

Bragg's law is used to explain the interference pattern of the X-rays scattered by the crystals. The set of d-spacing in a typical X-ray scan provides a unique characteristic of the crystalline QD samples.

In this thesis, XRD patterns of QDs were acquired using an X-ray diffractometer (X'pert PANalytical) equipped with a Cu K α radiation source ($\lambda=0.15406$ nm) using a voltage of 45 kV and a current of 40 mA. The samples for XRD measurements were prepared by dropping extensively purified QDs solution (in toluene) onto the surface of a glass substrate, followed by drying them at 50 °C in air condition in a fume hood. This procedure was repeated several times to make sure there is enough amount of QDs on the glass substrate for XRD measurement. XRD results are used to determine the crystalline structure of as-synthesized QDs.

2.2.2 TEM

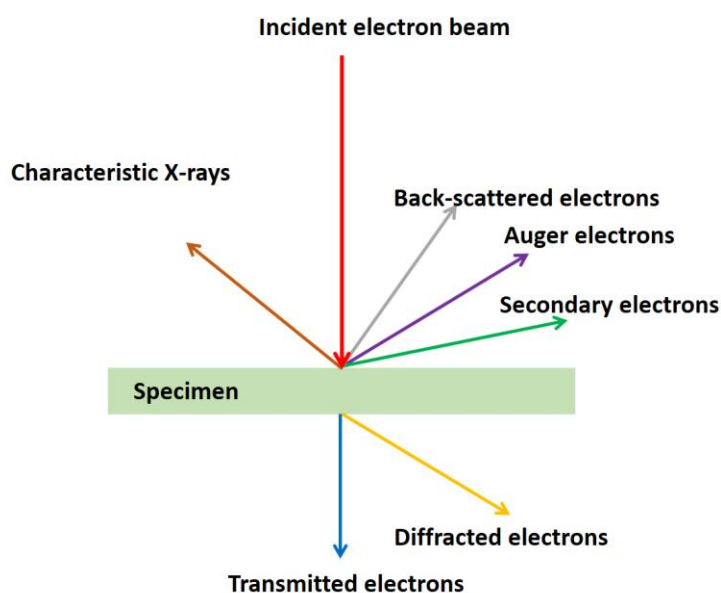


Figure 2.2 The most important interactions between the incident electron beam and specimen in a TEM.

TEM is an advanced technique to provide morphological, compositional and crystallographic information on samples from the interactions between samples and energetic electrons. It is a

microscopy technique in which an electron beam accelerated by high voltage (~200 KV) is transmitted through an ultra-thin (in general, less than 100 nm in thickness) specimen to form an image (as shown in Figure 2.2). TEM can directly observe the morphology and size of the as-synthesized QDs. In order to perform TEM measurements, a small drop of QDs solution (in toluene) was deposited onto a 200-mesh Cu grid coated with a thin carbon film. The grid was subsequently dried naturally by maintaining it under atmosphere condition in a fume hood. The QDs sample was observed by using a JEOL-2100F TEM (Université de Montréal, Montréal, Canada) operating at 200 kV for all experiments. Selected area electron diffraction (SAED) patterns and energy dispersive X-ray spectroscopy (EDS) of QDs were also acquired using a JEOL-2100F TEM during measurement.

In this thesis, TEM has been used to examine the morphology and size of the as-synthesized QDs. The average size of QDs was estimated by measuring about 100–200 individual QD particles for each sample in TEM images. The size distribution was further analyzed using a Gaussian distribution. SAED is used to determine the crystal structure of as-prepared QDs. EDS is used to confirm the elemental composition of QDs.

2.2.3 Scanning electron microscopy (SEM)

SEM is a powerful magnification technique that produces high-resolution images with information about the topography, morphology and composition on the surface of samples by scanning the surface with a focused beam of electrons. The incident electron beam interacts with atoms at or near the surface of the sample (as shown in Figure 2.3), generating a variety of signals such as backscattered electrons, secondary electrons, Auger electrons and characteristic X-rays that contain information about the sample's surface topography and composition. The detectors are used to collect and analyze these signals, in which the secondary electron is predominantly used for SEM imaging. The ratio of the displayed image size to the scanned sample area by the electron beam gives the magnification. The characteristic X-rays are used for elemental analysis.

In this thesis, the representative morphologies and images of the cross-sectional QDs/TiO₂ photoanodes (QDs on the scaffold of TiO₂ mesoporous film) were characterized and obtained by field emission SEM (FE-SEM) measurement using a JEOL JSM-6300F FE-SEM or a Tescan Vega3 equipment.

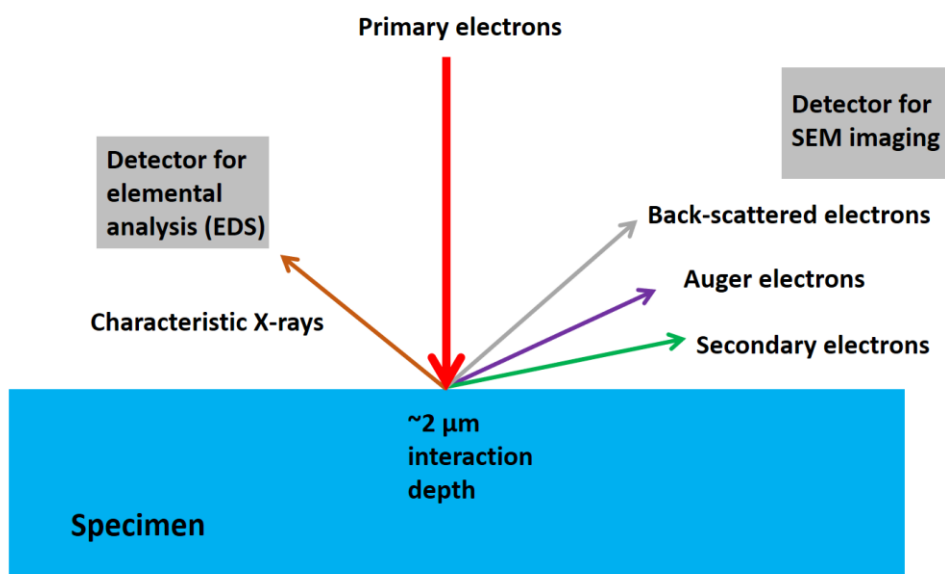


Figure 2.3 Signals generated from the interactions between the incident electron beam and specimen in an SEM.

2.2.4 EDS

EDS characterization is a powerful tool to investigate the elemental analysis of nanomaterials by analyzing the characteristic X-rays (as shown in Figure 2.2 in TEM and Figure 2.3 in SEM) formed from the interactions between samples and energetic electrons. In this thesis, the chemical composition of the as-synthesized QDs was performed by SEM/TEM apparatus equipped with an EDS detector. Meanwhile, the EDS spectra were measured at different locations on the sample. The composition of cross-sectional QDs/TiO₂ photoanode can be easily measured on a freshly cleaved cross-section of the photoanode and identified by using EDS, inside an SEM apparatus. The obtained EDS mapping images of all the elements (expected to be present in the fabricated

photoanodes) and EDS line scan were used to evaluate the laterally homogeneous distribution of the QDs in the TiO₂ mesoporous film of the photoanodes.

2.2.5 X-ray photoelectron spectroscopy (XPS)

XPS is based on the photoelectric effect. When the surface of the sample is illuminated by an incident X-ray, the energy of incident X-ray photons is completely absorbed by an electron. If the photon energy is large enough, the electron will escape from the atom and emit out of the surface, reaching the electron energy analyzer. The emitted electron with a certain kinetic energy is referred to as the photoelectron. As shown in Figure 2.4, the binding energy can be determined by the following equation:

$$E_B = h\nu - E_K - \phi \quad (9)$$

where E_B is the binding energy, $h\nu$ is the energy of incident X-ray photons, E_K is the kinetic energy of the photoelectron measured by the instrument and ϕ is the work function.

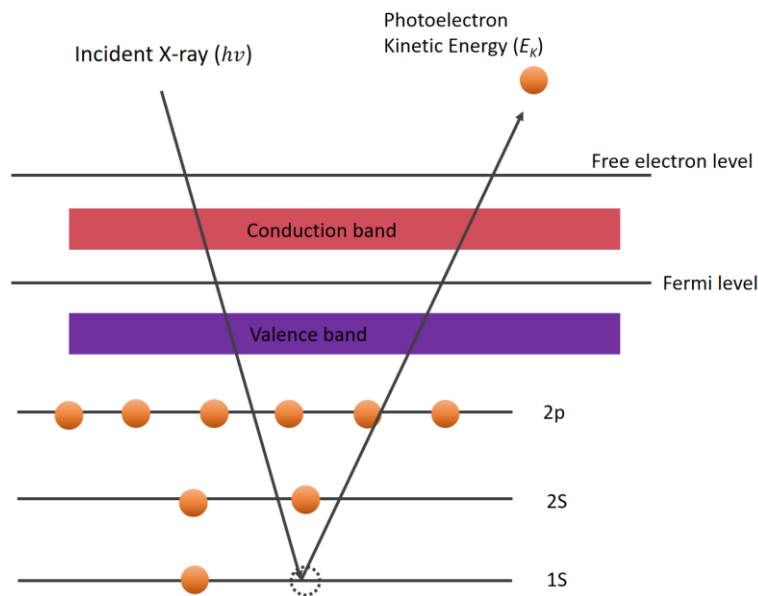


Figure 2.4 The illustration schematic of principle for XPS.

In this thesis, the high-resolution XPS spectra of small energy regions around the expected peak positions of each element were also acquired in a VG Escalab 220i-XL equipped with a hemispherical analyzer and an Al K_{α} twin anode X-ray source. The binding energies recorded in the XPS analysis were calibrated by referencing the C 1s peak to 284.8 eV. XPS results are used to analyze the elemental composition of the as-synthesized QDs.

2.2.6 Inductively coupled plasma optical emission spectrometry (ICP-OES)

ICP-OES is an elemental analysis technique that uses the plasma and a spectrometer of a sample to identify and quantify the composition of elements in samples. Each element has an own characteristic emission spectrum that is measured with a spectrometer. The light intensity on the wavelength is measured and with the calibration calculated into a concentration.

In this thesis, the Pb/Cd or Pb/Mn molar ratio was measured by using ICP-OES (PerkinElmer Model Optima 7300 DV). The measured molar ratio of Pb/Cd in Chapter 3 is used to calculate the CdS shell thickness. The measured molar ratio of Pb/Mn in Chapter 4 is used to estimate the average Mn ions number in one dot of Mn-doped PbS QDs.

2.2.7 Electron paramagnetic resonance (EPR)

EPR is a technique applied to paramagnetic species such as chemicals with unpaired electrons (transition metal ions, Mn^{2+}) in order to characterize their molecular frameworks and the chemical environments around them through the unpaired electrons.

In this thesis, EPR spectra were collected on an X-band EPR spectrometer (Bruker Elexsys 580 FT/CW EPR console). The modulation frequency was 100 kHz. Measurements at a lower temperature (114 K) were performed using liquid nitrogen. EPR results identify the existence and indicate the dopant position of Mn in Mn-doped PbS QDs.

2.2.8 Optical properties

In this thesis, absorption spectroscopy, PL spectroscopy and time-resolved PL (TRPL) were measured to identify the optical properties of QDs and photoanodes. Absorption spectra were acquired with a Cary 5000 UV-vis-NIR spectrophotometer (Varian) with a scan speed of 600 nm/min. All absorption data were corrected by the background of the solvent toluene. PL spectra were recorded with a Fluorolog®-3 system (Horiba Jobin Yvon) using a specific laser source. PL spectra for Mn-doped QDs as a function of temperature were recorded with the Fluorolog-3 system equipped with a temperature controller. The PL lifetime was measured in the time-correlated single-photon counting (TCSPC) mode using a pulsed excitation laser in the Fluorolog®-3 system. The PL decay curves were fitted by the following three-exponential equation, $I(t) = a_1 e^{(-\frac{t}{\tau_1})} + a_2 e^{(-\frac{t}{\tau_2})} + a_3 e^{(-\frac{t}{\tau_3})}$, where a_i ($i=1, 2, 3$) and τ_i ($i=1, 2, 3$) are the fitting coefficients of the PL decay results and characteristic lifetimes, respectively. The goodness of fitting can be given by the confidence factor (χ^2). The fitting results are regarded as reliable when the confidence factor is in the range of $0.8 < \chi^2 < 1.3$. In this thesis, all the fitting results of PL decay curves are in this range and reliable.

2.2.9 QY measurement

An indirect method was used to measure the PL spectrum and compare its integrated intensity with the same quantity for a reference (dye) system with a known QY. This measurement can be done using standard absorption and emission spectrometers.¹²¹ The QYs of CdS, CdS/CdSe core/shell QDs were measured by using Rhodamine 6G as a reference. Rhodamine 6G is a dye with an absorption range of 400-700 nm, which can be used to calculate the QYs of visible-emitting QDs.¹²² QYs measurement was conducted using IR-125 as a reference for PbS and Mn-doped PbS QDs.^{18, 123} IR-125, also named indocyanine green (ICG), which has the low toxicity and capacity to absorb and emit in the NIR spectral range.

The absolute QY values of the samples are calculated using reference which have a fixed and known QY value, according to the following equation: ¹²⁴

$$QY = QY_{\text{dye}} \frac{I_{\text{QDs}} A_{\text{dye}} n_{\text{QDs}}^2}{I_{\text{dye}} A_{\text{QDs}} n_{\text{dye}}^2} \quad (10)$$

Where QY and QY_{dye} are the QY of the sample and that of the dye (reference), respectively; A_{QDs} and A_{dye} are the absorbance of the sample and dye, respectively; I_{QDs} and I_{dye} are the integrated intensities (areas) of the sample and that of the dye, respectively; The n_{QDs} and n_{dye} are the refractive index of the sample and reference solvent, respectively.

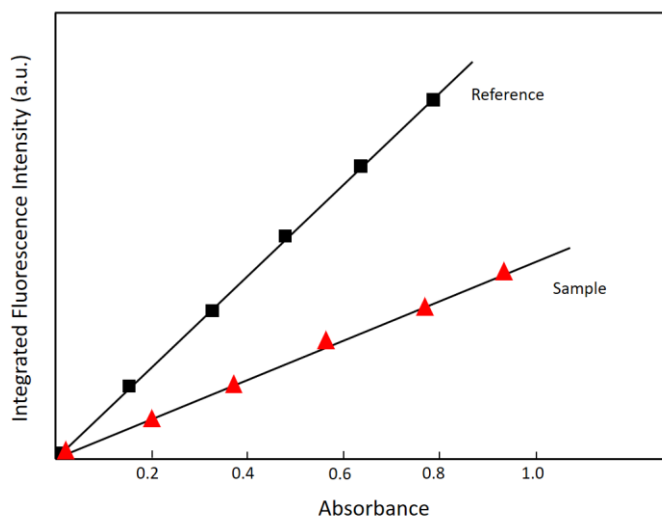


Figure 2.5 Linear plots for sample and reference. The gradient for each one is proportional to that of its QY. Conversion into an absolute QY is achieved through the equation given below.

To reduce the error, five or six sets of data were acquired from solutions with different concentrations of the sample and reference that can absorb in the region of 0-0.10 at the excitation wavelength. Then plot a graph of integrated PL intensity as a function of absorbance for each of them (as shown in Figure 2.5). The gradient of straight lines of sample and reference are denoted as G_{QDs} and G_{dye} , respectively. The QY of QDs can be calculated by the following equation.

$$QY = QY_{\text{dye}} \frac{G_{\text{QDs}}}{G_{\text{dye}}} \frac{n_{\text{QDs}}^2}{n_{\text{dye}}^2} \quad (11)$$

2.3 Device fabrication and characterization

2.3.1 Preparation of TiO₂ film

Transparent FTO-coated glass was treated by an ultrasonic wash in deionized water and ethanol for 15 min, respectively. Then the glasses were dried and cleaned in a UV environment for 10 min to remove the surface organic residue. A thin and compact TiO₂ blocking layer was then spin-coated on FTO-coated glass at 6000 rpm for 30s by using the commercial Ti-Nanoxide BL/SC (Solaronix) precursor solution. Then, the films were annealed in air at 500 °C for 30 min and cooled down to room temperature to form a thin and compact TiO₂ blocking layer.

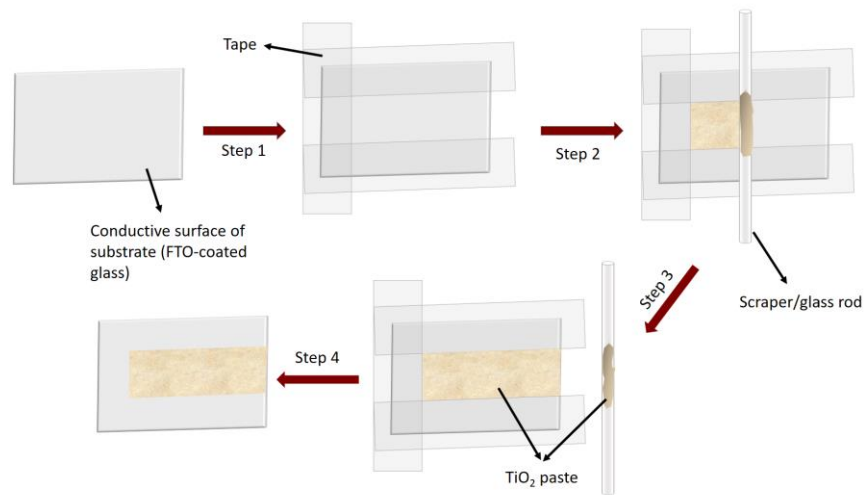


Figure 2.6 Schematic illustration of a flowchart for the doctor-blade method.

After preparation of the blocking layer, TiO₂ mesoporous film including a transparent and a scattering layer were prepared by a simple doctor-blade (tape-casting) method described in Figure 2.6. The doctor blade is one of the widely used techniques for producing thin films on a smooth substrate. In a typical procedure, first, the conductive side of the FTO-coated glass was taped with tape to reserve a conductive part for conduction and to secure the thickness of the TiO₂ on the surface of the substrate. Second, one drop of the paste was then put onto the surface

of a glass rod. Third, the TiO₂ paste was spread to provide a homogeneous paste on the substrate by uniformly moving a glass rod through the surface of the substrate. When a constant relative movement is established between the glass rod and the substrate, the paste spreads on the substrate to form a thin film. Finally, the tape was removed from the edges of the substrate carefully for further drying and annealing treatment.

In the experiment, a transparent layer was tape-casted on the above prepared TiO₂ compact blocking layer by using a paste composed of 20 nm TiO₂ nanoparticle named 18NR-T (paste A, from Dyesol). The drying process was followed for 15 min in the ambient atmosphere at room temperature and then on a hot plate at 120 °C for 6 min. Subsequently, a scattering layer was tape-casted on top of the transparent layer by using a paste composed of a blend of active anatase nanoparticles (~20 nm) and larger anatase nanoparticles (up to 450 nm) (18 NR-AO, paste B, from Dyesol), followed by the same drying process. After drying, the samples were annealed in the furnace at 500 °C for 30 min in ambient atmosphere, then cooling down to room temperature and forming a mesoporous film with a thickness of 12-14 μm, as measured by contact profilometry.

2.3.2 Sensitization of TiO₂ mesoporous film with QDs

As mentioned in Chapter 1, in the *in-situ* method (SILAR/CBD) for QDs synthesis, the QDs are directly grown on the surface of the scaffold in the TiO₂ mesoporous films. As shown in Figure 2.7, the sensitization process is completed simultaneously with the synthetic procedure.

However, the *ex-situ* colloidal synthetic approach enables pre-synthesized colloidal QDs, forming individually monodispersed QDs in the solvent. For further application in QDSCs or PEC cells for H₂ generation, the colloidal QDs need to be used to sensitize TiO₂ photoanode. Electrophoretic deposition (EPD)⁸⁸ and drop-casting^{100, 125} approaches are reported to deposit colloidal QDs into the scaffold of TiO₂ mesoporous film, sensitizing TiO₂ mesoporous film with as-prepared colloidal

QDs. The former one was used for sensitizing TiO₂ mesoporous film with oil-soluble colloidal QDs^{88, 101, 126}, while the latter one was used for sensitizing TiO₂ mesoporous film with water-soluble colloidal QDs^{100, 125}. The EPD approach is a technique that exploiting an electrical field to drive the deposition of colloidal QDs in solution upon the surface of the scaffold in TiO₂ mesoporous film.¹²⁷ It was reported that there is an equilibrium existing between the population of non-charged majority and positively/negatively charged minority in colloidal QDs.¹²⁸ These positively/negatively charged QDs enable the deposition of QDs in an electrical field.¹²⁷ In this thesis, the oil-soluble QDs are deposited by EPD for sensitization of TiO₂ mesoporous film.

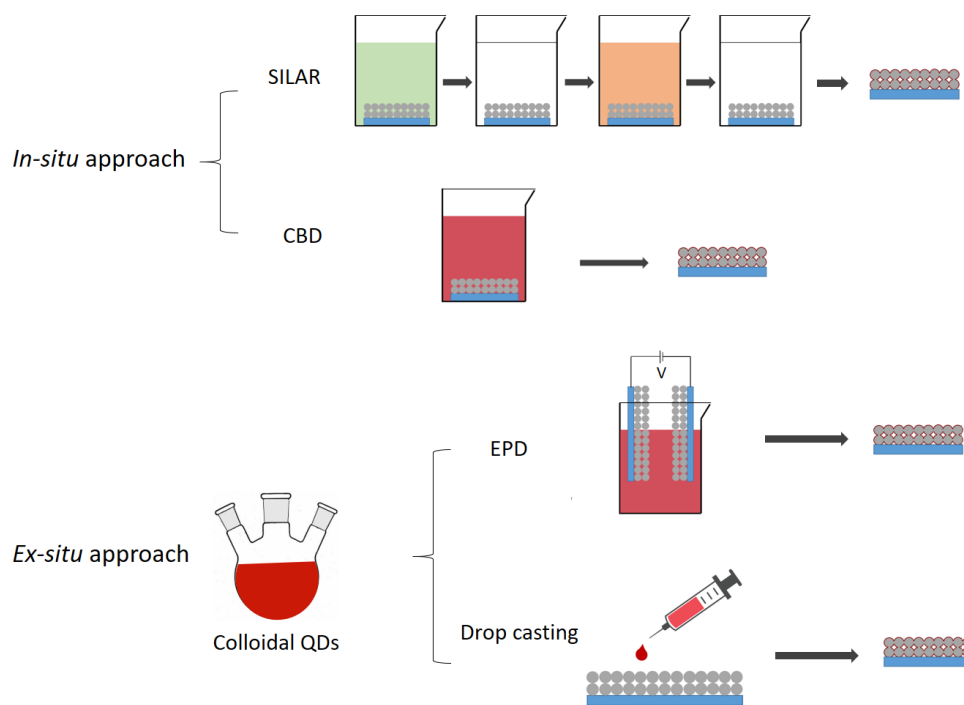


Figure 2.7 Schematic illustration of the sensitization of TiO₂ mesoporous film with QDs prepared through *in-situ* or *ex-situ* approach. For the *in-situ* approach, the QDs are grown directly on the surface of the scaffold in TiO₂ mesoporous film, forming a QDs/TiO₂ photoanode during synthesis. In comparison with CBD, SILAR method requires the repetitive immersing operation of a TiO₂ film in precursor solutions containing cation and anion ions. For the *ex-situ* approach, after synthesis of the colloidal QDs, EPD and drop-casting approaches are employed to prepare QDs/TiO₂ photoanode.

2.3.3 QDSCs fabrication and characterization

The QDs-sensitized TiO₂ film and Cu₂S were used as the photoanode and counter electrode, respectively. The polysulfide electrolyte solution is composed of 2.0 M sodium sulfide, 2.0 M sulfur, 0.2 M sodium hydroxide in distilled water and methanol (3:7, V/V). The photoanode and counter electrode were sandwiched together with a Teflon spacer (25 μm thickness) for the fabrication of QDSCs. The Cu₂S counter electrode was prepared by immersing a brass foil in a 37 % HCl solution at 75 °C for 10 min. Then the foil was vulcanized by immersing in a polysulfide electrolyte solution at room temperature for 10 min to generate the active Cu₂S. The current-voltage characteristics of the QDSCs were measured using a digital Keithley as source meter under one sun simulated sunlight by employing a Compact Solar Simulator Class AAA (Sciencetech SLB-300A) to be calibrated with the silicon reference diode. Transient photovoltage decay measurements were carried out by one sun simulated illumination as a light source to illuminate the devices to open-circuit voltage (V_{OC}), then the light was shut down and the V_{OC} decay was recorded. The transient V_{OC} values continuously decrease with time from V_{OC} to nearly 0 V in dark.

The commonly functional parameters in QDSCs related to a typical current density-voltage (J-V) curve are shown in Figure 2.8. Comparison of results from different research groups can be achieved by these parameters, which are defined as follows.

V_{OC} is the maximum voltage available from a solar cell under illumination when the current is zero. This means the photoanode is completely not connected with the counter electrode in the external circuit and the resistance between them tends to be infinite.

Short-circuit current density (J_{SC}) represents the current density produced through the cell when applying no external load. This means the photoanode is connected directly with the counter electrode in the external circuit and the resistance between them tends to be zero.

Fill factor (FF) is the ratio between the maximum power density output (P_{Max}) and the theoretical maximum given by the product of V_{OC} and J_{SC} . P_{Max} is calculated by the product of the maximum current density (J_{MP}) and maximum potential (V_{MP}). FF is a parameter to describe how well the solar cell approach the theoretical maximum power that the solar cell can generate. This factor is a measure of the quality of a solar cell. FF is a dimensionless number.

$$FF = \frac{P_{Max}}{J_{SC}V_{OC}} = \frac{J_{MP}V_{MP}}{J_{SC}V_{OC}} \quad (12)$$

PCE (η) is defined as the ratio of maximum power density obtained from solar cell to the incident light power density (P_{in}).

$$PCE (\eta) = \frac{P_{Max}}{P_{in}} = \frac{FFJ_{SC}V_{OC}}{P_{in}} \quad (13)$$

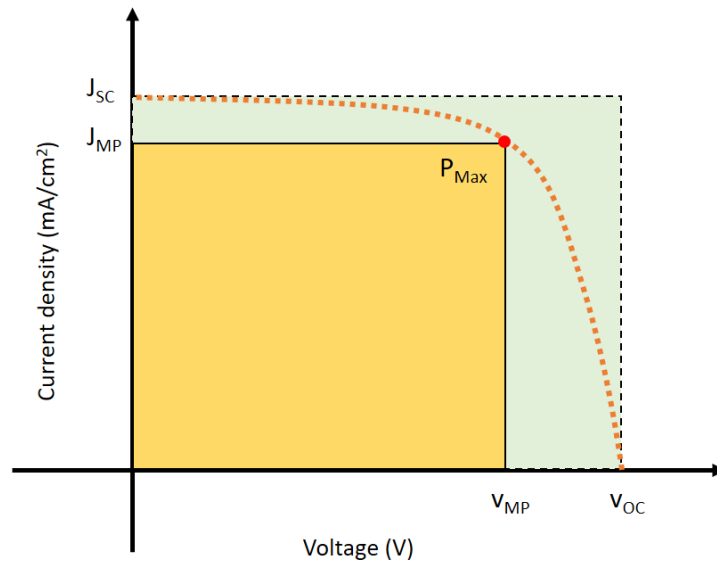


Figure 2.8 Schematic representation of J - V curve of a solar cell. The red point represents the maximum power density output.

In the experiments, the incident light is produced by a solar simulator and P_{in} is commonly fixed at Air Mass (AM) 1.5G, 100 mW/cm^2 . Here, AM 1.5G is used to represent the overall yearly average of the solar spectrum for the countries at mid-latitudes (Europe, China, Japan, USA). As

a standard solar spectrum utilized for comparison of experiment data, the solar industry has been using AM 1.5G for all standardized testing or rating of solar cells or modules. The J-V characteristics of the QDSCs were measured using a digital Keithley as source meter under one simulated sunlight (100 mW/cm^2 , AM 1.5G) calibrated with the silicon reference diode.

Transient photovoltage decay measurements were carried out by one sun simulated illumination as a light source to illuminate the devices to V_{OC} , then the light was shut down and the V_{OC} decay was recorded. The transient V_{OC} values continuously decrease with time from V_{OC} to nearly 0 V in dark.

The electrochemical impedance spectroscopy (EIS) measurements were carried out under dark condition using a SOLARTRON 1260 A Impedance/Gain-Phase Analyzer and SOLARTRON 1287.

2.3.4 PEC devices fabrication and characterization

The PEC performance of the photoanode was evaluated in the three-electrode configuration using a CHI 760D electrochemical workstation. Measurements were carried out in a typical three-electrode configuration system by employing the QDs/TiO₂ photoanode, Pt and Ag/AgCl as the working, counter and reference electrodes, respectively. All the current density vs. potential measurements were carried out at a 20 mV/s sweep rate. As the hole scavenger, the electrolyte is composed of 0.25 M Na₂S and 0.35 M Na₂SO₃ with the volume of 100 mL. The potential during electrochemical measurement was converted to the reversible hydrogen electrode (RHE) scale according to the equation $V_{RHE} = V_{Ag/AgCl} + 0.197 + \text{pH} \times 0.059$. The measurement was carried out at AM 1.5G with an intensity of $100 \text{ mW}\cdot\text{cm}^{-2}$. Prior to each measurement, a silicon reference diode (Sciencetech) was used to adjust the light intensity of solar simulator to guarantee the standard one sun illumination on the photoanode. The typical distance from sun simulator to photoanode of PEC cell is around 20 cm.

Incident photon-to-current efficiency (IPCE) measurement was conducted using a home-made setup qualitatively. To derive the IPCE values, current-voltage measurements were performed with the use of different band-pass optical filters (10nm band pass). The wavelength-dependent qualitative IPCE values can be calculated using the following equation:⁸⁸

$$IPCE (\%) = \frac{c \times h}{e} \frac{J}{\lambda \times I} = \frac{1240 \times J (mA/cm^2)}{\lambda (nm) \times I (mW/cm^2)} \times 100\% \quad (14)$$

where c is the speed of light (m/s), h is Planck's constant (J·s), e is the elementary electric charge (C), J represents the photocurrent density (mA/cm²), λ is the wavelength of the incident photon (nm), and I is the intensity of the incident radiation (mW/cm²) at a given wavelength, respectively.

H₂ evolution was measured by online gas chromatography (GC). A gas-tight cell filled with 30 mL electrolyte was used for online GC (9790 II, Fuli) electrolyte in a three-electrode cell configuration, using a TiO₂/QDs photoanode, saturated Ag/AgCl and Pt plate as working, reference and counter electrode, respectively. The electrolyte was continuously bubbled by N₂ (Praxair, 99.999%) with a flow rate of 20 standard cubic centimeters per minute (sccm) before and during the measurements. The gas outlet was introduced into a gas-sampling loop of the GC for the quantification of H₂. The GC was equipped with a packed HaySep A column and a packed MolSieve 5 A column with Ar (Praxair, 99.999%) as the carrier gas at a flow rate of 20 sccm. A thermal conductivity detector (TCD) was used to quantify H₂. A gas aliquot was injected into the GC for periodic sampling per 900 s. During the online GC, a chronoamperometric measurement was performed by applying a 0.6V vs. RHE potential in the three-electrode system under one sun illumination (AM 1.5G, 100 mW/cm²) for 2 h.

Theoretical calculation of H₂ evolution. The theoretical number of moles of evolved H₂ [$n_{H_2}(\textit{theoretical})$] can be calculated from Faraday's law using the following equation:⁹⁴

$$n_{H_2}(\textit{theoretical}) = \frac{q}{zF} = \frac{\int_{t_1}^{t_2} Idt}{zF} \quad (15)$$

where q is the total electric charge in coulombs (C), z is the number of transferred electrons per H_2 molecular during H_2 evolution reaction (*i.e.*, $z = 2$), I is the photocurrent in amperes (A), t is time in seconds (s), and F is the Faraday constant (*i.e.*, $96\,485.33\text{ C mol}^{-1}$).

The calculation of Faradaic efficiency (FE) follows the equation below:

$$FE = \frac{zFC_i v P}{IRT} \quad (16)$$

where C_i is the volume fraction of a certain product determined by online GC, v is around 20 sccm ($3.3 \times 10^{-7}\text{ m}^3\text{ s}^{-1}$), P is 101300 Pa; I is the measured photocurrent (A), R is the gas constant $8.314\text{ J mol}^{-1}\text{ K}^{-1}$, and T is 295 K.

The experimental H_2 evolution can be calculated by

$$n_{H_2}(\text{experimental}) = FE \times n_{H_2}(\text{theoretical}) \quad (17)$$

Chapter 3. Controlled synthesis of near-infrared quantum dots for optoelectronic devices

In this chapter, a facile and optimized approach is reported, based on lead oleate and substituted thiourea as lead and sulfur precursors to synthesize NIR PbS QDs. For lead oleate synthesis, a simple reaction was explored using lead acetate as the lead source and without using air-sensitive chemicals during the overall reaction process. Size-tunable NIR PbS QDs (with absorption excitonic peaks from 870 to 1400 nm) were synthesized by controlling the reaction parameters of the hot injection method. To further improve the air-stable performance of the PbS QDs towards their applicability in solar technologies, a Cd post-treatment was performed to create a thin passivating layer on the PbS QDs surface.¹²⁹ For application in solar-driven PEC cells for H₂ generation, a comparable photocurrent density was obtained based on QDs synthesized from different sulfur precursors. The as-prepared NIR QDs were also employed as sensitizers in QDSCs. For comparison, QDSCs with PbS QDs synthesized by traditional (TMS)₂S as sulfur precursor were also fabricated. Under one sun illumination, the device sensitized by QDs from thiourea shows an enhancement of 43% in PCE compared to the devices sensitized by QDs from (TMS)₂S. These results indicate that the developed synthetic methodology is a promising alternative for preparing PbS QDs without using very toxic and expensive chemicals. This approach provides a simple and greener strategy for the controlled synthesis of colloidal PbS QDs for potential applications in optoelectronics.

3.1 Experimental section

3.1.1 Synthesis of PbS QDs and further post-treated by Cd(oleate)₂

The synthetic route of PbS QDs consists in the following: first, for the synthesis of substituted thiourea, a solution of 1.7 mL aniline in 6 mL toluene was added to a solution of 5 g 3,5-

bis(trifluoromethyl)phenyl isothiocyanate in 6 mL toluene. The solution was stirred for 30 minutes before the exothermic reaction ended. The product was thoroughly dried under vacuum to remove trace toluene, resulting in the white powder of substituted thiourea.¹³⁰ Second, for the synthesis of lead oleate, 227.6 mg $\text{Pb}(\text{CH}_3\text{CO}_2)_2 \cdot 3\text{H}_2\text{O}$ and 0.4 mL OAc were mixed with 10 mL hexadecane in a 3-neck flask and flushed with nitrogen gas flow for 5 min, then transferred in an oil bath at 160 °C under stirring held for 1h in a Schlenk line. The temperature was then decreased to 95 °C. During this period, a mixture of 218.6 mg of as-prepared thiourea and 1.61 g diphenyl ether was heated to 95 °C, then this clear solution was rapidly injected into the flask containing lead oleate at 95 °C. After injection, the color of the reaction solution in the flask was observed to change from transparency to black quickly. The solution was maintained at the latter temperature for 2 minutes, then cooled down to room temperature by immersing the reaction flask in cold water. Finally, the QDs were purified by precipitation using centrifuge after the addition of ethanol/acetone (5:1 in volume) and then re-dispersed in toluene two times. The purification procedure is used to remove unreacted precursors or eliminate side chemicals.

The Cd post-treatment of QDs was performed as follows: typically, CdO (100 mg), OAc (2 mL) and ODE (10 mL) were heated to 240 °C under N_2 atmosphere for 30 min. The clear solution was then cooled down to 140 °C under vacuum for 15 min. The flask was subsequently reopened and N_2 flow was restored. The PbS QDs suspension in toluene was diluted in 10 mL toluene, purged with N_2 for 30 min and then immediately heated to 100 °C. The Cd/OAc mixture was added via a syringe. The solution was maintained at 100 °C for 5 minutes and then cooled down to room temperature by immersing the reaction flask in cold water. During this process, the color of the reaction solution in the flask was observed to change from black to light black slightly. Then the QDs were purified by ethanol and re-dispersed in toluene two times.¹³¹ PbS and Cd-treated QDs synthesized by using $(\text{TMS})_2\text{S}$ were also prepared for comparison, according to previous reports.^{132, 133}

The specific synthetic method of the TGA-capped water-soluble QDs was described below. The as-prepared oil-soluble QDs were transferred to the water by using TGA as the phase transfer agent via the ligand exchange method, following other reports.¹⁰² Specifically, 0.13 mL TGA was added to 1.0 mL methanol. The pH of the solution was adjusted to 8 with 30% NaOH, then was injected into the 5 mL of oil-soluble QDs and stirred for 10 min. Subsequently, 15 mL of deionized water was added into the solution and stirred for 5 min at room temperature. The solution was separated into two phases and QDs were distributed in the upper layer of water in the reaction solution. The water-soluble QDs were precipitated by adding acetone and then re-dispersed in pH=9 deionized water with 30% NaOH.

3.1.2 Fabrication of QDSCs and PEC Cells

TiO₂ film preparation. First, transparent FTO-coated glass (sheet resistance 8 Ω/square) was treated by an ultrasonic wash in deionized water and ethanol for 15 min, respectively. Then the glasses were dried and cleaned in a UV environment for 10 min to remove the surface organic residue. A compact and thin TiO₂ blocking layer was deposited on the substrate by spin coating (6000 rpm for 30 s), using the commercial Ti-Nanoxide BL/SC precursor solution.¹³⁴ The samples were then annealed at 500 °C in an ambient atmosphere for 30 minutes. TiO₂ mesoporous transparent and scattering layers were prepared by the doctor blade method as reported in previous work.⁸⁸ In brief, a transparent layer was tape-casted on the above prepared TiO₂ compact blocking layer. The drying process was followed for 15 min in the ambient atmosphere at room temperature and then at 120 °C for 6 min. A scattering layer was then tape-casted and dried under similar conditions. After drying, all the samples were annealed at 500 °C for 30 min in ambient atmosphere, forming a mesoporous film with a thickness of about 12–14 μm, as measured by contact profilometry.

TiO₂/QDs anode preparation. The above prepared TiO₂ films were sensitized with PbS QDs by using EPD as follows: a pair of TiO₂ films grown on FTO were vertically immersed in the QDs

solution facing each other with a distance of around 1 cm. A voltage of 200 V was applied for 2 hours.¹³⁵ During the EPD process, the current is observed around 2.3 mA. The samples were then rinsed with toluene and dried twice with N₂ flow at room temperature.

Fabrication of the PEC devices. For use in PEC devices, TiO₂ mesoporous film was sensitized by the as-synthesized PbS QDs through an EPD process. Subsequently, two cycles of ZnS layers were applied by the SILAR method. Hereafter, an insulating glue was then used to cover the sample's non-active area to avoid direct contact between the electrolyte and conducting back-contact. The PEC performance was evaluated in a three-electrode configuration with photoanode, Pt and saturated Ag/AgCl as the working, counter and reference electrode, respectively. The electrolyte consists of 0.35 M Na₂SO₃ and 0.25 M Na₂S with a volume of ~100 mL, serving as the hole scavenger.

Fabrication of the QDSCs. After the EPD process, five cycles of CdS and four cycles of ZnS were subsequently deposited by SILAR.^{66, 136} Specifically, the QD-sensitized TiO₂ film was treated with five cycles of CdS by immersing into 0.1 M Cd(CH₃COO)₂·2H₂O and 0.1 M Na₂S aqueous solutions for one min alternately, then four cycles of ZnS by immersing into 0.1 M Zn(CH₃COO)₂·2H₂O and 0.1 M Na₂S aqueous solutions for one min alternately. Silica coating was then performed by immersing the sample into 0.01 M ethanolic solution of tetraethyl orthosilicate at 35-40 °C for 2h. The Cu₂S counter electrode was obtained by immersing a brass foil in a 37 % HCl solution at 75 °C for 10 min. The foil was then vulcanized by immersion in a polysulfide electrolyte solution for 10 min to generate the active Cu₂S. The polysulfide electrolyte solution composed of 2.0 M sodium sulfide, 2.0 M sulfur, 0.2 M sodium hydroxide in distilled water and methanol (3:7, V/V) was injected into the cell. The QDs-sensitized TiO₂ film photoanode and the as-prepared Cu₂S counter electrode were sandwiched together with a Teflon spacer (25 μm thickness) for the fabrication of QDSCs. Devices were then clamped for functional performance analysis. For each type of QDSCs, at least three samples were prepared and evaluated in parallel.

The fabrication of QDSCs sensitized by water-soluble QDs is described below. TiO₂/QDs anode preparation is performed with the dip method. Specifically, TGA-capped water-soluble QDs were deposited on the mesoporous TiO₂ film by dropping 40 μL water-soluble QDs solution on a mesoporous TiO₂ film and then stored in a refrigerator (4 °C) for 3 h. Following rinsing in water and ethanol, the photoanodes were subsequently treated and QDSCs were assembled in the same way as described in the experimental section for the fabrication of QDSCs sensitized by oil-soluble QDs.

3.1.3 Characterization

Materials characterization. The morphology of the Cd-PbS QDs was characterized using a JEOL 2100F TEM. The composition of the films was measured on a freshly cleaved cross-section of the photoanode, imaging by FE-SEM using a JEOL JSM-6300F FE-SEM equipped with an EDS. Absorption spectra were acquired with a Cary 5000 UV–visible–NIR spectrophotometer (Varian) with a scan speed of 600 nm min⁻¹. The Cd/Pb ratio was measured by using ICP-OES (PerkinElmer Model Optima 7300 DV).

Device characterization. The PEC performance of the photoanode was evaluated in the three-electrode configuration described above, using a CHI 760D electrochemical workstation. The potential during electrochemical measurement was converted to the RHE scale according to the equation $V_{\text{RHE}} = V_{\text{Ag/AgCl}} + 0.197 + \text{pH} \times 0.059$.^{137, 138} The measurement was carried out at AM 1.5G with intensity 100 mW·cm⁻². A silicon reference diode (Sciencetech) was used to adjust the distance between the photoanode and solar simulator before each measurement to guarantee the standard one sun illumination on the photoanode. The typical distance from sun simulator to the PEC cell is ~20 cm. The J-V characteristics of the QDSCs were measured using a digital Keithley as source meter under one sun simulated sunlight calibrated with the silicon reference diode. Transient photovoltage decay measurements were carried out by one sun simulated illumination as a light source to illuminate the devices to V_{oc}, then the light was shut down and

the V_{OC} decay was recorded. The transient V_{OC} values continuously decrease with time from V_{OC} to nearly 0 V in dark. The EIS measurements were carried out under dark condition using a SOLARTRON 1260 A Impedance/Gain-Phase Analyzer and SOLARTRON 1287 at forward bias ranging from 0 to 650 mV over the frequency range of 10^{-3} Hz to 300 kHz with applied AC amplitude of 10 mV.

3.2 Results and discussion

Hendricks *et al.* reported PbS QDs synthetic route by involving a series of substituted thioureas as sulfur precursor instead of the “traditional” $(TMS)_2S$, which is toxic and expensive. The new procedure also increased the extent of crystal nucleation by exploiting the conversion kinetics of thiourea, which is faster.¹³⁰ However, in the synthetic route of PbS nanocrystals, a complex reaction was performed with the assistance of a glove box to prepare lead precursors. For example, a complex reaction was conducted for the synthesis of lead precursor (powder lead oleate). At the moment a glove box environment is needed to handle air-sensitive chemicals (*e.g.*, trifluoroacetic anhydride and trifluoroacetic acid) for this type of synthesis. In addition, several air-sensitive chemicals were used, which should be stored and handled in an inert atmosphere. Here, the synthetic route was modified by replacing the air-sensitive chemicals. Specifically, the optimized synthetic route was based on lead acetate as the lead source. This can be easily obtained and without using a glove box. On the other hand, OAc was used directly to react with lead acetate to prepare the precursor solution, other than to prepare lead oleate powder.¹³⁰ The overall synthetic methodology avoided toxic $(TMS)_2S$ while applying a facile approach for lead precursors. The yield of PbS QDs is up to 140 mg for one batch.

3.2.1 Morphological, structural and optical properties

The as-synthesized PbS QDs present well-controlled absorption peaks and narrow size distributions (Figure 3.1). The QDs show the typical first absorption excitonic peak ranging from

870 up to 1400 nm by simple variation of the reaction parameters, such as reaction time, injection temperature, *etc.* The representative TEM images of corresponding PbS QDs are shown in Figure 3.1a-e. The average sizes measured from TEM images are 3.0, 3.2, 3.7, 4.1 and 5.1 nm, respectively, which is consistent with the gradually red shift of absorption peaks shown in Figure 3.1f.

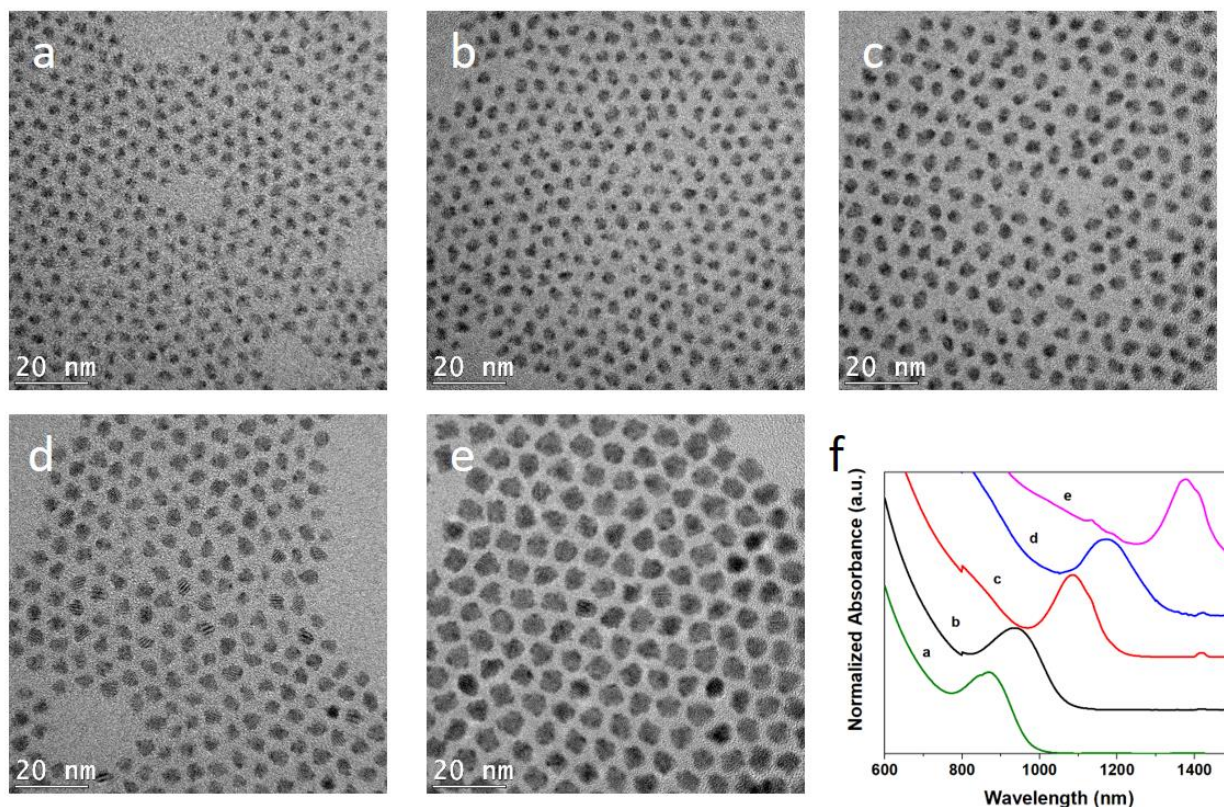


Figure 3.1 TEM images for different sizes of the as-synthesized QDs by controlling injection temperature and reaction time with size ranging from 3.0 to 5.1 nm: (a) 95 °C and 2 min, (b) 100 °C and 5 min, (c) 105 °C and 5 min, (d) 110 °C and 1 min and (e) 115 °C and 1 min. (f) The corresponding absorption spectra of PbS QDs.

After synthesis, the applicability of the prepared QDs in PEC cells and QDSCs was explored. Two types of similar size of PbS QDs (3.0 ± 0.3 nm in diameter) synthesized from sulfur precursor of thiourea and $(\text{TMS})_2\text{S}$ were chosen for comparison. However, colloidal PbS QDs capped with pure organic ligand shells suffer from surface oxidation which has an adverse effect during the

fabrication of solar energy devices in air atmosphere. Cd post-treatment was implemented before device fabrication since a thin CdS layer can protect the PbS core from surface oxidation during photoanode fabrication in ambient conditions.¹⁰² Figure 3.2a-b display representative TEM images of the morphology of Cd-PbS QDs obtained from $(\text{TMS})_2\text{S}$ and thiourea, respectively, indicating that the sizes of both types of Cd-PbS nanocrystals are very uniform. The epitaxial CdS layer is difficult to image by TEM because of the very similar crystalline structure and lattice constant of CdS and PbS.¹⁰² HR-TEM images in the inset of Figure 3.2a-b show crystal lattice fringes with spacing of 0.34 nm, corresponding to the interplanar distance of the (111) planes of rock-salt lead sulfide. The size distributions of colloidal Cd-PbS QDs obtained from $(\text{TMS})_2\text{S}$ and thiourea are displayed in Figure 3.2c-d relative to TEM images, which show that the prepared QDs exhibit a uniform size distribution. Both the QDs obtained from $(\text{TMS})_2\text{S}$ and thiourea have an average diameter of ~ 3.0 nm. The Pb-to-Cd atomic ratio was measured by using ICP-OES for further calculating the shell thickness of CdS layer. Based on this ratio and the overall diameter measured from TEM images, the calculated shell thickness is about 0.2 nm for QDs synthesized using $(\text{TMS})_2\text{S}$ or thiourea.

Figure 3.2e-f report the UV-Visible-NIR absorbance spectra of the as-prepared PbS and Cd-PbS QDs from $(\text{TMS})_2\text{S}$ and thiourea, respectively. The PbS QDs from $(\text{TMS})_2\text{S}$ display an absorption peak at ~ 918 nm, which is located at ~ 875 nm for PbS from thiourea. The blue-shift of the absorption curve after cation exchange is apparent due to the slight decrease of the PbS core size during the replacement of Pb^{2+} by Cd^{2+} .^{123, 139} In Figure 3.2f, the disappearance of the first-excitonic absorption peak for the thiourea sample after Cd treatment is due to the relative broad PbS core size distribution, consistent with the previous report for small-sized PbS/CdS QDs.¹³³

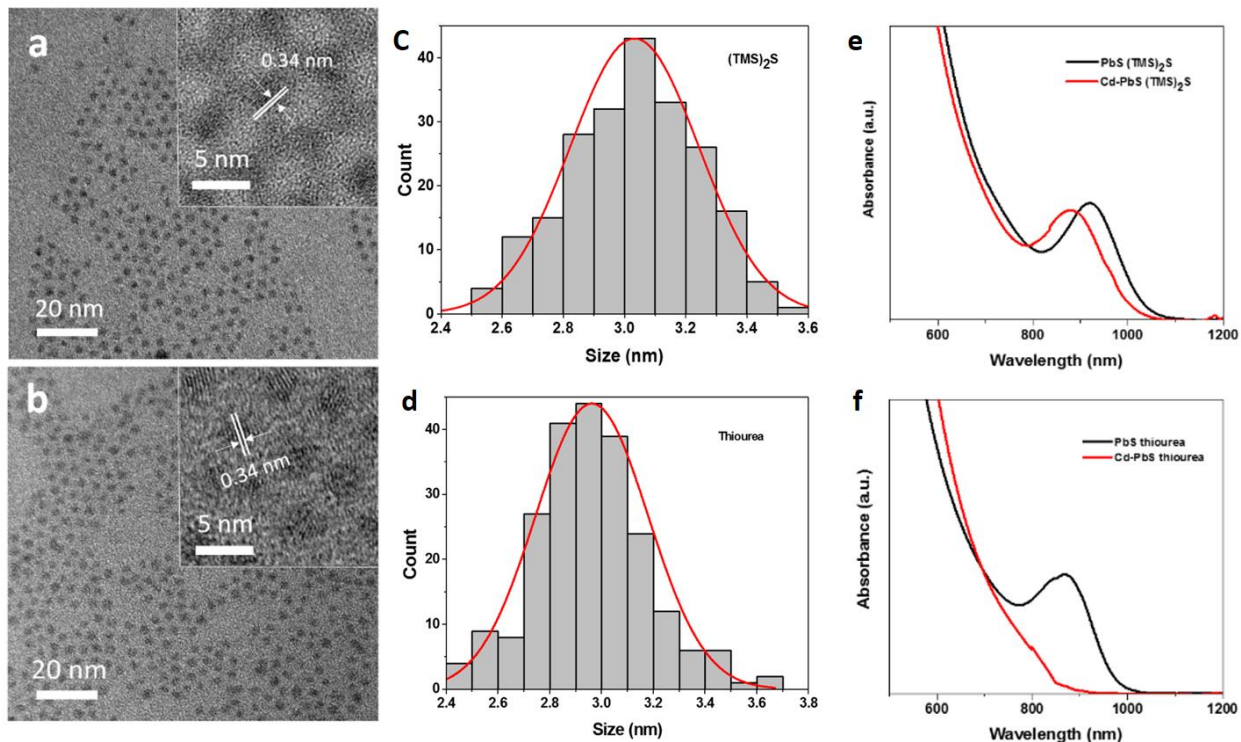


Figure 3.2 Representative TEM images of Cd-PbS QDs from (a) $(\text{TMS})_2\text{S}$ and (b) thiourea. Inset of (a) and (b) is HR-TEM images of two different kinds of QDs. The size distribution of colloidal Cd-PbS QDs from (c) $(\text{TMS})_2\text{S}$ and (d) thiourea. Red lines show the fitting results. Sizes are measured from more than 200 QDs in the TEM images respectively. The absorbance spectra of prepared pure PbS and Cd-PbS QDs from (e) $(\text{TMS})_2\text{S}$ and (f) thiourea.

3.2.2 Quality of photoanode

For both photoanodes in PEC cells and QDSCs, a ZnS layer was coated by SILAR following the QDs tethered on TiO_2 . In the case of PEC cells, electron recombination is suppressed by the ZnS layer coating, which acts as an energy barrier prohibiting photoexcited electron transfer into the electrolyte, thereby increasing the photocurrent.⁸⁸ For QDSCs, charge recombination at the interface of photoanode and electrolyte in devices could be effectively and significantly reduced via the wide band ZnS barrier layer capped around the QDs sensitized photoanode.¹⁴⁰ To further investigate the distribution of QDs tethering on TiO_2 mesoporous film and the ZnS passivation layer on the surface of QDs, cross section analyses of the prepared fresh TiO_2/QDs anode capped with ZnS layer were performed by SEM, EDS 2D mapping and line mapping. Figure 3.3a displays

a cross-sectional SEM image of the QDs on TiO₂ mesoporous film capped with a ZnS layer. Figure 3.3b-i shows the EDS mapping images of different elements, indicating the presence of Ti, O, Si, Sn, Cd, Zn, Pb and S elements and the homogeneous distribution of the adsorbed QDs and ZnS layer in the mesoporous TiO₂ film. Si and Sn are from glass and FTO, respectively. Figure 3.3j displays the EDS spectra, in which the semi-quantified element weight percentage is labeled. Figure 3.3k reports the EDS line mapping presenting the relative weight ratio of elements along the blue highlighted line in Figure 3.3a which comprises both glass/FTO substrate (initial 1.5 μm) and photoanode (remaining 13.5 μm). The Cd-PbS QDs are distributed homogeneously on the TiO₂ film, resulting in high-quality TiO₂/QDs anodes.

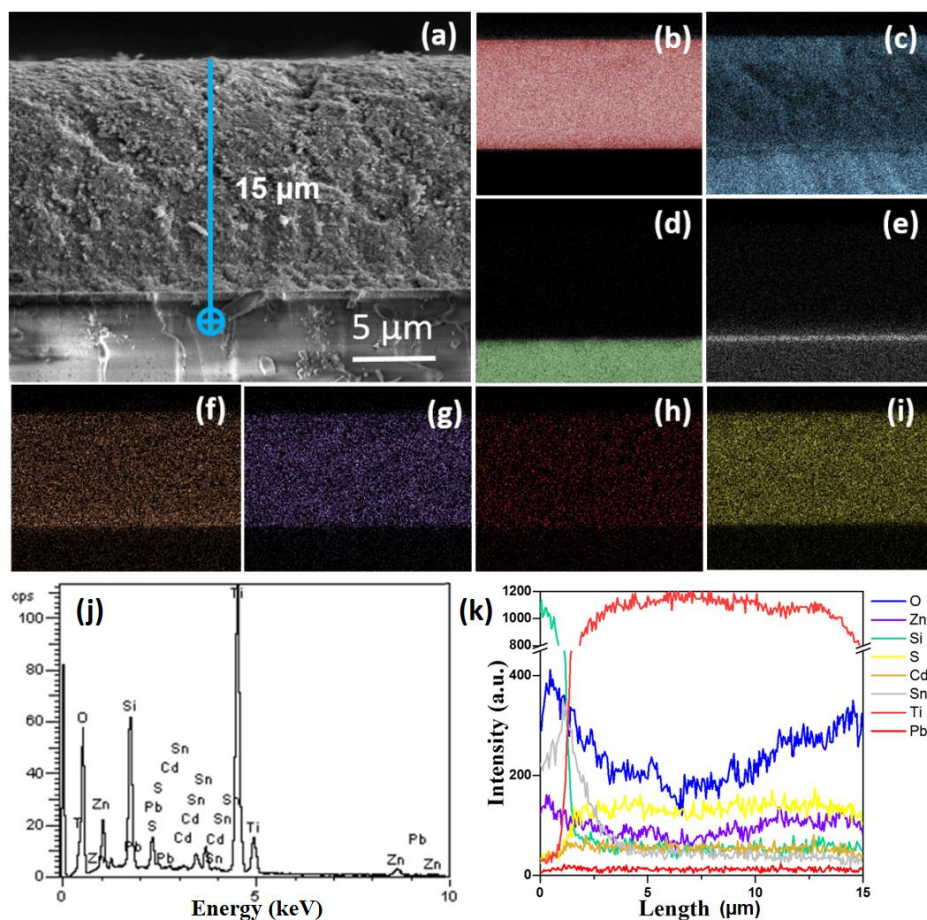


Figure 3.3 (a) Representative SEM cross-sectional image of TiO₂/QDs photoanode capped with ZnS, (b-i) EDS 2D mapping: the elements distribution of (b) Ti, (c) O, (d) Si, (e) Sn, (f) Cd, (g) Zn, (h) Pb and (i) S; (j) EDS spectra; (k) EDS line mapping.

3.2.3 Properties of PEC cells

The anode was then used to fabricate PEC cells for solar-driven H₂ generation. The schematic illustration of PEC cells with the prepared QDs as light harvesters is shown in Figure 3.4. Under illumination, the QDs generate excitons after absorption of photons with energy larger than its bandgap. Photoexcited exciton dissociation occurs at the QDs/TiO₂ interface, and the electrons that were photoexcited in the CB of the QDs can be effectively injected into the CB of TiO₂. Electron transport occurs in the TiO₂ mesoporous film and charges are collected by the FTO film, then transferred to the Pt counter electrode, where H₂ generation takes place.¹⁴¹ Na₂S and Na₂SO₃ hole scavengers in the electrolyte provide a shuttle for the photoexcited holes.^{66, 108, 142}

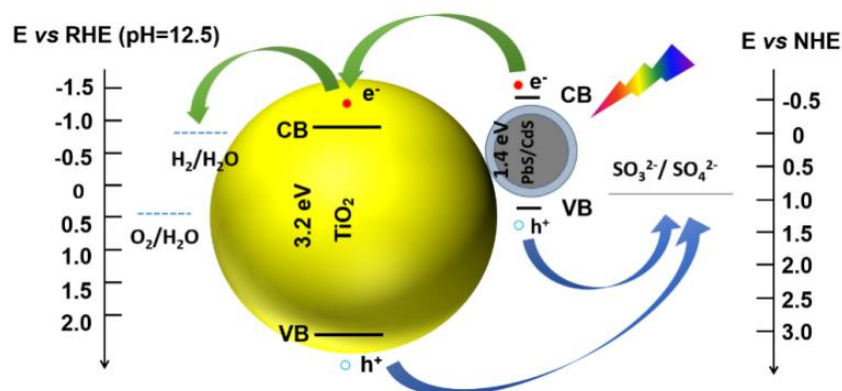


Figure 3.4 Schematic illustration of PEC cells with the prepared QDs as light harvesters. Energy levels (at pH=12.5) of TiO₂,¹⁴³ prepared QDs (3 nm in diameter),^{123, 144} related characteristic redox potentials.¹⁴⁵ The arrows indicate the electrons and holes transfer process.

PEC solar-driven H₂ generation was carried out in a three-electrode system under 100 mW/cm² AM 1.5G illumination in 0.25 M Na₂S and 0.35 M Na₂SO₃ (pH=12.5) aqueous solution (shown in Figure 3.5a). A set of linear-sweep voltammograms were conducted by using different photoanodes in the dark and under simulated solar illumination. Under the light condition, the photocurrent density gradually increases with the increase of voltage before obtaining a saturated photocurrent density. To identify the contribution of bare TiO₂ to the observed efficiency of PEC cells, devices only using TiO₂ as photoanode (without using QDs) were fabricated. The photocurrent density is only 0.3 mA/cm² (see Figure 3.5b). Figure 3.6a-b show the photocurrent

response measured with the PEC cell in the dark condition, in one simulated sunlight illumination condition and under chopped discontinuous one sun simulated sunlight illumination. A saturated photocurrent density of $2.03 \text{ mA}\cdot\text{cm}^{-2}$ was observed for the PEC cell made of QDs from thiourea, which is very similar to that of $(\text{TMS})_2\text{S}$ ($1.97 \text{ mA}/\text{cm}^2$). These values are much higher than those obtained in the PEC cells based on QDs/ TiO_2 system reported above, demonstrating the important role of QDs in enhancing the photocurrent density in PEC cells.

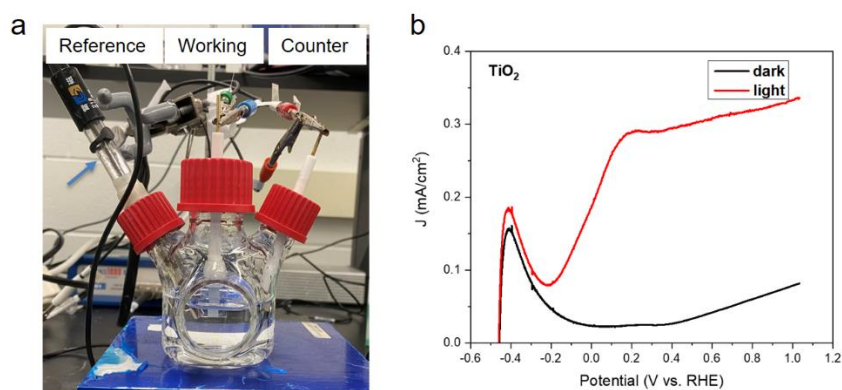


Figure 3.5 (a) A typical photograph of the configuration for PEC measurement, (b) Photocurrent density versus the applied voltage (vs. RHE) curves of PEC devices assembled using bare TiO_2 under one simulated sunlight illumination (AM 1.5G, $100 \text{ mW}\cdot\text{cm}^{-2}$) in the dark (black line) and constant one sunlight illumination (red line).

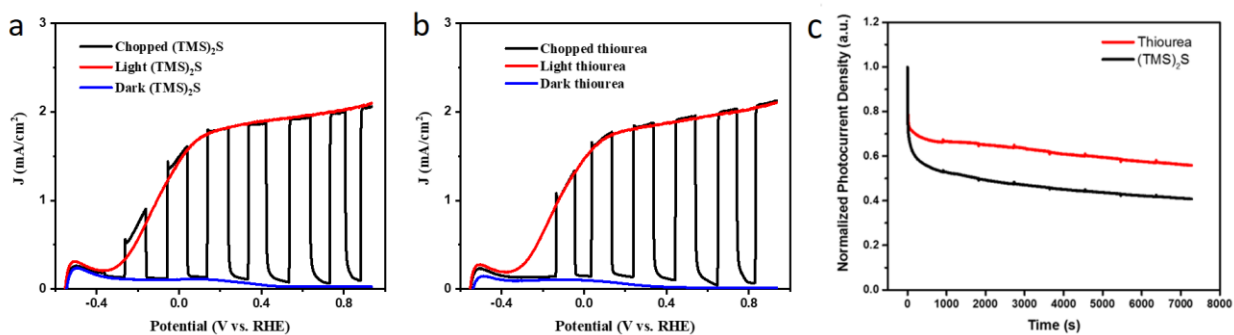


Figure 3.6 Photocurrent density versus the applied voltage (vs. RHE) curves of PEC devices assembled using the as-prepared QDs from (a) $(\text{TMS})_2\text{S}$ and (b) thiourea respectively under one simulated sunlight illumination (AM 1.5G, $100 \text{ mW}\cdot\text{cm}^{-2}$) in the dark (blue line) under chopped (black line) and constant one sunlight illumination (red line), (c) Measured current density as a function of time for the devices of PbS QDs from $(\text{TMS})_2\text{S}$ and thiourea at 0.4 V versus RHE under $100 \text{ mW}\cdot\text{cm}^{-2}$ illumination with AM 1.5G filter.

The stability of the PEC cells was carried out in a three-electrode system. A photocurrent density as a function of time in the PEC system at 0.4 V vs. RHE is shown in Figure 3.6c. For the photoanode based on PbS QDs synthesized via thiourea, the photocurrent density gradually decreased. After 2 h illumination under one sun (100 mW/cm^2), the photocurrent density still maintains 56% of its initial value. In the photoanode based on PbS QDs synthesized via $(\text{TMS})_2\text{S}$, the photocurrent density decreased rapidly in the first 5 minutes and then gradually decreased during 2 h illumination. After 2 h, the current density decreases to 41% of its initial value. The results demonstrate that the as-prepared PbS QDs synthesized from sulfur precursor of thiourea are suitable for application in PEC cells for H_2 generation.

3.2.4 Properties of QDSCs

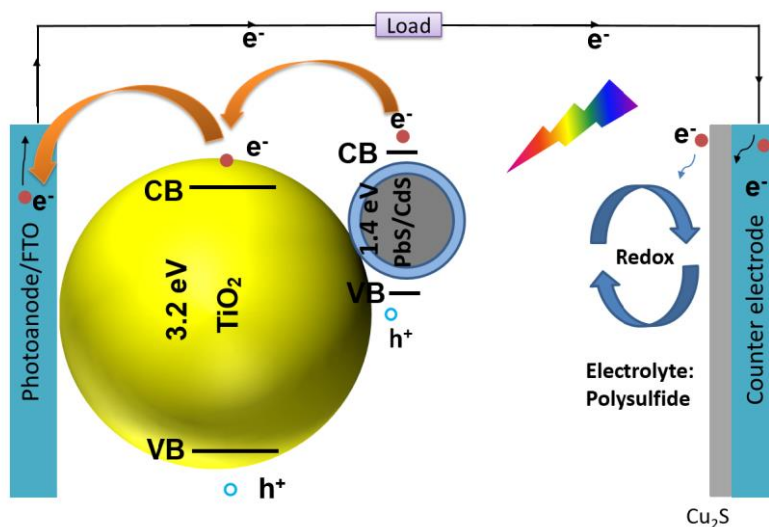


Figure 3.7 Schematic illustration of QDSCs with the prepared QDs as sensitizer for photoanode and Cu_2S as the counter electrode.

In a separate set of experiments, the QDs obtained by different sulfur precursors were employed as sensitizers for application in QDSCs. Figure 3.7 illustrates the operating mechanism of QDSCs based on the as-prepared QDs sensitized TiO_2 mesoporous film as the photoanode, $\text{S}^{2-}/\text{S}_n^{2-}$ redox couple as the electrolyte and Cu_2S as the counter electrode. Under one sun illumination,

photoexcited excitons yield at the interface between QDs and TiO_2 , QDs and $\text{S}^{2-}/\text{S}_n^{2-}$ redox couple electrolyte. The electrons are injected from the CB of QDs to the CB of TiO_2 and then transport to the external circuit, while holes in VB of QDs are collected by the electrolyte. Electrons finally reach the counter electrode to participate in the reduction reaction of the counter electrode and electrolyte interface.¹⁴⁶

To identify the contribution of bare TiO_2 to the observed PCE of QDSCs, devices by using bare TiO_2 as photoanode material (without sensitizing with QDs) were fabricated. The J - V curves of QDSCs sensitized by bare TiO_2 are shown in Figure 3.8. The device yields a J_{sc} of 0.293 mA/cm^2 , V_{oc} of 0.184 V , FF of 0.427 and exhibits a PCE of only 0.023% .

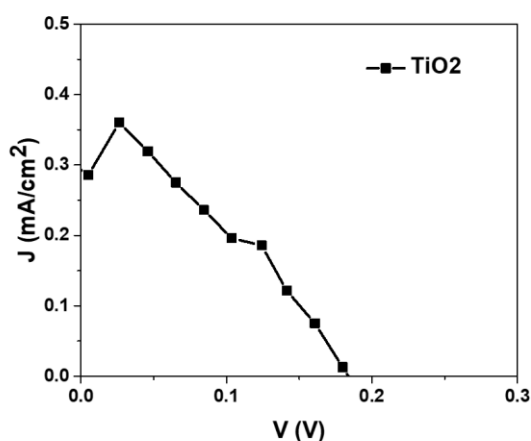


Figure 3.8 J - V curves of devices with only TiO_2 as light harvester under one simulated sunlight. The current density versus voltage (J - V) curves of fabricated QDSCs are shown in Figure 3.9a and the corresponding functional parameters are reported in Table 3.1. The device based on QDs synthesized via thiourea yields a J_{sc} of 7.84 mA/cm^2 , V_{oc} of 0.52 V , FF of 0.49 and PCE of 2.00% , showing an overall better photovoltaic (PV) performance compared to the device sensitized by QDs based on $(\text{TMS})_2\text{S}$ with J_{sc} of 6.95 mA/cm^2 , V_{oc} of 0.48 V , FF of 0.42 and PCE of 1.40% , respectively. However, these values are significantly higher as compared to the PCE of 0.023% obtained from devices based on only TiO_2 (see Figure 3.8) as light harvester. This demonstrates the promising role of QDs as sensitizers, to increase the PCE of QDSCs.

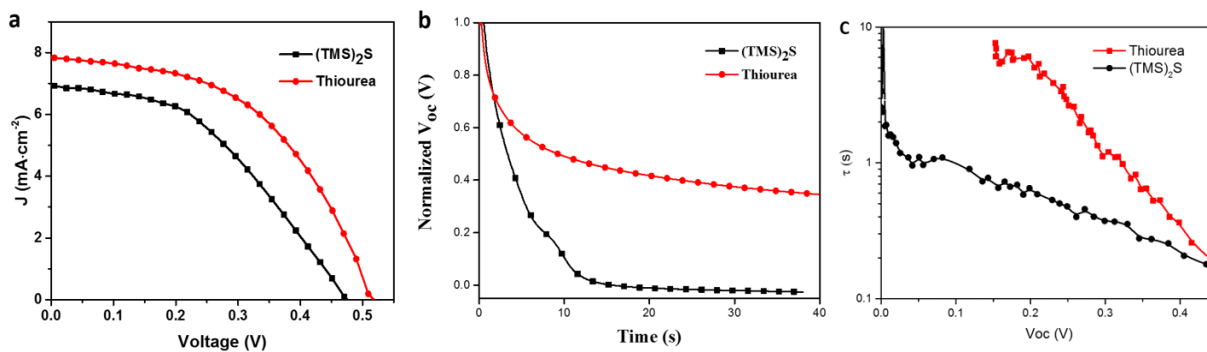


Figure 3.9 (a) J - V curves of QDSCs sensitized by the as-prepared QDs from sulfur precursors of thiourea and (TMS)₂S respectively, under one simulated sunlight, (b) Transient photovoltage decay measurements of corresponding QDSCs, (c) Extracted electron lifetime as a function of V_{oc} .

Table 3.1 Functional parameters of QDSCs sensitized with QDs from different sulfur precursors.

| QDs from different sulfur precursor | J_{sc} (mA/cm ²) | V_{oc} (V) | FF | PCE (%) |
|-------------------------------------|--------------------------------|---------------------|---------------------|---------------------|
| (TMS) ₂ S | 6.95 (± 0.08) | 0.48 (± 0.05) | 0.42 (± 0.03) | 1.40 (± 0.03) |
| Thiourea | 7.84 (± 0.16) | 0.52 (± 0.04) | 0.49 (± 0.01) | 2.00 (± 0.07) |

The measurements of transient photovoltage decay were carried out to investigate more details about the carrier dynamics in devices based on QDs synthesized using different sulfur precursors. In this measurement, both devices were illuminated under one sun simulated sunlight (100 mW·cm⁻²) until reaching a steady voltage (V_{oc} of the device) and then sun-simulator shutter was closed and the voltage decay rate of the device was measured and recorded under dark conditions. Figure 3.9b shows the systematic comparison of the transient photovoltage decay of devices based on QDs synthesized by using different sulfur precursors. The results displayed that the device fabricated with QDs from (TMS)₂S reveals a rapid drop of photovoltage with respect to the device fabricated with QDs from thiourea. Results show that carrier recombination is higher in the former device at the QDs/TiO₂ interface as compared to the latter one. The electron lifetime (τ) values were derived from the V_{oc} decay measurement using the following equation: ¹⁰¹

$$\tau = -\left(\frac{k_b T}{e}\right) \left(\frac{dV_{oc}}{dt}\right)^{-1} \quad (18)$$

where k_b is Boltzmann's constant, e is the electronic charge, and T is the absolute temperature.

Figure 3.9c shows that the electron lifetime is higher for the device based on QDs from thiourea as compared to the device based QDs from $(TMS)_2S$, which is consistent with the obtained PV performance of the respective devices. At a particular value of V_{oc} (~ 0.25 V), the calculated electron lifetime values for the device based on QDs from thiourea is almost double as compared to the device based on QDs from $(TMS)_2S$. These results confirmed that the QDs-thiourea device has reduced non-radiative carrier recombination at the QDs/ TiO_2 /electrolyte interface due to fewer surface traps in the respective QDs as compared to its counter-part QDs based on $(TMS)_2S$. As these surface trap-states act as active sites for recombination during device operation, the overall functional performance of the device degrades.

Table 3.2 Functional performances of QDSCs sensitized with QDs of 3.2 ± 0.3 nm size from different sulfur precursors.

| QDs from different sulfur precursor | J_{sc} (mA/cm ²) | V_{oc} (V) | FF | PCE (%) |
|-------------------------------------|--------------------------------|---------------------|---------------------|---------------------|
| $(TMS)_2S$ | 5.50 (± 0.10) | 0.38 (± 0.07) | 0.46 (± 0.08) | 0.96 (± 0.06) |
| Thiourea | 5.35 (± 0.12) | 0.40 (± 0.05) | 0.53 (± 0.05) | 1.14 (± 0.08) |

The QDSCs were also fabricated by using QDs with an overall size of ~ 3.2 nm and shell thickness of ~ 0.2 nm, produced using either thiourea or $(TMS)_2S$ as precursors. The results further confirm that the QDSCs using QDs synthesized via thiourea exhibit better performance compared to that of QDSCs using QDs produced by $(TMS)_2S$. The J - V curves are shown in Figure 3.10 and the corresponding functional parameters are reported in Table 3.2.

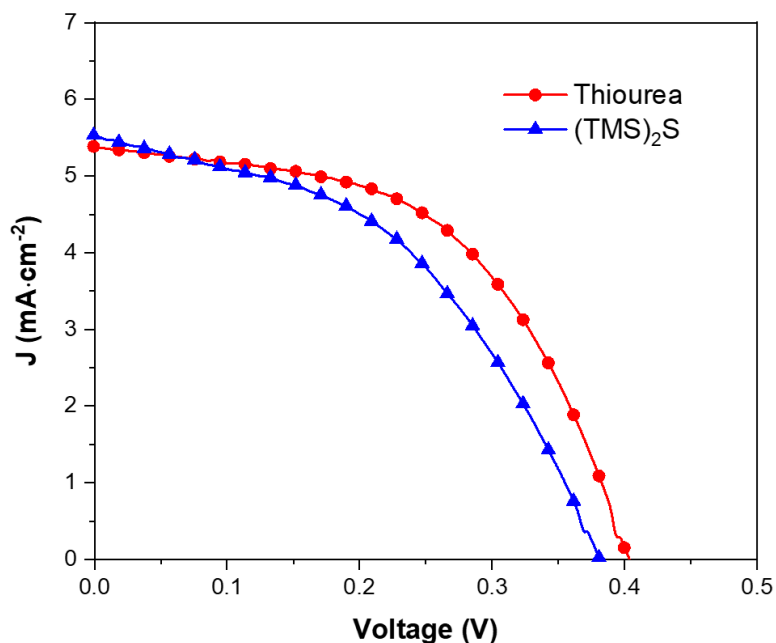


Figure 3.10 J - V curves of QDSCs which sensitized by prepared QDs with similar overall size of 3.2 nm and shell thickness of 0.2 nm from different sulfur precursors under one simulated sunlight.

To further improve the PCE of QDSCs, the oil-soluble QDs were transferred into water (the method is described in the experiment section). The J - V curves of QDSCs sensitized by water-soluble QDs are shown in Figure 3.11 and the corresponding functional parameters are reported in Table 3.3. The device based on water-soluble QDs yields a J_{sc} of 10.72 mA/cm², V_{oc} of 0.55 V, FF of 0.50 and PCE of 2.95%, demonstrating better functional performance compared with the device sensitized by oil-soluble QDs.

Table 3.3 Functional performances of QDSCs sensitized with oil-soluble and water-soluble QDs from sulfur precursor of thiourea.

| QDs | J_{sc} (mA/cm ²) | V_{oc} (V) | FF | PCE (%) |
|---------------|--------------------------------|--------------------|--------------------|--------------------|
| Oil-soluble | 7.84 (\pm 0.16) | 0.52 (\pm 0.04) | 0.49 (\pm 0.01) | 2.00 (\pm 0.07) |
| Water-soluble | 7.96 (\pm 0.04) | 0.60 (\pm 0.06) | 0.62 (\pm 0.03) | 2.95 (\pm 0.03) |

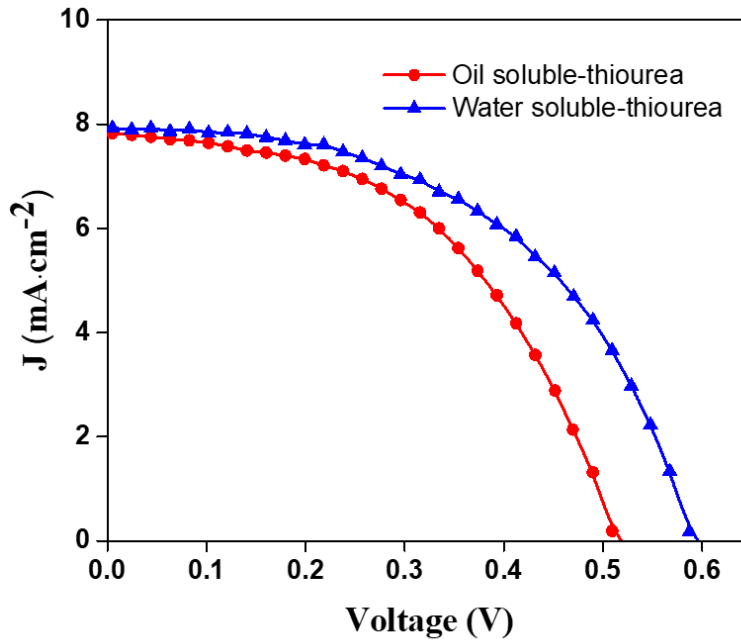


Figure 3.11 J - V curves of QDSCs which sensitized by prepared oil-soluble and water-soluble QDs from sulfur precursor of thiourea under one simulated sunlight.

EIS characterizations (Figure 3.12) were also carried out to investigate the carrier recombination for the devices sensitized with QDs from thiourea and $(\text{TMS})_2\text{S}$, respectively.

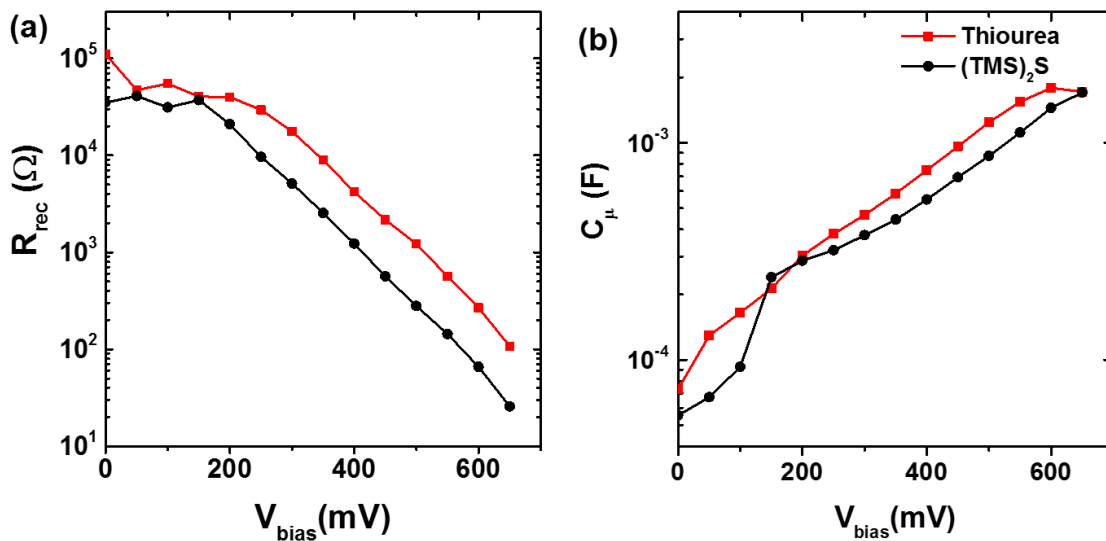


Figure 3.12 EIS of representative samples of devices sensitized with QDs from thiourea and $(\text{TMS})_2\text{S}$. (a) Recombination resistance, (b) chemical capacitance.

EIS characterization was carried out for further understanding the carrier recombination and transport for devices fabricated with QDs from thiourea and $(\text{TMS})_2\text{S}$. The recombination resistance (R_{rec}) considers recombination phenomena occurring at the photoanode/electrolyte interfaces.^{147, 148} Figure 3.12a shows the dependence of R_{rec} on the forward bias applied to the devices. For the whole range of V_{bias} , the values of R_{rec} for the devices sensitized with QDs from thiourea are higher than those made with QDs from $(\text{TMS})_2\text{S}$. As the R_{rec} is inversely proportional to the carrier recombination rate, the significantly improved R_{rec} value for devices fabricated with QDs from thiourea implies that the carrier recombination rate is significantly suppressed, boosting the injection of electrons in photoanode. This observation is in good agreement with the device's functional performance (as shown in Table 3.1) and also consistent with electron lifetime results, reported in Figure 3.9c. The chemical capacitance (C_{μ}) stands for the variation of electron density in the band gap of the TiO_2 matrix.¹⁴⁷ As shown in Figure 3.12b, similar C_{μ} values of both devices are observed, indicating that the different QDs sensitizers do not affect the CB edge position of TiO_2 .^{90, 148, 149}

3.3 Conclusions

A simple approach was designed to synthesize NIR colloidal PbS QDs by using lead acetate and thiourea as lead and sulfide sources, respectively. By adjusting the reaction parameters, the size-tunable NIR PbS QDs (with absorption excitonic peaks from 870 to 1400 nm) were obtained with narrow size distribution (<10%). Further Cd post-treatment was conducted to generate a passivating layer to improve the stability of the QDs. The as-prepared QDs were employed for application in both solar-driven H_2 generation and QDSCs. Under identical measurement conditions, the as-prepared devices using thiourea as new inexpensive and air-stable precursor show comparable or better performance with respect to QDs synthesized using the commonly used toxic and air-sensitive $(\text{TMS})_2\text{S}$ precursor. This work provides a simple methodology for PbS QDs synthesis and holds potential and promising applications in PbS QDs based optoelectronic

devices, such as solar cells, PEC solar-driven H₂ production cells, photodetectors, sensors, light-emitting devices, luminescent solar concentrators, *etc.*

Chapter 4. Near-infrared colloidal manganese doped quantum dots: photoluminescence mechanism and temperature response

The optical properties of QDs can be tunable by not only changing size (as described in Chapter 3) or designing core/shell structure but also introducing dopant (such as Mn, Cu and Ag). Mn dopant was reported to have the possibility to enlarge the Stokes shift and obtain long-lived charge carriers, which make it suitable for application in some QD-based devices. In this chapter, the synthesis of oil-soluble small-sized Mn-doped PbS QDs in organic phase was reported with uniform size distribution and well-controlled Mn content. The optical, magnetic properties, including absorption, PL, PL decay and EPR spectra of the colloidal QDs, have been studied for Mn-doped PbS QDs with identical size ($\sim 2.8 \pm 0.4$ nm in diameter) and different Mn content of 0.00%, 0.70% and 1.66% (given in molar concentration). The absorption peaks remain similar for PbS and Mn-doped PbS QDs, whereas the PL peaks reveal a significantly red shift after the incorporation of Mn, resulting in larger Stokes shifts compared to that in pure PbS QDs. A schematic illustration was proposed for the PL mechanism in the emission process, which does not correspond to the well-known exciton emission in intrinsic pure QDs nor to the reported d-emission in doped QDs. Subsequently, the PL behavior of as-prepared pure PbS and Mn-doped PbS QDs was studied in the 96–296 K temperature range. The temperature dependence of PL is investigated by exploring both the PL peak energy shifts and the PL intensity variations. The effect of temperature on the PL peak position in Mn-doped PbS QDs exhibits a different behavior compared to that in pure QDs, which is caused by the different emission processes. The device based on Mn-doped PbS QDs was found to be more sensitive to temperature compared to pure PbS QDs, which makes it a potential candidate for application in thermal sensing.

4.1 Experiment section

4.1.1 Synthesis of pure PbS QDs and Mn-doped PbS QDs

The synthetic approach of pure PbS QDs is as similar as the procedures (the synthesis of substituted thiourea and lead oleate) reported in section 3.1.1. For the injection procedure, a mixture of 145.7 mg of as-prepared thiourea and 1.61 g diphenyl ether was heated to 95 °C, then this clear solution was injected quickly into the flask containing lead oleate at 95 °C. After injection, the color of the reaction solution in the flask was observed to change from transparency to black quickly. The solution was maintained at this temperature for one minute. The reaction flask was then cooled down to room temperature by immersing it in cold water. Finally, the QDs were purified with ethanol/acetone (5:1 in volume) and re-dispersed in toluene three times.

The synthesis of Mn-doped PbS QDs was achieved by a hot injection method. In detail, three different doped PbS QDs with different Mn incorporation content were synthesized. The sample synthesized with 432.0 mg $\text{Pb}(\text{CH}_3\text{CO}_2)_2 \cdot 3\text{H}_2\text{O}$, 14.7 mg $\text{Mn}(\text{CH}_3\text{CO}_2)_2 \cdot 4\text{H}_2\text{O}$ was denoted as $\text{Mn}_{0.007}\text{PbS}$ in the following. The sample synthesized with 387 mg $\text{Pb}(\text{CH}_3\text{CO}_2)_2 \cdot 3\text{H}_2\text{O}$, 44.1 mg $\text{Mn}(\text{CH}_3\text{CO}_2)_2 \cdot 4\text{H}_2\text{O}$ was denoted as $\text{Mn}_{0.0115}\text{PbS}$. The sample synthesized with 364.0 mg $\text{Pb}(\text{CH}_3\text{CO}_2)_2 \cdot 3\text{H}_2\text{O}$, 58.8 mg $\text{Mn}(\text{CH}_3\text{CO}_2)_2 \cdot 4\text{H}_2\text{O}$ was denoted as $\text{Mn}_{0.0166}\text{PbS}$. The precursors of Pb, Mn and 0.8 mL OAc were mixed with 18 mL ODE in a 3-neck flask with a stir bar for stirring at 350 rpm and flushed with nitrogen gas flow for 5 minutes, then transferred in oil bath for heating at 160 °C held for 1h. Then thiourea (291.5 mg in 3.22 g diphenyl ether) was injected into the Mn and Pb mixed precursors at 95 °C. The solution was maintained for one minute, then cooled down to room temperature by immersing reaction flask in cold water. Finally, the QDs were purified with ethanol/acetone (5:1 in volume) and re-dispersed in toluene three times.

4.1.2 QDs film preparation

The QDs in toluene solution were mixed with PMMA in chloroform, followed by spin-coating on a glass substrate at 300 rpm for one minute. The concentration of QDs in the mixture solution was ~1 μ M. The concentration of PMMA was 1 wt %.

4.1.3 Characterization

The morphologies of PbS and Mn-doped PbS QDs were characterized by using a JEOL 2100F TEM. The Pb/Mn ratio was measured by using ICP-OES (PerkinElmer Model Optima 7300 DV). SEM and EDS were employed to investigate the elemental analysis of the as-synthesized QDs by using Tescan Vega3 equipment. XRD of extensively purified QDs was performed using a Philips X'pert diffractometer with a Cu K α radiation source ($\lambda = 0.15418$ nm). EPR spectra were collected on an X-band EPR spectrometer (Bruker Elexsys 580 FT/CW EPR console). The modulation frequency was 100 kHz. Measurements at lower temperature (114 K) were performed using liquid nitrogen. The size distribution of QDs was calculated by measuring ~100–200 QDs for each sample and then analyzed by using a Gaussian distribution. Absorption spectra were acquired with a Cary 5000 UV–vis–NIR spectrophotometer (Varian) with a scan speed of 600 nm/min. PL spectra were recorded with a Fluorolog-3 system (Horiba Jobin Yvon) equipped with a temperature controller. The excitation wavelength was set at 450 nm.

The optical properties of pure PbS and Mn-doped PbS QDs were measured in the PMMA matrix by recording the variation of their PL spectra in the 96–296 K temperature range using THMS 600 temperature-controlled stages.

4.2 Results and discussions

4.2.1 Morphological and structural properties

PbS QDs and Mn-doped PbS QDs were synthesized using an organometallic hot injection method in which different contents of Mn (manganese acetate trihydrate) were introduced into the reaction

mixture, to facilitate the incorporation of the Mn atoms during the nucleation and growth of the QDs. Substituted thiourea was used as the sulfur precursor due to its inexpensive and air-stable advantages compared to widely used $(\text{TMS})_2\text{S}$ and higher reaction activity with respect to elemental sulfur precursor.^{118, 130} By controlling the Pb/Mn stoichiometry during the reaction, different concentrations of Mn dopant were introduced in the QDs. Figure 4.1 displays the representative TEM images of PbS, $\text{Mn}_{0.007}\text{PbS}$, $\text{Mn}_{0.0115}\text{PbS}$ and $\text{Mn}_{0.0166}\text{PbS}$ QDs. The as-prepared QDs have a uniform size distribution with an average diameter of approximately 2.8 nm, according to the size distribution curves shown in Figure 4.2. An HR-TEM image is shown in the inset of Figure 4.1. The spacing of crystal lattice fringes is 0.34 nm, which corresponds to the interplanar distance of the (111) plane of PbS. This result confirms the Mn-doped PbS QDs retain a highly crystalline rock-salt structure of bulk lead sulfide.¹⁰² The sizes of pure PbS and Mn-doped PbS QDs as a function of band gap are shown in Figure 4.3 and are consistent with the following empirical equation:^{150, 151}

$$E_g = 0.41 + (0.0252d^2 + 0.283d)^{-1} \quad (18)$$

where E_g is the band gap of PbS QDs as determined by the first-excitonic peak feature in the absorption spectrum and d is the diameter of QDs in nm. This result also indicates that the size of the QDs does not change after the incorporation of Mn, as observed in the TEM micrographs presented in Figure 4.1.

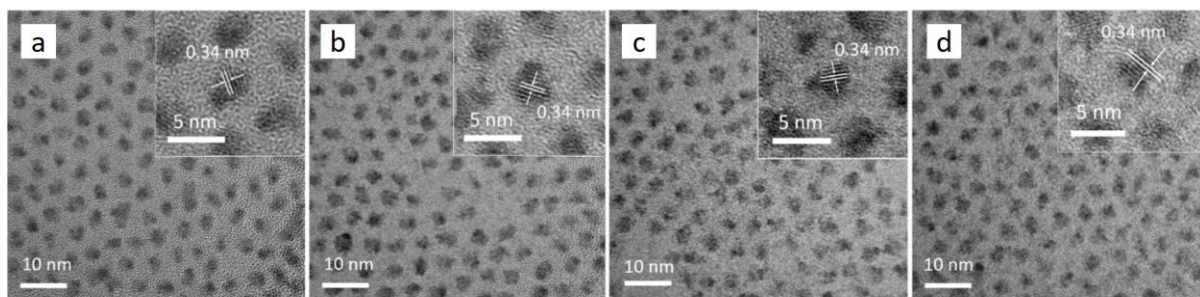


Figure 4.1 Representative TEM images of (a) pure PbS QDs, (b) $\text{Mn}_{0.007}\text{PbS}$, (c) $\text{Mn}_{0.0115}\text{PbS}$ and (d) $\text{Mn}_{0.0166}\text{PbS}$. The inset images are the HR-TEM images of each QDs.

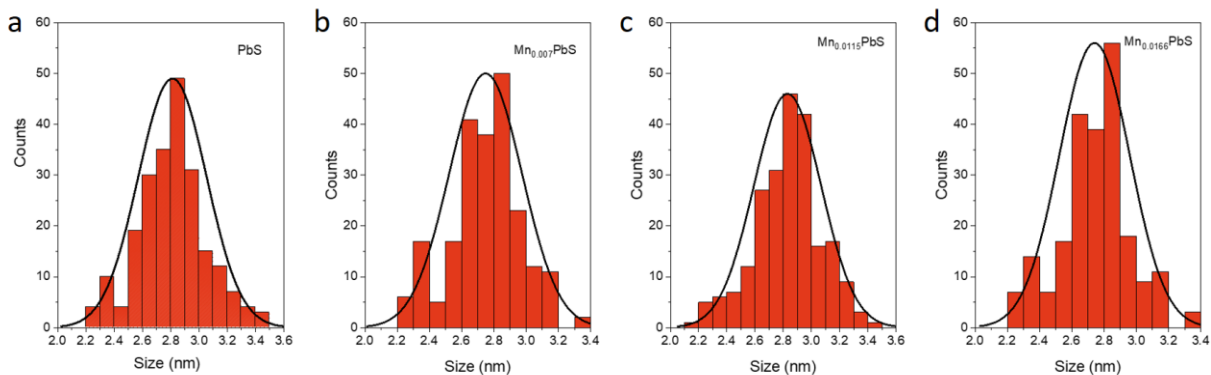


Figure 4.2 Size distributions of (a) PbS QDs, (b) $\text{Mn}_{0.007}\text{PbS}$ sample, (c) $\text{Mn}_{0.0115}\text{PbS}$ sample and (d) $\text{Mn}_{0.0166}\text{PbS}$ sample.

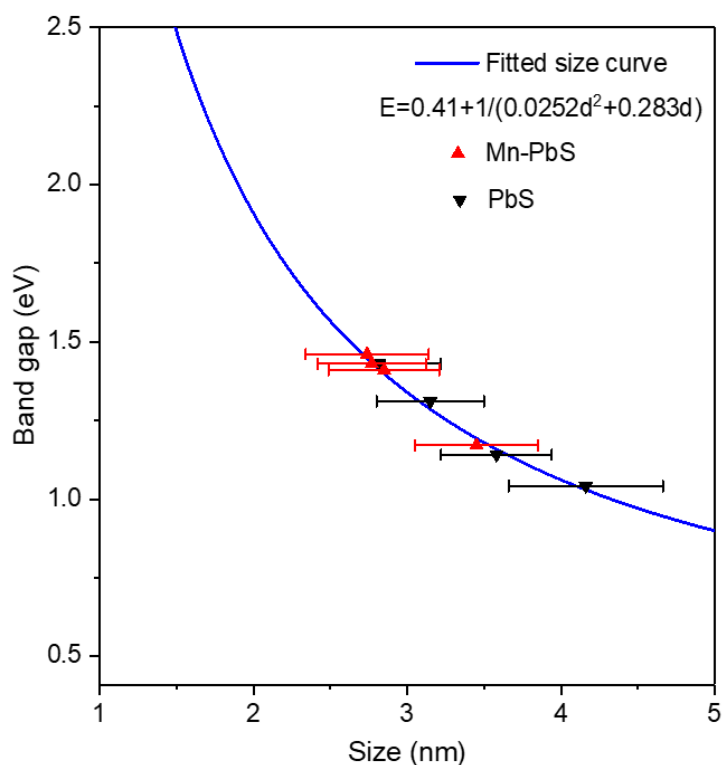


Figure 4.3 Different sizes of PbS and Mn-doped PbS QDs as a function of band gaps.

The molar concentrations of Mn in the synthesized QDs were measured by ICP-OES. As shown in Table 4.1, the measured Mn molar concentrations were 0.00 %, 0.70 %, 1.15 % and 1.66 % in the PbS QDs, $\text{Mn}_{0.007}\text{PbS}$, $\text{Mn}_{0.0115}\text{PbS}$ and $\text{Mn}_{0.0166}\text{PbS}$ samples, respectively. As shown in Figure 4.4, EDS spectra show a characteristic Mn peak at 5.9 keV in $\text{Mn}_{0.0166}\text{PbS}$ and $\text{Mn}_{0.0115}\text{PbS}$

samples. However, no clear Mn peak is observed for $\text{Mn}_{0.007}\text{PbS}$ samples, since the Mn concentration is lower than the detection limit of the instrument. The Mn concentration in the QDs is controlled by tuning the reaction parameters and adjusting the molar feeding ratio of Pb/Mn precursors. To make sure the pure PbS and Mn-doped PbS QDs are similar in size, the same reaction temperature and reaction time was used for each size of them. It was found that further improving the doping concentration of Mn is difficult under the selected reaction parameters.

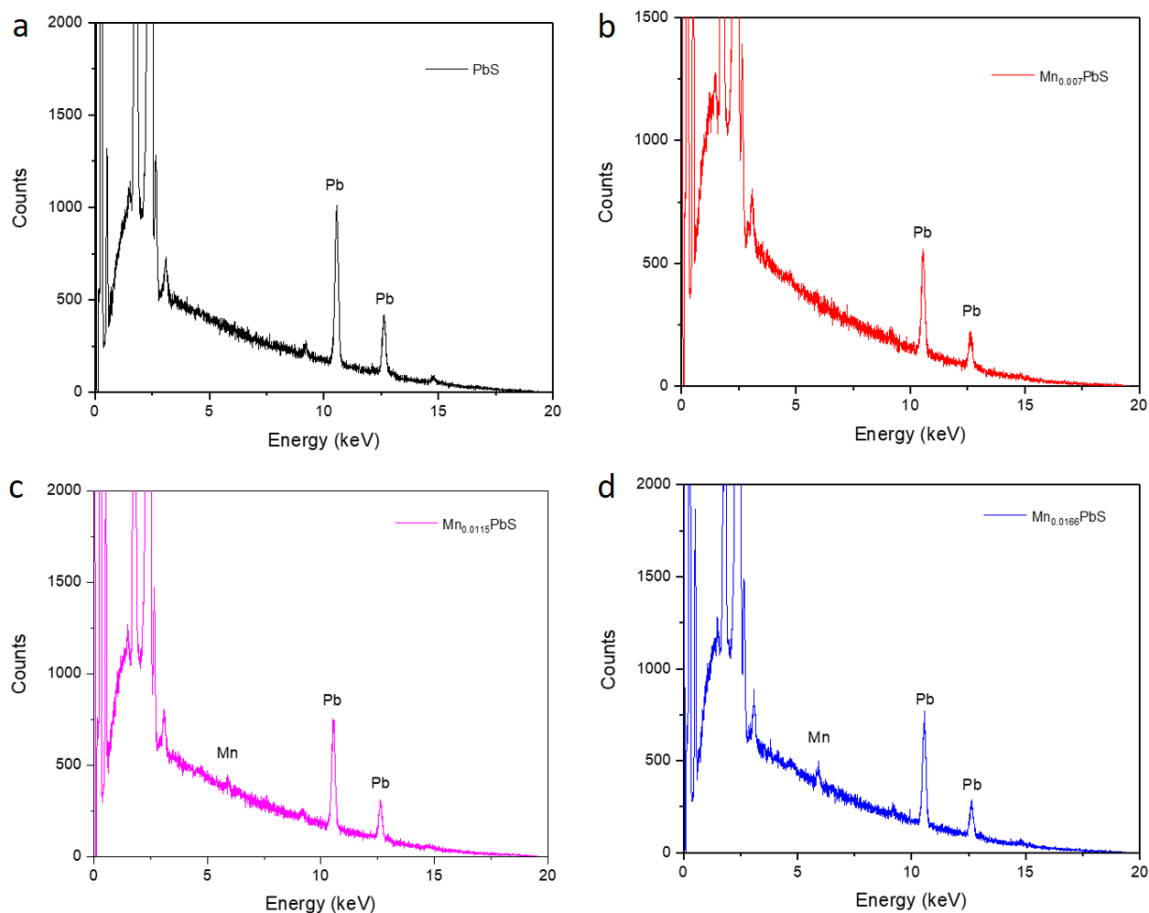


Figure 4.4 EDS spectra of (a) PbS, (b) $\text{Mn}_{0.007}\text{PbS}$, (c) $\text{Mn}_{0.0115}\text{PbS}$ and (d) $\text{Mn}_{0.0166}\text{PbS}$ QDs.

To analyze how many Mn ions are doped into one dot with an average QD size, a simple assumption was made that each dot has a standard spherical shape. The doped Mn ions number in each dot was calculated by using the following equation, $\rho \cdot \frac{4}{3} \cdot \pi R^3 = M^* n_{\text{PbS}} / N_A$, where ρ is the

density of PbS (7.60 g/cm^3), R is the radius of the dot, M is the molar mass of PbS (239.30 g/mol), N_A is the Avogadro constant ($6.02 \times 10^{23} \text{ mol}^{-1}$), n_{PbS} is the average PbS molecule number of one dot. The average Mn atom number of each dot, n_{Mn} , is, therefore, $n_{Mn} = n^* n_{PbS}$, i.e., $n_{Mn} = 4n\rho N_A \pi R^3 / 3M$, where n is the concentration of Mn in each sample. The calculated results show that n_{PbS} is around 220 in the as-prepared QDs with 2.8 nm in diameter. As a result, the average number of Mn ions was estimated as 0, 1.54, 2.53, 3.65 for PbS, $\text{Mn}_{0.007}\text{PbS}$, $\text{Mn}_{0.0115}\text{PbS}$ and $\text{Mn}_{0.0166}\text{PbS}$, respectively.

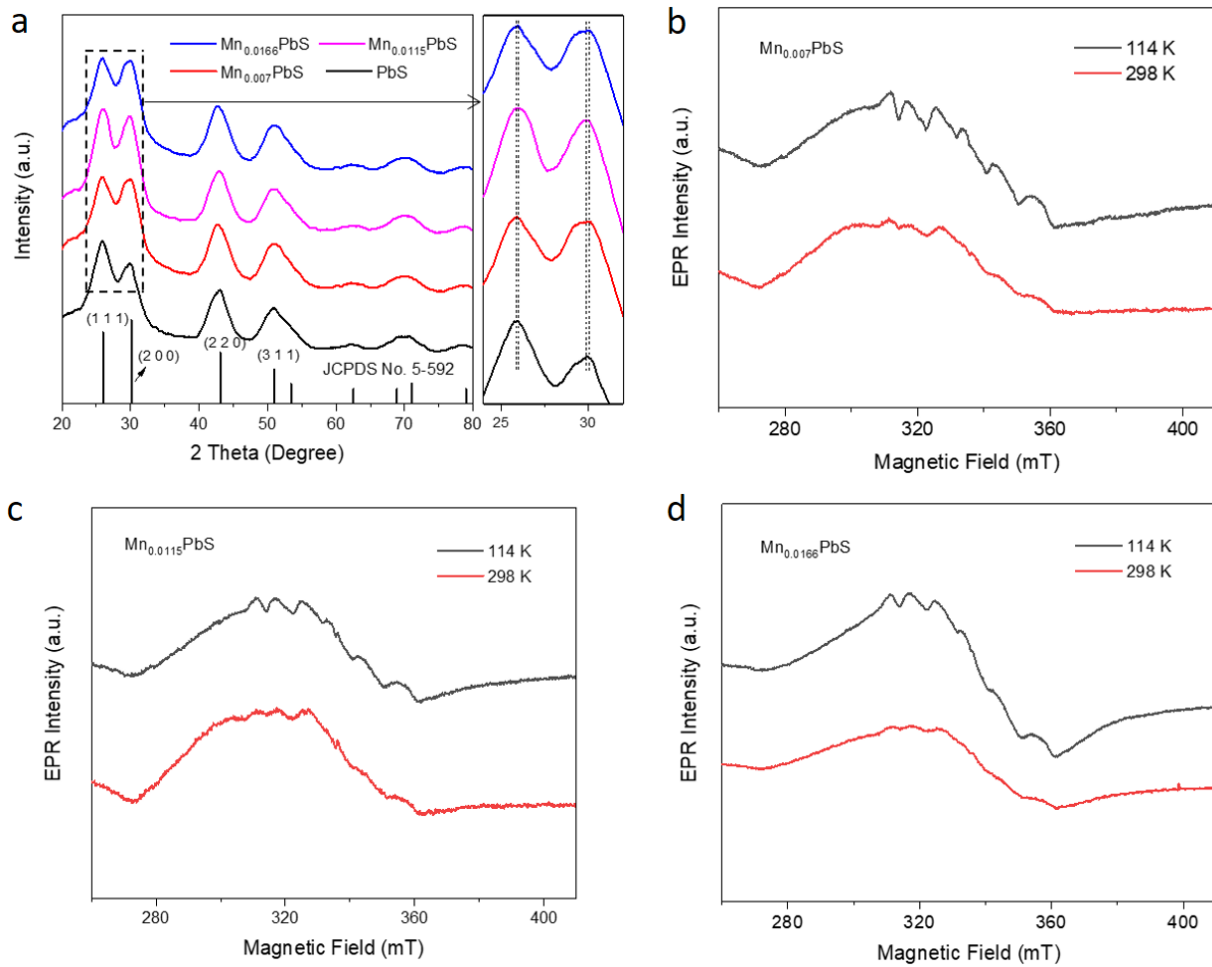


Figure 4.5 (a) XRD spectra of the as-synthesized pure and Mn-doped PbS QDs. The right pattern shows the XRD spectra from 24° to 32° . The JCPDS card data for PbS (No. 05-0592, black line) is shown for identification. EPR spectra of the as-synthesized (b) $\text{Mn}_{0.007}\text{PbS}$ sample, (c) $\text{Mn}_{0.0115}\text{PbS}$ sample and (d) $\text{Mn}_{0.0166}\text{PbS}$ sample at 298 K and 114 K, respectively.

Figure 4.5a shows the XRD patterns of as-synthesized PbS (black) and Mn-PbS samples (red and blue). For pure PbS QDs sample, all the diffraction peaks are indexed to a face centered cubic rock-salt structure of PbS in good agreement with the Joint Committee on Powder Diffraction Standards (JCPDS) No. 05-0592. The peaks with the four highest intensity correspond to (1 1 1), (2 0 0), (2 2 0) and (3 1 1) planes, respectively. The XRD spectra of Mn-doped PbS samples demonstrate similar patterns compared to pure PbS QDs, indicating that the rock-salt crystal structure is still maintained despite the incorporation of Mn ions into QDs.¹⁵² As the Mn ion concentration is very low, the XRD signal from MnS cannot be detected. However, the characteristic peaks show slight shifts toward high diffraction angle values with the incorporation of Mn, as shown in Figure 4.5a (right pattern). This indicates a decrease in the lattice constant due to the substitution of larger Pb ions (133 pm) by smaller dopant Mn ions (97 pm), which is consistent with the previous report.¹⁵³

EPR spectra for pure PbS and Mn-doped PbS QDs containing different Mn ions concentrations were measured at two different temperatures (298 and 114 K). EPR spectroscopy is very sensitive to unpaired electrons and was used to explore the local environment of Mn ions in the doped QDs.¹⁵⁴ For pure PbS QDs, EPR spectra in Figure 4.6 show no noticeable signals at both room temperature and at 114K. In Figure 4.5b-d, all the EPR lines show sextet signals superimposed on a broad background, which is attributed to the hyperfine interaction between *d* electrons. The hyperfine interaction constant (*A*) values are used to indicate the dopant location in Mn-doped nanocrystals.^{60, 155} The EPR spectra lead to *A* values of 9.12, 9.14 and 9.18 mT for Mn_{0.007}PbS, Mn_{0.0115}PbS and Mn_{0.0166}PbS samples respectively. These values are very close to the reported 9.22 mT reported in the literature, corresponding to the surface doped Mn.¹⁵⁶ However, the broad background in the EPR spectra and asymmetric shape of EPR lines suggest that part of Mn ions are also located in the near surface or the core of QDs.^{116, 117, 157} The EPR spectra of Mn_{0.007}PbS, Mn_{0.0115}PbS and Mn_{0.0166}PbS samples (Figure 4.5b-d) clearly show significant six line hyperfine

structures of Mn at 298 K. At low temperature of 114 K, the EPR spectra remain the same, but exhibit obvious peak intensity enhancements compared to that at 298 K. Compared with the three samples, the doped QDs with higher Mn concentration display a decreasing resolution of six peaks in the EPR spectra at each temperature, which can be attributed to increased strength of Mn-Mn dipolar interactions and consistent with the previous report.¹⁵⁴

4.2.2 Optical properties

The optical properties of as-synthesized QDs were investigated by absorption and PL spectroscopy. The normalized absorption and PL spectra of PbS, Mn_{0.007}PbS, Mn_{0.0115}PbS and

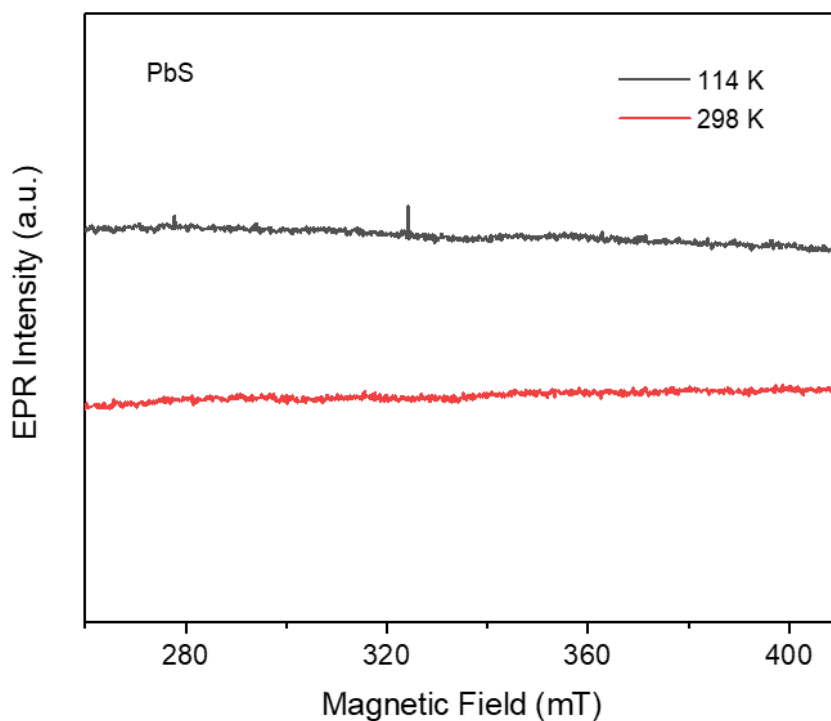


Figure 4.6 EPR spectra of the as-synthesized pure PbS sample at 298 K and 114 K, respectively. Mn_{0.0166}PbS QDs are shown in Figure 4.7a. The absorption spectra show the characteristic PbS QDs absorbance.¹⁵⁸ Similar results were obtained for the absorption spectra of the Mn-doped PbS QDs. With identical first-excitonic absorption peak positions (same size of PbS QDs), PL spectra indicate that the as-prepared PbS and Mn-doped PbS QDs exhibit different PL emissions.

Specifically, as shown in Table 4.1, the absorption peak positions are found to be at 870, 866, 879 and 850 nm for PbS, $\text{Mn}_{0.007}\text{PbS}$, $\text{Mn}_{0.0115}\text{PbS}$ and $\text{Mn}_{0.0166}\text{PbS}$ QDs, respectively. A single PL peak was observed for both PbS, $\text{Mn}_{0.007}\text{PbS}$, $\text{Mn}_{0.0115}\text{PbS}$ and $\text{Mn}_{0.0166}\text{PbS}$ QDs samples, and their corresponding PL peak positions are 1000, 1039, 1052 and 1044 nm, respectively. With similar size, pure PbS QDs reveal a Stokes shift of 180 meV, smaller than the values of 240 meV for $\text{Mn}_{0.007}\text{PbS}$ QDs, 232 meV for $\text{Mn}_{0.0115}\text{PbS}$ and 269 meV for $\text{Mn}_{0.0166}\text{PbS}$, respectively. Hence, it is found that the incorporation of Mn in PbS QDs enlarges the Stokes shift.

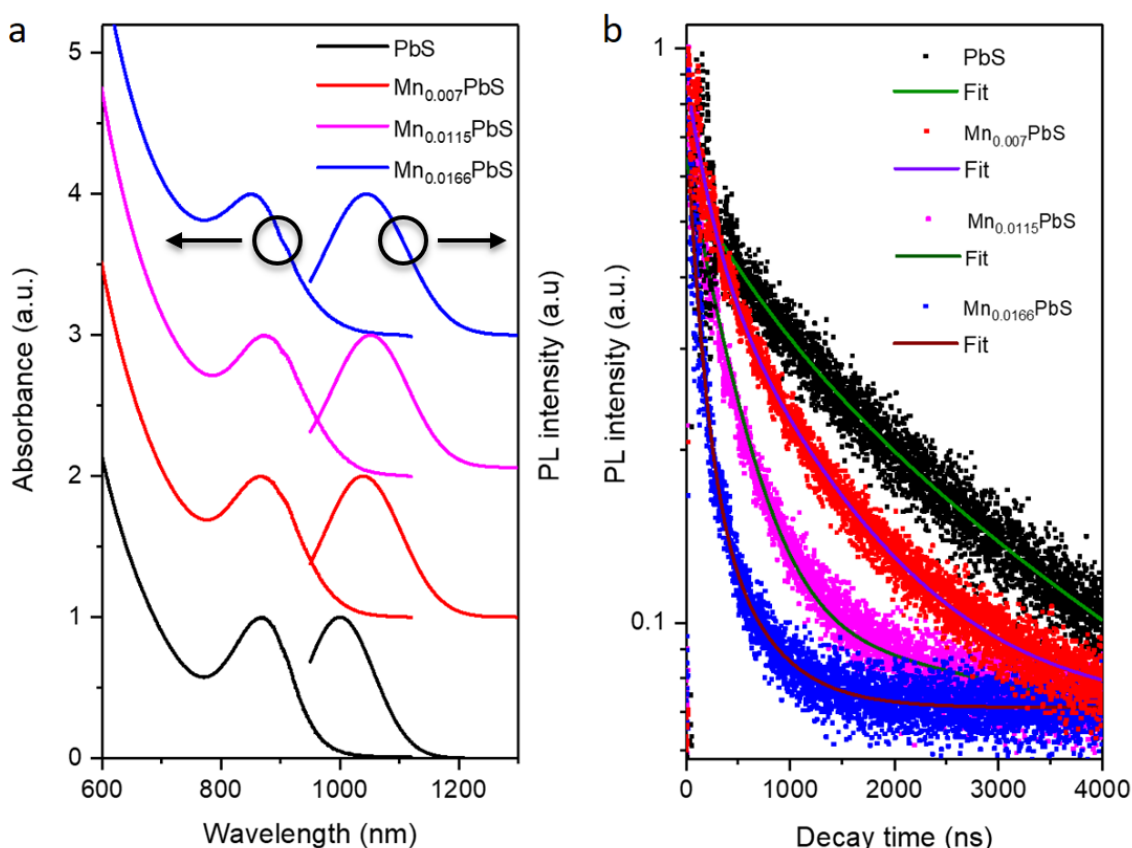


Figure 4.7 Optical properties of PbS QDs and Mn-doped PbS QDs in toluene: (a) absorption and PL spectra. The excitation wavelength is $\lambda_{\text{ex}} = 450$ nm; (b) PL decay curves. The excitation wavelength is $\lambda_{\text{ex}} = 444$ nm.

The TRPL curves are reported in Figure 4.7b. The decay demonstrates that the lifetime continuously decreases with the increase of Mn dopant content. The intensity-weighted average

lifetime (τ) is calculated from the fitting of the PL decay, according to the following equation: ^{88, 93,}

94, 129, 159, 160

$$\tau = \frac{\sum a_i \tau_i^2}{\sum a_i \tau_i} \quad (19)$$

where a_i ($i=1, 2, 3\dots$) and τ_i ($i=1, 2, 3\dots$) are the fitting coefficients of the PL decay results and characteristic lifetimes, respectively. The measured lifetimes are 2.37 μs , 1.29 μs , 0.62 μs and 0.36 μs for PbS, $\text{Mn}_{0.007}\text{PbS}$, $\text{Mn}_{0.0115}\text{PbS}$ and $\text{Mn}_{0.0166}\text{PbS}$ QDs, respectively (Table 4.1). The decrease of PL decay lifetime was observed with the increase of Mn incorporation content in PbS QDs. By controlling the Mn concentration in the as-prepared QDs, the PL lifetime can be tuned regularly from hundreds of nanoseconds to several microseconds.

Table 4.1 Size, absorption peak, PL peak and Stokes shift, Mn molar concentration and lifetime of as-prepared PbS QDs and Mn-doped PbS QDs in toluene.

| Samples | Size (nm) | Absorption peak (nm) | PL peak (nm) | Stokes shift (eV) | Mn concentration (by molar) | Life time (μs) |
|--------------------------------|-----------------|----------------------|--------------|-------------------|-----------------------------|-----------------------------|
| PbS | 2.81 ± 0.40 | 870 | 1000 | 0.18 | 0.00 % | 2.37 |
| $\text{Mn}_{0.007}\text{PbS}$ | 2.77 ± 0.35 | 866 | 1039 | 0.24 | 0.70 % | 1.29 |
| $\text{Mn}_{0.0115}\text{PbS}$ | 2.84 ± 0.40 | 879 | 1052 | 0.23 | 1.15 % | 0.62 |
| $\text{Mn}_{0.0166}\text{PbS}$ | 2.75 ± 0.35 | 850 | 1044 | 0.27 | 1.66 % | 0.36 |

The average lifetime of the PL decay is commonly used to compare QY upon a certain treatment of an ensemble of QDs based on the following equations: ¹⁶¹

$$\text{QY} = \frac{K_{et}}{K_{et} + K_{net}} \quad (20)$$

$$\tau = \frac{1}{K_{et} + K_{net}} \quad (21)$$

where K_{et} , K_{net} and τ are the radiative decay rate, the non-radiative decay rate and the experimentally detected lifetime extracted from equation (19), respectively. The QYs of as-prepared QDs were measured and values of K_{et} and K_{net} are calculated from the above-mentioned equations (11) and (12), which are reported in Table 4.2. The QYs are 71.0%, 7.6%, 3.5% and 2.1% for PbS, Mn_{0.007}PbS, Mn_{0.0115}PbS and Mn_{0.0166}PbS QDs, respectively. The results show that the QYs decrease after the incorporation of Mn ions, as well as K_{et} . It is also found that the K_{et} values are very similar (namely, $0.589 \times 10^5 \text{ s}^{-1}$ for Mn_{0.007}PbS, $0.572 \times 10^5 \text{ s}^{-1}$ for Mn_{0.0115}PbS and $0.583 \times 10^5 \text{ s}^{-1}$ for Mn_{0.0166}PbS) for Mn-doped PbS QDs with different Mn dopant concentrations. However, K_{et} of PbS ($2.996 \times 10^5 \text{ s}^{-1}$) is significantly higher than that of Mn-doped PbS QDs. These results demonstrate that there is an intrinsic difference in the emission behaviors between pure and Mn-doped PbS QDs. The K_{net} values increase with the increasing concentration of incorporated Mn ions, which could be attributed to the traps.

Table 4.2 QY, K_{et} and K_{net} of as-prepared PbS and Mn-doped PbS QDs in toluene.

| Samples | QY (%) | K_{et} (10^5 s^{-1}) | K_{net} (10^5 s^{-1}) |
|--------------------------|----------|------------------------------------|-------------------------------------|
| PbS | 71.0±7.0 | 2.996 | 1.22 |
| Mn _{0.007} PbS | 7.6±0.8 | 0.589 | 7.16 |
| Mn _{0.0115} PbS | 3.5±0.4 | 0.572 | 15.76 |
| Mn _{0.0166} PbS | 2.1±0.2 | 0.583 | 27.19 |

To further investigate the varying Stokes shift before and after Mn incorporation at different sizes of QDs, PbS and Mn-doped PbS QDs with different sizes were synthesized and their optical properties were studied. Figure 4.8 reported the summarized Stokes shifts as a function of the absorption peak of as-synthesized PbS and Mn-doped PbS QDs. These values indicate that Mn-doped PbS QDs show consistently increased Stokes shifts at different sizes, whereas the value of the difference decreases with the red shift of the absorption peak position.

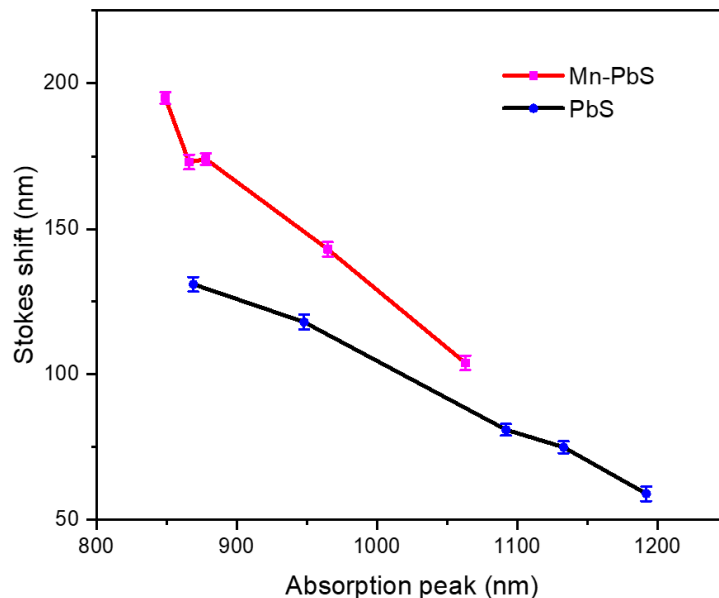


Figure 4.8 Summarized Stokes shift as a function of the absorption peak of PbS and Mn-doped PbS QDs.

4.2.3 Emission mechanism

The difference in PL spectra between Mn-doped PbS QDs and Mn-doped wide band gap QDs is revealed by the following two aspects: (i) The ${}^4T_1 - {}^6A_1$ d-d transition of Mn ions was not observed in Mn-doped PbS QDs, while this emission was widely reported in other Mn-doped wide band gap semiconductors^{60, 162}; (ii) A significantly red shift was observed for the PL peak of doped QDs compared to pure host materials at the identical size and same temperature. Such results cannot be explained from the schematic diagrams of Mn-doped in wide band gap QDs previously reported in the literature.^{53, 162} PbS is a narrow band gap semiconductor, with a bulk band gap of 0.41 eV and a large exciton Bohr radius of 18 nm.¹⁵⁰ To date, most reported PbS QDs reveal a first-excitonic absorption peak ranging from 800 to 2000 nm, with tunable band gaps from 0.6-1.5 eV.^{130, 163} Figure 4.9a shows the band energy levels of PbS QDs and d-state of Mn ions. For PbS QDs with the absorption peak of ~850 nm, the band gap is ~1.4 eV, which is much lower than the energy for ${}^4T_1 - {}^6A_1$ transition (2.12 eV). Generally speaking, depending on the bandgap of the host semiconductor, the ligand field states of 4T_1 and 6A_1 of the doped ions could be involved in

the PL emission.¹⁶⁴ The band edge positions of PbS QDs, Mn 4T_1 and 6A_1 state positions were given according to previous reports.^{162, 165, 166} In the case of this work, it is different from other Mn-doped in wide band gap QDs (for instance, ZnSe and CdSe QDs), in which the 4T_1 and 6A_1 Mn d-state are located between the VB and CB of QDs. As shown in Figure 4.9a, the 4T_1 energy state is located between the VB and CB of PbS QDs, while 6A_1 energy state lies below the VB of PbS QDs. Radiative and non-radiative processes are indicated as straight lines and wavy lines, respectively. The rate of energy transferred from the photoexcited nanocrystal to Mn ions (\sim ps,⁴⁶ shown in green wavy lines in Figure 4.9a) significantly exceeds that of exciton recombination (\sim μ s), enabling the energy transfer towards Mn ions.

Schematic diagrams of the electronic transitions involved in light-modulated PL from PbS and Mn-doped PbS QDs are shown in Figure 4.9b (left). When a pure PbS QD is excited by photons with energy higher than its band gap, the direct recombination of the electron-hole pairs displays the general exciton emission. The schematic diagram of the electronic transitions path of Mn-doped PbS QDs is also shown in Figure 4.9b (right). Initially, electrons are pumped from the VB to the CB of the PbS host, and subsequently transferred to the 4T_1 level of the Mn dopant non-radiatively. As the 6A_1 level lies below the VB of the PbS host, the photogenerated electrons will radiatively relax towards the VB of QDs instead of 6A_1 level of Mn dopant, resulting in a 'Mn-PbS' emission. This is the reason why no 580 nm PL peak associated with Mn 4T_1 - 6A_1 d-emission was observed (alternatively, its intensity may be below the detection limit), whereas this peak was reported by other wide band gap QDs doped with Mn.⁵³ Meanwhile, the unique exciton behavior results in a large red shift of the PL peak position, consistent with the PL spectra shown in Figure 4.7a. When the size of Mn-doped PbS QDs increases, the band gap decreases, so that the CB of PbS becomes lower, and the energy difference between exciton emission and 'Mn-PbS' emission decreases. This explains why the difference of Stokes shift between pure PbS and the similar-sized Mn-doped PbS QDs shows a decreasing trend with the increase of QDs size, as shown in

Figure 4.8. On the other hand, it was reported that the Mn ${}^4T_1 - {}^6A_1$ d-emission is spin forbidden resulting in a very long lifetime in the range of several hundreds of microseconds.³³ As shown in Table 4.1, the lifetime of Mn-doped PbS QDs is very different from those of the d-emission and band-edge emission in PbS QDs, thus indicating the occurrence of a different emission mechanism in the as-synthesized Mn-doped PbS QDs.

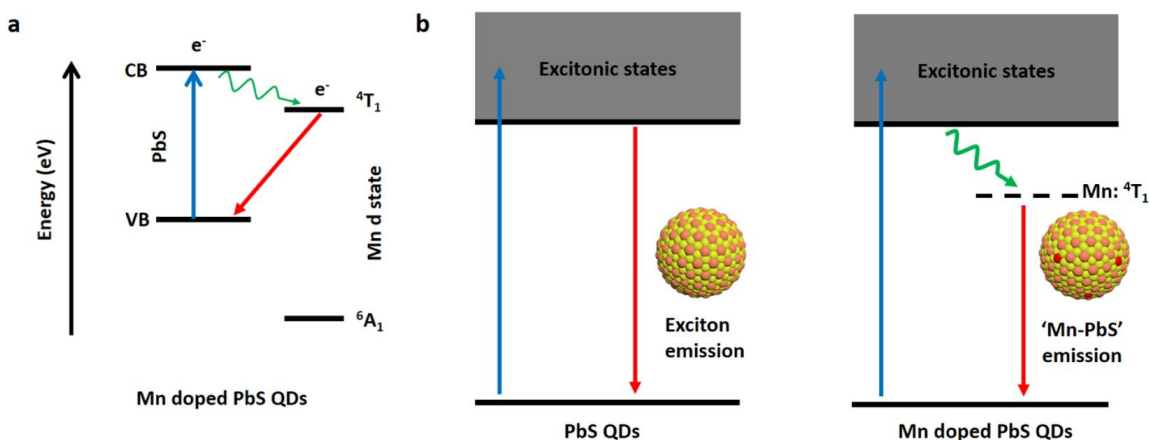


Figure 4.9 (a) Band energy levels of PbS QDs and Mn d-state (left). Radiative processes are indicated as straight lines and non-radiative processes as wavy lines. (b) Schematic illustration of the change in emitting excited state of PbS QDs (left) and with the incorporation of Mn in PbS QDs (right).

4.2.4 Temperature response

PMMA is widely used in fabricating QD-based optical related devices due to its excellent optical property with high transparency, low reabsorption losses as well as good environmental stability.^{75, 158} Here, PMMA is used to fix the QDs on the substrate to protect it from moving by N₂ flow at low temperature measurements. The as-prepared QDs/PMMA films were then used for the temperature-dependent PL measurements. The temperature-dependence of the PL of as-prepared PbS and Mn-doped PbS QDs was investigated by controlling the temperature of the QDs during PL measurements. Figure 4.10 exhibits the evolution of PL spectra of PbS, Mn_{0.007}PbS, Mn_{0.0115}PbS and Mn_{0.0166}PbS QDs upon excitation at 450 nm for a broad temperature

window from 96 to 296 K. For both PbS and Mn-doped PbS QDs, the PL spectra show markedly temperature dependence. The spectral variations show that decreasing the temperature systematically increases the PL intensity and shifts the emission peak towards longer wavelengths.

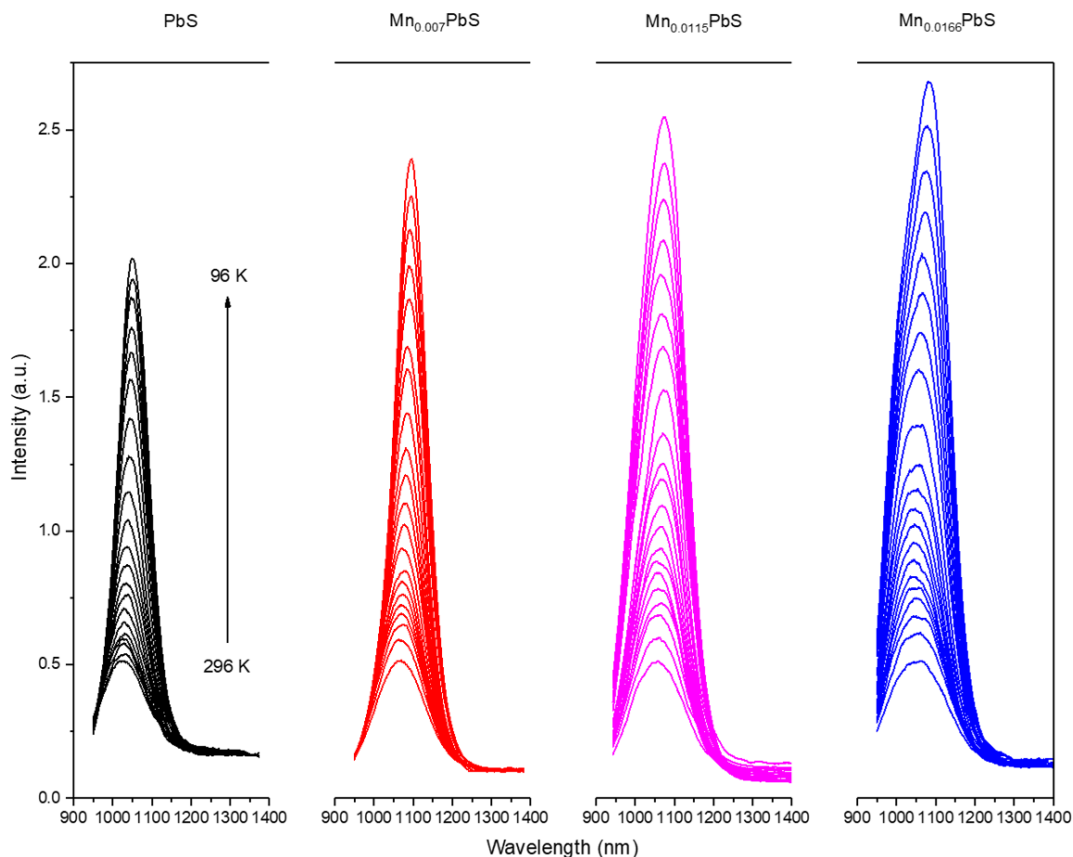


Figure 4.10 Temperature-related PL quenching. Normalized PL spectra of PbS QDs and Mn-doped PbS QDs (from left to right, corresponding to samples of PbS, $\text{Mn}_{0.007}\text{PbS}$, $\text{Mn}_{0.0115}\text{PbS}$ and $\text{Mn}_{0.0166}\text{PbS}$, respectively) recorded at different temperatures. From top to bottom: 96, 106, 116, 126, 136, 146, 156, 166, 176, 186, 196, 206, 216, 226, 236, 246, 256, 266, 276, 286 and 296 K. The excitation wavelength is $\lambda_{\text{ex}} = 450$ nm for the three samples of QDs.

The PL emission spectra were fitted using a single Gaussian function. The integrated PL intensities were calculated at different temperatures for each sample. Figure 4.11a shows the integrated PL intensity of QDs versus inverse temperature ($1000/T$) for PbS QDs and Mn-doped

PbS QDs. The plots show a similar trend for all samples, demonstrating an increase of the PL intensity with temperature decrease. At higher temperature (296 K-156 K) the increasing rate is faster than that at lower temperature, and the increase rate become relatively slower at lower temperature (156 K-96 K). The temperature dependence of the exciton PL intensity is well understood. Typically, such temperature-dependent increase of PL intensity in different types of QDs has been mainly attributed to the suppression of carrier trapping by defects/traps and phonon-assisted thermal escape.^{158, 167, 168} In general, since the charge carrier trapping process is a thermally activated process, it becomes faster at higher temperatures, resulting in deterioration of the PL intensity with increasing temperature. For higher temperatures, the PL intensity decreases as a result of an increase in charge carrier trapping, which is consistent with the behavior observed in other types of QDs.¹⁶⁴ In Figure 4.10 and 4.11a, the increase of the integrated area is faster for Mn-doped PbS QDs than pure PbS QDs, indicating that the Mn-doped QDs are more sensitive to temperature effects. For instance, compared to pure PbS QDs, the $\text{Mn}_{0.0166}\text{PbS}$ displays enhancement in integrated PL area of 1.95 times at 126 K and 2.45 times at 96 K. For Mn-doped PbS QDs, the K_{net} is higher than that of pure PbS QDs, thus the traps in Mn-doped PbS QDs is more than the pure one. As there is a higher concentration of defects in the Mn-doped QDs as indicated by their higher values of K_{net} , at lower temperature, the PL quenching due to defects can be limited, leading to the increase of PL intensity compared to bare QDs. This explains the higher PL temperature sensitivity in Mn-doped QDs. Figure 4.11c reported the full width at half-maximum (FWHM) of the PL peak for the as-synthesized pure PbS and Mn-doped PbS QDs by varying the temperature. The FWHM values gradually decrease with temperature decreasing from 296 to 96 K, which is mainly due to phonon broadening.¹⁵⁴

The temperature-dependence of the PL peak energy of pure and Mn-doped PbS QDs is reported in Figure 4.11b. In pure PbS QDs, the red shift towards longer wavelengths as the temperature decreases can be associated with the decrease in the energy gap. Previous works reported that

the PL peak energy of CdSe/ZnS core/shell QDs¹⁶⁹ and ZnCuInS/ZnSe/ZnS QDs¹⁷⁰ reveal a linear decrease with the increase of temperature from 96 to 296 K. The effect of the temperature on the PL peak energy of PbS QDs was already reported by Zhao *et al.*¹⁵⁸ In this study, the PL peak energy shifts of the spectra were found to vary almost linearly with the temperature for pure PbS QDs samples, in agreement with the previous results.¹⁵⁸ However, for Mn-doped PbS QDs, strong discrepancies were observed. Once the temperature decreases, the Mn_{0.007}PbS bandgap remains almost unchanged up to 250 K and then gradually decreases. Meanwhile, Mn_{0.0115}PbS and Mn_{0.0166}PbS show more obviously stable behavior at the beginning of the cooling cycle, then gradually decreases as same as pure PbS QDs. The different temperature behavior between pure and Mn-doped PbS QDs could be related to the schematic illustration of band alignment of VB and CB of PbS and Mn ions shown in Figure 4.9a. Previous work indicates that the incorporation of Mn ions altered the temperature-dependence behavior of the PL energy in colloidal QDs.¹⁷¹ Several reports demonstrated that Mn-doped QDs exhibit a significant temperature dependence.^{47, 164, 172} For example, Park *et al.*¹⁶⁴ reported that the Mn ⁴T₁ - ⁶A₁ transition shows a blue-shift at higher temperatures. The effect of the temperature on the bandgap of PbS host and energy of Mn ⁴T₁ - ⁶A₁ of the ligand field transition is ascribed to the thermal expansion of the crystalline lattice that directly influences the electronic structure of the semiconductor host and the strength of the ligand field on the Mn ions.¹⁷² In this work, the 'Mn-PbS' emission involves both the VB energy of PbS host and the ⁴T₁ energy state of Mn ions, which dominate the PL process. The combined shifts of the PbS band edges and Mn ⁴T₁ state result in the different temperature-dependence of PL peak energy shifts in Mn-doped PbS QDs with respect to pure PbS QDs. MacKay *et al.*¹⁷³ reported that the Mn emission exhibited a shift towards lower energy when the temperature decreased from 300 to 100 K. At the higher temperatures of this range, the shifting rate is much slower. When further decreasing the temperature, the shifting rate accelerates at lower temperatures. Considering the different variation trend of the temperature dependent PL peak position between pure and Mn-doped PbS QDs observed in f

4.11b, it can be concluded that the Mn 4T_1 energy level makes dominant effect on the ‘Mn-PbS’ emission in Mn-doped PbS QDs at higher temperature. This explains the difference between pure and Mn-doped PbS QDs in the temperature dependent PL peak variation at a higher temperature, as shown in Figure 4.11b. As the temperature-dependent PL response of Mn-doped PbS QDs is significantly improved compared to the pure QDs, this work suggests that Mn-doped PbS QDs holds potential for application in thermal sensors, which make it possible to precisely monitor the local temperature at the nanoscale.

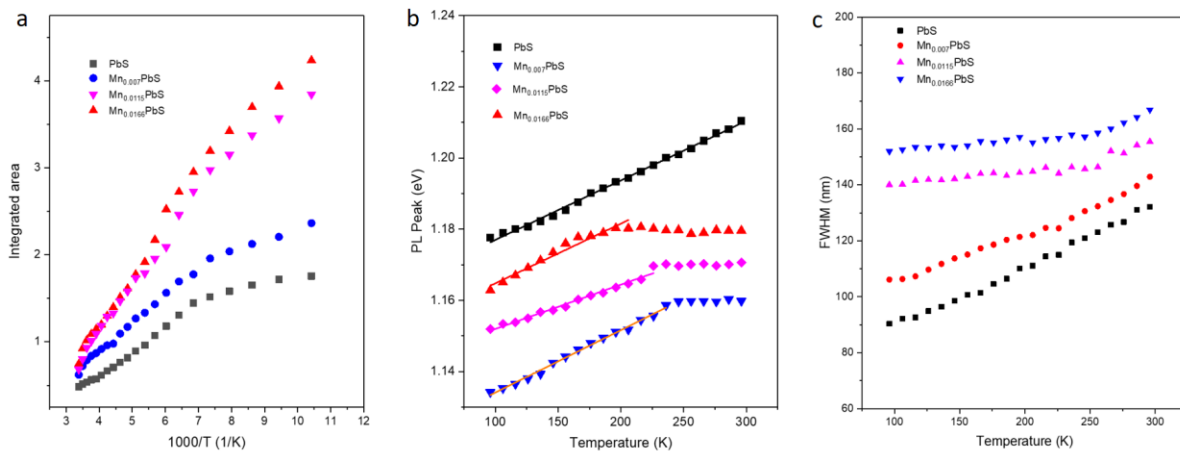


Figure 4.11 (a) Normalized integrated area of PL peak as a function of 1000/T for pure and Mn-doped PbS QDs, where T is temperature. (b) PL peak position as a function of temperature for pure and Mn-doped PbS QDs. (c) Temperature dependence of FWHM of PbS, Mn_{0.007}PbS, Mn_{0.0115}PbS and Mn_{0.0166}PbS QDs.

4.3 Conclusions

The synthesis of oil-soluble Mn-doped PbS QDs was reported with well-controlled Mn concentration and uniform size distribution. The optical performance indicates that Mn-doped PbS QDs reveals a larger Stokes shift than pure PbS QDs samples with identical size. The schematic illustration of ‘Mn-PbS’ emission was proposed by investigating the band alignment of band edges of PbS QDs and Mn d-state. The midgap states created by Mn doping cause electrons to be transferred from the CB of the PbS host to Mn 4T_1 state and inhibit direct recombination with holes

in the VB, which leads to a 'Mn-PbS' emission. The temperature-dependent optical properties were investigated for pure PbS and Mn-doped PbS QDs by exploring the PL peak energy shift and PL intensity variation in the 96-296 K temperature range. The temperature response of Mn-doped PbS QDs improves significantly as compared to the pure PbS QDs. This work demonstrates that Mn-doped PbS QDs are potential candidates for application in thermal sensors and provides new fundamental knowledge of the emission mechanism and temperature dependent optical properties on Mn-doped QDs.

Chapter 5. Efficient and stable photoelectrochemical hydrogen generation using optimized colloidal heterostructured quantum dots

In the 1970s, TiO₂ semiconductor was first developed to use in PEC cells for H₂ generation. Later, QDs were considered to sensitize TiO₂ as the photoanode to extend the absorption range for application in PEC cells. CdS QDs sensitized TiO₂ photoanode has slightly improved absorption range (< 500 nm) and high driving force (electron injection between CB of QDs and that of TiO₂), achieving a photocurrent density of ~5.0 mA/cm². CdSe QDs sensitized TiO₂ photoanode has further improved absorption range (up to 710 nm), but the low driving force only allows a slight increase in photocurrent density (6.0 mA/cm²). To combine the advantages of high absorption range and high electron driving force of QDs for application in PEC cells, in this chapter, colloidal heterostructured CdS/CdSe core/shell QDs were designed and synthesized to engineer the electronic band alignment and tune the electron transfer efficiency by varying the CdSe shell thickness (0.6-1.9 nm). The changes in structural and optical properties of the core/shell QDs were investigated with tunable shell thickness. Complementing the experimental results, the theoretical electron and hole wave functions were calculated, and then the evolution of their overlap as a function of shell thickness was reported. Experimental values of radiative lifetimes show a characteristic increase at very thin shell thickness followed by a decrease with the further increase of the shell thickness, consistent with the wave function overlap results obtained theoretically. The band structures of heterostructured core/shell CdS/CdSe QDs could be engineered from a quasi type-II band structure at a very thin shell (0.6 nm) to a typical inverted type-I band structure at thicker shells. The as-synthesized CdS/CdSe core/shell QDs were used as building blocks to absorb solar energy in PEC cells, showing a suitable band alignment as indicated in Figure 5.1. Due to the synergistic effects of the extended light absorption range and effective photoelectron transport, the PEC cells that employed CdS/CdSe core/shell QDs with

optimized shell thickness (1.6 nm) exhibit high saturated current density of $\sim 16.0 \text{ mA/cm}^2$ (at 0.9 V vs. the RHE) under one sun illumination (highest value reported for PEC cells based on CdS/CdSe QDs) and improved long-term stability while maintaining 83% of its initial value after continuous one sun illumination for 4 hours. The transfer rate of electron was also investigated, providing insights into the high photocurrent density obtained in the optimized device.

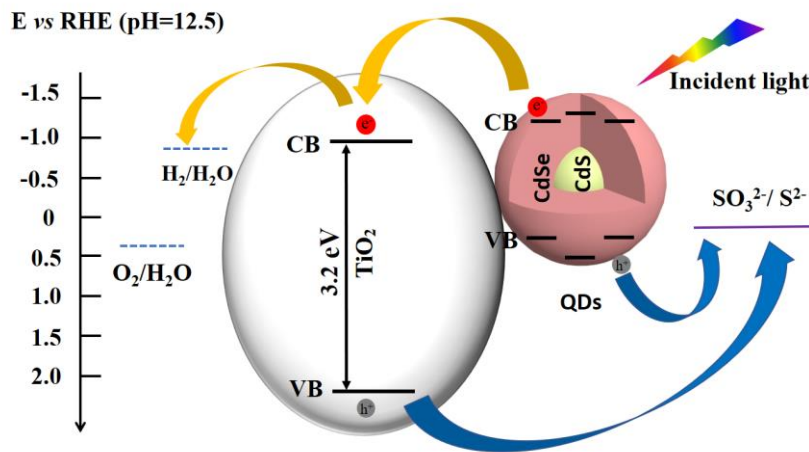


Figure 5.1 Approximate energy levels (correspond to pH=12.5) of TiO_2 and QDs, together with related characteristic redox potentials. The arrows show the electron and hole transfer processes.

5.1 Experimental section

5.1.1 Synthesis of CdS QDs

For the synthesis of CdS QDs, the hot injection method was used, which was adapted from literature^{130, 174} in a Schlenk line under argon (Ar) atmosphere employing substituted thiourea¹³⁰ and cadmium oxide¹⁷⁴ as sulfur and cadmium precursor, respectively. First, for the synthesis of substituted thiourea, a solution of aniline (1.74 g, 1.7 mL) in toluene (6.0 mL) was mixed with a solution of phenyl isothiocyanate (2.53 g, 2.2 mL) in toluene (6.0 mL). The mixture was allowed to stir for 2 h before the exothermic reaction ended. The product was dried overnight under vacuum to remove the residual toluene, resulting in a white powder of substituted thiourea.¹³⁰ Second, for the synthesis of CdS QDs, 0.9 mmol (115.2 mg) cadmium oxide and 5.4 mL OAc

were mixed with 26 mL ODE in a 3-neck flask with a stir bar for stirring at 350 rpm and flushed with argon gas flow for 5 minutes, then transferred in an oil bath for heating. The temperature was further increased to 250 °C and held for 1 h. During this period, a mixture of as-synthesized substituted thiourea (103.0 mg) was dissolved in diphenyl ether (1.8 g) by heating the mixture to 95 °C, the obtained transparent solution was then injected quickly into the flask containing cadmium oleate [Cd(OAc)₂]. After injection, the color of the reaction solution in the flask was observed to change from transparency to yellow. The reaction was maintained at 250 °C for 10 minutes before being cooled down to room temperature by immersing reaction flask in cold water. Finally, the as-synthesized CdS QDs were purified with ethanol and re-dispersed in toluene three times.

5.1.2 Synthesis of CdS/CdSe core/shell QDs

The growth of the CdSe shell was also carried out in a Schlenk line under Ar atmosphere adapted from literature approach^{23, 175}, starting from bare CdS QDs. First, the precursor of 0.2 M Cd(OA)₂ was prepared by dissolving 513.6 mg cadmium oxide and 7 mL OAc in 13 mL ODE at 250 °C. Separately, the precursor of 0.2 M TOP-Se was prepared by dissolving 316 mg selenium in 20 mL TOP. Secondly, 2 mL CdS QDs (A= 1.68 at the first excitonic peak position, 5.8×10^{-8} mol dots in toluene, the concentration of CdS QDs was determined by the method reported by Yu *et al.*¹⁹), 1.7 mL OLA and 15 mL ODE were mixed in a 3-neck flask with a stir bar for stirring at 350 rpm and transferred in an oil bath for heating, the mixture was increased to 240 °C under Ar gas atmosphere and then held for 30 mins. Hereafter, the prepared Cd(OA)₂ and TOP-Se precursors mixture were injected into the reaction flask at a rate of 1 mL/h. With the addition and increasing amount of shell precursors, the color of the reaction solution in flask was observed to change from yellow to red gradually. To obtain QDs with different shell thicknesses, desired amount of Cd and Se precursor mixture was added during each reaction. The as-prepared QDs obtained from injected precursor volume of 0.8 mL, 2.6 mL, 5.6 mL and 10.4 mL are denoted as CdS/CdSe (0.6

nm), CdS/CdSe (1.1 nm), CdS/CdSe (1.6 nm) and CdS/CdSe (1.9 nm), respectively. Finally, the reaction was cooled down to room temperature by immersing reaction flask in cold water, followed by purifying CdS/CdSe QDs with ethanol 2 times and re-dispersing them in toluene for further characterization.

5.1.3 Synthesis of CdSe QDs

CdSe QDs were prepared by a hot injection method adapted from Qu *et al.*¹²² Typically, TOPO (1 g) was mixed with Cd-oleate (0.4 mmol, 2 mL) and ODE (8 mL) in a flask and purged by N₂ at room temperature for 30 min. After the degassing process for 30 min at 100 °C, the mixture was heated to 310 °C. A mixture of TOP-Se (0.4 mmol, 4 mL), OLA (3 mL), and ODE (1 mL) was quickly injected into the reaction system under stirring at 350 r/min. The temperature was maintained at 300 °C for CdSe growth. The reaction time was controlled from 1 min to 4 h. The reaction was then quenched by immersing the flask in cold water. The as-synthesized QDs were precipitated with ethanol, centrifuged to eliminate unreacted precursors, and finally dispersed in toluene for further test and fabrication of PEC cells.

5.1.4 Fabrication of PEC cells

TiO₂ films were prepared using the same method described in section 3.1.2.

CNTs-TiO₂ hybrid anode film preparation. The CNTs were mixed with commercial TiO₂ paste during the preparation of the photoanodes. The procedure is similar with the above details described in TiO₂ film preparation by only changing the original TiO₂ paste with the newly prepared TiO₂-CNTs hybrid paste. The CNTs were dispersed in ethanol and sonicated for 4 hours. The TiO₂-CNTs hybrid pastes were prepared by mixing the desired amount of ethanolic suspension of CNTs into a known weight of TiO₂ paste. CNTs and TiO₂ weight ratio is 0.015%. For a systematic comparison, the TiO₂ and CNTs-TiO₂ hybrid anode films were measured with a total thickness of ~14 μm by using contact profilometry.

ZrO₂ film preparation. ZrO₂ films were prepared using a commercial ZrO₂ nanopowder. A single layer of ZrO₂ film was tape-casted on FTO glass followed by annealing in air at 500 °C for 30 min and cooled down to room temperature.

QDs/TiO₂ photoanode preparation. The TiO₂ films were sensitized with as-synthesized QDs by using EPD. In brief, two of the as-prepared TiO₂ films were immersed into the QDs/toluene solution vertically facing each other in a distance of ~0.5 cm. Afterwards, a voltage of 200 V was applied for 2 hours to deposit the QDs into the mesoporous holes using a digital Keithley as the power source. The photoanode was then rinsed with toluene to remove the unabsorbed QDs and dried with N₂ flow twice at room temperature. Prior to ZnS capping, the photoanodes were treated with the ligand exchange process by using two cycles of SILAR of methanolic solution CTAB and methanol for washing and removing the chemical residuals on the surface for 1 min dipping, respectively. Afterwards, two cycles of ZnS were deposited by SILAR. Specifically, the QDs-sensitized TiO₂ films were treated twice by immersing into 0.1 M Zn(CH₃COO)₂·2H₂O and 0.1 M Na₂S aqueous solutions for 1 min alternately. Subsequently, insulating glue was used to cover the sample's non-active area. For each kind of QDs, more than three samples were prepared and evaluated in parallel.

QDs/ZrO₂ film preparation. The QDs/ZrO₂ film was prepared by depositing QDs into ZrO₂ film using EPD with an applied voltage of 200 V for 2 hours (the distance between two ZrO₂ films is around 0.5 cm). Then as obtained films were used as reference for electron transfer rate measurements.

5.1.5 Characterization

The morphologies and SAED patterns of CdS and CdS/CdSe core/shell QDs were characterized using a JEOL JEM2100F TEM operating at 200 kV for all experiments. The size distribution of the QDs was estimated by measuring about 100–200 QDs for each sample and further analyzed

using a Gaussian distribution. EDS was used to investigate the elemental analysis of the as-synthesized QDs. XRD patterns of extensively purified as-synthesized QDs were acquired with a Philips X'pert diffractometer using a Cu K α radiation source ($\lambda = 0.15406$ nm). SEM and EDS were employed to investigate the elemental analysis of the QDs/TiO $_2$ photoanode by using a Tescan Vega3 equipment. XPS were acquired in a VG Escalab 220i-XL equipped with a hemispherical analyzer and a monoenergetic Al K α Anode X-Ray Source. Absorption spectra were acquired with a Cary 5000 UV-vis-NIR spectrophotometer (Varian) with a scan speed of 600 nm/min. PL spectra were recorded with a Fluorolog-3 system (Horiba Jobin Yvon). The excitation wavelength was set at 380 nm for CdS QDs and 450 nm for CdS/CdSe core/shell QDs. The PL lifetime was measured in the TCSPC mode using a 380 nm (for CdS QDs) and 444 nm (for CdS/CdSe core/shell QDs) laser. QYs of QDs were measured using Rhodamine 6G as a reference, as referred to the reported literature.¹²²

The PEC performance measurement is similar to the procedures described in section 3.1.3. The PEC performance of the as-prepared QDs/TiO $_2$ photoanodes was also measured with or without a 650 nm long-pass filter for comparison.

IPCE measurement was conducted for PEC devices based on the as-synthesized QDs. To derive the qualitative IPCE values, current-voltage measurements were performed with the use of different band-pass optical filters (10 nm band pass).

H $_2$ evolution was measured during the PEC stability test. The produced H $_2$ gas was detected using a GC equipped with a thermal conductivity detector. Ar was used as the carrier gas for GC analysis.

The electron transfer rate was studied by acquiring TRPL measurements from QDs deposited into TiO $_2$ and ZrO $_2$ mesoporous films. The ZrO $_2$ /QDs film serves as a benchmark sample, in which the energy levels block electron transfer. The electron transfer rate was calculated by employing TiO $_2$ as an electron scavenger.

5.1.6 Theoretical methods

The energies and spatial distribution of the carriers were obtained using a simple model for QDs having a spherical potential well, in which the time-independent Schrödinger equation is solved numerically. The physical system is described using the material properties, setting the bulk band structure as the constraining potential well at the different regions of the sphere. Bulk values were used for the electron effective masses (m_e) and hole effective masses (m_h), namely $m_e = 0.2 m_0$ and $m_h = 0.7 m_0$ for CdS, and $m_e = 0.13 m_0$ and $m_h = 0.45 m_0$ for CdSe, where m_0 is the electron rest mass.¹⁷⁶ The bulk bandgap energies are 2.50 eV and 1.75 eV for CdS and CdSe, respectively.^{176, 177} The LUMO and HOMO levels for the bulk CdS are set at -3.3 eV and -5.8 eV, respectively.¹⁰¹ The CB offset between CdS and CdSe is 30 meV.¹⁷⁷ Using this model, the solutions were tracked for the lowest energy of the problem defined at the CBs and the VBs. In terms of implementation, the above results were obtained by COMSOL Multiphysics (a commercial package implementing numerical solvers in a finite element method framework).

5.2 Results and discussions

5.2.1 Synthesis and structural characterization

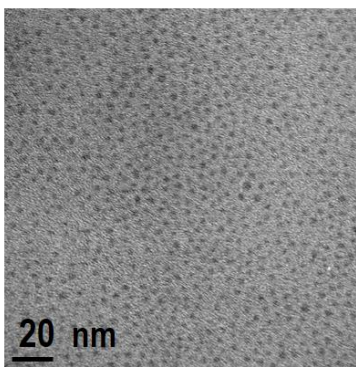


Figure 5.2 TEM image of the as-synthesized CdS QDs.

The synthesis of CdS/CdSe QDs is reported by two different approaches: first, the *in-situ* growth of QDs on the scaffold of mesoporous metal oxide films (for example, TiO₂) by a low-temperature SILAR or CBD approach; and second, *ex-situ* synthesis of colloidal core/shell QDs surrounded

by organic ligands at high temperature. To achieve the fine control of the shell thickness and good crystallization, the QDs were synthesized by the latter approach. First, CdS QDs were synthesized by the hot injection method. These CdS QDs were subsequently used as seeds to grow a CdSe shell, as detailed in the experimental section. The spherical shape of the CdS QDs was observed by TEM (Figure 5.2). CdS QDs with a radius (R) of about 1.5 ± 0.1 nm were used as the core to synthesize CdS/CdSe core/shell QDs. Figure 5.3a-d show representative TEM images of the CdS/CdSe core/shell QDs with different shell thickness (H) [R/H: 1.5/0.6, denoted as CdS/CdSe (0.6 nm); R/H: 1.5/1.1, CdS/CdSe (1.1 nm); R/H: 1.5/1.6, CdS/CdSe (1.6 nm); and R/H: 1.5/1.9, CdS/CdSe (1.9 nm)]. The core/shell CdS/CdSe QDs retain the regular quasi-spherical shape with uniform and narrow size distribution after shell growth, as confirmed by TEM imaging (Figure 5.2 and Figure 5.3a-d) and measured size distribution (Figure 5.4). A typical HR-TEM image of CdS/CdSe (1.6 nm) QDs is shown in Figure 5.3e. It is hard to distinguish the core/shell interface by HR-TEM imaging due to the very small CdS core size and the small lattice mismatch between CdS core and CdSe shell.¹⁷⁵

SAED patterns (Figure 5.3f and 5.5) present the evolution of the QDs from a ZB crystal structure (CdS core) to a WZ structure (CdSe shell) with a gradual increase of shell thickness. The interplanar spacing values of 0.338, 0.206 and 0.176 nm measured in Figure 5.5a were derived for the core CdS QDs, in good agreement with the crystal lattice planes (1 1 1), (2 2 0) and (3 1 1) of ZB CdS. After the growth of the CdSe shell, SAED patterns of CdS/CdSe core/shell QDs (Figure 5.3f and 5.5b-d) show the occurrence of a hexagonal WZ structure signal related to the shell formation. In the SAED pattern of CdS/CdSe (1.9 nm) QDs, the distances of interplanar spacing are 0.371, 0.350, 0.329, 0.215, 0.201 and 0.180 nm, attributed to the (1 0 0), (0 0 2), (1 0 1), (1 1 0), (1 0 3) and (1 1 2) lattice planes of WZ CdSe, respectively.

EDS was employed to further confirm the elemental composition of the QDs. As shown in Figure 5.3g, the EDS spectra show characteristic peaks originating from Cd, S in bare CdS sample and

Cd, S, Se peaks in the CdS/CdSe core/shell QDs. Furthermore, the intensity of Se/S peak ratios were found to become larger with increasing CdSe shell thickness, consistent with the gradual growth of the CdSe shell. Figure 5.3h shows the size and electronic band structure alignment evolution of core/shell QDs with the growth of CdSe shells with different thicknesses.

The crystal structures of as-synthesized CdS/CdSe core/shell QDs were characterized by XRD, as shown in Figure 5.3i. The XRD pattern reveals that CdS core has a cubic zinc blende (ZB) crystal structure corresponding to the JCPDS No. 00-001-0647. The three highest intensity peaks occur at 26.4° , 44.0° and 51.9° , which correspond to the (1 1 1), (2 2 0) and (3 1 1) lattice planes, respectively. After growing the CdSe shell over the CdS core, the peaks in heterostructured core/shell QDs appear between the ZB CdS phase and hexagonal wurtzite (WZ) crystal structure of CdSe. The peaks in the diffraction patterns of core/shell CdS/CdSe QDs gradually shift towards smaller angles for the WZ CdSe phase with increasing shell thickness, originating from the increasing volume of the CdSe in the shell. For the pattern of the CdS/CdSe (1.9 nm) QDs (magenta line), the diffraction peaks, located at 35.1° , 42.0° , 45.7° and 49.7° , are indexed to the (1 0 2), (1 1 0), (1 0 3) and (1 1 2) lattice planes of WZ structure CdSe in good agreement with JCPDS No. 00-002-0330. However, the peaks originating from the (1 0 0), (0 0 2) and (1 0 1) lattice planes of WZ CdSe merge into one peak in the XRD pattern due to the three very close peak positions and the signal from the (1 1 1) plane of the ZB CdS core. In the XRD patterns for CdS/CdSe core/shell QDs with thicker shell, WZ crystal phase is dominated due to the relatively large volume of the CdSe shell compared to the CdS core. These results are consistent with SAED results. Epitaxial growth has been reported previously for a CdSe/CdS core/shell system where the crystalline phase of the shell is dictated by the crystal structure of the core.¹⁷⁸ However, other studies described WZ CdSe shell growth on a ZB core^{179, 180}, which was ascribed to the presence of the additional coordinating solvent of trioctylphosphine (TOP) in selenium precursor during reaction.¹⁸⁰

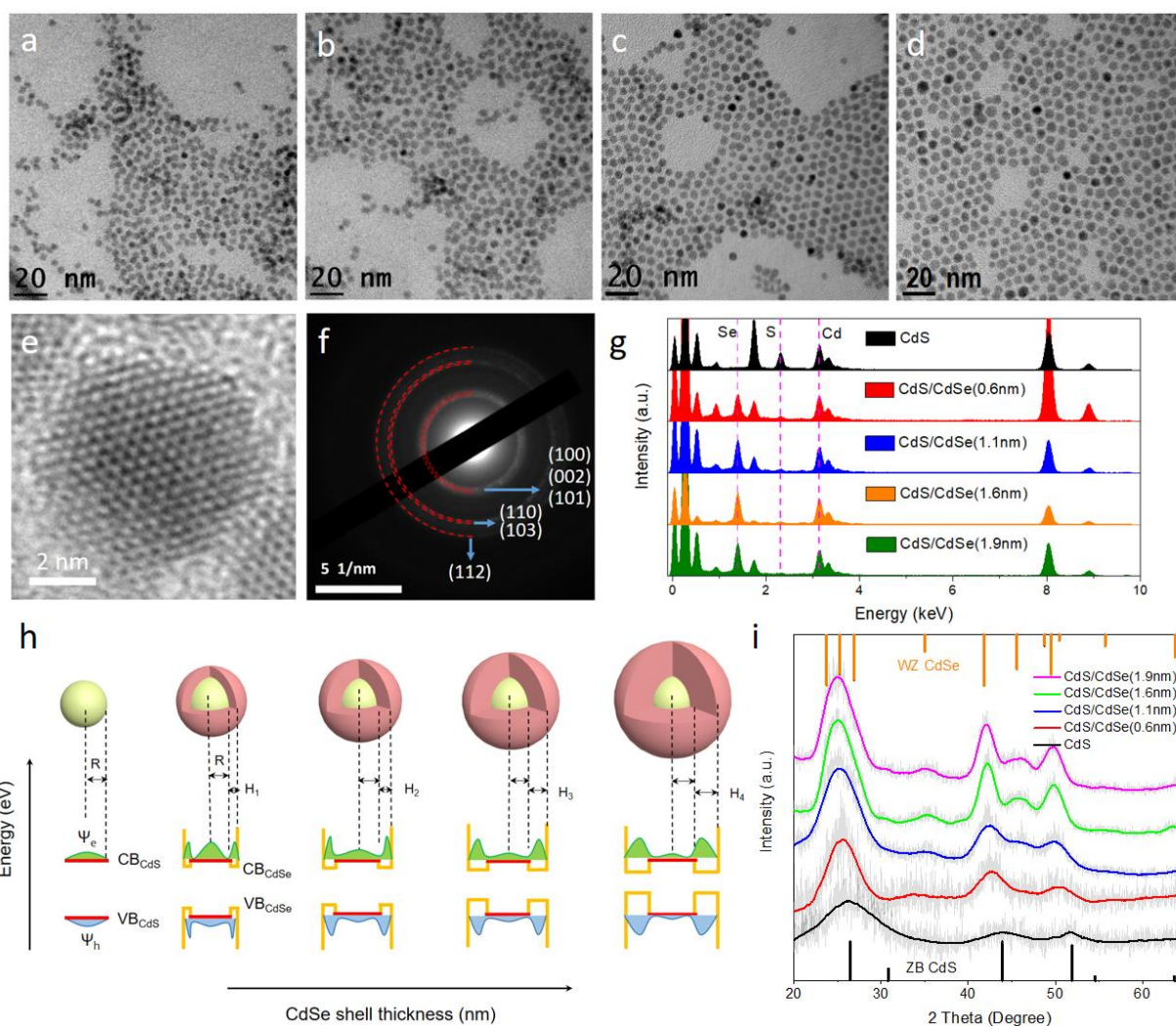


Figure 5.3 Representative TEM images of (a) CdS/CdSe (0.6 nm) QDs, (b) CdS/CdSe (1.1 nm) QDs, (c) CdS/CdSe (1.6 nm) QDs and (d) CdS/CdSe (1.9 nm) QDs. (e) A representative HR-TEM image and (f) SAED pattern of CdS/CdSe (1.6 nm) QDs. (g) EDS spectra of CdS (dark color), CdS/CdSe (0.6 nm) (red color), CdS/CdSe (1.1 nm) (blue color), CdS/CdSe (1.6 nm) (orange color) and CdS/CdSe (1.9 nm) QDs (green color), respectively. (h) Schematic illustration of band alignment of the as-synthesized QDs by tuning the shell thickness. The electron and hole distribution probability with varying shell thickness is shown as green and blue areas, respectively. (i) XRD patterns of CdS and CdS/CdSe core/shell QDs. The JCPDS for ZB crystal structure of CdS (No. 00-001-0647, dark vertical line) and WZ crystal structure of CdSe (No. 00-002-0330, orange vertical line) are shown for identification.

XPS was employed to analyze the elemental composition of the as-synthesized CdS/CdSe (1.6 nm) core/shell QDs. The high-resolution XPS spectra of small energy regions around the

expected peak positions of each element are shown in Figure 5.6a-c. The binding energies recorded in the XPS analysis were calibrated by referencing the C 1s peak to 284.8 eV. As shown in Figure 5.6a, the spectra for Cd 3d can be resolved into $3d_{5/2}$ and $3d_{3/2}$ peaks at 405.0 and 411.8 eV, in agreement with other reports.⁹⁴ Similarly, as shown in Figure 5.6b, the XPS spectra in the range from 157 to 170 eV can be resolved into four peaks, specifically Se $3p_{1/2}$, S $2p_{1/2}$, S $2p_{3/2}$ and Se $3p_{3/2}$ at around 166.1, 162.8, 161.7 and 160.3 eV, respectively.¹⁸¹ Figure 5.6c shows the high-resolution XPS spectrum of Se 3d. The Se $3d_{5/2}$ peak observed at a binding energy of 54.0 eV corresponds to the characteristic signature of Se. These results demonstrate the presence of Cd, Se and S in the CdS/CdSe core/shell QDs.

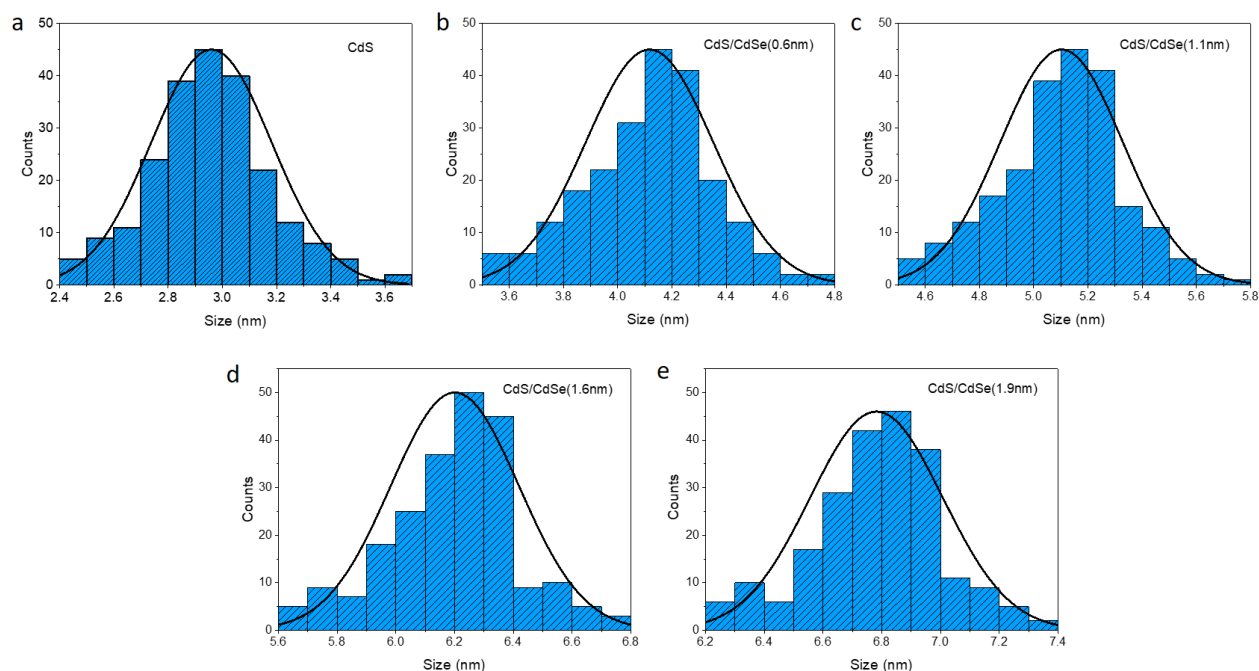


Figure 5.4 Size distributions of (a) CdS, (b) CdS/CdSe (0.6 nm), (c) CdS/CdSe (1.1 nm), (d) CdS/CdSe (1.6 nm) and (e) CdS/CdSe (1.9 nm) QDs, respectively.

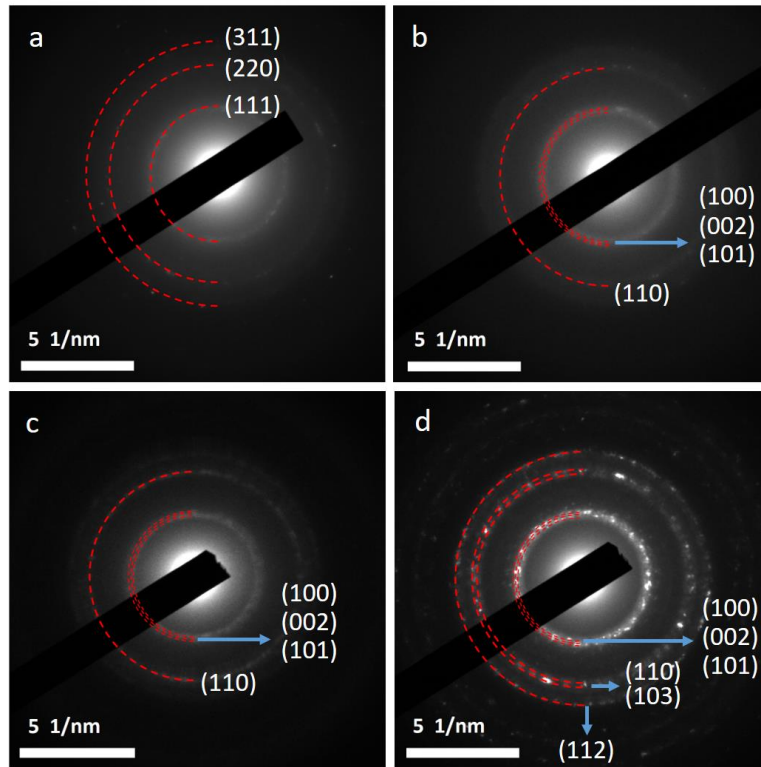


Figure 5.5 SAED patterns of (a) CdS, (b) CdS/CdSe (0.6 nm), (c) CdS/CdSe (1.1 nm), and (d) CdS/CdSe (1.9 nm) QDs, respectively.

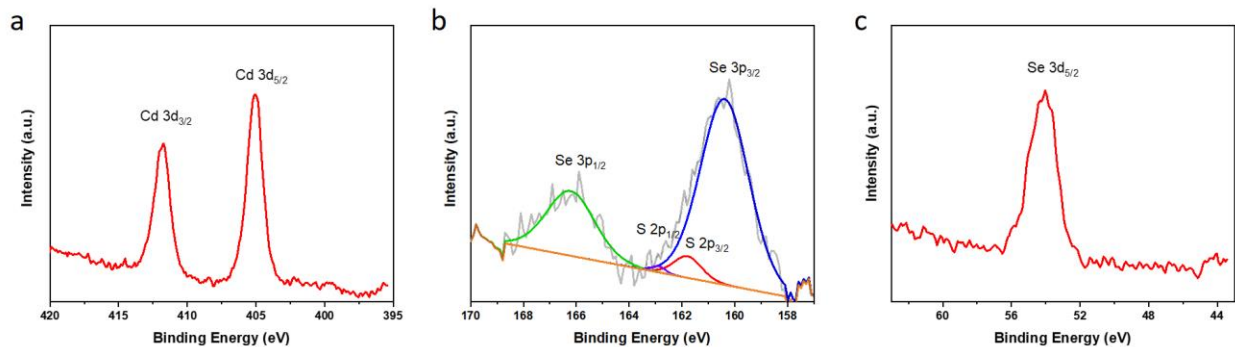


Figure 5.6 High-resolution XPS spectra of (a) Cd 3d, (b) S 2p, Se 3p and (c) Se 3d for CdS/CdSe (1.6 nm) QDs.

5.2.2 Optical properties

The optical properties of as-prepared QDs were characterized by absorption and PL spectroscopy. Normalized absorption and PL spectra of as-synthesized bare CdS QDs and the CdS/CdSe core/shell QDs with different shell thickness are shown in Figure 5.7.

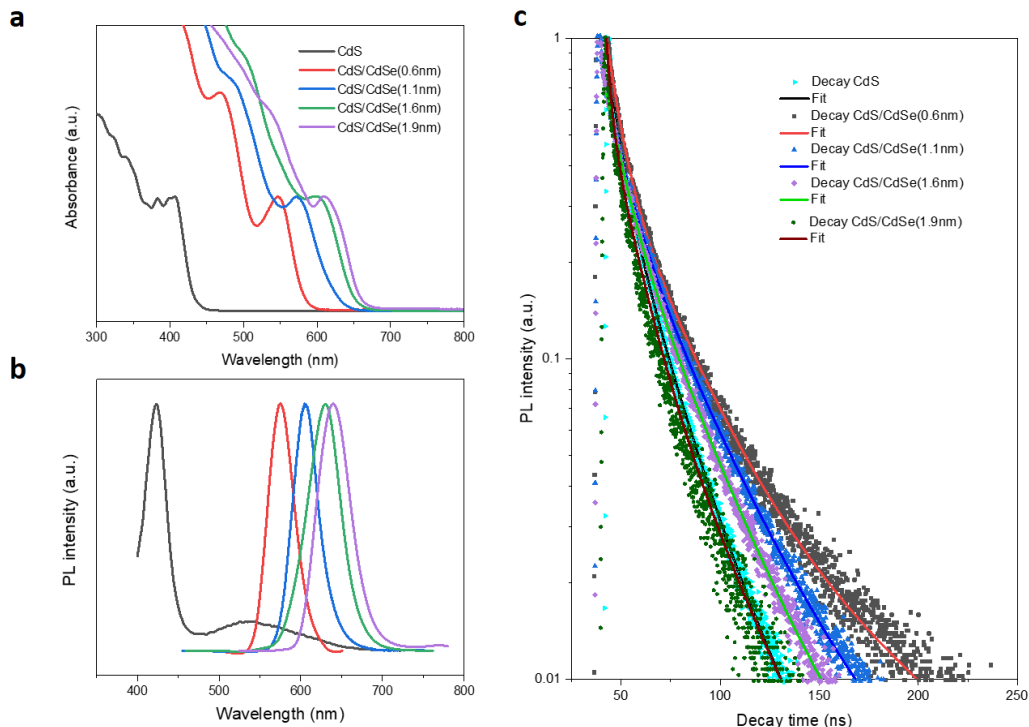


Figure 5.7 Optical properties of CdS and CdS/CdSe QDs in toluene. (a) Absorption spectra, (b) PL spectra. The PL of the CdS QDs shows a noticeable secondary emission peak at the range of 500-650 nm, arising from recombination at the surface trap states. The excitation wavelength is $\lambda_{ex}= 400$ nm. (c) Experimental TRPL measurements of CdS (cyan color), CdS/CdSe (0.6 nm) (dark color), CdS/CdSe (1.1 nm) (blue color) and CdS/CdSe (1.6 nm) (green color), and CdS/CdSe (1.9 nm) (purple) QDs in toluene. Fitted curves are shown in black, red, blue, green and brown color lines, respectively. The excitation wavelengths are $\lambda_{ex}= 380$ nm for CdS QDs and $\lambda_{ex}= 444$ nm for CdS/CdSe QDs samples.

As seen in Figure 5.7a, the first-excitonic absorption peak position shows a clearly red shift with increasing CdSe shell thickness, located at 407, 548, 573, 601 and 611 nm for CdS bare QDs, CdS/CdSe (0.6 nm), CdS/CdSe (1.1 nm), CdS/CdSe (1.6 nm), and CdS/CdSe (1.9 nm), respectively. (Table 5.1) Similarly, the PL spectrum shows a gradually red shift of the peak with increasing shell thickness (Figure 5.7b). This red shift may be attributed to the growth of the smaller band gap shell (CdSe) over the larger band gap core (CdS). The displayed PL peaks are observed at ~419 nm (CdS), 575 nm [CdS/CdSe (0.6 nm)], 605 nm [CdS/CdSe (1.1 nm)], 631 nm [CdS/CdSe (1.6 nm)] and 641 nm [CdS/CdSe (1.9 nm)], respectively (reported in Table 5.1). The

very small Stokes shifts of 12-32 nm (0.088-0.114 eV) demonstrate that these emission peaks originate from band edge rather than trap-related emission. The bare CdS QDs also exhibit a noticeable broad surface-trap emission (from 500 to 650 nm) in addition to the band edge emission at 419 nm. This surface trap emission is a feature commonly observed in the PL spectra of CdS QDs.^{182, 183} The absence of trap emission in the core/shell QDs is favorable for high photo-to-current conversion efficiency in PEC cells due to the decrease of electron recombination.^{64, 94}

To better understand the role of the shell thickness on the carrier dynamics in QDs, the TRPL of CdS/CdSe core/shell QDs with different shell thickness were studied. Figure 5.7c shows the measured and fitted TRPL of CdS QDs (aqua points and black fitted curve), CdS/CdSe (0.6 nm) (dark points and red fitted curve), CdS/CdSe (1.1 nm) (blue points and blue fitted curve), CdS/CdSe (1.6 nm) (purple points and green fitted curve) and CdS/CdSe (1.9 nm) (dark green points and brown fitted curve).

Table 5.1 Optical and size parameters of the as-synthesized bare CdS and CdS/CdSe core/shell QDs with tunable shell thickness in toluene. (^aR is the CdS core radius and ^bH is the CdSe shell thickness)

| Samples | ^a D (nm) | ^a R (nm) | ^b H (nm) | Absorption peak (nm) | PL peak (nm) | Lifetime (ns) | QY |
|-------------------|---------------------|---------------------|---------------------|----------------------|--------------|---------------|-----|
| CdS | 3.0 ± 0.3 | 1.5 ± 0.1 | 0 | 407 | 419 | 21 | 8% |
| CdS/CdSe (0.6 nm) | 4.1 ± 0.4 | 1.5 ± 0.1 | 0.6 | 548 | 575 | 57 | 17% |
| CdS/CdSe (1.1 nm) | 5.1 ± 0.4 | 1.5 ± 0.1 | 1.1 | 573 | 605 | 46 | 13% |
| CdS/CdSe (1.6 nm) | 6.2 ± 0.5 | 1.5 ± 0.1 | 1.6 | 601 | 631 | 35 | 11% |
| CdS/CdSe (1.9 nm) | 6.8 ± 0.6 | 1.5 ± 0.1 | 1.9 | 611 | 641 | 20 | 9% |

The intensity-weighted average lifetime (τ) is calculated from fitting the TRPL results using the equation (19).^{94, 129} The measured lifetimes are 21, 57, 46, 35 and 20 ns for CdS, CdS/CdSe (0.6 nm), CdS/CdSe (1.1 nm), CdS/CdSe (1.6 nm) and CdS/CdSe (1.9 nm), respectively. This shows

that, at the very beginning, the lifetime increases after a thin CdSe shell growth ($H = 0.6$ nm), then decreases with further increase of the CdSe shell thickness ($H = 1.1-1.9$ nm). The radiative lifetime and the non-radiative lifetime (Table 5.2) was calculated according to the following equation:¹⁶¹

$$QY = \frac{1/\tau_r}{1/\tau_r + 1/\tau_{nr}} = \frac{1/\tau_r}{1/\tau} = \frac{\tau}{\tau_r} \quad (22)$$

where τ , τ_r and τ_{nr} are the measured overall lifetime, radiative lifetime and non-radiative lifetime, respectively. To gain a deeper insight into the role of the rates of radiative and non-radiative recombination of the exciton state in the carrier recombination process, the radiative decay rate ($K_{et} = 1/\tau_r$) and non-radiative decay rate ($K_{net} = 1/\tau_{nr}$) were calculated, which are also reported in Table 5.2. The K_{et} typically depends on the size, shape and heterostructure of the QDs.¹²⁶ The K_{net} in bare CdS QDs is induced mainly by the surrounding surface chemical states, such as surface traps, defects and quenchers. In CdS/CdSe core/shell QDs, the K_{net} values depend on both the surface defects/traps and the electronic band structure of the core/shell materials.¹²⁶ To account for the observed trends in the radiative lifetimes, theoretical simulations of these CdS/CdSe core/shell QDs were carried out and are discussed in the following section.

Table 5.2 Calculated radiative lifetime, non-radiative lifetime, radiative decay rate and non-radiative decay rate of the as-synthesized bare and core/shell QDs.

| Samples | Radiative lifetime τ_r (ns) | Non-radiative lifetime τ_{nr} (ns) | Radiative decay rate K_{et} (10^6 s ⁻¹) | Non-radiative decay rate K_{net} (10^7 s ⁻¹) |
|-------------------|----------------------------------|---|--|---|
| CdS | 263 | 23 | 3.8 | 4.3 |
| CdS/CdSe (0.6 nm) | 335 | 69 | 2.9 | 1.4 |
| CdS/CdSe (1.1 nm) | 354 | 53 | 2.8 | 1.9 |
| CdS/CdSe (1.6 nm) | 318 | 39 | 3.1 | 2.6 |
| CdS/CdSe (1.9 nm) | 222 | 22 | 4.5 | 4.5 |

5.2.3 Theoretical simulation

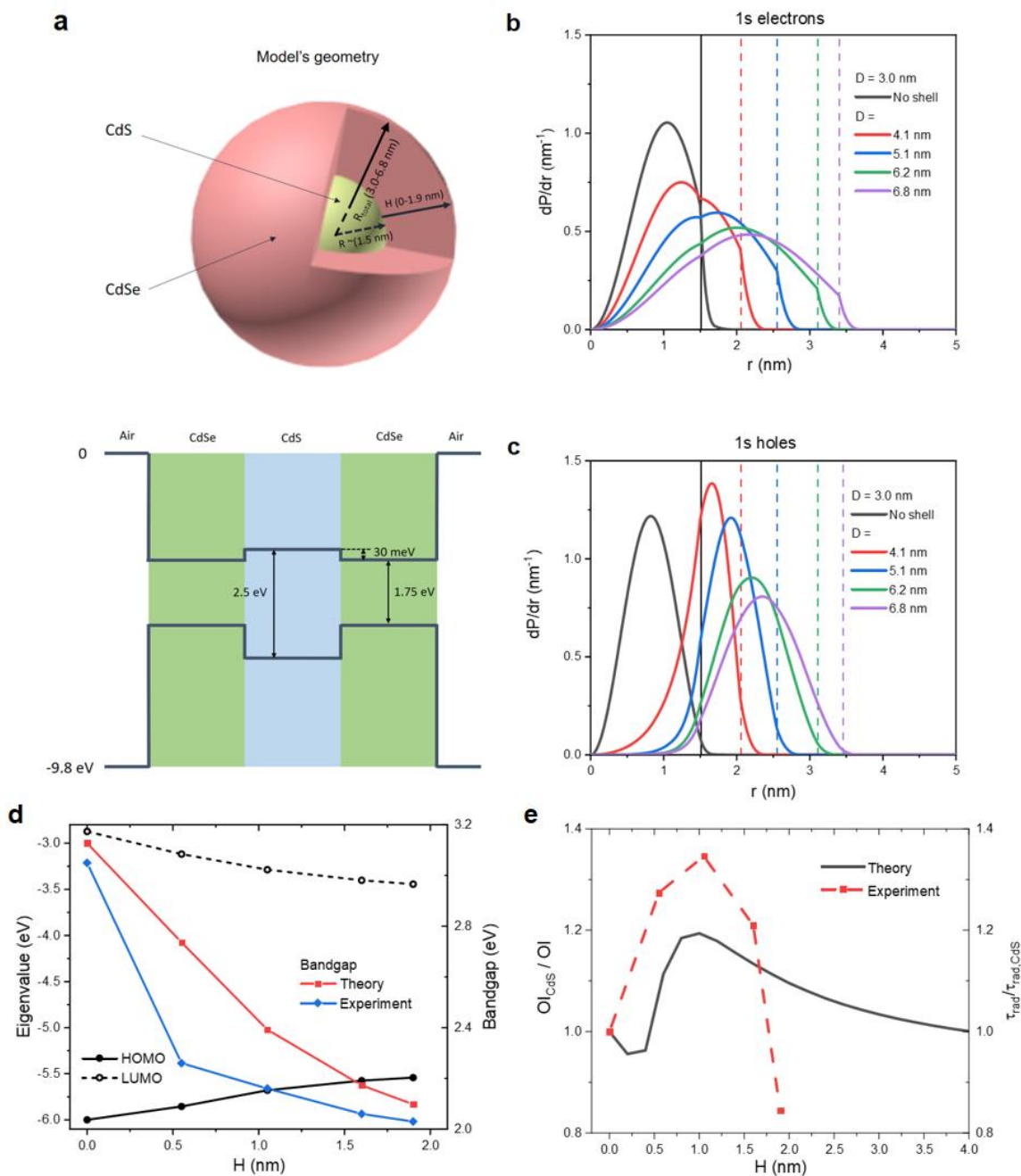


Figure 5.8 Theoretical modelling of the CdS/CdSe core/shell QDs. (a) Geometrical model of the spherical CdS/CdSe core/shell QDs, alongside the key geometrical parameters, radius core and thickness shell (top panel). R_{total} represents the radius of the core/shell QDs. The QDs are assumed to have a standard spherical shape. Band alignment diagram of bulk CdS and CdSe showing the positions of CB and VB (bottom panel). (b, c) Radial probability distribution,

$dP/dr = 4\pi r^2 |\Psi|^2$, (b) electrons and (c) holes in the model system, showing how the low-energy carriers are more likely to populate the volume of the shell when it becomes thicker. (d) Evolution of the HOMO and LUMO, each taken as the lowest eigenstate of the corresponding quantum potential well for electrons and holes. The evolution of the theoretical bandgap, calculated as the difference between these states, is compared with the experimental bandgaps, estimated from the absorption wavelengths listed in Table 5.1. (e) The inverse electron and hole overlap (solid black line), normalized over its value for the CdS QDs, and $\tau_{rad}/\tau_{rad\ core}$ (red dash line) values as a function of shell thickness.

The size-dependence of the bandgap is a well-known and important feature of semiconductor nanostructures, arising from the quantum confinement effect.¹⁸⁴ Different band alignment types can arise for heterogeneous core/shell QDs as a result of differences in the intrinsic band gaps of the core and shell materials as well as variations in their sizes.^{62, 185}

Complementing the experimental studies, numerical results calculated from the theoretical modeling of the QDs are presented here. These simulations are based on solving the time-independent Schrödinger equation for spherical heterostructures using bulk parameters of the materials obtained from the literature (see Figure 5.8a).^{176, 177} This allows us to determine the wave functions of the lowest-energy states of electrons and holes. Observing their spatial extension along the radial direction in Figure 5.8b and c, the delocalization trend of these carriers to the shell as it increases in thickness is readily apparent. However, the likelihood of this delocalization is different for electrons and holes, due to the band alignment of CdS and CdSe. The tendency of the carriers to preferentially reside in the shell is consistent with expectations for an inverted type-I semiconductor nanostructure. However, for a shell thickness of 0.6 nm, the first eigenstate of both CB and VB still extends inside the core, indicating that the shell might be too thin to fully support the charge carrier states, resulting in a greater probability to be found at the core/shell interface. The observation provides qualitative support for the inhibited transfer rates of electrons found for the core/shell QDs with a thin shell of 0.6 nm, as discussed in more details in the following section. When the size of the shell is further increased, the lowest energy carriers

become localized in the shell layer, as shown schematically in Figure 5.3h. The calculated probability distributions in Figure 5.8b and c indicate a different occupation of the shell between electrons and holes, with the latter having a higher probability of leaking into the shell. This effect is most pronounced for QDs with a thin shell of 0.6 nm, in which electrons are localized over the entire QDs region but holes are mostly delocalized in the shell region, as for a quasi type-II band structure.⁶³ Further growth of the shell (from 0.6 to 1.9 nm) leads to a transition from the quasi type-II to inverted type-I, followed by gradual consolidation of localization regime of an inverted type-I, in which both holes and electrons are largely delocalized to shell region of the heterogeneous core/shell QDs. Several reports described the transition of the band structure by tailoring the shell thickness of the core/shell heterogeneous structure.^{62, 185} For instance, Balet *et al.*⁶² observed tunable localization regimes between type-I and type-II by varying the shell thickness in ZnSe/CdSe core/shell nanocrystals. Zhang *et al.*¹⁸⁵ reported tunable band alignment by optimizing CdS layers to remove the barrier for charge transfer in the TiO₂/CdS/CdSe structure. These findings illustrate the size-dependent band structure in CdS/CdSe core/shell QDs and its evolution from quasi type-II to inverted type-I with increasing shell thickness.

Furthermore, the energies of the highest occupied molecular orbital (HOMO) and lowest unoccupied molecular orbital (LUMO) in the theoretical model of QDs as a function of shell thickness were calculated. The HOMO and LUMO positions and theoretical bandgaps are shown in Figure 5.8d. The relatively simple theoretical approach used here is found to recover the experimental trend from the optical data. The QDs with small sizes imply that their carriers will be subject to quantum confinement, thus widening the bandgap with respect to the values in bulk, as observed in both theory and experiment. The largest deviation is observed for the core/shell QDs with the thinnest CdSe shell (the size of shell in a few atoms scale), which can be likely attributed to the interfacial strain due to the lattice mismatch between CdS and CdSe interface (not taken into account in the model).¹⁷⁶

Finally, Figure 5.8e compares the theoretical estimation of the probability of radiative recombination of the carriers as a function of shell thickness with the experimental results. The spatial overlap integral (OI) between holes and electrons is calculated by the following expression:

$$OI = \left| \int \psi_e(\mathbf{r}) \psi_h(\mathbf{r}) d\mathbf{r}^3 \right|^2 \quad (23)$$

with $\psi_e(\mathbf{r})$ and $\psi_h(\mathbf{r})$ being the calculated normalized wave functions of the electrons and holes, respectively. As mentioned above, the measured lifetime for the QDs consists of two components, τ_r and τ_{nr} , corresponding to radiative and non-radiative decay processes, respectively. For this theoretical approach, the spatial overlap between electrons and holes is considered only to affect the τ_r value.¹⁰¹ Therefore, the inverse of this overlap integral (normalized to that of the bare CdS particles) is used as a proxy for the radiative lifetime (normalized in the same manner) and compared with the experimental lifetimes. As seen in Figure 5.8e, the theoretical model predicts an increase in the radiative lifetime as the size of the shell is increased up to ~1.1 nm. Increasing the shell thickness beyond this value increases the spatial overlap of the carriers, thus reverting the gains in carrier lifetimes. The theoretical estimate adequately reproduces the trend in the radiative lifetimes observed in experiments.

5.2.4 PEC measurements

While many studies detailed the tunable optoelectronic properties of CdSe/CdS core/shell QDs^{4, 61, 101, 176-178, 186}, fewer reports have focused on the inverted structure of CdS/CdSe QDs^{64-66, 187, 188}. For example, Pan *et al.* reported colloidal CdS/CdSe QDs for use in QDSCs, achieving high values of power conversion efficiency.⁶⁴ Most other reports have discussed CdS/CdSe QDs synthesized via room-temperature SILAR or CBD method. The carrier transfer scenarios in these systems display a fundamental discrepancy originating from the significantly structural variations in photoanodes fabricated with CdS/CdSe QDs prepared by different preparation processes such as low-temperature CBD/SILAR and high temperature colloidal synthesized methods (as shown

in Figure 5.9). Specifically, in the CBD/SILAR-based QDs/TiO₂ system, the cascade structure of TiO₂/CdS/CdSe indicates that the CdS directly attaches to the surface of TiO₂.⁶⁵ However, when colloidal synthesized QDs are used the CdSe shell directly attaches to the TiO₂ surface, while the CdS core has no contact with TiO₂ (Figure 5.1). In addition, compared with colloidal CdS/CdSe QDs, QDs synthesized by the low-temperature SILAR or CBD method suffer from an increased density of surface traps and a broad size distribution due to lack of control over nucleation and growth of the QDs, making it difficult to tune the optoelectronic properties.⁸⁸

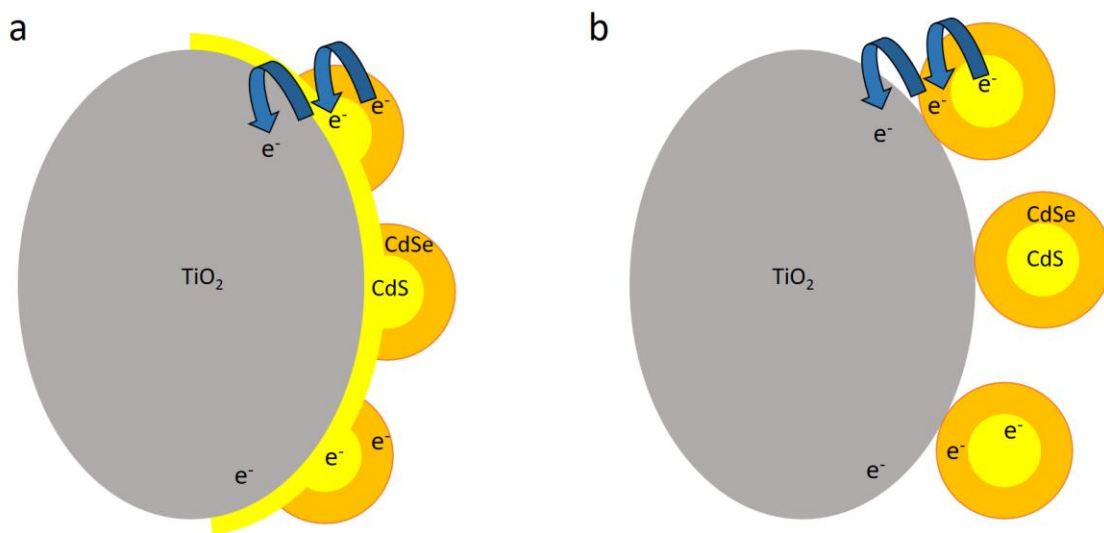


Figure 5.9 Schematic illustration of the structural variations in photoanodes sensitized with CdS/CdSe QDs made via different preparation processes of (a) *in-situ* CBD/SILAR method and (b) *ex-situ* colloidal synthesized CdS/CdSe QDs method. The scenarios of electron transfer in these two cases exhibit fundamental differences, as indicated by the blue arrows. This difference is caused by a significant structural discrepancy in photoanodes fabricated via these two different approaches.

As a proof-of-concept, the as-synthesized QDs were employed as light-harvesting materials in PEC cells. The schematic illustration of PEC cells with as-prepared QDs as light harvesters is shown in Figures 5.1 and 5.11a. Under illumination, QD absorbs photons with energy higher than its bandgap, generating excitons. Photoexcited exciton dissociation occurs at the QDs/TiO₂

interface, and the photoexcited electrons in the CB of the QDs can be effectively injected into the CB of TiO₂. Electron transport occurs in the TiO₂ mesoporous film and charges are collected by the FTO film, to be then transferred through the external circuit to the Pt counter electrode, where H₂ generation takes place. Na₂S/Na₂SO₃ hole scavengers in the electrolyte provide a function for absorbing the photoexcited holes.^{108, 142} To prevent recombination of electrons from the FTO to the oxidized species in the electrolyte, a thin blocking layer of TiO₂ was deposited between the mesoporous layer of TiO₂ and the FTO-coated glass. TiO₂ mesoporous photoanodes consist of transparent and scattering layers. The transparent layer is composed of 20 nm TiO₂ nanoparticles with a high surface-to-volume ratio, which acts as a scaffold for loading a large amount of QDs. The scattering layer on top of the transparent layer is composed of a blend of 20 nm and 450 nm sized TiO₂ nanoparticles, which acts as a light scattering barrier to extend the time spent by light inside the active layer. Consequently, a scattering layer enhances the possibility of light to be captured by the QDs in a photoanode and hence improves the performance of PEC devices.

The colloidal heterostructured CdS/CdSe core/shell QDs were first employed to sensitize TiO₂ for application as the photoanode in PEC cells for H₂ generation. To further investigate the distribution of QDs on the TiO₂ mesoporous film, cross-sectional analyses of a freshly prepared QDs/TiO₂ photoanode were performed by scanning electron microscopy (SEM) with EDS mapping. Figure 5.10a shows a representative cross-sectional SEM image of the QDs on the TiO₂ mesoporous film while Figure 5.10b–f display the EDS images of all the elements (O, Ti, S, Se and Cd), expected to be present in the as-prepared photoanodes. These maps suggest a laterally homogeneous distribution of the adsorbed QDs in the mesoporous TiO₂ film. An EDS line mapping (Figure 5.10g) along the blue highlighted arrow in Figure 5.10a indicates that the CdS/CdSe core/shell QDs are distributed homogeneously in the vertical direction as well, resulting in high-quality TiO₂/QDs photoanodes. Absorption spectra of the QDs sensitized TiO₂ films (only transparent layer) were also measured, as shown in Figure 5.10h. It is found that the

absorption spectra of different QDs on TiO₂ films show similar trend with QDs in solution (Figure 5.7a).

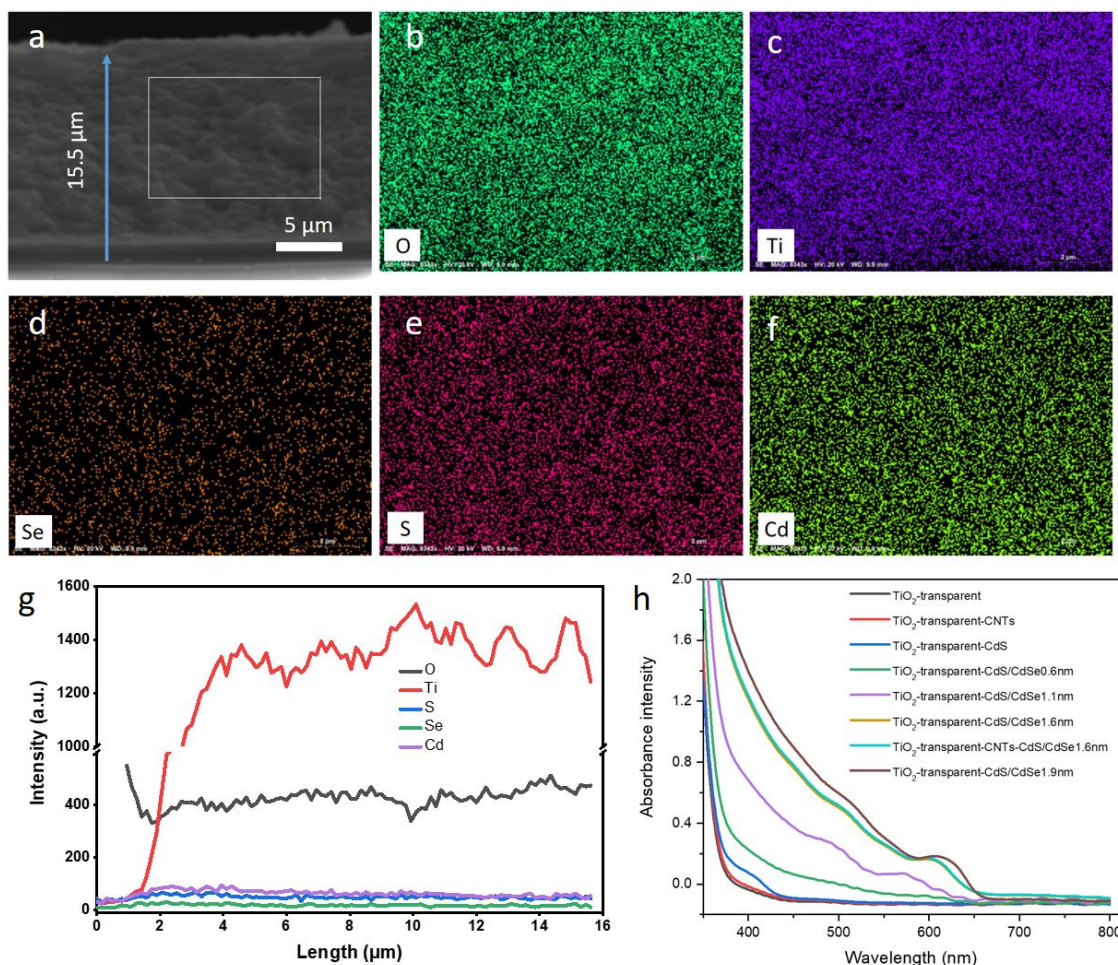


Figure 5.10 (a) Representative cross-sectional SEM image of CdS/CdSe (1.6 nm) QDs-sensitized photoanode. (b-g) EDS 2D mapping (in the selected area surrounded by the white line): the elemental distributions of (b) O, (c) Ti, (d) Se, (e) S and (f) Cd. (g) EDS line mapping of all the elements as the direction of the arrow in image (a). (h) Absorption spectra of the QDs sensitized TiO₂ films (only transparent layer).

The inorganic CTAB ligands passivation strategy introduced Br⁻ to cap the surface cations by replacing the long-chain OAc ligands, forming an inorganic and halide anion-passivated QDs.¹⁸⁹ This strategy is known to improve carrier mobility and reduce defect density, reducing the carrier recombination in QDs after EPD and providing better surface passivation. Therefore, this strategy is proved to be favorable for improving the stability of PEC cells.¹⁹⁰ Two cycles of ZnS layer were

applied before the PEC test to protect the QDs against photocorrosion.⁹⁴ Previous work had shown that ZnS can also significantly suppress charge recombination at the surface trap states on the QDs and facilitate electrons flow from QDs to TiO₂.⁹⁴

The PEC activity of the QDs/TiO₂ photoanode system towards the H₂ evolution reaction was evaluated in the three-electrode configuration with 0.25 M Na₂S and 0.35 M Na₂SO₃ acting as hole scavengers at room temperature (25 °C) by using a CHI 760D electrochemical workstation. The measurement was carried out at AM 1.5G with an intensity of 100 mW·cm⁻². Pt was used as the counter electrode and Ag/AgCl electrode was used as the reference electrode. A set of linear-sweep voltammograms was carried out by using photoanodes in the dark and under one sun illumination. The photocurrent density under illumination increases gradually with increasing voltage before reaching a saturated photocurrent density. Figure 5.11b shows the photocurrent response measured with the PEC cells for different QDs under the dark condition and one simulated sunlight illumination condition (AM 1.5G, 100 mW·cm⁻²), respectively. The PEC cell based on bare CdS QDs reveals a saturated current density of 2.7 mA/cm² (at 0.9 V vs. RHE) (Figure 5.11b and Table 5.3). The low current density is likely due to the limited absorption range and high density of trap states on the surface of QDs, which act as sites for non-radiative carrier recombination after illumination. An enhancement of the saturated photocurrent density is observed for all the cells based on core/shell QDs, exhibiting saturated photocurrent densities (at 0.9 V vs. RHE) of 5.4, 9.8, 15.0 and 13.0 mA/cm² for CdS/CdSe (0.6 nm), CdS/CdSe (1.1 nm), CdS/CdSe (1.6 nm) and CdS/CdSe (1.9 nm), respectively (Figure 5.11b and Table 5.3). The CdS/CdSe (1.6 nm) QDs based cells show the highest saturated photocurrent density of 15.0 mA/cm² (at 0.9 V vs. RHE), which is more than a five-fold enhancement compared to that of the device based on bare CdS QDs (only 2.7 mA/cm²). It was reported that, for type-I core/shell QDs, the shell can hinder the injection of electrons from the core to TiO₂ and accelerate charge recombination at the TiO₂/QDs interface, which represents a major issue for their use in

optoelectronic devices.^{185, 191} In the CdS/CdSe core/shell QDs (either quasi type-II in thin shell QDs or inverted type-I structure), the CB of the shell is located within the CB of the CdS core and TiO₂ film, facilitating efficient electron transfer from the QDs to the TiO₂ film, compared to a type-I band alignment. Furthermore, the growth of a CdSe shell over the CdS core broadens the absorption spectra towards longer wavelengths. Both the above-mentioned properties contribute to the higher current density observed in PEC cells based on CdS/CdSe core/shell QDs. The differences in PEC performance of the QDs with different shell thickness are also associated with the system's charge dynamics, which are discussed in detail in the following section.

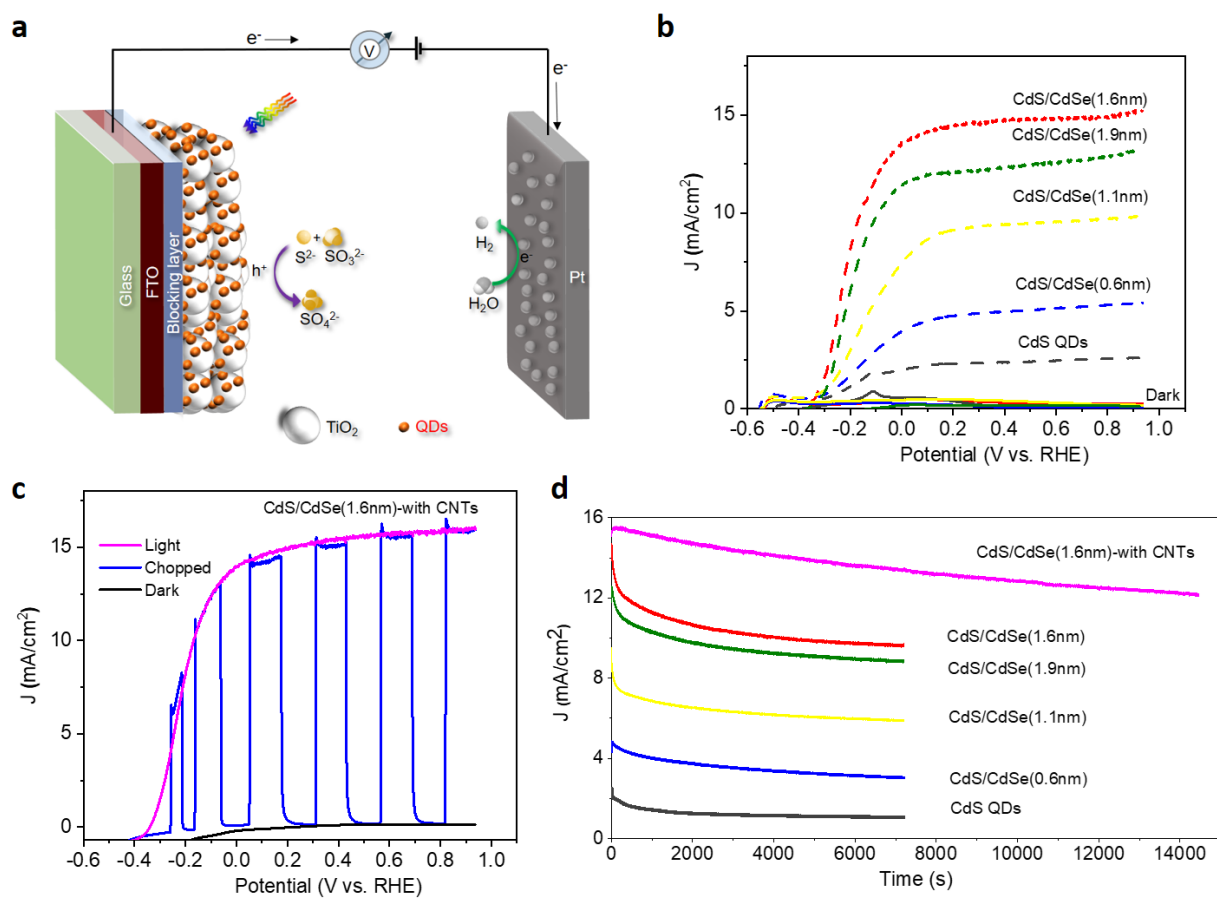


Figure 5.11 (a) Schematic of the working mechanism of a PEC device based on TiO₂ nanoparticle mesoporous anode sensitized colloidal heterostructured CdS/CdSe core/shell QDs. (b) Photocurrent density versus the applied voltage (vs. RHE) curves of PEC cells fabricated using the as-synthesized QDs of CdS, CdS/CdSe (0.6 nm), CdS/CdSe (1.1 nm), CdS/CdSe (1.6 nm),

and CdS/CdSe (1.9 nm) in dark (solid line) and under continuous one sun illumination (dash line). (c) CdS/CdSe (1.6 nm) with CNTs-TiO₂ photoanode in dark (black line), under constant one sunlight illumination (magenta line) and under chopped one simulated sunlight illumination (blue line). (d) Measured photocurrent density versus time for PEC devices at 0.6 V vs. RHE under continuous 100 mW·cm⁻² illumination.

Table 5.3 Comparison of saturated photocurrent density of PEC devices based on various types of QDs sensitized TiO₂ of this work and reported in the literature. The configuration of the PEC cell is identical in all devices.

| QDs | QDs types | Size (nm) | Current Density (mA/cm ²) | Reference |
|---|---------------------|-----------|---------------------------------------|-----------|
| CdS | Colloidal | 3.0 | 2.7 | This work |
| CdS/CdSe (1.6 nm) | Colloidal | 6.2 | 16.0 | This work |
| CdSe/5CdSe _{0.5} S _{0.5} /CdS | Colloidal | 8.1 | 12.0 | 126 |
| CdSe | Colloidal | 3.3 | 6.0 | 94 |
| CdSe/CdS | Colloidal | 6 | 10.0 | 94 |
| PbS/CdS/CdS | Colloidal/CBD-based | 3.6 | 11.3 | 88 |
| CdS | CBD-based | N/A | ~5.0 | 66 |
| CdS/CdSe | CBD-based | N/A | 14.9 | 66 |
| CdS/CdSe | SILAR-based | N/A | 6.0 | 192 |
| CdS/CdSe | SILAR-based | N/A | 7.4 | 193 |
| CdS/CdSe | CBD/SILAR-based | N/A | 2.8 | 194 |

To further optimize the PEC performance, CNTs were incorporated into the TiO₂ based photoanode during PEC cell fabrication. Figure 5.10h shows that the incorporation of CNTs has no significant influence on the absorption of QDs/TiO₂ films. This is because the very small amount of CNTs does not affect significantly the transparency of film. These hybrid photoanodes were used in conjunction with CdS/CdSe (1.6 nm) QDs, achieving an average photocurrent density of up to 16.0 mA/cm² (at 0.9 V vs. RHE), a 7 % improvement compared to devices

assembled by TiO₂ photoanodes without CNTs (as shown in Figure 5.11c). Incorporation of CNTs in TiO₂ improves electron transport (by reducing the charge transfer resistance) within the photoanode, enabling the directional path for transport of photo-injected electrons towards the FTO without significantly altering the structural and optical properties of the photoanode.^{195, 196} The saturated photocurrent densities of different types of QD-based PEC devices with identical configurations from this work are summarized and benchmarked against previous results from the literature in Table 5.3. The saturated photocurrent value of the PEC cell based on the heterostructured QDs obtained in this work [16.0 mA/cm² (at 0.9 V vs. RHE)] is significantly higher than the device based on bare CdSe QDs⁹⁴, CdS QDs⁶⁶ or other core/shell structured QDs such as CdSe/CdS⁹⁴, PbS/CdS/CdS⁸⁸ and CdSe/5CdSe_{0.5}S_{0.5}/CdS QDs¹²⁶ in an identical configuration, reported previously. This saturated photocurrent density value is 6 times higher than the one reported for PEC cells based on bare CdS QDs. More importantly, this is also the highest value ever reported for PEC cells based on CdS/CdSe QDs.^{66, 192-194}

Long-term stability is another important parameter of PEC cell that must be improved to facilitate commercialization. The stability was investigated under continuous one sun illumination at 0.6 V vs. RHE. As seen in Figure 5.11d, the photocurrent densities of both bare CdS and CdS/CdSe QD-based PEC cells gradually decrease during illumination. The photocurrent density in CdS QD-based devices rapidly decays to ~2.1 mA/cm² within 10 min, then gradually decreased to a photocurrent density of 42% of its initial value after 2 hours. The devices with CdS/CdSe core/shell QDs of different shell thickness, though starting at different initial photocurrent densities, all exhibit similar stability curves with the photocurrent density maintaining ~60-65% of its initial value after 2 hours of light irradiation at 100 mW/cm².

To investigate the possible reasons for the decrease in photocurrent density of PEC devices based on CdS/CdSe QDs over time, XPS measurements were conducted for the TiO₂-CdS/CdSe (1.6 nm) QDs photoanodes treated with a ZnS passivation layer before and after 2 h of PEC

stability test (as shown in Figure 5.12). The high-resolution XPS spectra of Cd 3d and Zn 2p before and after 2 h of PEC stability measurement are shown in Figure 5.12. As shown in Figure 5.12a, the binding energies of Cd 3d_{3/2} and Cd 3d_{5/2} of CdS/CdSe QDs deposited on TiO₂ are located at 411.8 eV and 405.1 eV, respectively. A 6.7 eV difference between the binding energies of Cd 3d_{3/2} and Cd 3d_{5/2} peaks for photoanode is very close to the XPS result of CdS/CdSe (1.6 nm) QDs in solution (Figure 5.6), which confirms that the structural properties of QDs do not obviously change in the photoanode before the PEC stability test. Figure 5.12b shows the spectrum of Zn 2p before stability test with a pair of peaks at 1045.2 and 1022.2 eV, which corresponds to Zn 2p_{1/2} and 2p_{3/2}, respectively.¹⁹⁷ A typical splitting energy of 23.0 eV was observed, consistent with the previously reported values for ZnS.¹⁹⁷ Figure 5.12c and d demonstrate that, after 2 h of PEC stability test, the two Cd 3d peaks and two Zn 2p peaks were observed to shift by 0.3 and 0.5 eV towards lower binding energies, respectively. These shifts could probably be assigned to the partial oxidation of CdS/CdSe QDs and ZnS, forming Cd(OH)₂ and ZnO on the surface of the photoanode.^{198, 199}

The degraded PEC stability could be attributed to the hole-induced self-oxidative decomposition of metal chalcogenide (QDs and ZnS) on the surface of photoanode, as a consequence of hole accumulation on the surface of photoanode during the PEC measurement.

These results demonstrate that the incorporation of the shell significantly improves the photocurrent density while also enhancing the stability of PEC cells. Most significantly, it is found that the cells based on CdS/CdSe (1.6 nm) QDs in conjunction with the CNTs-TiO₂ hybrid photoanodes show a significantly improved long-term stability as compared to photoanodes without CNTs, retaining 83 % of its initial value even after 4 hours of continuous illumination. This result shows an improvement on previous reports of PEC cells based on colloidal CdSe/CdS or CdSe/CdSe_xS_{1-x}/CdS core/shell QDs with an identical configuration.^{94, 195} The increased temperature of the photoanodes under continuous one sun illumination creates thermal stress,

which can damage interconnections in the mesoporous TiO₂ film, hindering electron transport and hence degrading the performance of the PEC cells. However, due to their high thermal conductivity, the presence of CNTs in the TiO₂ film enhances the thermal stability and improves the overall long-term stability of these devices.²⁰⁰

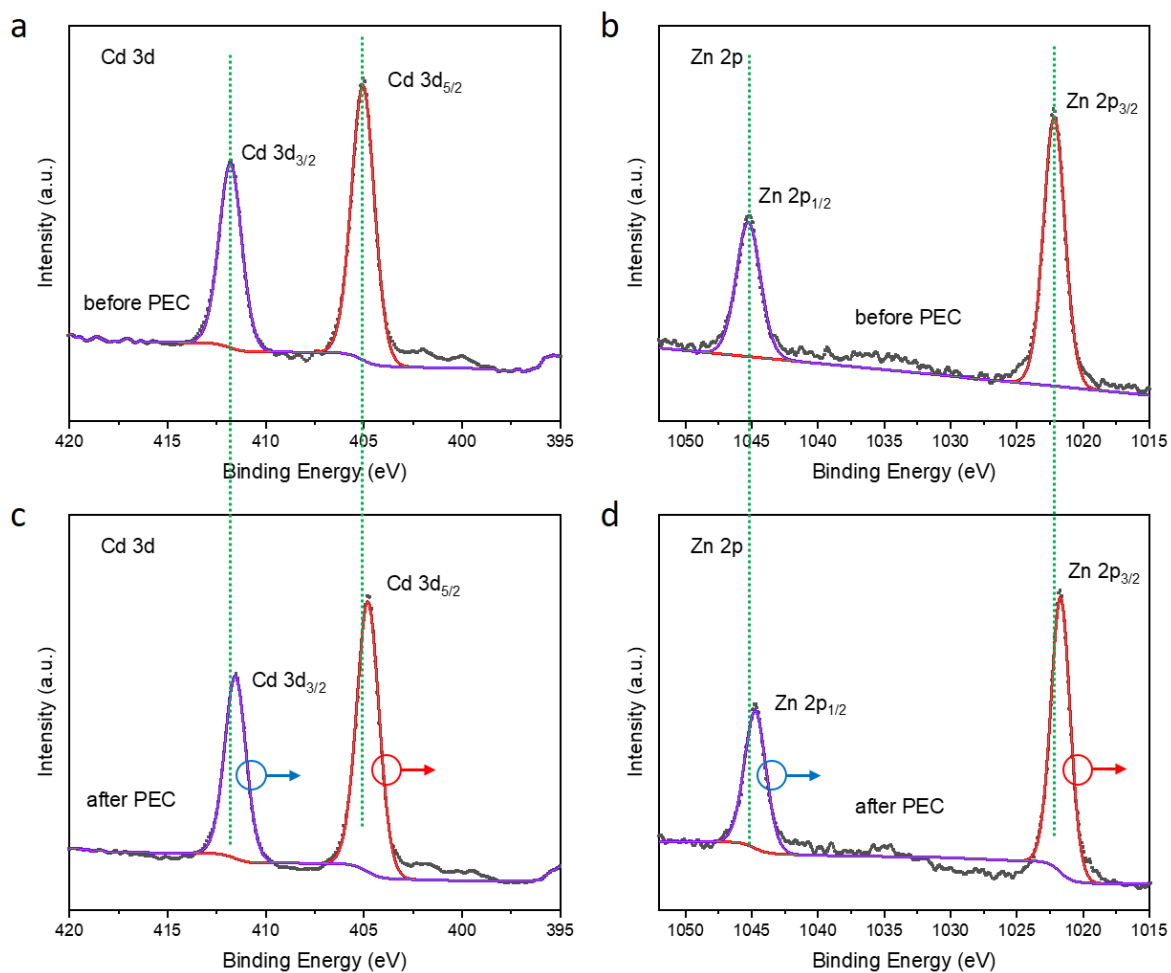


Figure 5.12 The high-resolution XPS spectra of Cd 3d and Zn 2p for photoanodes based on CdS/CdSe (1.6 nm) QDs treated with ZnS passivation layer (a and b) before and (c and d) after 2 h of PEC stability test.

To confirm that the obtained photocurrent leads to H₂ production in the experiment, GC was used to measure H₂ evolution and calculate the Faradaic efficiency (FE). As shown in Figure 5.13, the calculated FE for H₂ production has an average value of 81.7 % for CdS/CdSe (1.6 nm) QDs based PEC cells, indicating that the obtained photocurrent is mainly attributed to H₂ production.

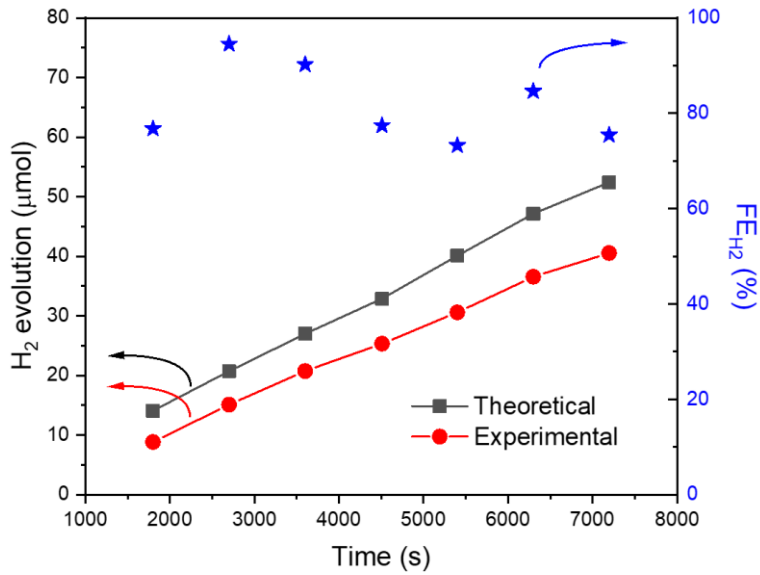


Figure 5.13 H₂ evolution of PEC cells based on CdS/CdSe (1.6 nm) QDs sensitized CNTs-TiO₂ photoanode as a function of time. The measurement was conducted at 0.6 V vs. RHE under continuous one sun illumination (100 mW/cm², AM 1.5G). The theoretical (calculated from the measured photocurrent) and experimental (measured from GC) evolution of H₂ are shown as black square and red circle, respectively. The FE value (blue star) of the corresponding PEC device is shown in the right vertical axis.

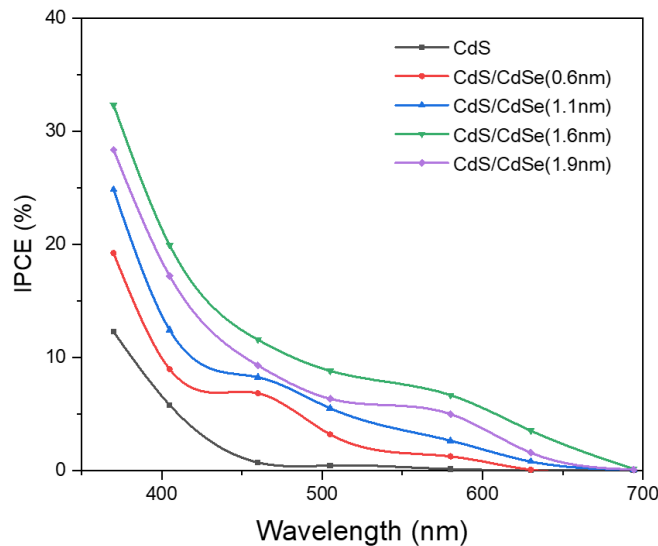


Figure 5.14 IPCE spectra of PEC devices based on CdS/CdSe QDs with different CdSe shell thickness (0, 0.6, 1.1, 1.6 and 1.9 nm), measured at 0.9 V vs. RHE.

In this work, as we did not use the real monochromatic incident photons, IPCE describes the ratio of photogenerated electrons collected by electrodes over the number of incident photons qualitatively. The qualitative IPCE values were measured and calculated for representative samples of PEC devices based on different types of as-prepared QDs. A systematic comparison of the qualitative IPCE values for PEC devices based on core/shell QDs with different shell thicknesses is shown in Figure 5.14. The qualitative IPCE values (at different wavelengths) of the PEC devices based on CdS/CdSe (1.6 nm) QDs are clearly higher than those of the other PEC devices based on CdS/CdSe core/shell QDs with different shell thickness (0, 0.6, 1.1 and 1.9 nm), over the whole visible spectrum from 370 to 690 nm. This is consistent with the obtained differences in the photocurrent density values.

To evaluate the performance of CdSe bare QDs for application in PEC cells, CdSe QDs with different sizes were synthesized. Then the optical properties of as-synthesized CdSe QDs were investigated by absorption and PL spectroscopy. Figure 5.15 shows the normalized absorption and PL spectra of as-synthesized CdSe QDs with different sizes. The first-excitonic absorption and PL peaks show gradually red shift with increasing size. The absorption peaks are located at 541, 560, 570, 584, 599 and 611 nm, respectively (Figure 5.15a). Accordingly, PL peaks are observed at 571, 579, 585, 595, 614 and 621 nm, respectively (Figure 5.15b). The sizes of the CdSe QDs are estimated from the first-excitonic absorption peaks by the following empirical equation:¹⁹

$$d = (1.6122 \times 10^{-9}) \lambda^4 - (2.6575 \times 10^{-6}) \lambda^3 + (1.6242 \times 10^{-3}) \lambda^2 - 0.4277 \lambda + 41.57 \quad (24)$$

where d is the diameter of QDs expressed in nm. The diameters of as-synthesized CdSe QDs are around 2.9, 3.2, 3.5, 4.0, 4.5 and 5.1 nm, respectively. Afterwards, CdSe QDs with sizes of 2.9, 3.5 and 5.1 nm were employed as photon absorber materials for PEC H₂ generation with an identical configuration of PEC cells based on CdS/CdSe core/shell QDs. As shown in Figure 5.16 and Table 5.4, the measured saturated photocurrent densities are 6.2, 5.3 and 4.2 mA/cm² for

PEC devices based on CdSe QDs with diameters of 2.9, 3.5 and 5.1 nm, respectively. Although the absorption is broadened with increasing size in CdSe QDs, the reducing electron injection efficiency in TiO₂/QDs system²⁰¹ largely limits the photon-to-current efficiency of PEC cells. The results confirm that the photocurrent density enhancement in PEC cells based on core/shell CdS/CdSe QDs when shell is thick cannot be achieved by only using CdSe bare QDs of comparable size.

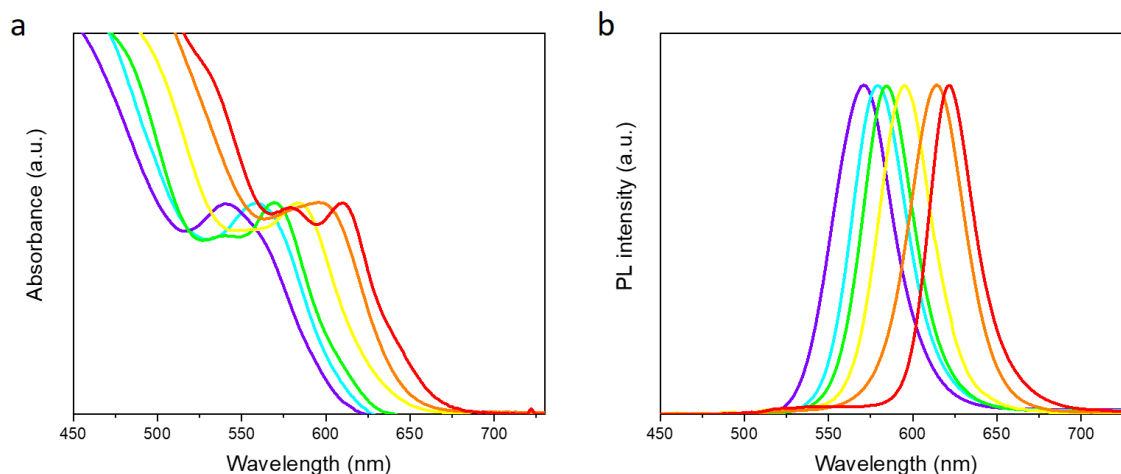


Figure 5.15 (a) Absorption spectra and (b) PL spectra of a series of CdSe QDs in toluene with different size synthesized by adjusting the reaction time: 1 min (violet color), 3 min (cyan color), 30 min (green color), 1 h (yellow color), 2.5 h (orange color) and 4 h (red color), respectively. The excitation wavelength is $\lambda_{ex} = 405$ nm.

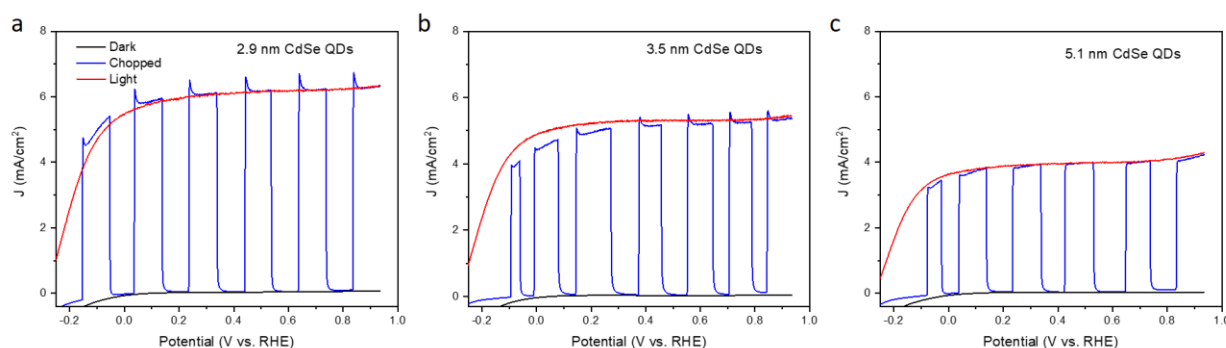


Figure 5.16 Photocurrent density versus the applied voltage (vs. RHE) curves of PEC devices assembled using the as-prepared QDs from CdSe, with sizes of (a) 2.9, (b) 3.5 and (c) 5.1 nm in

dark (black line), under constant one sun illumination (AM 1.5G, $100 \text{ mW} \cdot \text{cm}^{-2}$, red line) and under chopped one simulated sunlight illumination (blue line).

Table 5.4 Comparison of photocurrent densities of PEC devices based on bare CdSe QDs, and that based on the similar size of CdS/CdSe core/shell QDs.

| QDs | CdSe | | CdS/CdSe (1.1 nm) | |
|--|------|-----|-------------------|-----|
| Size (nm) | 2.9 | 3.5 | 5.1 | 5.1 |
| Photocurrent density (mA/cm^2) | 6.2 | 5.3 | 4.2 | 9.8 |

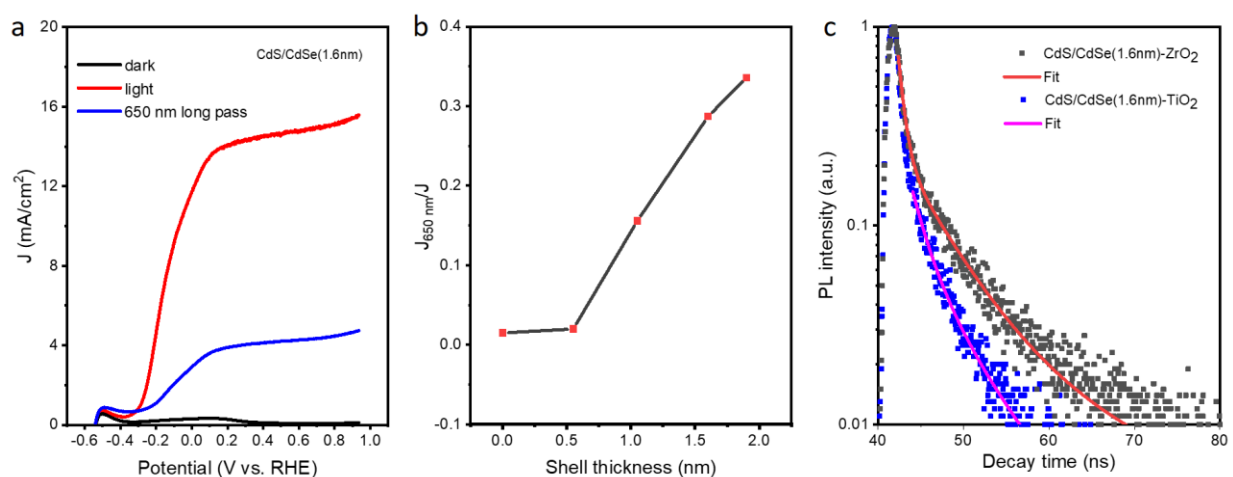


Figure 5.17 (a) Photocurrent density versus potential (vs. RHE) curves of PEC cells fabricated using CdS/CdSe (1.6 nm) QDs in dark (black curve), under 650 nm long-pass filter (blue curve) and under continuous one sun illumination (red curve). (b) The ratio of photocurrent density with or without 650 nm long-pass filter ($J_{650 \text{ nm}}/J$) as a function of shell thickness. (c) TRPL dynamic study of CdS/CdSe (1.6 nm) core/shell QDs deposited on TiO₂ and ZrO₂ mesoporous film. The excitation wavelength is $\lambda_{\text{ex}} = 444 \text{ nm}$.

To obtain further insights into the contribution for PEC performance from broadened absorption of the QDs, photocurrent densities of the photoanodes fabricated using different QDs under an optical filter were investigated, which can only pass light over 650 nm. As shown in Figure 5.17a and Figure 5.18a-d, the photocurrent density versus potential (vs. RHE) curves of PEC devices assembled using as-synthesized CdS/CdSe (1.1 nm), CdS/CdSe (1.6 nm) and CdS/CdSe (1.9 nm) QDs sensitized TiO₂ photoanodes under 650 nm long-pass filter demonstrate a significant

contribution to the saturated photocurrent density. However, the CdS bare QDs and CdS/CdSe (0.6 nm) core/shell QDs show almost no response of photocurrent under 650 nm filter. Figure 5.17b shows the ratio of photocurrent density with or without 650 nm long-pass filter (J_{650nm}/J) as a function of shell thickness. Results confirm that core/shell CdS/CdSe QDs offer a broader range of photon absorption during illumination and hence enhances the performance of PEC devices.

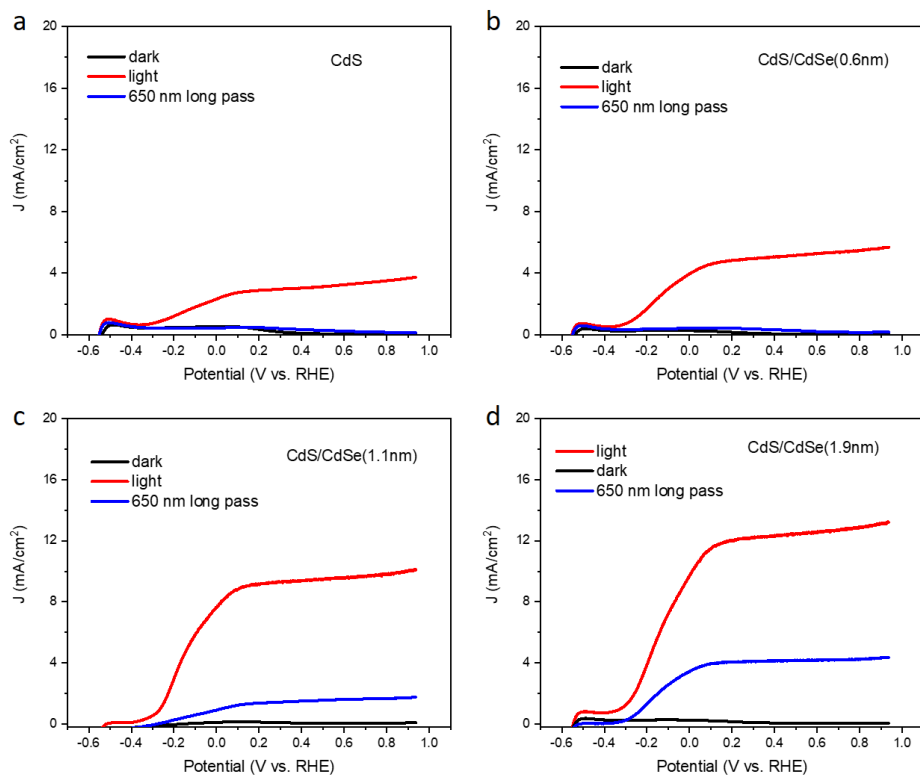


Figure 5.18 Photocurrent density versus potential (RHE) curves of PEC devices assembled using as-synthesized (a) CdS, (b) CdS/CdSe (0.6 nm), (c) CdS/CdSe (1.1 nm) and (d) CdS/CdSe (1.9 nm) QDs sensitized TiO₂ photoanode in the dark (black curve), under 650 nm long-pass filter (blue curve) and continuous one sun illumination (red curve), respectively.

5.2.5 Carrier dynamics

The electron transfer rate was measured by investigating the lifetime of QDs adsorbed on TiO₂ and ZrO₂ mesoporous films. ZrO₂ is used as a benchmark where the charge injection does not occur due to unfavourable electronic band alignment between ZrO₂ and QDs and PL degradation

can be attributed to charge recombination in the QDs. The electron transfer rate can be calculated using the following equation:⁹⁴

$$k_{ET} = \frac{1}{\tau(QDs/TiO_2)} - \frac{1}{\tau(QDs/ZrO_2)} \quad (25)$$

where k_{ET} is the electron transfer rate, which reflects the efficiency of the separation of the photo-induced exciton and subsequent carrier transport. $\tau(QDs/TiO_2)$ and $\tau(QDs/ZrO_2)$ are the average PL lifetimes for QDs adsorbed on TiO_2 and ZrO_2 , respectively. Figure 5.17c and 5.19a-d show the typical TRPL measurements for all the QDs samples adhered to the two different mesoporous films. The carrier transfer rates are obtained by fitting the PL decay curves of QDs on TiO_2 and ZrO_2 using equation (19) and are reported in Table 5.5. The k_{ET} shows a maximum value when the CdSe shell thickness is 1.6 nm, showing a more efficient electron transfer from the CB of CdS/CdSe (1.6 nm) towards that of TiO_2 , compared to other samples.

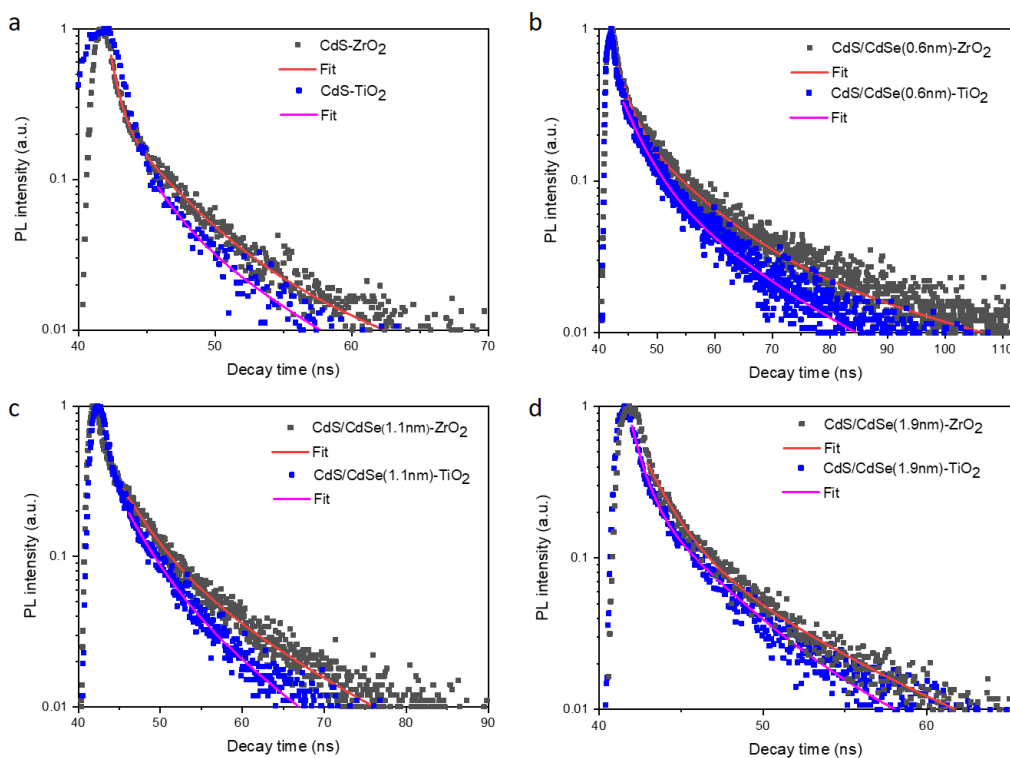


Figure 5.19 TRPL dynamic study of (a) CdS, (b) CdS/CdSe (0.6 nm), (c) CdS/CdSe (1.1 nm) and (d) CdS/CdSe (1.9 nm) QDs deposited on TiO_2 and ZrO_2 mesoporous film, respectively.

The decrease in k_{ET} reported for the thinnest shell QDs can be attributed to the formation of interfacial defects resulting from the lattice mismatch between CdS and CdSe (~3.3%)¹⁷⁵ as well as the fact that the electrons are not completely localized in the shell for these QDs (see Figure 5.8b). For core/shell QDs, the electron transfer was reported to be affected by the driving force of the electron injection and the electron density at the QD surface.^{201, 202} The driving force of the electron injection relies on the energy difference between the CB of the QDs and TiO₂.¹⁸⁵ As described in the theoretical simulations and depicted in Figure 5.3h, the thicker the shell, the smaller the driving force between CB of QDs and TiO₂, and the larger the electron density at the QD surface. As a result, even increasing CdSe shell thickness from 1.6 to 1.9 nm enhances the electron density on the surface of QD, the efficiency of electron injection decreases due to the decreased driving force. The higher k_{ET} values in the case of CdS/CdSe (1.6 nm) with respect to CdS/CdSe (1.9 nm) QDs, making the former suitable for charge separation in PEC cells. As a consequence, even though CdS/CdSe (1.9 nm) QDs show wider photo absorption compared to CdS/CdSe (1.6 nm) QDs, the latter has demonstrated a higher saturated photocurrent density value as a result of more favorable electrons transfer from QDs to the TiO₂ mesoporous film. In addition, the higher lifetime of CdS/CdSe (1.6 nm) QDs is also favorable for its higher photocurrent density in PEC cells. These findings show that the band structure and optoelectronic properties of heterostructured CdS/CdSe core/shell QDs can be tuned by altering the shell thickness. PEC cells based on CdS/CdSe (1.6 nm) QDs show an optimized photon-to-current conversion efficiency, thanks to the synergistic effect of improved light absorption and favorable band alignment.

Table 5.5 PL lifetimes of QDs with different substrates and calculated electron transfer rate.

| Samples | Lifetime with TiO ₂ τ (QDs/TiO ₂) (ns) | Lifetime with ZrO ₂ τ (QDs/ZrO ₂) (ns) | Electron transfer rate k_{ET} (10^7 s ⁻¹) |
|---------|---|---|---|
| CdS | 15 | 18 | 1.11 |

| | | | |
|-------------------|----|----|------|
| CdS/CdSe (0.6 nm) | 35 | 48 | 0.77 |
| CdS/CdSe (1.1 nm) | 28 | 38 | 0.94 |
| CdS/CdSe (1.6 nm) | 21 | 31 | 1.54 |
| CdS/CdSe (1.9 nm) | 14 | 17 | 1.26 |

5.3 Conclusions

In conclusion, CdS/CdSe core/shell QDs with the same CdS core (3.0 nm in diameter) and different CdSe shell thickness (0.6-1.9 nm) were designed and synthesized. Compared to CdS bare QDs, the light absorption of the CdS/CdSe core/shell QDs is extended significantly to longer wavelengths (up to 680 nm). Theoretical calculations illustrate how the band alignment evolves from a quasi type-II to an inverted type-I, as electrons gradually and holes rapidly delocalize into the shell region with progressively increased shell thickness. At the same time, changes in the radiative lifetime suggest a different likelihood of electrons and holes migrating to the shell for small shell thicknesses, in good agreement with the trend predicted from the overlap of hole and electron spatial probability distributions. Tuning the band alignment in this colloidal core/shell QD system has enabled the demonstration of a PEC cell with a photocurrent density of up to 16.0 mA/cm² (at 0.9 V vs. RHE) under one sun illumination. This is the highest value for the reported PEC cells based on CdS/CdSe QDs. In addition, the fabricated PEC cells also show significantly improved long-term stability, maintaining 83 % of its initial value after continuous one sun illumination for 4 h. These results show that the designed CdS/CdSe core/shell QDs hold great potential for applications in QD-based PEC cells for H₂ generation. The synergistic effect of a broadened light absorption range and improved electron transfer rate in this QD/TiO₂ system allows a more favorable light-harvesting and photoelectron transport. Results also highlight how engineering electron/hole wave functions of core/shell QDs offers an effective strategy to optimize

the optoelectronic properties of QDs for the development of cost-effective, highly efficient and stable PEC cells for H₂ generation and other optoelectronic devices.

Chapter 6. CONCLUSIONS AND PERSPECTIVES

6.1 Conclusions

In this thesis, first, a simple approach was designed to synthesize NIR colloidal PbS QDs using lead acetate and thiourea as lead and sulfide sources, respectively. By adjusting the reaction parameters, the size-tunable NIR PbS QDs (with the first-excitonic absorption peaks from 870 to 1400 nm) were obtained with narrow size distribution (<10%), high yield and good batch-to-batch consistency. Further Cd post-treatment was conducted to generate a passivating layer to improve the stability of the QDs. The as-prepared QDs were employed for application in both solar-driven H₂ generation and QDSCs. Under identical measurement conditions, the as-synthesized PbS QDs using thiourea as new inexpensive and air-stable precursor show a comparable or better device performance with respect to QDs synthesized using the commonly used toxic and air-sensitive (TMS)₂S precursor.

Second, the synthesis of oil-soluble Mn-doped PbS QDs was reported with well-controlled Mn concentration and uniform size distribution. The optical performance indicates that Mn-doped PbS QDs reveals a larger Stokes shift than pure PbS QDs samples with identical size. The schematic illustration of 'Mn-PbS' emission was proposed by investigating the band alignment of band edges of PbS QDs and Mn d-state. The midgap states created by Mn doping cause electrons to be transferred from the CB of the PbS host to Mn ⁴T₁ state and inhibit direct recombination with holes in the VB, which leads to a 'Mn-PbS' emission. The temperature-dependent optical properties were investigated for pure PbS and Mn-doped PbS QDs by exploring the PL peak energy shift and PL intensity variation in the 96-296 K temperature range. The temperature response of Mn-doped PbS QDs improves significantly as compared to the pure PbS QDs. This work demonstrates that Mn-doped PbS QDs are potential candidates for application in thermal sensors

and provides new fundamental knowledge of the emission mechanism and temperature dependent optical properties on Mn-doped QDs.

Third, colloidal and heterostructured CdS/CdSe core/shell QDs with the same CdS core (3.0 nm in diameter) and different CdSe shell thickness (0.6-1.9 nm) were designed and synthesized. Compared to bare CdS QDs, the light absorption of the core/shell QDs containing a CdSe layer is significantly extended towards longer wavelengths (up to 680 nm). Theoretical calculations by using the time-independent Schrödinger equation for spherical heterostructures illustrate how the band alignment evolves from a quasi type-II at a thin CdSe shell (0.6 nm) to a typical inverted type-I at thicker CdSe shell (1.1-1.9 nm), as electrons gradually and holes rapidly delocalize into the shell region with progressively increased shell thickness. At the same time, changes in the radiative lifetime suggest a different likelihood of electrons and holes migrating to the shell for small shell thicknesses, in good agreement with the trend predicted by considering the overlap of electron and hole spatial probability distributions obtained from the simple theoretical model described here. Tuning the band alignment in this colloidal core/shell QD system has enabled the demonstration of a PEC cell with a photocurrent density of up to 16.0 mA/cm² (at 0.9 V vs. RHE) under one sun illumination. This is the highest value ever reported for PEC cells based on CdS/CdSe QDs. In addition, the fabricated PEC cells also show significantly improved long-term stability, maintaining 83 % of its initial value after continuous one sun illumination for 4 hours. These results demonstrate that the designed core/shell QDs based photoanode holds great potential for applications in QD-based PEC cells. The synergistic effect of broadened light absorption and improved electron transfer rate in this QD/TiO₂ system allows a more favorable light-harvesting and photoelectron transport. Based on both the theoretical and experimental aspects, these results provide fundamental insights and offer an effective strategy to optimize the optoelectronic properties of QDs for the development of cost effective, high efficiency and stable PEC cells and other optoelectronic devices.

6.2 Perspectives

This thesis provides a simple and “greener” methodology for PbS QDs synthesis and holds great potential in advancing the systematic development of solution-processed QDs applications such as PbS QDs based devices including solar cells, solar-driven PEC cells for H₂ generation, photodetectors, sensors, light-emitting devices, luminescent solar concentrators.

A strategy of Mn doping in PbS QDs is developed to tune the Stokes shift. This strategy can be further developed in other elements (Ag, Cu, *etc.*) doped narrow band gap materials (PbSe, InAs, *etc.*). Moreover, the unique properties also make Mn-doped PbS QDs a potential candidate for future application in optoelectronics. For example, the enlarged Stokes shift in Mn-doped PbS QDs is favorable for fabricating high-efficiency luminescent solar concentrators. However, the QY of the as-synthesized Mn-doped PbS QDs is still very low, as opposed to a high QY demand for application in luminescent solar concentrators. The low QY is probably due to structural defects and surface traps caused by the partial Mn ions on the surface of QDs. These structural defects and surface traps may serve as non-radiative recombination centers. As such, improving the QY of the Mn-doped PbS QDs is an interesting research topic. It has been reported that coating a thin CdS shell on the surface of PbS QDs can significantly improve the QY. Future work could be focused on coating a thin CdS shell on the surface of Mn-doped PbS QDs, aiming to improve QY. The as-synthesized Mn-doped PbS/CdS QDs could be subsequently employed as emitters for luminescent solar concentrators and other optoelectronic devices.

Compared to the core/shell QDs with CdSe shell, a gradient CdSe_xS_{1-x} (for example, x=0.8, 0.6, 0.4, 0.2 and 0 for each monolayer) shell structure has the possibility to reduce core and shell sharp interface caused by lattice mismatch between CdS and CdSe. As such, it is interesting to explore a shell engineering approach to highlight the influence of shell components on the optoelectronic properties of core/shell QDs. The CdS/CdSe_xS_{1-x} QDs with gradient shell of CdS/CdSe_xS_{1-x} could be achieved by tailoring the molar ratios of Se and S during the growth of

each interfacial layer via high-temperature SILAR method. Then thorough investigation and discussion could be dedicated to how shell engineering in core/shell QDs affects their optoelectronic properties and carrier dynamics for further application in solar energy conversion technologies (photovoltaics and PEC devices for H₂ generation).

Future work could also be focused on the tuning of the optoelectronic properties in heterostructured core/shell QD systems by exploring different core sizes and compositions. In addition, its urgent need to promote the development of optoelectronic devices with low environmental impact. A prerequisite for the real applications of solar energy conversion devices is that the whole device is eco-friendly with better durability. In particular, for PbS, CdS and CdSe QDs based QDSC and PEC cells, there are concerns related to the use of toxic materials such as heavy-metal elements of Cd and Pb. Alternative such as Pb/Cd-free QDs based on ternary I-III-VI group materials such as CuInS₂ and CuInSe_xS_{2-x} have been proposed and they are promising for future applications. However, CuInS₂/CuInSe₂ QDs based optoelectronic devices have still issues of stability and the efficiency are still far behind compared to Cd/Pb based devices. Such investigations should also focus on extending the band engineering approach for developing suitable heavy-metal-free core/shell QDs for PEC H₂ generation.

Moreover, the design and synthesis of other types of core/shell QDs such as quasi type-II and type-II structured core/shell QDs, especially by choosing heavy-metal-free elements as core and shell components could be an interesting research direction. The optical properties and electronic band alignment can be optimized by tailoring the core and shell sizes of QDs. There is a chance to simultaneously obtain favorable band alignment and a desirable spatial separation of carriers in these two types of core/shell QDs, allowing reduced carrier recombination for application in QD-based PEC cells for H₂ generation. Then efforts should be dedicated in the investigation of the deep insights about carrier dynamics, light absorption and electron transfer rate in PEC cells based on both the theoretical and experimental aspects.

BIBLIOGRAPHY

1. Michalet, X.; Pinaud, F. F.; Bentolila, L. A.; Tsay, J. M.; Doose, S.; Li, J. J.; Sundaresan, G.; Wu, A. M.; Gambhir, S. S.; Weiss, S. *Science* **2005**, 307, (5709), 538-544.
2. Wen, L.; Qiu, L.; Wu, Y.; Hu, X.; Zhang, X. *Sensors* **2017**, 17, (8), 1736.
3. Yuan, M.; Liu, M.; Sargent, E. H. *Nature Energy* **2016**, 1, (3), 16016.
4. Meinardi, F.; Colombo, A.; Velizhanin, K. A.; Simonutti, R.; Lorenzon, M.; Beverina, L.; Viswanatha, R.; Klimov, V. I.; Brovelli, S. *Nature Photonics* **2014**, 8, 392.
5. Bradshaw, L. R.; Knowles, K. E.; McDowall, S.; Gamelin, D. R. *Nano Letters* **2015**, 15, (2), 1315-1323.
6. Sun, S.; Jaouen, F.; Dodelet, J.-P. *Advanced Materials* **2008**, 20, (20), 3900-3904.
7. Sung, J.; Ma, J.; Choi, S.-H.; Hong, J.; Kim, N.; Chae, S.; Son, Y.; Kim, S. Y.; Cho, J. *Advanced Materials* **2019**, 31, (33), 1900970.
8. Cheng, F.; Yang, X.; Zhang, S.; Lu, W. *Journal of Power Sources* **2020**, 450, 227678.
9. Enright, B.; Fitzmaurice, D. *The Journal of Physical Chemistry* **1996**, 100, (3), 1027-1035.
10. Wan, Y.; Norman, J.; Bowers, J., Chapter Nine - Quantum dot microcavity lasers on silicon substrates. In *Semiconductors and Semimetals*, Lourduoss, S.; Bowers, J. E.; Jagadish, C., Eds. Elsevier: 2019; Vol. 101, pp 305-354.
11. Mino, L.; Agostini, G.; Borfecchia, E.; Gianolio, D.; Piovano, A.; Gallo, E.; Lamberti, C. *Journal of Physics D: Applied Physics* **2013**, 46, (42), 423001.
12. Zherebetsky, D.; Scheele, M.; Zhang, Y.; Bronstein, N.; Thompson, C.; Britt, D.; Salmeron, M.; Alivisatos, P.; Wang, L.-W. *Science* **2014**, 344, (6190), 1380-1384.
13. Rossetti, R.; Hull, R.; Gibson, J. M.; Brus, L. E. *The Journal of Chemical Physics* **1985**, 83, (3), 1406-1410.
14. Brus, L. *The Journal of Physical Chemistry* **1986**, 90, (12), 2555-2560.
15. Murray, C. B.; Norris, D. J.; Bawendi, M. G. *Journal of the American Chemical Society* **1993**, 115, (19), 8706-8715.
16. Zhao, H.; Benetti, D.; Tong, X.; Zhang, H.; Zhou, Y.; Liu, G.; Ma, D.; Sun, S.; Wang, Z. M.; Wang, Y.; Rosei, F. *Nano Energy* **2018**, 50, 756-765.
17. Meinardi, F.; Ehrenberg, S.; Dharmo, L.; Carulli, F.; Mauri, M.; Bruni, F.; Simonutti, R.; Kortshagen, U.; Brovelli, S. *Nature Photonics* **2017**, 11, (3), 177-185.
18. Hines, M. A.; Scholes, G. D. *Advanced Materials* **2003**, 15, (21), 1844-1849.
19. Yu, W. W.; Qu, L.; Guo, W.; Peng, X. *Chem. Mater.* **2003**, 15, (14), 2854-2860.
20. Fuhr, A. S.; Yun, H. J.; Makarov, N. S.; Li, H.; McDaniel, H.; Klimov, V. I. *ACS Photonics* **2017**, 4, (10), 2425-2435.
21. McDaniel, H.; Fuke, N.; Pietryga, J. M.; Klimov, V. I. *The Journal of Physical Chemistry Letters* **2013**, 4, (3), 355-361.
22. Ma, W.; Luther, J. M.; Zheng, H.; Wu, Y.; Alivisatos, A. P. *Nano Letters* **2009**, 9, (4), 1699-1703.

23. Razgoniaeva, N.; Moroz, P.; Yang, M.; Budkina, D. S.; Eckard, H.; Augspurger, M.; Khon, D.; Tarnovsky, A. N.; Zamkov, M. *Journal of the American Chemical Society* **2017**, 139, (23), 7815-7822.
24. Yu, W. W.; Peng, X. *Angewandte Chemie International Edition* **2002**, 41, (13), 2368-2371.
25. Zhang, W.; Yang, W.; Zhong, P.; Mei, S.; Zhang, G.; Chen, G.; He, G.; Guo, R. *Opt. Mater. Express* **2017**, 7, (9), 3065-3076.
26. Wang, J.; Liu, G.; Merkoçi, A. *Journal of the American Chemical Society* **2003**, 125, (11), 3214-3215.
27. Peng, H.; Zhang, L.; Kjällman, T. H. M.; Soeller, C. *Journal of the American Chemical Society* **2007**, 129, (11), 3048-3049.
28. Zhao, H.; Rosei, F. *Chem* **2017**, 3, (2), 229-258.
29. Reiss, P.; Protière, M.; Li, L. *Small* **2009**, 5, (2), 154-168.
30. Cademartiri, L.; Montanari, E.; Calestani, G.; Migliori, A.; Guagliardi, A.; Ozin, G. A. *Journal of the American Chemical Society* **2006**, 128, (31), 10337-10346.
31. Liu, Y.; Kim, D.; Morris, O. P.; Zhitomirsky, D.; Grossman, J. C. *ACS Nano* **2018**, 12, (3), 2838-2845.
32. Guria, A. K.; Dutta, S. K.; Adhikari, S. D.; Pradhan, N. *ACS Energy Letters* **2017**, 2, (5), 1014-1021.
33. Santra, P. K.; Kamat, P. V. *J. Am. Chem. Soc.* **2012**, 134, (5), 2508-2511.
34. Bhargava, R. N.; Gallagher, D.; Hong, X.; Nurmikko, A. *Phys. Rev. Lett.* **1994**, 72, (3), 416-419.
35. Jana, S.; Srivastava, B. B.; Pradhan, N. *The Journal of Physical Chemistry Letters* **2011**, 2, (14), 1747-1752.
36. Beaulac, R.; Archer, P. I.; Ochsenein, S. T.; Gamelin, D. R. *Advanced Functional Materials* **2008**, 18, (24), 3873-3891.
37. Beaulac, R.; Archer, P. I.; Gamelin, D. R. *Journal of Solid State Chemistry* **2008**, 181, (7), 1582-1589.
38. Zeng, R.; Rutherford, M.; Xie, R.; Zou, B.; Peng, X. *Chem. Mater.* **2010**, 22, (6), 2107-2113.
39. Hazarika, A.; Pandey, A.; Sarma, D. D. *The Journal of Physical Chemistry Letters* **2014**, 5, (13), 2208-2213.
40. Peka, P.; Schulz, H. J. *Physica B: Condensed Matter* **1994**, 193, (1), 57-65.
41. Men, L.; Rosales, B. A.; Gentry, N. E.; Cady, S. D.; Vela, J. *ChemNanoMat* **2019**, 5, (3), 334-339.
42. Zou, S.; Liu, Y.; Li, J.; Liu, C.; Feng, R.; Jiang, F.; Li, Y.; Song, J.; Zeng, H.; Hong, M.; Chen, X. *Journal of the American Chemical Society* **2017**, 139, (33), 11443-11450.
43. Liu, H.; Wu, Z.; Shao, J.; Yao, D.; Gao, H.; Liu, Y.; Yu, W.; Zhang, H.; Yang, B. *ACS Nano* **2017**, 11, (2), 2239-2247.
44. Mir, W. J.; Jagadeeswararao, M.; Das, S.; Nag, A. *ACS Energy Letters* **2017**, 2, (3), 537-543.

45. Thompson, M. J.; Blakeney, K. J.; Cady, S. D.; Reichert, M. D.; Pilar-Albaladejo, J. D.; White, S. T.; Vela, J. *Chemistry of Materials* **2016**, 28, (6), 1668-1677.
46. Erickson, C. S.; Bradshaw, L. R.; McDowall, S.; Gilbertson, J. D.; Gamelin, D. R.; Patrick, D. L. *ACS Nano* **2014**, 8, (4), 3461-3467.
47. Vlaskin, V. A.; Janssen, N.; van Rijssel, J.; Beaulac, R.; Gamelin, D. R. *Nano Lett.* **2010**, 10, (9), 3670-3674.
48. Li, Z.-J.; Hofman, E.; Blaker, A.; Davis, A. H.; Dzikovski, B.; Ma, D.-K.; Zheng, W. *ACS Nano* **2017**, 11, (12), 12591-12600.
49. Davis, A. H.; Hofman, E.; Chen, K.; Li, Z.-J.; Khammang, A.; Zamani, H.; Franck, J. M.; Maye, M. M.; Meulenberg, R. W.; Zheng, W. *Chem. Mater.* **2019**, 31, (7), 2516-2523.
50. Li, Z.-J.; Hofman, E.; Davis, A. H.; Khammang, A.; Wright, J. T.; Dzikovski, B.; Meulenberg, R. W.; Zheng, W. *Chem. Mater.* **2018**, 30, (18), 6400-6409.
51. Pradhan, N.; Battaglia, D. M.; Liu, Y.; Peng, X. *Nano Lett.* **2007**, 7, (2), 312-317.
52. Debnath, T.; Maity, P.; Maiti, S.; Ghosh, H. N. *The Journal of Physical Chemistry Letters* **2014**, 5, (16), 2836-2842.
53. Irvine, S. E.; Staudt, T.; Rittweger, E.; Engelhardt, J.; Hell, S. W. *Angew. Chem.* **2008**, 120, (14), 2725-2728.
54. McLaurin, E. J.; Vlaskin, V. A.; Gamelin, D. R. *Journal of the American Chemical Society* **2011**, 133, (38), 14978-14980.
55. Park, Y.-S.; Bae, W. K.; Pietryga, J. M.; Klimov, V. I. *ACS Nano* **2014**, 8, (7), 7288-7296.
56. Hou, X.; Kang, J.; Qin, H.; Chen, X.; Ma, J.; Zhou, J.; Chen, L.; Wang, L.; Wang, L.-W.; Peng, X. *Nature Communications* **2019**, 10, (1), 1750.
57. Li, Y.; Ding, T.; Luo, X.; Chen, Z.; Liu, X.; Lu, X.; Wu, K. *Nano Research* **2019**, 12, (3), 619-623.
58. Barrows, C. J.; Rinehart, J. D.; Nagaoka, H.; deQuilettes, D. W.; Salvador, M.; Chen, J. I. L.; Ginger, D. S.; Gamelin, D. R. *The Journal of Physical Chemistry Letters* **2017**, 8, (1), 126-130.
59. Wu, P.; He, Y.; Wang, H.-F.; Yan, X.-P. *Anal. Chem.* **2010**, 82, (4), 1427-1433.
60. Norris, D. J.; Yao, N.; Charnock, F. T.; Kennedy, T. A. *Nano Lett.* **2001**, 1, (1), 3-7.
61. Tan, R.; Yuan, Y.; Nagaoka, Y.; Eggert, D.; Wang, X.; Thota, S.; Guo, P.; Yang, H.; Zhao, J.; Chen, O. *Chemistry of Materials* **2017**, 29, (9), 4097-4108.
62. Balet, L. P.; Ivanov, S. A.; Piryatinski, A.; Achermann, M.; Klimov, V. I. *Nano Letters* **2004**, 4, (8), 1485-1488.
63. Piryatinski, A.; Ivanov, S. A.; Tretiak, S.; Klimov, V. I. *Nano Letters* **2007**, 7, (1), 108-115.
64. Pan, Z.; Zhang, H.; Cheng, K.; Hou, Y.; Hua, J.; Zhong, X. *ACS Nano* **2012**, 6, (5), 3982-3991.
65. Lee, Y.-L.; Lo, Y.-S. *Advanced Functional Materials* **2009**, 19, (4), 604-609.
66. Lee, Y.-L.; Chi, C.-F.; Liao, S.-Y. *Chemistry of Materials* **2010**, 22, (3), 922-927.
67. Ko, D.-K.; Brown, P. R.; Bawendi, M. G.; Bulović, V. *Advanced Materials* **2014**, 26, (28), 4845-4850.

68. Carey, G. H.; Abdelhady, A. L.; Ning, Z.; Thon, S. M.; Bakr, O. M.; Sargent, E. H. *Chem. Rev.* **2015**, 115, (23), 12732-12763.
69. Grätzel, M. *Nature* **2001**, 414, 338.
70. Sargent, E. H. *Nature Photonics* **2012**, 6, 133.
71. Selopal, G. S.; Zhao, H.; Wang, Z. M.; Rosei, F. *Advanced Functional Materials* **2020**, 30, (13), 1908762.
72. Liu, M.; de Arquer, F. P. G.; Li, Y.; Lan, X.; Kim, G.-H.; Voznyy, O.; Jagadamma, L. K.; Abbas, A. S.; Hoogland, S.; Lu, Z.; Kim, J. Y.; Amassian, A.; Sargent, E. H. *Advanced Materials* **2016**, 28, (21), 4142-4148.
73. Jin, L.; AlOtaibi, B.; Benetti, D.; Li, S.; Zhao, H.; Mi, Z.; Vomiero, A.; Rosei, F. *Advanced Science* **2016**, 3, (3), n/a-n/a.
74. Kamat, P. V.; Tvrđy, K.; Baker, D. R.; Radich, J. G. *Chemical Reviews* **2010**, 110, (11), 6664-6688.
75. Zhao, H.; Benetti, D.; Jin, L.; Zhou, Y.; Rosei, F.; Vomiero, A. *Small* **2016**, 12, (38), 5354-5365.
76. Konstantatos, G.; Howard, I.; Fischer, A.; Hoogland, S.; Clifford, J.; Klem, E.; Levina, L.; Sargent, E. H. *Nature* **2006**, 442, (7099), 180-183.
77. Lee, J.-S.; Kovalenko, M. V.; Huang, J.; Chung, D. S.; Talapin, D. V. *Nat Nano* **2011**, 6, (6), 348-352.
78. Sun, Q.; Wang, Y. A.; Li, L. S.; Wang, D.; Zhu, T.; Xu, J.; Yang, C.; Li, Y. *Nat Photon* **2007**, 1, (12), 717-722.
79. Chuang, C.-H. M.; Brown, P. R.; Bulović, V.; Bawendi, M. G. *Nat Mater* **2014**, 13, (8), 796-801.
80. Lan, X.; Voznyy, O.; Kiani, A.; García de Arquer, F. P.; Abbas, A. S.; Kim, G.-H.; Liu, M.; Yang, Z.; Walters, G.; Xu, J.; Yuan, M.; Ning, Z.; Fan, F.; Kanjanaboos, P.; Kramer, I.; Zhitomirsky, D.; Lee, P.; Perelgut, A.; Hoogland, S.; Sargent, E. H. *Advanced Materials* **2016**, 28, (2), 299-304.
81. Zhao, H.; Vomiero, A.; Rosei, F. *Small* **2015**, 11, (43), 5741-5746.
82. Han, S.; Yang, X.; Zhu, Y.; Tan, C.; Zhang, X.; Chen, J.; Huang, Y.; Chen, B.; Luo, Z.; Ma, Q.; Sindoro, M.; Zhang, H.; Qi, X.; Li, H.; Huang, X.; Huang, W.; Sun, X. W.; Han, Y.; Zhang, H. *Angew. Chem. Int. Ed.* **2017**, 56, (35), 10486-10490.
83. Pan, Z.; Rao, H.; Mora-Seró, I.; Bisquert, J.; Zhong, X. *Chem. Soc. Rev.* **2018**, 47, (20), 7659-7702.
84. Heiniger, L.-P.; O'Brien, P. G.; Soheilnia, N.; Yang, Y.; Kherani, N. P.; Grätzel, M.; Ozin, G. A.; Tétreault, N. *Adv. Mater.* **2013**, 25, (40), 5734-5741.
85. Mao, W.; Zheng, J.; Zhang, Y.; Chesman, A. S. R.; Ou, Q.; Hicks, J.; Li, F.; Wang, Z.; Graystone, B.; Bell, T. D. M.; Rothmann, M. U.; Duffy, N. W.; Spiccia, L.; Cheng, Y.-B.; Bao, Q.; Bach, U. *Angew. Chem. Int. Ed.* **2017**, 56, (41), 12486-12491.
86. Chan, S.; Liu, M.; Latham, K.; Haruta, M.; Kurata, H.; Teranishi, T.; Tachibana, Y. *Journal of Materials Chemistry C* **2017**, 5, (8), 2182-2187.
87. Navarro-Pardo, F.; Zhao, H.; Wang, Z. M.; Rosei, F. *Accounts of Chemical Research* **2018**, 51, (3), 609-618.

88. Jin, L.; AlOtaibi, B.; Benetti, D.; Li, S.; Zhao, H.; Mi, Z.; Vomiero, A.; Rosei, F. *Advanced Science* **2016**, 3, (3), 1500345.
89. Wang, G.; Wei, H.; Luo, Y.; Wu, H.; Li, D.; Zhong, X.; Meng, Q. *Journal of Power Sources* **2016**, 302, 266-273.
90. Pan, Z.; Mora-Seró, I.; Shen, Q.; Zhang, H.; Li, Y.; Zhao, K.; Wang, J.; Zhong, X.; Bisquert, J. *Journal of the American Chemical Society* **2014**, 136, (25), 9203-9210.
91. Pan, Z.; Zhao, K.; Wang, J.; Zhang, H.; Feng, Y.; Zhong, X. *ACS Nano* **2013**, 7, (6), 5215-5222.
92. Zhao, H.; Sirigu, G.; Parisini, A.; Camellini, A.; Nicotra, G.; Rosei, F.; Morandi, V.; Zavelani-Rossi, M.; Vomiero, A. *Nanoscale* **2016**, 8, (7), 4217-4226.
93. Jin, L.; Sirigu, G.; Tong, X.; Camellini, A.; Parisini, A.; Nicotra, G.; Spinella, C.; Zhao, H.; Sun, S.; Morandi, V.; Zavelani-Rossi, M.; Rosei, F.; Vomiero, A. *Nano Energy* **2016**, 30, (Supplement C), 531-541.
94. Adhikari, R.; Jin, L.; Navarro-Pardo, F.; Benetti, D.; AlOtaibi, B.; Vanka, S.; Zhao, H.; Mi, Z.; Vomiero, A.; Rosei, F. *Nano Energy* **2016**, 27, 265-274.
95. Zhao, K.; Pan, Z.; Zhong, X. *The Journal of Physical Chemistry Letters* **2016**, 7, (3), 406-417.
96. Sun, J.-K.; Jiang, Y.; Zhong, X.; Hu, J.-S.; Wan, L.-J. *Nano Energy* **2017**, 32, 130-156.
97. Chen, H.; Zhu, L.; Liu, H.; Li, W., 10 - Zinc Hydroxyfluoride (ZnOHF) Nanostructure as Photoelectrode of Quantum Dot-Sensitized Solar Cells. In *Photonic and Electronic Properties of Fluoride Materials*, Tressaud, A.; Poepelmeier, K., Eds. Elsevier: Boston, 2016; pp 199-210.
98. Kamat, P. V. *The Journal of Physical Chemistry Letters* **2013**, 4, (6), 908-918.
99. Semonin, O. E.; Luther, J. M.; Choi, S.; Chen, H.-Y.; Gao, J.; Nozik, A. J.; Beard, M. C. *Science* **2011**, 334, (6062), 1530-1533.
100. Zhang, H.; Fang, W.; Wang, W.; Qian, N.; Ji, X. *ACS Applied Materials & Interfaces* **2019**, 11, (7), 6927-6936.
101. Selopal, G. S.; Zhao, H.; Tong, X.; Benetti, D.; Navarro-Pardo, F.; Zhou, Y.; Barba, D.; Vidal, F.; Wang, Z. M.; Rosei, F. *Advanced Functional Materials* **2017**, 27, (30), 1701468.
102. Jiao, S.; Wang, J.; Shen, Q.; Li, Y.; Zhong, X. *Journal of Materials Chemistry A* **2016**, 4, (19), 7214-7221.
103. Nozik, A. J. *Physica E: Low-dimensional Systems and Nanostructures* **2002**, 14, (1), 115-120.
104. Nozik, A. J. *Chemical Physics Letters* **2008**, 457, (1), 3-11.
105. Fujishima, A.; Honda, K. *Nature* **1972**, 238, 37.
106. Kudo, A.; Miseki, Y. *Chemical Society Reviews* **2009**, 38, (1), 253-278.
107. Wu, H. W.; Emadi, A.; de Graaf, G.; Leijtens, J.; Wolffenbuttel, R. F. *Procedia Engineering* **2011**, 25, 527-530.
108. Hensel, J.; Wang, G.; Li, Y.; Zhang, J. Z. *Nano Letters* **2010**, 10, (2), 478-483.
109. Yang, X.; Wolcott, A.; Wang, G.; Sobo, A.; Fitzmorris, R. C.; Qian, F.; Zhang, J. Z.; Li, Y. *Nano Letters* **2009**, 9, (6), 2331-2336.

110. Li, X.; Zhang, Z.; Chen, L.; Liu, Z.; Cheng, J.; Ni, W.; Xie, E.; Wang, B. *Journal of Power Sources* **2014**, 269, 866-872.
111. Chen, C. K.; Shen, Y.-P.; Chen, H. M.; Chen, C.-J.; Chan, T.-S.; Lee, J.-F.; Liu, R.-S. *European Journal of Inorganic Chemistry* **2014**, 2014, (4), 773-779.
112. Wu, L.; Chen, S.-Y.; Fan, F.-J.; Zhuang, T.-T.; Dai, C.-M.; Yu, S.-H. *Journal of the American Chemical Society* **2016**, 138, (17), 5576-5584.
113. Tong, X.; Kong, X.-T.; Wang, C.; Zhou, Y.; Navarro-Pardo, F.; Barba, D.; Ma, D.; Sun, S.; Govorov, A. O.; Zhao, H.; Wang, Z. M.; Rosei, F. *Advanced Science* **2018**, 5, (8), 1800656.
114. Wang, D.; Baral, J. K.; Zhao, H.; Gonfa, B. A.; Truong, V.-V.; El Khakani, M. A.; Izquierdo, R.; Ma, D. *Advanced Functional Materials* **2011**, 21, (21), 4010-4018.
115. Yuan, M.; Kemp, K. W.; Thon, S. M.; Kim, J. Y.; Chou, K. W.; Amassian, A.; Sargent, E. H. *Advanced Materials* **2014**, 26, (21), 3513-3519.
116. Turyanska, L.; Moro, F.; Knott, A. N.; Fay, M. W.; Bradshaw, T. D.; Patanè, A. *Particle & Particle Systems Characterization* **2013**, 30, (11), 945-949.
117. Turyanska, L.; Hill, R. J. A.; Makarovskiy, O.; Moro, F.; Knott, A. N.; Larkin, O. J.; Patane, A.; Meaney, A.; Christianen, P. C. M.; Fay, M. W.; Curry, R. J. *Nanoscale* **2014**, 6, (15), 8919-8925.
118. Zhang, H.; Selopal, G. S.; Zhou, Y.; Tong, X.; Benetti, D.; Jin, L.; Navarro-Pardo, F.; Wang, Z.; Sun, S.; Zhao, H.; Rosei, F. *Nanoscale* **2017**, 9, (43), 16843-16851.
119. Zhang, H.; Liu, J.; Wang, C.; Selopal, G. S.; Barba, D.; Wang, Z. M.; Sun, S.; Zhao, H.; Rosei, F. *ACS Photonics* **2019**, 6, (10), 2421-2431.
120. Zhang, H.; Besteiro, L. V.; Liu, J.; Wang, C.; Selopal, G. S.; Chen, Z.; Barba, D.; Wang, Z. M.; Zhao, H.; Lopinski, G. P.; Sun, S.; Rosei, F. *Nano Energy* **2021**, 79, 105416.
121. Brouwer, A. M. *Pure and Applied Chemistry* **2011**, 83, (12), 2213.
122. Qu, L.; Peng, X. *J. Am. Chem. Soc.* **2002**, 124, (9), 2049-2055.
123. Zhao, H.; Wang, D.; Zhang, T.; Chaker, M.; Ma, D. *Chemical Communications* **2010**, 46, (29), 5301-5303.
124. Zhu, R.; Lu, R.; Yu, A. *Physical Chemistry Chemical Physics* **2011**, 13, (46), 20844-20854.
125. Wang, W.; Feng, W.; Du, J.; Xue, W.; Zhang, L.; Zhao, L.; Li, Y.; Zhong, X. *Advanced Materials* **2018**, 30, (11), 1705746.
126. Zhao, H.; Liu, G.; Vidal, F.; Wang, Y.; Vomiero, A. *Nano Energy* **2018**, 53, 116-124.
127. Purcell-Milton, F.; Curutchet, A.; Gun'ko, Y. *Materials* **2019**, 12, (24), 4089.
128. Cirillo, M.; Strubbe, F.; Neyts, K.; Hens, Z. *ACS Nano* **2011**, 5, (2), 1345-1352.
129. Zhao, H.; Fan, Z.; Liang, H.; Selopal, G. S.; Gonfa, B. A.; Jin, L.; Soudi, A.; Cui, D.; Enrichi, F.; Natile, M. M.; Concina, I.; Ma, D.; Govorov, A. O.; Rosei, F.; Vomiero, A. *Nanoscale* **2014**, 6, (12), 7004-7011.
130. Hendricks, M. P.; Campos, M. P.; Cleveland, G. T.; Jen-La Plante, I.; Owen, J. S. *Science* **2015**, 348, (6240), 1226.
131. Zhao, H.; Chaker, M.; Ma, D. *Journal of Materials Chemistry* **2011**, 21, (43), 17483-17491.

132. Zhang, T.; Zhao, H.; Riabinina, D.; Chaker, M.; Ma, D. *The Journal of Physical Chemistry C* **2010**, 114, (22), 10153-10159.
133. Zhou, Y.; Benetti, D.; Fan, Z.; Zhao, H.; Ma, D.; Govorov, A. O.; Vomiero, A.; Rosei, F. *Advanced Energy Materials* **2016**, 6, (11), n/a-n/a.
134. Docampo, P.; Ball, J. M.; Darwich, M.; Eperon, G. E.; Snaith, H. J. *Nature Communications* **2013**, 4, 2761.
135. Jin, L.; Zhao, H.; Ma, D.; Vomiero, A.; Rosei, F. *Journal of Materials Chemistry A* **2015**, 3, (2), 847-856.
136. Yang, H. B.; Miao, J.; Hung, S.-F.; Huo, F.; Chen, H. M.; Liu, B. *ACS Nano* **2014**, 8, (10), 10403-10413.
137. van de Krol, R.; Grätzel, M., *Photoelectrochemical Hydrogen Production*. Springer US: 2011.
138. Trevisan, R.; Rodenas, P.; Gonzalez-Pedro, V.; Sima, C.; Sanchez, R. S.; Barea, E. M.; Mora-Sero, I.; Fabregat-Santiago, F.; Gimenez, S. *The Journal of Physical Chemistry Letters* **2013**, 4, (1), 141-146.
139. Kang, I.; Wise, F. W. *J. Opt. Soc. Am. B* **1997**, 14, (7), 1632-1646.
140. Ren, Z.; Wang, J.; Pan, Z.; Zhao, K.; Zhang, H.; Li, Y.; Zhao, Y.; Mora-Sero, I.; Bisquert, J.; Zhong, X. *Chemistry of Materials* **2015**, 27, (24), 8398-8405.
141. Pattantyus-Abraham, A. G.; Kramer, I. J.; Barkhouse, A. R.; Wang, X.; Konstantatos, G.; Debnath, R.; Levina, L.; Raabe, I.; Nazeeruddin, M. K.; Grätzel, M.; Sargent, E. H. *ACS Nano* **2010**, 4, (6), 3374-3380.
142. Jin-nouchi, Y.; Hattori, T.; Sumida, Y.; Fujishima, M.; Tada, H. *ChemPhysChem* **2010**, 11, (17), 3592-3595.
143. Grätzel, M. *Nature* **2001**, 414, (6861), 338-344.
144. Hyun, B.-R.; Zhong, Y.-W.; Bartnik, A. C.; Sun, L.; Abruña, H. D.; Wise, F. W.; Goodreau, J. D.; Matthews, J. R.; Leslie, T. M.; Borrelli, N. F. *ACS Nano* **2008**, 2, (11), 2206-2212.
145. Wu, K.; Chen, Z.; Lv, H.; Zhu, H.; Hill, C. L.; Lian, T. *Journal of the American Chemical Society* **2014**, 136, (21), 7708-7716.
146. Thulasi-Varma, C. V.; Rao, S. S.; Ikkurthi, K. D.; Kim, S.-K.; Kang, T.-S.; Kim, H.-J. *Journal of Materials Chemistry C* **2015**, 3, (39), 10195-10206.
147. Mora-Seró, I.; Giménez, S.; Fabregat-Santiago, F.; Gómez, R.; Shen, Q.; Toyoda, T.; Bisquert, J. *Accounts of Chemical Research* **2009**, 42, (11), 1848-1857.
148. González-Pedro, V.; Xu, X.; Mora-Seró, I.; Bisquert, J. *ACS Nano* **2010**, 4, (10), 5783-5790.
149. Du, J.; Du, Z.; Hu, J.-S.; Pan, Z.; Shen, Q.; Sun, J.; Long, D.; Dong, H.; Sun, L.; Zhong, X.; Wan, L.-J. *Journal of the American Chemical Society* **2016**, 138, (12), 4201-4209.
150. Moreels, I.; Lambert, K.; Smeets, D.; De Muynck, D.; Nollet, T.; Martins, J. C.; Vanhaecke, F.; Vantomme, A.; Delerue, C.; Allan, G.; Hens, Z. *ACS Nano* **2009**, 3, (10), 3023-3030.
151. Neo, D. C. J.; Cheng, C.; Stranks, S. D.; Fairclough, S. M.; Kim, J. S.; Kirkland, A. I.; Smith, J. M.; Snaith, H. J.; Assender, H. E.; Watt, A. A. R. *Chem. Mater.* **2014**, 26, (13), 4004-4013.

152. Yost, A. J.; Pimachev, A.; Rimal, G.; Tang, J.; Dahnovsky, Y.; Chien, T. *Appl. Phys. Lett.* **2017**, 111, (23), 233101.
153. Dantas, N. O.; Pelegrini, F.; Novak, M. A.; Morais, P. C.; Marques, G. E.; Silva, R. S. *J. Appl. Phys.* **2012**, 111, (6), 064311.
154. Yang, X.; Pu, C.; Qin, H.; Liu, S.; Xu, Z.; Peng, X. *J. Am. Chem. Soc.* **2019**, 141, (6), 2288-2298.
155. Zheng, W.; Wang, Z.; Wright, J.; Goundie, B.; Dalal, N. S.; Meulenberg, R. W.; Strouse, G. F. *The Journal of Physical Chemistry C* **2011**, 115, (47), 23305-23314.
156. Silva, R. S.; Morais, P. C.; Qu, F.; Alcalde, A. M.; Dantas, N. O.; Sullasi, H. S. L. *Appl. Phys. Lett.* **2007**, 90, (25), 253114.
157. Hofman, E.; Robinson, R. J.; Li, Z.-J.; Dzikovski, B.; Zheng, W. *J. Am. Chem. Soc.* **2017**, 139, (26), 8878-8885.
158. Zhao, H.; Liang, H.; Vidal, F.; Rosei, F.; Vomiero, A.; Ma, D. *The Journal of Physical Chemistry C* **2014**, 118, (35), 20585-20593.
159. Selopal, G. S.; Zhao, H.; Liu, G.; Zhang, H.; Tong, X.; Wang, K.; Tang, J.; Sun, X.; Sun, S.; Vidal, F.; Wang, Y.; Wang, Z. M.; Rosei, F. *Nano Energy* **2019**, 55, 377-388.
160. Zhao, H.; Liu, J.; Vidal, F.; Vomiero, A.; Rosei, F. *Nanoscale* **2018**, 10, (36), 17189-17197.
161. Pu, C.; Qin, H.; Gao, Y.; Zhou, J.; Wang, P.; Peng, X. *Journal of the American Chemical Society* **2017**, 139, (9), 3302-3311.
162. Beaulac, R.; Archer, P. I.; Liu, X.; Lee, S.; Salley, G. M.; Dobrowolska, M.; Furdyna, J. K.; Gamelin, D. R. *Nano Lett.* **2008**, 8, (4), 1197-1201.
163. Tan, L.; Zhou, Y.; Ren, F.; Benetti, D.; Yang, F.; Zhao, H.; Rosei, F.; Chaker, M.; Ma, D. *Journal of Materials Chemistry A* **2017**, 5, (21), 10250-10260.
164. Park, Y.; Son, D. H. *Bull. Korean Chem. Soc.* **2015**, 36, (3), 757-761.
165. Tvrđy, K.; Frantsuzov, P. A.; Kamat, P. V. *Proceedings of the National Academy of Sciences* **2011**, 108, (1), 29-34.
166. Du, K.; Liu, G.; Chen, X.; Wang, K. *J. Electrochem. Soc.* **2015**, 162, (10), E251-E257.
167. Lewis, J. E.; Wu, S.; Jiang, X. *Nanotechnology* **2010**, 21, (45), 455402.
168. Nordin, M. N.; Juerong, L.; Clowes, S. K.; Curry, R. J. *Nanotechnology* **2012**, 23, (27), 275701.
169. Valerini, D.; Cretí, A.; Lomascolo, M.; Manna, L.; Cingolani, R.; Anni, M. *Physical Review B* **2005**, 71, (23), 235409.
170. Liu, W.; Zhang, Y.; Zhai, W.; Wang, Y.; Zhang, T.; Gu, P.; Chu, H.; Zhang, H.; Cui, T.; Wang, Y.; Zhao, J.; Yu, W. W. *The Journal of Physical Chemistry C* **2013**, 117, (38), 19288-19294.
171. Beaulac, R.; Schneider, L.; Archer, P. I.; Bacher, G.; Gamelin, D. R. *Science* **2009**, 325, (5943), 973-976.
172. Chen, H.-Y.; Maiti, S.; Nelson, C. A.; Zhu, X.; Son, D. H. *The Journal of Physical Chemistry C* **2012**, 116, (44), 23838-23843.
173. MacKay, J. F.; Becker, W. M.; Spaek, J.; Debska, U. *Physical Review B* **1990**, 42, (3), 1743-1749.

174. Peng, Z. A.; Peng, X. *J. Am. Chem. Soc.* **2001**, 123, (1), 183-184.
175. Jeong, B. G.; Park, Y.-S.; Chang, J. H.; Cho, I.; Kim, J. K.; Kim, H.; Char, K.; Cho, J.; Klimov, V. I.; Park, P.; Lee, D. C.; Bae, W. K. *ACS Nano* **2016**, 10, (10), 9297-9305.
176. Brovelli, S.; Schaller, R. D.; Crooker, S. A.; García-Santamaría, F.; Chen, Y.; Viswanatha, R.; Hollingsworth, J. A.; Htoon, H.; Klimov, V. I. *Nature Communications* **2011**, 2, 280.
177. Brovelli, S.; Bae, W. K.; Galland, C.; Giovanella, U.; Meinardi, F.; Klimov, V. I. *Nano Letters* **2014**, 14, (2), 486-494.
178. Nan, W.; Niu, Y.; Qin, H.; Cui, F.; Yang, Y.; Lai, R.; Lin, W.; Peng, X. *Journal of the American Chemical Society* **2012**, 134, (48), 19685-19693.
179. Chin, P. T. K.; de Mello Donegá, C.; van Bavel, S. S.; Meskers, S. C. J.; Sommerdijk, N. A. J. M.; Janssen, R. A. J. *Journal of the American Chemical Society* **2007**, 129, (48), 14880-14886.
180. Hanson, C. J.; Hartmann, N. F.; Singh, A.; Ma, X.; DeBenedetti, W. J. I.; Casson, J. L.; Grey, J. K.; Chabal, Y. J.; Malko, A. V.; Sykora, M.; Piryatinski, A.; Htoon, H.; Hollingsworth, J. A. *Journal of the American Chemical Society* **2017**, 139, (32), 11081-11088.
181. Li, J. J.; Wang, Y. A.; Guo, W.; Keay, J. C.; Mishima, T. D.; Johnson, M. B.; Peng, X. *Journal of the American Chemical Society* **2003**, 125, (41), 12567-12575.
182. Cao, Y. C.; Wang, J. *Journal of the American Chemical Society* **2004**, 126, (44), 14336-14337.
183. Hendricks, M. P.; Cossairt, B. M.; Owen, J. S. *ACS Nano* **2012**, 6, (11), 10054-10062.
184. Baskoutas, S.; Terzis, A. F. *Journal of Applied Physics* **2006**, 99, (1), 013708.
185. Zhang, B.; Zheng, J.; Li, X.; Fang, Y.; Wang, L.-W.; Lin, Y.; Pan, F. *Chemical Communications* **2016**, 52, (33), 5706-5709.
186. Zhou, J.; Pu, C.; Jiao, T.; Hou, X.; Peng, X. *Journal of the American Chemical Society* **2016**, 138, (20), 6475-6483.
187. Hossain, M. A.; Jennings, J. R.; Koh, Z. Y.; Wang, Q. *ACS Nano* **2011**, 5, (4), 3172-3181.
188. Zhu, G.; Pan, L.; Xu, T.; Sun, Z. *ACS Applied Materials & Interfaces* **2011**, 3, (8), 3146-3151.
189. Tang, J.; Kemp, K. W.; Hoogland, S.; Jeong, K. S.; Liu, H.; Levina, L.; Furukawa, M.; Wang, X.; Debnath, R.; Cha, D.; Chou, K. W.; Fischer, A.; Amassian, A.; Asbury, J. B.; Sargent, E. H. *Nature Materials* **2011**, 10, (10), 765-771.
190. Jin, L.; Sirigu, G.; Tong, X.; Camellini, A.; Parisini, A.; Nicotra, G.; Spinella, C.; Zhao, H.; Sun, S.; Morandi, V.; Zavelani-Rossi, M.; Rosei, F.; Vomiero, A. *Nano Energy* **2016**, 30, 531-541.
191. Hossain, M. A.; Jennings, J. R.; Shen, C.; Pan, J. H.; Koh, Z. Y.; Mathews, N.; Wang, Q. *J. Mater. Chem.* **2012**, 22, (32), 16235-16242.
192. Li, C.; Zhang, H.; Cheng, C. *RSC Advances* **2016**, 6, (44), 37407-37411.
193. Ahmed, R.; Xu, Y.; Zangari, G. *Electrochimica Acta* **2018**, 259, 1095-1103.
194. Chang, Y.-S.; Choi, M.; Baek, M.; Hsieh, P.-Y.; Yong, K.; Hsu, Y.-J. *Applied Catalysis B: Environmental* **2018**, 225, 379-385.
195. Selopal, G. S.; Mohammadnezhad, M.; Navarro-Pardo, F.; Vidal, F.; Zhao, H.; Wang, Z. M.; Rosei, F. *Nanoscale Horizons* **2019**, 4, (2), 404-414.

196. Dembele, K. T.; Selopal, G. S.; Soldano, C.; Nechache, R.; Rimada, J. C.; Concina, I.; Sberveglieri, G.; Rosei, F.; Vomiero, A. *The Journal of Physical Chemistry C* **2013**, 117, (28), 14510-14517.
197. Acharya, S. A.; Maheshwari, N.; Tatikondewar, L.; Kshirsagar, A.; Kulkarni, S. K. *Crystal Growth & Design* **2013**, 13, (4), 1369-1376.
198. Majumder, S.; Mendhe, A. C.; Kim, D.; Sankapal, B. R. *J. Alloys Compd.* **2019**, 788, 75-82.
199. Ranjith, K. S.; Senthamizhan, A.; Balusamy, B.; Uyar, T. *Catalysis Science & Technology* **2017**, 7, (5), 1167-1180.
200. Yen, C.-Y.; Lin, Y.-F.; Hung, C.-H.; Tseng, Y.-H.; Ma, C.-C. M.; Chang, M.-C.; Shao, H. *Nanotechnology* **2008**, 19, (4), 045604.
201. Robel, I.; Kuno, M.; Kamat, P. V. *Journal of the American Chemical Society* **2007**, 129, (14), 4136-4137.
202. Zhu, H.; Song, N.; Lian, T. *Journal of the American Chemical Society* **2010**, 132, (42), 15038-15045.

APPENDIX A ABBREVIATIONS

| | |
|------------------|--|
| 0D | 0-dimensional |
| 1D | 1-dimensional |
| 2D | 2-dimensional |
| 3D | 3-dimensional |
| QDs | Quantum dots |
| DOS | Density of states |
| TEM | Transmission electron microscopy |
| HR-TEM | High-resolution transmission electron microscopy |
| CB | Conduction band |
| VB | Valence band |
| PL | Photoluminescence |
| UV | Ultraviolet |
| NIR | Near infrared |
| QY | Quantum yield |
| Mn | Manganese |
| Cu | Copper |
| d-emission | Dopant emission |
| MEG | Multiple exciton generation |
| QDSC | Quantum dots sensitized solar cell |
| PEC | Photoelectrochemical |
| H ₂ | Hydrogen |
| TiO ₂ | Titanium dioxide |
| PCE | Power conversion efficiency |
| Pt | Platinum |

| | |
|---------------------------------|--|
| CBD | Chemical bath deposition |
| SILAR | Successive ionic layer adsorption and reaction |
| (TMS) ₂ S | Bis(trimethylsilyl) sulfide |
| S | Sulfur |
| OAc | Oleic acid |
| CdO | Cadmium oxide |
| ODE | 1-octadecene |
| TOP | Trioctylphosphine |
| PMMA | Poly(methylmethacrylate) |
| TGA | Thioglycolic acid |
| NaOH | Sodium hydroxide |
| OLA | Oleylamine |
| ICG | Indocyanine green |
| HCl | Hydrochloric acid |
| Na ₂ S | Sodium sulfide |
| Na ₂ SO ₃ | Sodium sulfite |
| ZrO ₂ | Zirconium(IV) oxide |
| CNTs | Carbon nanotubes |
| CTAB | Cetyl-trimethyl ammonium bromide |
| FTO | Fluorine-doped tin oxide |
| XRD | X-ray diffraction |
| SAED | Selected area electron diffraction |
| SEM | Scanning electron microscopy |
| EDS | Energy dispersive X-ray spectroscopy |
| XPS | X-ray photoelectron spectroscopy |

| | |
|-----------|--|
| ICP-OES | Inductively coupled plasma optical emission spectrometry |
| EPR | Electron paramagnetic resonance |
| TRPL | Time-resolved photoluminescence |
| TCSPC | Time-correlated single-photon counting |
| V_{OC} | Open-circuit voltage |
| J_{SC} | Short-circuit current density |
| FF | Fill factor |
| P_{Max} | Maximum power density output |
| J_{MP} | Maximum current density |
| V_{MP} | Maximum potential |
| P_{in} | Incident light power density |
| AM | Air Mass |
| RHE | Reversible hydrogen electrode |
| EPD | Electrophoretic deposition |
| FWHM | Full width at half maximum |
| EIS | Electrochemical impedance spectroscopy |
| GC | Gas chromatography |
| sccm | Standard cubic centimeters per minute |
| TCD | Thermal conductivity detector |
| FE | Faradaic efficiency |
| HOMO | Highest occupied molecular orbital |
| LUMO | Lowest unoccupied molecular orbital |
| OI | Spatial overlap integral between electrons and holes |
| IPCE | Incident photon-to-current efficiency |

APPENDIX B RÉSUMÉ

Conception et synthèse de points quantiques colloïdaux et leurs propriétés optoélectroniques

Introduction et contexte

Les nanomatériaux, communément définis comme des matériaux dont la taille moyenne est inférieure d'au moins un ordre de grandeur à 100 nanomètres (nm), attirent de plus en plus l'attention des chercheurs depuis plusieurs décennies en raison de leur rapport surface-volume élevé par rapport aux matériaux massifs, les rendant très populaires comme éléments de base dans les applications modernes de haute technologie telles que l'imagerie biologique, la biodétection, les cellules solaires, les piles à combustible, les batteries lithium-ion, les supercondensateurs et les concentrateurs solaires luminescents. Les points quantiques (*quantum dots* ou QD) sont de très petits nanocristaux semi-conducteurs (de quelques nm à quelques dizaines de nm) aux propriétés uniques, qui dépendent de leur taille en raison de l'effet de confinement quantique dans les trois dimensions de l'espace. Un QD est composé de centaines à des milliers d'atomes et entouré de ligands organiques, inorganiques ou hybrides organiques/inorganiques, qui peuvent le rendre stable en solution organique/inorganique.

Une propriété fondamentale importante des QD est l'effet de confinement quantique. Pour mieux comprendre cet effet, nous devons d'abord savoir ce qu'est le rayon de Bohr d'un exciton. En général, lorsqu'un semi-conducteur massif est illuminé par des photons incidents d'énergie supérieure à sa bande interdite, l'électron est excité dans la bande de conduction (BC), laissant un trou dans la bande de valence (BV). Cette paire électron-trou est appelée exciton et occupe un certain espace physique. Cet espace (la distance entre ces deux porteurs de charge) se nomme rayon de Bohr de l'exciton et dépend des masses effectives de l'électron et du trou, spécifiques à chaque matériau. Si les dimensions de ces QD sont inférieures à leur rayon de Bohr

excitonique, alors la particule se trouve dans le régime de confinement fort et les bandes qui s'approchaient d'un continuum d'énergie s'apparentent alors plutôt à celles des molécules, c'est-à-dire qu'elles deviennent discrètes. Dans un solide semi-conducteur massif, tous les états d'une bande forment un continuum et la différence d'énergie entre la BC et la BV est la bande interdite de ce matériau spécifique. Dans les QD, l'énergie de bande interdite augmente lorsque la taille des QD diminue. De plus, grâce au confinement quantique, les QD semi-conducteurs peuvent avoir des spectres optiques accordables dans une large fenêtre spectrale, autant pour l'absorption que pour la photoluminescence (PL), simplement en modifiant leur taille, alors que leur composition reste constante.

Les dopants dans les QD semi-conducteurs peuvent créer des états électroniques qui permettent de modifier la dynamique de recombinaison des excitons. Parmi les différents types de QD (QD cœur, QD dopés, QD cœur-coquille, *etc.*), les QD dopés présentent des caractéristiques uniques, en particulier des propriétés magnétiques, optiques et électroniques provenant de l'interaction en confinement entre les porteurs de charge du semi-conducteur et les ions dopants.

Les QD colloïdaux possèdent d'excellentes propriétés optiques, notamment des bandes d'excitation larges et consécutives, une grande absorptivité, une émission étroite et symétrique, une longue durée de vie de la PL, une bonne photostabilité et une longueur d'onde d'émission accordable. Cependant, en raison de leur petite taille (grand rapport surface/volume), les QD colloïdaux de type cœur (tels que le PbS, le CdS, le CdSe, le InP, *etc.*) souffrent d'une forte densité de défauts de surface et d'états de piège de surface qui agissent comme des centres non radiatifs rapides pour la recombinaison des porteurs photogénérés et entraînent une réduction de la photostabilité à long terme et une diminution du rendement quantique (*quantum yield* ou QY) de la PL. Une structure de QD de type cœur-coquille permet d'améliorer la stabilité ainsi que la durée de vie et le QY de la PL, grâce à la passivation améliorée de la surface obtenue en protégeant le cœur des défauts de surface et des sites de pièges. Ce type de structure offre

également la possibilité d'optimiser l'alignement des bandes d'électrons entre le cœur et la coquille. Ainsi, les QD hétérostructurés cœur-coquille figurent parmi les matériaux les plus intéressants à utiliser dans les technologies solaires, notamment pour les cellules solaires à QD (QDSC) et les cellules photoélectrochimiques (PEC) à base de QD pour la production d'hydrogène (H_2), car leurs propriétés optoélectroniques peuvent être adaptées en modifiant les éléments et les dimensions du cœur et/ou de la coquille.

Objectifs de recherche

Mon projet de recherche se concentrera sur la recherche de synthèse contrôlée de différentes classes de QD semi-conducteurs colloïdaux tels que les QD cœurs, les QD dopés et les QD cœur-coquille ainsi que sur l'exploration de leurs propriétés électroniques et optiques, dépendant de leur taille, de leur composition et de leur structure, basées sur l'effet de confinement quantique. Ensuite, les QD seront utilisés comme capteurs de lumière pour évaluer leur potentiel d'application dans des dispositifs de conversion de l'énergie solaire, notamment les QDSC et les cellules PEC à base de QD pour la génération d' H_2 . Mes projets de recherche auront les sous-objectifs suivants :

(1) Je prévois développer une approche simple et optimisée basée sur l'utilisation de thiourée comme précurseur en tant qu'alternative au sulfure de bis(triméthylsilyle) $[(TMS)_2S]$, un précurseur « traditionnel » sensible à l'air et instable, pour synthétiser des QD de PbS dans le proche infrarouge (near infrared ou NIR) par la méthode d'injection à chaud. L'objectif est de parvenir à une synthèse contrôlée des QD de PbS et de développer une approche simple et plus écologique avec une bonne reproductibilité et des manipulations faciles. Je les utiliserai ensuite comme capteurs de lumière et j'évaluerai leurs performances pour les appliquer à la production de H_2 avec des PEC à l'énergie solaire et aux QDSC.

(2) Je prévois synthétiser des QD de petite taille de PbS à bande interdite étroite dopés au Mn afin d'obtenir des propriétés uniques par rapport aux QD de PbS pur. Les propriétés optiques des QD de PbS dopés au Mn seront étudiées de manière approfondie. Le mécanisme d'émission et les propriétés optiques dépendant de la température des QD de PbS dopés au Mn seront bien étudiés et présentés.

(3) Je prévois synthétiser des QD colloïdaux hétérostructurés de type cœur-coquille de CdS/CdSe puis optimiser l'épaisseur de la coquille des QD pour adapter leurs propriétés optoélectroniques et l'alignement de leurs bandes d'énergie. Les QD tels que préparés seront par la suite utilisés comme capteurs de lumière pour des applications dans les cellules PEC à énergie solaire à base de QD pour la génération d'H₂. Je vais ensuite étudier et discuter en profondeur les éléments-clés dans la conception et la fabrication de dispositifs optoélectroniques efficaces et stables, en me basant sur des aspects théoriques et expérimentaux tels que la dynamique des porteurs, l'absorption de la lumière et le taux de transfert des électrons.

Résultats et discussions

Synthèse contrôlée de points quantiques dans le proche infrarouge pour les dispositifs optoélectroniques

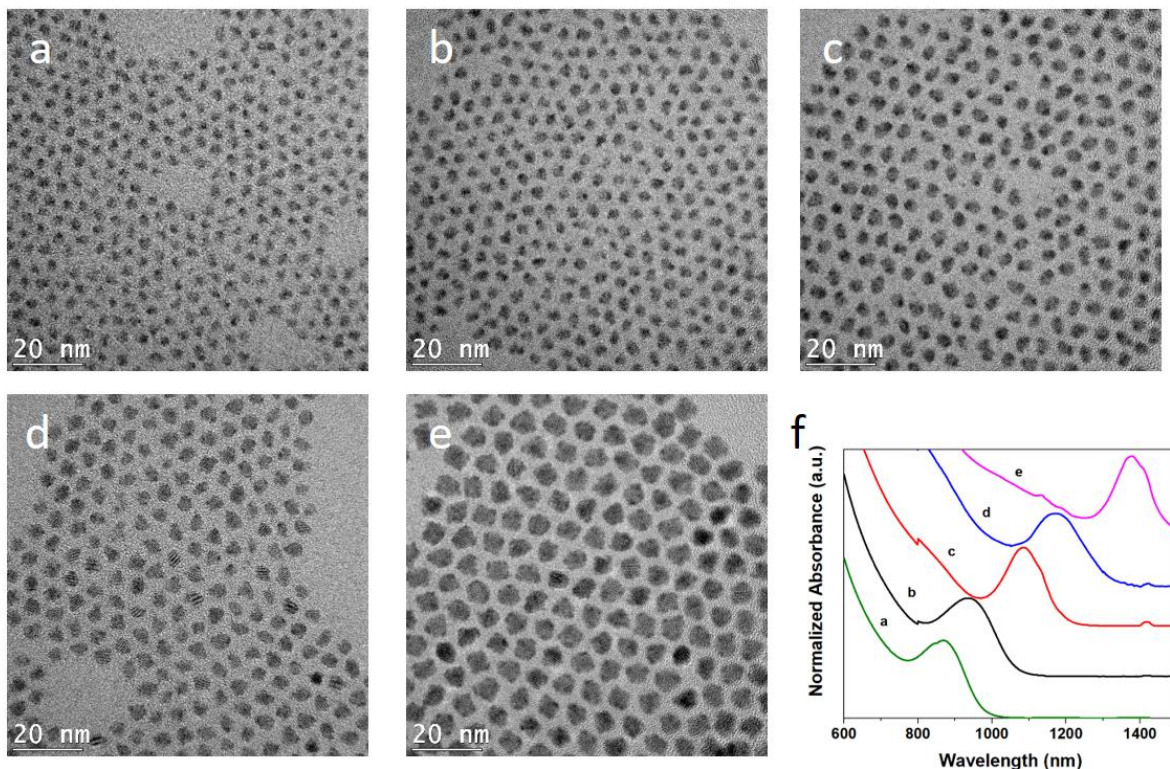


Figure R1 Images MET pour différentes tailles de QD tels que synthétisés en contrôlant la température d'injection et le temps de réaction avec des tailles allant de 3,0 à 5,1 nm : (a) 95°C et 2 min, (b) 100°C et 5 min, (c) 105°C et 5 min, (d) 110°C et 1 min et (e) 115°C et 1 min. (f) Les spectres d'absorption correspondants des QD de PbS.

Les images représentatives des QD de PbS tels que synthétisés obtenues au microscope électronique à transmission (MET) sont présentées aux figures R1a-e et montrent des tailles moyennes de 3,0 à 5,1 nm contrôlées simplement en variant les paramètres de réaction, tels que le temps de réaction et la température d'injection. Les QD de PbS présentent un spectre d'absorption bien contrôlé avec un pic d'absorption étroit (figure R1f). Les QD présentent un premier pic d'absorption excitonique typique allant de 870 à 1400 nm, ce qui est cohérent avec l'augmentation progressive des tailles observée sur les images MET.

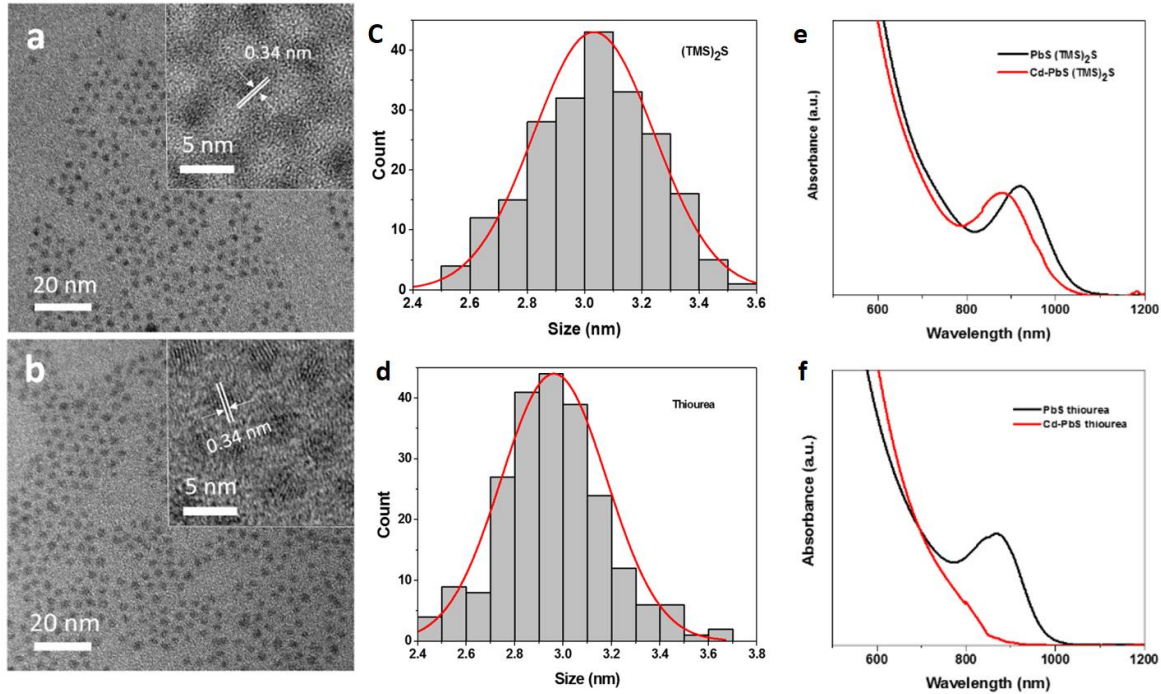


Figure R2 Images MET et HRMET représentatives des QD de Cd-PbS à partir de (a) $(\text{TMS})_2\text{S}$ et (b) de thiourée. La distribution de tailles mesurée sur les images MET des QD de Cd-PbS à partir de (c) $(\text{TMS})_2\text{S}$ et (d) de thiourée. Les spectres d'absorbance des QD de PbS pur et de Cd-PbS préparés à partir de (e) $(\text{TMS})_2\text{S}$ et (f) de thiourée.

Après la synthèse, nous avons étudié l'applicabilité des QD préparés dans les cellules PEC et les QDSC. Deux types de QD de taille similaire d'environ 3 nm provenant de différents précurseurs soufrés, thiourée et $(\text{TMS})_2\text{S}$, ont été choisis pour la comparaison. Le post-traitement des Cd a été mis en œuvre avant la fabrication du dispositif, car une fine couche de CdS peut protéger le cœur de PbS de l'oxydation de surface lors de la fabrication de la photoanode dans les conditions ambiantes. Les figures R2a-b présentent des images MET représentatives de la morphologie des QD de Cd-PbS obtenus à partir de $(\text{TMS})_2\text{S}$ et de thiourée, respectivement, montrant que les tailles des deux types de nanocristaux de Cd-PbS sont très uniformes. Les images MET à haute résolution (HRMET) dans les encarts des figures R2a-b montrent des franges d'interférence du réseau cristallin avec un espacement de 0,34 nm, correspondant à la distance interréticulaire des plans (111) du sulfure de plomb à structure « sel ». Les distributions de tailles des QD colloïdaux de Cd-PbS obtenus à partir de $(\text{TMS})_2\text{S}$ et de thiourée sont présentées sur les figures R2c-d, qui

indiquent que les QD préparés montrent une distribution de tailles uniforme. Le diamètre moyen des QD obtenus à partir de $(\text{TMS})_2\text{S}$ et de thiourée est d'environ 3,0 nm dans les deux cas. Afin d'étudier plus en détail l'épaisseur de la coquille de CdS, nous avons mesuré le rapport atomique Pb-Cd par spectrométrie d'émission optique à plasma à couplage inductif (ICP-OES). Sur la base de ce rapport atomique et du diamètre mesuré à partir des images MET, l'épaisseur calculée pour la coquille est d'environ 0,2 nm pour les QD synthétisés à partir de $(\text{TMS})_2\text{S}$ ou de thiourée.

Les figures R2e-f présentent les spectres d'absorbance UV-Visible-NIR des QD de PbS et de Cd-PbS tels que préparés à partir de $(\text{TMS})_2\text{S}$ et de thiourée, respectivement. Les QD de PbS de type cœur provenant du $(\text{TMS})_2\text{S}$ présentent un pic d'absorption excitonique à environ 918 nm, qui se situe à environ 875 nm pour le PbS provenant de la thiourée. Le décalage vers le bleu de la courbe d'absorption après l'échange de cations provient de la légère diminution de la taille du cœur de PbS lors du remplacement du Pb^{2+} par le Cd^{2+} .

Les figures R3a-b montrent la réponse en photocourant mesurée avec les cellules PEC. Une densité de photocourant saturée de $2,03 \text{ mA}\cdot\text{cm}^{-2}$ a été observée pour la cellule PEC constituée de QD préparés à partir de thiourée et est très similaire à celle pour les QD à partir de $(\text{TMS})_2\text{S}$ ($1,97 \text{ mA}/\text{cm}^2$). La figure R3c montre que les dispositifs tels que préparés à partir de thiourée présentent une meilleure stabilité à long terme (conservent 56% de leur valeur initiale après 2 h) par rapport aux QD synthétisés à l'aide du précurseur $(\text{TMS})_2\text{S}$ (conservent 41% de leur valeur initiale).

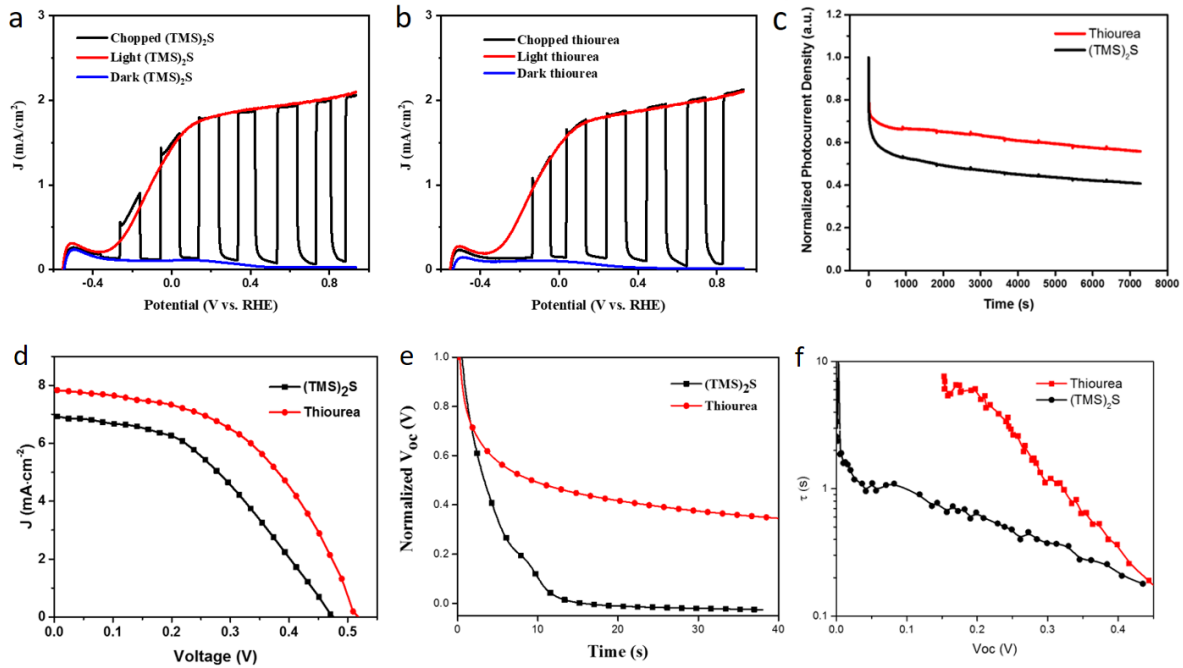


Figure R3 Pour les cellules PEC : Courbes de densité de photocourant en fonction du potentiel [vs électrode réversible à hydrogène (ERH)] des dispositifs PEC assemblés à l'aide de nos QD tels que préparés à partir de (a) $(\text{TMS})_2\text{S}$ et (b) de thiourée, (c) Densité de courant mesurée en fonction du temps pour les dispositifs à base de QD de PbS à partir de $(\text{TMS})_2\text{S}$ et de thiourée. Pour les QDSC : (d) Courbes $J-V$ des QDSC à base de nos QD tels que préparés à partir de thiourée et de $(\text{TMS})_2\text{S}$, (e) Mesures de la décroissance de la phototension transitoire des QDSC correspondants, (f) Durée de vie obtenue pour les électrons en fonction de V_{oc} .

Les courbes de densité de courant en fonction de la tension ($J-V$) des QDSC fabriqués sont présentées à la figure R3d. Le dispositif à base de QD synthétisés via thiourée livre une efficacité de conversion de puissance (*power conversion efficiency* ou PCE) de 2,00%, montrant une meilleure performance photovoltaïque globale par rapport au dispositif à base de QD synthétisés à partir de $(\text{TMS})_2\text{S}$, qui a une PCE de 1,40%. La figure R3e illustre que le dispositif à base de QD à partir de $(\text{TMS})_2\text{S}$ présente une chute rapide de la phototension comparativement au dispositif à base de QD à partir de thiourée, ce qui signifie que la recombinaison des porteurs à l'interface QD/ TiO_2 est plus élevée dans le premier dispositif que dans le second. La figure R3f montre que la durée de vie des électrons est plus longue pour le dispositif formé de QD à partir

de thiourée que pour celui formé de QD à partir de $(\text{TMS})_2\text{S}$, ce qui concorde avec les performances photovoltaïques obtenues pour ces dispositifs. Ces résultats ont confirmé que le dispositif à base de QD de thiourée a une plus faible recombinaison non radiative de porteurs à l'interface QD/ TiO_2 /électrolyte en raison d'un moins grand nombre de pièges de surface dans les QD comparativement aux QD synthétisés à partir de $(\text{TMS})_2\text{S}$.

Points quantiques colloïdaux dopés au manganèse dans le proche infrarouge : mécanisme de photoluminescence et réponse en température

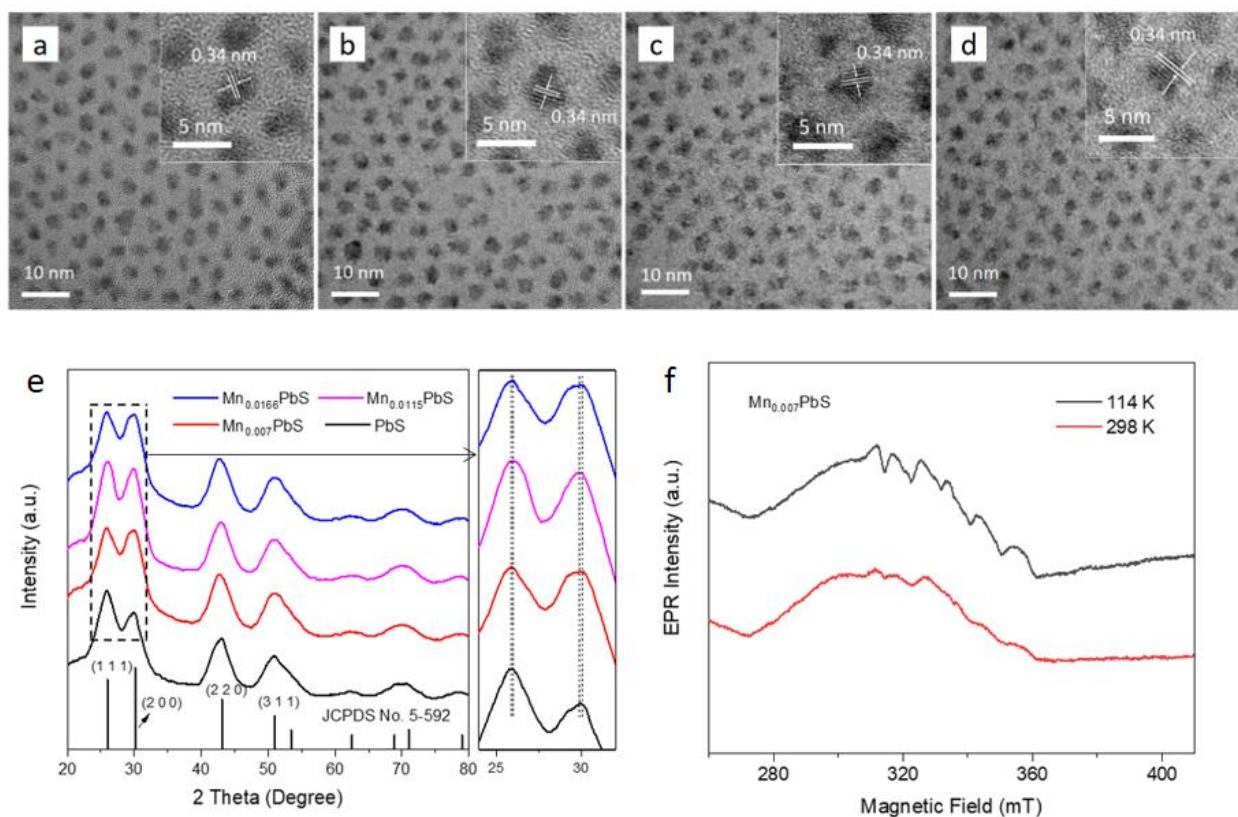


Figure R4 Images MET représentatives de QD (a) de PbS pur, (b) de $Mn_{0,007}PbS$, (c) de $Mn_{0,0115}PbS$ et (d) de $Mn_{0,0166}PbS$. Les images en encart sont les images HRMET pour chaque type de QD. (e) Spectres de diffraction des rayons X (XRD) des QD de PbS pur et dopés au Mn tels que synthétisés. L'encadré de droite montre un agrandissement des spectres XRD de 24° à 32° . Les données de la fiche JCPDS pour le PbS (n° 05-0592, ligne noire) sont indiquées à des fins d'identification. (f) Spectres de résonance paramagnétique électronique (RPE) de l'échantillon de $Mn_{0,007}PbS$ tel que synthétisé à 298 K et à 114 K, respectivement.

Nous avons utilisé un substitut de thiourée comme précurseur soufre en raison de son faible coût et de sa stabilité dans l'air par rapport au $(TMS)_2S$ largement utilisé et de son activité réactionnelle plus élevée par rapport à un précurseur de soufre élémentaire. En contrôlant la stœchiométrie Pb/Mn pendant la réaction, différentes concentrations de dopant Mn ont été introduites dans les QD. Les figures R4a-d montrent les images MET représentatives des QD de PbS, de $Mn_{0,007}PbS$, de $Mn_{0,0115}PbS$ et de $Mn_{0,0166}PbS$. Les QD tels qu'ils ont été préparés ont une distribution de tailles

uniforme avec un diamètre moyen d'environ 2,8 nm. Les images HRMET en encart des figures R4a-d confirment que les QD de PbS dopés au Mn conservent la structure « sel » hautement cristalline du sulfure de plomb massif.

Sur la figure R4e, les spectres XRD des échantillons de PbS pur et de PbS dopés au Mn montrent que la structure cristalline « sel » est toujours maintenue malgré l'incorporation d'ions Mn dans les QD. Comme les concentrations molaires d'ions Mn mesurées par ICP-OES sont très faibles dans les QD synthétisés (0,00%, 0,70%, 1,15% et 1,66% dans les QD de PbS, de $Mn_{0,007}PbS$, de $Mn_{0,0115}PbS$ et de $Mn_{0,0166}PbS$ respectivement), nous ne pouvons pas détecter le signal XRD du MnS. Cependant, les pics caractéristiques présentent un léger décalage vers des angles de diffraction plus élevés avec l'incorporation de Mn, comme le montre la figure R4e (encadré de droite). Cela indique une diminution du paramètre de maille, ce qui est cohérent avec ce qui a été rapporté précédemment. Les spectres RPE (figure R4f) pour les QD de $Mn_{0,007}PbS$ indiquent que les ions Mn viennent doper la surface, la surface proche et le cœur des QD.

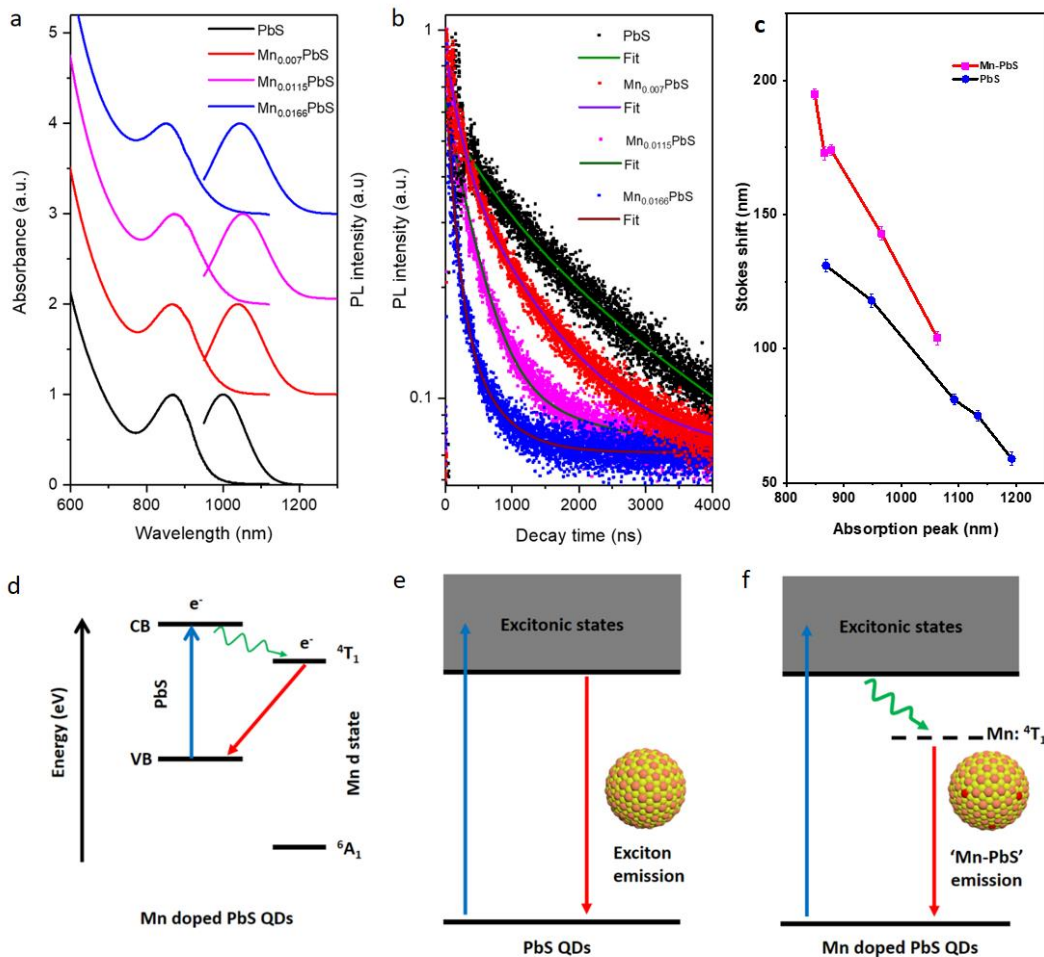


Figure R5 Propriétés optiques des QD de PbS et des QD de PbS dopés au Mn dans le toluène : a) Spectres d'absorption et de PL. La longueur d'onde d'excitation est $\lambda_{ex} = 450$ nm ; (b) Courbes de décroissance de la PL. La longueur d'onde d'excitation est $\lambda_{ex} = 444$ nm. (c) Ensemble des déplacements de Stokes en fonction du pic d'absorption des QD de PbS et de PbS dopés au Mn. (d) Niveaux des bandes d'énergie des QD de PbS et de l'état d du Mn. Les processus radiatifs sont indiqués par des lignes droites et les processus non radiatifs, par des lignes ondulées. Illustration schématique du changement de l'état excité émetteur (e) pour les QD de PbS et (f) après l'incorporation de Mn dans les QD de PbS.

La figure R5a montre que l'incorporation de Mn dans les QD de PbS fait augmenter le déplacement de Stokes. À taille égale, les QD de PbS pur présentent un déplacement de Stokes de 180 meV, inférieur aux valeurs de 240 meV pour les QD de Mn_{0,007}PbS, de 232 meV pour Mn_{0,0115}PbS et de 269 meV pour Mn_{0,0166}PbS. La figure R5b montre une diminution de la durée

de vie de décroissance de la PL lorsque la teneur en Mn augmente dans les QD de PbS. Les durées de vie mesurées sont de 2,37 μs , 1,29 μs , 0,62 μs et 0,36 μs pour les QD de PbS, de $\text{Mn}_{0,007}\text{PbS}$, de $\text{Mn}_{0,0115}\text{PbS}$ et de $\text{Mn}_{0,0166}\text{PbS}$, respectivement.

Le QY de la PL est respectivement de 71,0%, 7,6%, 3,5% et 2,1% pour les QD de PbS, de $\text{Mn}_{0,007}\text{PbS}$, de $\text{Mn}_{0,0115}\text{PbS}$ et de $\text{Mn}_{0,0166}\text{PbS}$. Les résultats montrent que le QY ainsi que le taux de désactivation radiatif (K_{et}) diminuent après l'incorporation d'ions Mn. Nous constatons également que les valeurs de K_{et} sont très similaires pour les QD de PbS dopés au Mn avec différentes concentrations de dopant Mn. Cependant, le K_{et} du PbS est significativement plus élevé que celui des QD de PbS dopés au Mn. Ces résultats montrent qu'il existe une différence intrinsèque en ce qui a trait à l'émission entre les QD de PbS pur et de PbS dopés au Mn.

La figure R5c montre l'ensemble des déplacements de Stokes qui ont été mesurés en fonction du pic d'absorption des QD de PbS et de PbS dopés au Mn pour différentes tailles de QD. Ces valeurs indiquent que les QD de PbS dopés au Mn présentent un déplacement de Stokes qui augmente dans chaque avec la taille, mais la différence de déplacement de Stokes est de plus en plus petite avec le décalage vers le rouge du pic d'absorption.

Comme le montre la figure R5d, l'état énergétique 4T_1 se situe entre la BV et la BC des QD de PbS, tandis que l'état énergétique 6A_1 se situe en dessous de la BV des QD de PbS. Le taux d'énergie transféré du nanocrystal photoexcité aux ions Mn ($\sim\text{ps}$, représenté par les lignes vertes ondulées à la figure R5d) dépasse largement celui de la recombinaison des excitons ($\sim\mu\text{s}$), permettant le transfert d'énergie vers les ions Mn.

Les diagrammes schématiques des transitions électroniques impliquées dans la PL des QD de PbS et de PbS dopés au Mn sont présentés à la figure R5e. Lorsqu'un QD de PbS pur est excité par des photons d'énergie supérieure à sa bande interdite, l'émission d'exciton généralement observée provient de la recombinaison directe des paires électron-trou. Le diagramme schématique du chemin des transitions électroniques dans les QD de PbS dopés au Mn est

présenté à la figure R5f. Au départ, les électrons sont pompés de la BV vers la BC de « l'hôte » PbS, puis sont transférés de manière non radiative au niveau 4T_1 du dopant Mn. Comme le niveau 6A_1 est inférieur à la BV de l'hôte PbS, les électrons photogénérés se relaxent de manière radiative vers la BV des QD au lieu du niveau 6A_1 du dopant Mn, ce qui entraîne une émission de « Mn-PbS ».

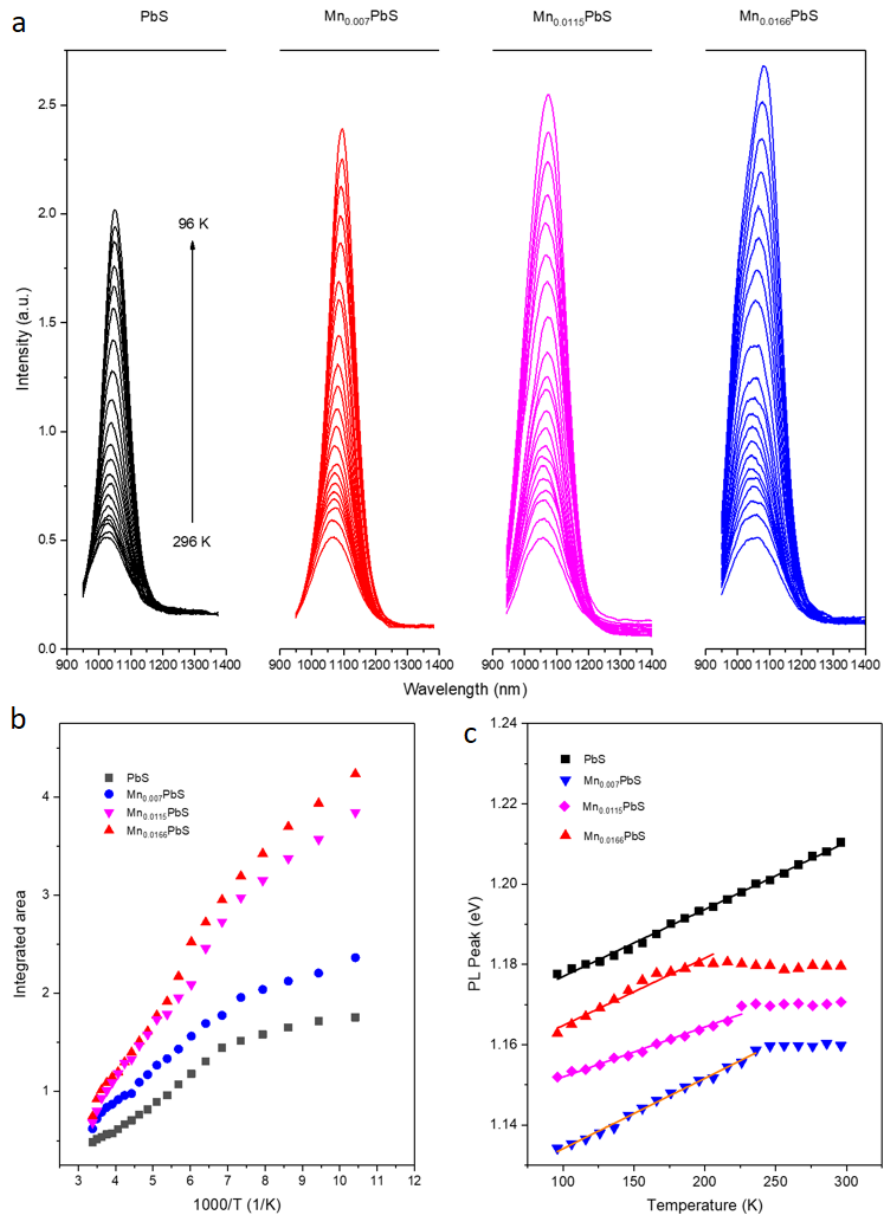


Figure R6 (a) Spectres de PL normalisés pour des QD de PbS et des QD de PbS dopés au Mn (plus spécifiquement, de gauche à droite, des échantillons de PbS, de $Mn_{0.007}PbS$, de $Mn_{0.0115}PbS$

et de $\text{Mn}_{0,0166}\text{PbS}$, respectivement) enregistrés à différentes températures de 96 à 296 K. La longueur d'onde d'excitation est $\lambda_{\text{ex}} = 450$ nm. (b) Pic de PL intégré normalisé en fonction de $1000/T$ pour les QD de PbS pur et dopés au Mn, où T est la température. (c) Position du pic de PL en fonction de la température pour les QD de PbS pur et dopés au Mn.

La figure R6a montre que, pour les QD de PbS et de PbS dopés au Mn, les spectres de PL présentent une dépendance marquée à la température. Les variations spectrales indiquent qu'une diminution de la température augmente systématiquement l'intensité de la PL et décale le pic d'émission vers des longueurs d'onde plus élevées.

La figure R6b montre une tendance similaire pour tous les échantillons, qui consiste en une augmentation de l'intensité de la PL avec la diminution de la température. Dans la figure R6a-b, l'augmentation de la surface intégrée est plus rapide pour les QD de PbS dopés au Mn que pour les QD de PbS pur, ce qui indique que les QD dopés au Mn sont plus sensibles aux effets de la température.

La dépendance en température du pic d'énergie de PL des QD de PbS pur et dopés au Mn est exposée à la figure R6c. La différence de comportement en température entre les QD de PbS pur et dopés au Mn pourrait être expliquée grâce à l'illustration schématique de l'alignement des bandes BV et BC des ions PbS et Mn présentée à la figure R5d. L'émission de « Mn-PbS » implique à la fois l'énergie de la BV de l'hôte PbS et le niveau d'énergie 4T_1 des ions Mn, qui dominant le processus de PL. Le décalage combiné des bandes de PbS et de l'état 4T_1 du Mn se traduit par un changement du comportement en température du décalage en énergie des pics de PL dans les QD de PbS dopés au Mn par rapport aux QD de PbS pur. En considérant les différences observées sur la figure R6c entre les QD de PbS pur et dopés au Mn en ce qui a trait à la variation de la position du pic de PL en fonction de la température, nous concluons que le niveau d'énergie 4T_1 du Mn a un effet dominant sur l'émission de « Mn-PbS » dans les QD de PbS dopés au Mn à des températures élevées.

Ces résultats apportent de nouvelles connaissances fondamentales sur le mécanisme d'émission et sur les propriétés optiques dépendantes de la température des QD dopés au Mn et démontrent que les QD de PbS dopés au Mn ont du potentiel pour des applications liées aux capteurs thermiques.

Génération photoélectrochimique efficace et stable d'hydrogène à l'aide de points quantiques colloïdaux hétérostructurés optimisés

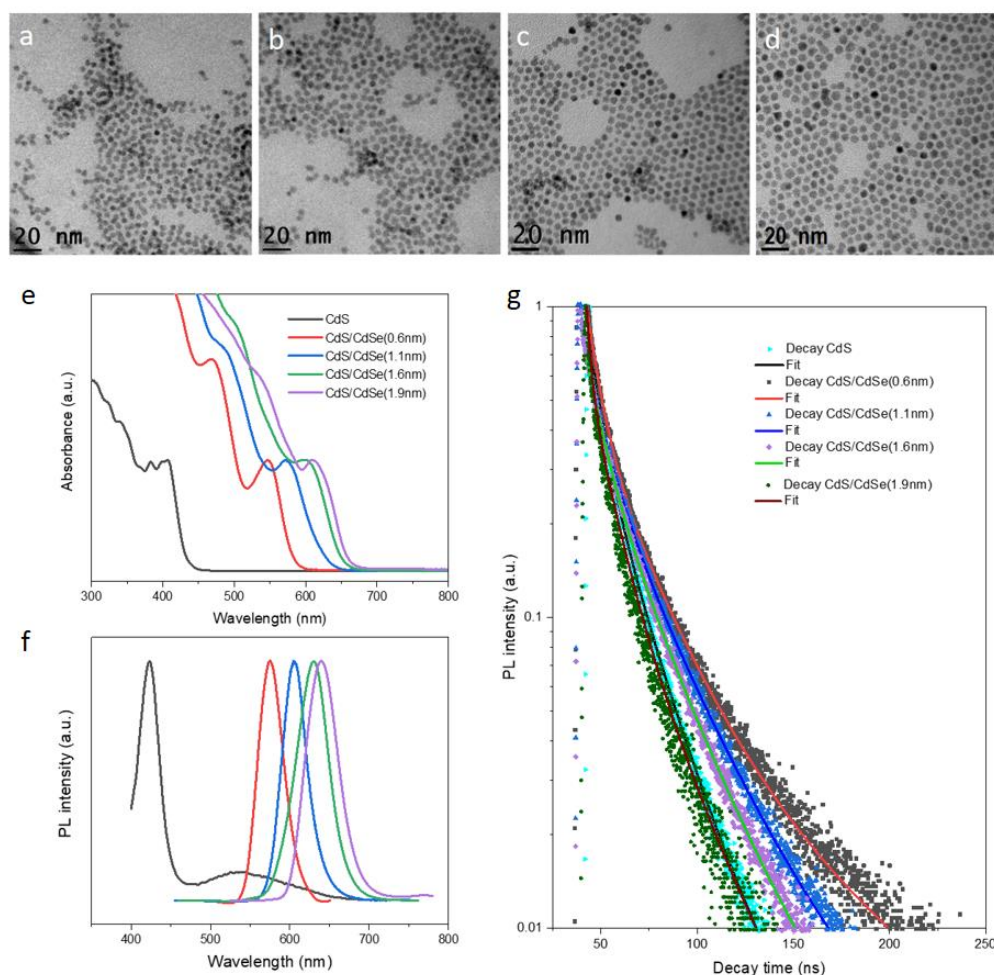


Figure R7 Images MET représentatives a) de QD CdS/CdSe (0,6 nm), b) de QD CdS/CdSe (1,1 nm), c) de QD CdS/CdSe (1,6 nm) et d) de QD CdS/CdSe (1,9 nm). Propriétés optiques des QD de CdS et CdS/CdSe dans le toluène : (e) spectres d'absorption, (f) spectres de PL. g) Mesures expérimentales de photoluminescence résolue en temps (TRPL) des QD tels que synthétisés dans le toluène.

La forme sphérique des QD de CdS a été observée au MET. Les figures R7a-d montrent des images MET représentatives des QD cœur-coquille CdS/CdSe avec différentes épaisseurs de coquille. Les QD cœur-coquille conservent leur forme régulière quasi-sphérique avec une distribution de tailles étroite et uniforme (<10%) après la croissance de la coquille, comme le

confirme la distribution de tailles mesurée au MET. Les figures R7e-f montrent que, par rapport aux QD de CdS de type cœur, les QD cœur-coquille contenant une couche de CdSe possèdent une absorption lumineuse considérablement plus étendue vers les longueurs d'onde plus élevées (jusqu'à 680 nm). Les durées de vie mesurées présentées à la figure R7g sont de 21, 57, 46, 35 et 20 ns pour le CdS, le CdS/CdSe (0,6 nm), le CdS/CdSe (1,1 nm), le CdS/CdSe (1,6 nm) et le CdS/CdSe (1,9 nm), respectivement. Cela montre que la durée de vie augmente d'abord au tout début, après la croissance d'une mince coquille de CdSe ($H = 0,6$ nm), puis diminue par la suite lorsque l'épaisseur de la coquille de CdSe croît ($H = 1,1-1,9$ nm).

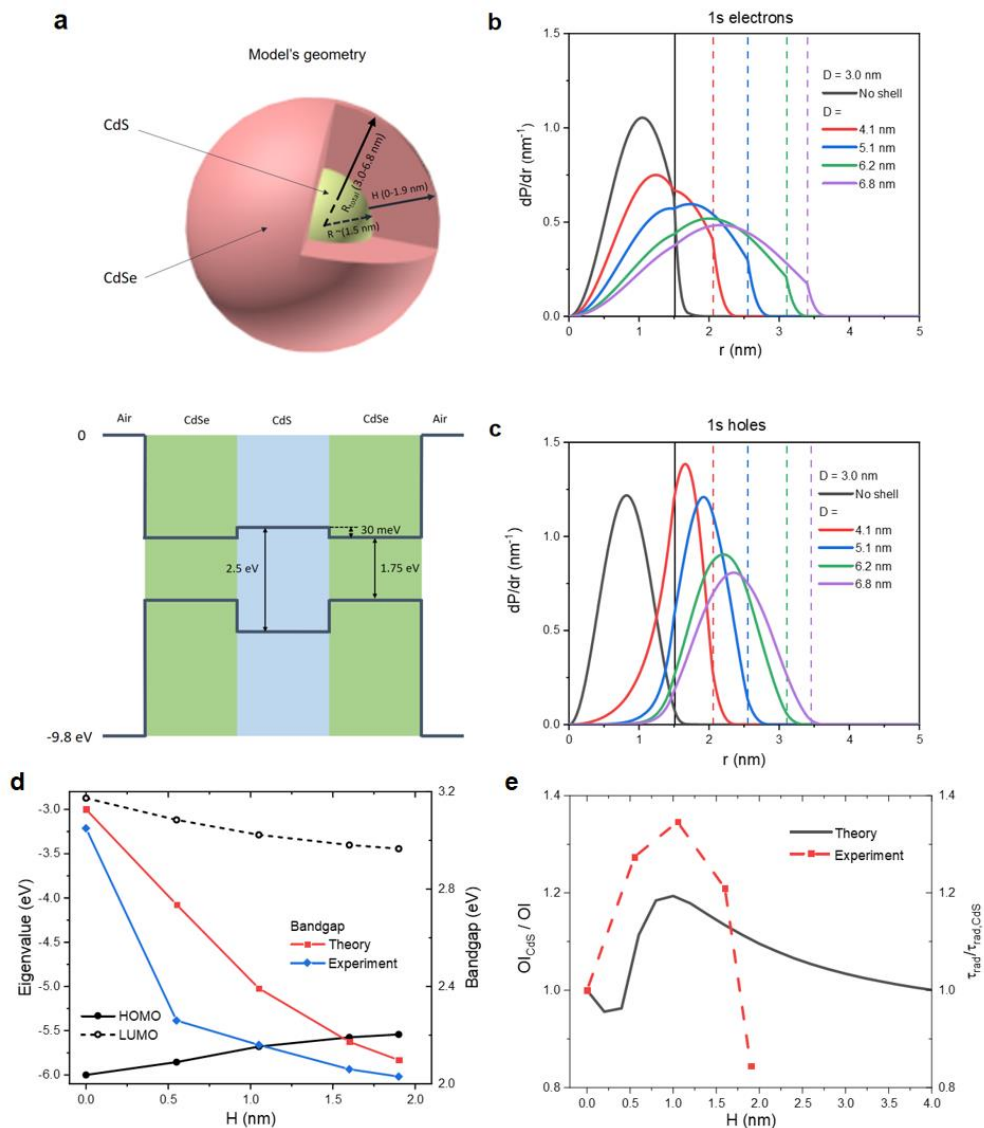


Figure R8 (a) Modèle géométrique de QD cœur-coquille CdS/CdSe sphériques. (b, c) Distribution radiale de probabilité de présence des (b) électrons et (c) des trous dans le système modèle. (d) Évolution de la plus haute orbitale moléculaire occupée (HOMO) et de la plus basse orbitale moléculaire inoccupée (LUMO), chacune étant considérée comme l'état propre le plus bas du puits de potentiel quantique correspondant pour les électrons et pour les trous. L'évolution de la bande interdite théorique est comparée à celle des bandes interdites expérimentales (estimées à partir des longueurs d'onde d'absorption). (e) L'inverse du chevauchement des électrons et des trous (ligne noire pleine), normalisée par sa valeur pour les QD de CdS, et le rapport de la durée de vie radiative des QD cœur-coquille sur celle des QD de CdS de type cœur ($T_{rad}/T_{rad\ cœur}$) (ligne rouge pointillée) en fonction de l'épaisseur de la coquille.

En complément à nos études expérimentales, nous présentons des résultats numériques obtenus à partir de la modélisation théorique des QD basée sur la résolution de l'équation de Schrödinger indépendante du temps pour des hétérostructures sphériques en utilisant les paramètres des matériaux massifs (voir figure R8a).

Les figures R8b-c mettent en évidence la tendance des porteurs à se délocaliser vers la coquille à mesure que son épaisseur augmente. Cependant, la probabilité de délocalisation n'est pas la même pour les électrons et pour les trous en raison de l'alignement des bandes d'énergie du CdS et du CdSe. Les calculs théoriques montrent l'évolution de l'alignement des bandes entre un quasi type II et un type I inversé, alors que les électrons se délocalisent progressivement et les trous, rapidement, vers la région de la coquille lorsque l'épaisseur de la coquille augmente progressivement.

De plus, les positions des orbitales HOMO et LUMO ainsi que les bandes interdites théoriques sont indiquées dans la figure R8d. L'approche théorique relativement simple utilisée ici permet de faire ressortir une tendance expérimentale à partir des résultats optiques obtenus.

Comme le montre la figure R8e, le modèle théorique prévoit une augmentation de la durée de vie radiative avec l'augmentation de la taille de la coquille jusqu'à ~1,1 nm. L'augmentation de l'épaisseur de la coquille au-delà de cette valeur augmente le chevauchement spatial des

porteurs, ce qui annule les gains pour la durée de vie de ces porteurs. Les estimations théoriques reproduisent correctement les tendances observées expérimentalement pour les durées de vie radiatives.

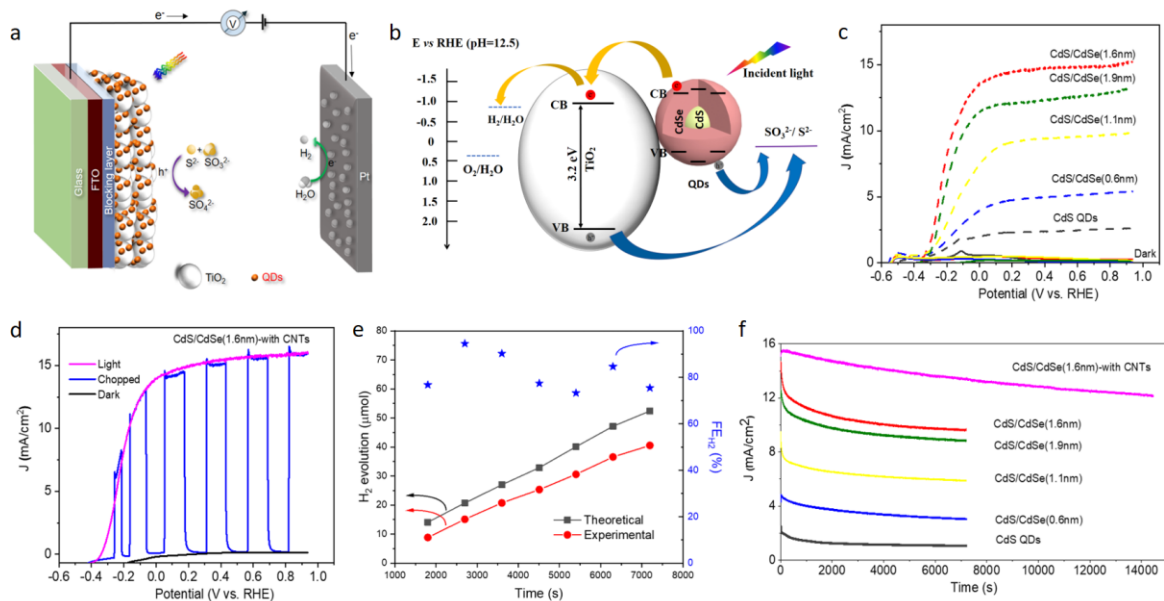


Figure R9 (a) Schéma du mécanisme de fonctionnement d'un dispositif PEC avec une photoanode à base de QD/TiO₂. (b) Niveaux d'énergie approximatifs du TiO₂ et des QD, avec les potentiels rédox caractéristiques correspondants. (c) Courbes de densité de photocourant en fonction du potentiel (vs ERH) de dispositifs PEC assemblés à base de différents QD. (d) Performance des dispositifs PEC avec photoanode de hybride CNT-TiO₂ avec des QD CdS/CdSe (1,6 nm). (e) Évolution de H₂ et valeurs de RF en fonction du temps pour les cellules PEC fabriquées à partir de QD CdS/CdSe (1,6 nm) avec photoanode de hybride CNT-TiO₂. (f) Densité de courant mesurée en fonction du temps pour les dispositifs PEC.

La figure R9a présente une illustration schématique du mécanisme de fonctionnement d'un dispositif PEC avec photoanode à base de QD/TiO₂. La figure R9b montre les niveaux d'énergie approximatifs du TiO₂ et des QD, ainsi que les potentiels rédox caractéristiques associés.

Comme le montre la figure R9c, les cellules PEC à base de QD de CdS de type cœur révèlent une densité de courant saturée de 2,7 mA/cm². Cette faible densité de courant est probablement due à la plage d'absorption limitée et à la forte densité d'états de piège à la surface des QD, qui

servent de sites de recombinaison non radiative des porteurs après illumination. Une amélioration du niveau de saturation de la densité de photocourant est observée pour tous les dispositifs à base de QD cœur-coquille, avec une densité de photocourant saturée qui atteint 5,4, 9,8, 15,0 et 13,0 mA/cm² pour le CdS/CdSe (0,6 nm), le CdS/CdSe (1,1 nm), le CdS/CdSe (1,6 nm) et le CdS/CdSe (1,9 nm), respectivement.

La figure R9d montre que le réglage de l'alignement des bandes d'énergie dans ce système de QD colloïdaux cœur-coquille et l'utilisation d'une photoanode de hybride CNT (nanotubes de carbone)-TiO₂ ont permis de fabriquer une cellule PEC avec une densité de photocourant atteignant 16,0 mA/cm² sous une illumination de 1 soleil. Plus important encore, il s'agit de la valeur la plus élevée jamais enregistrée pour des cellules PEC à base de QD CdS/CdSe. La mesure de chromatographie en phase gazeuse (CPG) de la figure R9e montre que le rendement de Faraday (RF) calculé pour la production d'H₂ a une valeur moyenne de 81,7% pour les cellules PEC à base de QD CdS/CdSe (1,6 nm), indiquant que le photocourant obtenu est principalement attribué à la production d'H₂. En outre, les cellules PEC fabriquées présentent une stabilité à long terme nettement améliorée, puisqu'elles conservent 83% de leur valeur initiale de densité de courant après une illumination continue de 1 soleil pendant 4 h (voir figure R9f). Ces résultats démontrent que la photoanode à base de QD cœur-coquille conçue présente un grand potentiel d'application dans les cellules PEC à base de QD pour la production d'H₂.

L'effet combiné de l'élargissement de la plage d'absorption lumineuse et de l'augmentation du taux de transfert d'électrons dans ce système QD/TiO₂ permet une collecte de la lumière et un transport des photoélectrons plus efficaces. Nos résultats mettent également en évidence le fait que l'ingénierie des fonctions d'ondes des électrons/trous des QD cœur-coquille constitue une stratégie efficace pour optimiser les propriétés optoélectroniques des QD en vue du développement de cellules PEC et d'autres dispositifs optoélectroniques rentables, à haut rendement et stables.